The Einstein Telescope beam pipe vacuum system: Exploring novel techniques and materials for a cost-effective design solution

Von der Fakultät für Mathematik, Informatik und Naturwissenschaften der RWTH Aachen University zur Erlangung des akademischen Grades eines Doktors der Ingenieurwissenschaften genehmigte Dissertation

vorgelegt von

Carlo Scarcia M.Eng.

aus

Tricase, Italien

Berichter: Prof. Dr. Thomas Hebbeker
Prof. Dr.-Ing. habil. Ulrich Krupp
Prof. Dr. Achim Stahl

Tag der mündlichen Prüfung: 17.07.2025

The Einstein Telescope beam pipe vacuum system: Exploring novel techniques and materials for a cost-effective design solution - *Carlo Scarcia*
Doctoral Thesis, RWTH, Aachen, 2025

The research described in this thesis has been sponsored by the Wolfgang Gentner Programme of the German Federal Ministry of Education and Research (grant no. 13E18CHA).

Abstract

In the coming decades, the next generation of gravitational wave detectors (3G-GWDs), such as the Cosmic Explorer (CE) and Einstein Telescope (ET), will enable us to study the universe's evolution back to the formation of the first stars.

These detectors are designed to operate with sensitivities an order of magnitude better than those of the current generation (2G-GWDs).

Achieving this improved performance will require significantly longer detector arms operating in Ultra High Vacuum (UHV) conditions, with partial pressures one order of magnitude lower than those in existing large-scale interferometers.

Scaling current production and vacuum solutions would lead to beam pipe vacuum systems costing around 1/3 of the forecasted budget and requiring nearly two decades to complete. To overcome these challenges, it is crucial to identify more cost-effective UHV-compatible alloys to replace the currently used austenitic stainless steel. Additionally, designing a reliable vacuum system that meets stringent requirements while ensuring operational efficiency is essential.

This thesis provides two key contributions: First, a comprehensive study of the UHV compatibility of commercially available ferritic alloys. The selected grades, from the mild steel and ferritic stainless steel families, are quantitatively analysed and compared with as-received austenitic stainless steel in unbaked and baked conditions. Thermal Programmed Desorption (TPD) is used to study hydrogen content and the characteristic desorption curve. Due to a lack of data in the literature, custom tests were developed to determine water vapour binding energies. These findings were then validated through simulations of bakeout cycles, predicting the resulting ultimate water vapour partial pressure. Furthermore, the effectiveness of low-temperature bakeout is explored as a potential economical solution for reducing commissioning costs. In addition, thin-walled corrugated prototypes made from three different alloys—austenitic stainless steel, mild steel, and ferritic stainless steel—were developed and tested. These prototypes were tested under bakeout and scaled pumping conditions to simulate the environment of a GWD beam pipe vacuum sector.

After setting the boundary conditions based on the experiment, the second contribution utilises the vacuum properties of the analysed alloys and the developed model to design the ET beam pipe vacuum system and outline a commissioning procedure. A preliminary cost estimation is provided and compared to previous cost projections.

In summary, this thesis demonstrates that using inexpensive steel grades and a well-considered design, the beam pipe vacuum system for next-generation gravitational wave detectors can be constructed at a fraction of the cost previously forecasted without compromising UHV performance—and potentially even surpassing the original vacuum performances.

Zusammenfassung

In den kommenden Jahrzehnten wird die nächste Generation von Gravitationswellendetektoren (3G-GWDs), wie der Cosmic Explorer (CE) und das Einstein-Teleskop (ET), es ermöglichen, die Entwicklung des Universums bis zurück zur Entstehung der ersten Sterne zu erforschen. Diese Detektoren sind so konzipiert, dass sie mit einer um eine Größenordnung besseren Empfindlichkeit arbeiten als die der aktuellen Generation (2G-GWDs). Um diese verbesserte Leistungsfähigkeit zu erreichen, sind deutlich längere Detektorarme erforderlich, die unter Ultrahochvakuumbedingungen (UHV) betrieben werden, mit einem Partialdruck, der um eine Größenordnung niedriger ist als in den bestehenden großmaßstäbigen Interferometern. Die Skalierung der derzeitigen Produktions- und Vakuumlösungen würde jedoch dazu führen, dass die Vakuumsysteme der Strahlrohre etwa ein Drittel des prognostizierten Budgets ausmachen und fast zwei Jahrzehnte für ihre Fertigstellung benötigen. Um diese Herausforderungen zu bewältigen, ist es entscheidend, kostengünstigere UHV-kompatible Legierungen zu identifizieren, die den derzeit verwendeten austenitischen Edelstahl ersetzen können. Darüber hinaus ist die Entwicklung eines zuverlässigen Vakuumsystems, das die strengen Anforderungen erfüllt und gleichzeitig eine effiziente Betriebsweise gewährleistet, von entscheidender Bedeutung.

Diese Dissertation liefert zwei zentrale Beiträge: Zunächst, eine umfassende Untersuchung der UHV-Kompatibilität kommerziell verfügbarer ferritischer Legierungen. Die ausgewählten Legierungen, die aus den Familien von Baustahl und ferritischem Edelstahl stammen, werden quantitativ analysiert und mit dem unbehandelten sowie ausgeheiztem austenitischen Edelstahl verglichen. Mittels Thermischer Desorptionsspektroskopie (TPD) wird der Wasserstoffgehalt und die charakteristische Desorptionskurve untersucht. Da in der Literatur entsprechende Daten nicht vorhanden sind, wurden speziell angepasste Tests entwickelt, um die Bindungsenergien von Wasserdampf zu bestimmen. Diese Ergebnisse wurden anschließend durch Simulationen von Ausheizzyklen validiert, um den resultierenden ultimativen Wasserdampfpartialdruck vorherzusagen. Außerdem wird die Wirksamkeit der Ausheizens bei niedrigen Temperaturen als potenzielle wirtschaftliche Lösung zur Reduzierung der Inbetriebnahmekosten untersucht. Zusätzlich wurden dünnwandige, gewellte Prototypen aus drei verschiedenen Legierungen – austenitischer Edelstahl, Baustahl und ferritischer Edelstahl – entwickelt und getestet. Diese Prototypen wurden unter Ausheizung und skalierbaren Pumpbedingungen getestet, um die Umgebung eines GWD-Strahlrohr-Vakuumsektors zu simulieren.

Nachdem die Randbedingungen auf Grundlage des Experiments festgelegt wurden, wird in dem zweiten Beitrag der Dissertation die Vakuumeigenschaften der analysierten Legierungen und des entwickelten Modells genutzt, um das ET-Strahlrohr-Vakuumsystem zu entwerfen und ein Inbetriebnahmeverfahren zu skizzieren. Es wird eine vorläufige Kostenabschätzung erstellt und mit früheren Kostenvorhersagen verglichen. Zusammenfassend zeigt diese Arbeit, dass mit der Verwendung kostengünstiger Stahllegierungen und einem durchdachten Design das Strahlrohr-Vakuumsystem

für Gravitationswellendetektoren der nächsten Generation zu einem Bruchteil der zuvor prognostizierten Kosten gebaut werden kann ohne die UHV-Leistung zu beeinträchtigen und möglicherweise sogar die ursprünglichen Vakuumeigenschaften übertrifft.

Contents

- The Motivation -

1. Introduction

..So sieht man, dass A in allen nur denkbaren Fallen einen praktisch verschwindenden Wert haben muss.

-Albert Einstein, 1916-

1.1 Gravitational waves

In 1915, Albert Einstein revolutionised our understanding of the universe by introducing General Relativity (GR) [1]. GR extends the principles of Special Relativity (SR) and modifies Newton's law of universal gravitation by introducing the concept of curved spacetime. This groundbreaking theory has transformed how we observe the universe and laid the foundation for new fields of astronomy. Einstein's field equation solution has yielded numerous physical consequences, with many being experimentally demonstrated. These include the existence, among others, of massive entities like black holes and neutron stars and effects such as gravitational lensing. However, the most challenging concept to fathom and accept, even for Einstein himself, is that of gravitational waves (GW).

In 1916, Einstein introduced the concept of GW while attempting to linearize the field equation under weak field conditions [2]. The outcome of this linearization, when applied far from matter, is a wave equation that describes a wave propagating at the speed of light. In a rudimentary interpretation of GR, spacetime can be depicted as a stiff medium that can bend due to the presence of an astronomical object in a given

position. Moreover, when the object is in accelerated motion, the curvature of the spacetime changes and propagates outwards at the speed of light. The typical example to visualise the phenomenon is to consider a binary system in spacetime comprising two objects with dissimilar masses orbiting each other (see Fig.1.1).

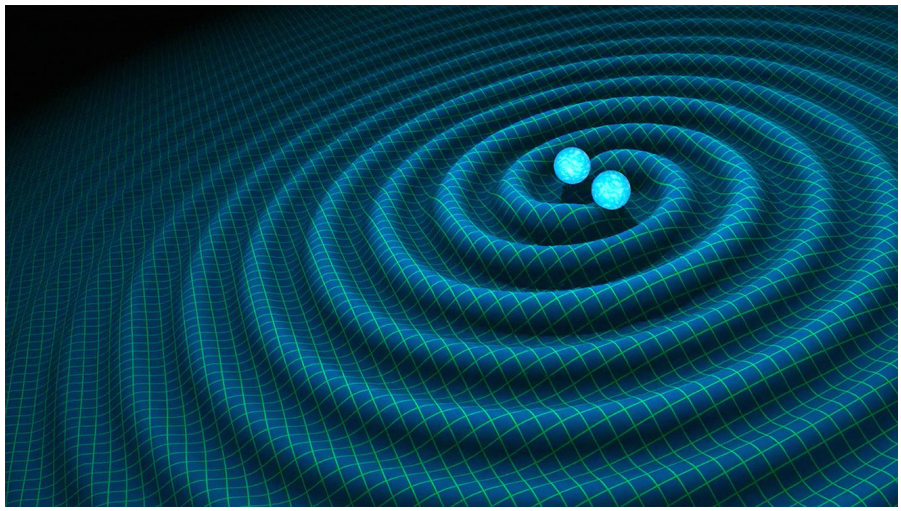

Figure 1.1: Artistic representation of gravitational waves generated by two in-spiralling neutron stars. Credit R. Hurt/Caltech-JPL

Gravitational waves, as they propagate, cause a spacetime deformation, leading to a tidal effect in the direction of propagation. Additionally, they cause a deformation in the spacetime region perpendicular to the propagation direction, which is determined by their polarization. In accordance with GR, Gravitational Waves (GWs) have two independent polarizations, commonly referred to as "plus" and "cross" [3]. To better understand the effect of these polarizations, consider the case of a set of points circularly distributed. If a gravitational wave carrying a plus polarization is propagating along the z direction, it will cause alternate stretching and compression of space in the x and y directions, as depicted in figure 1.2. Similarly, it will do the cross-polarization but rotated by a 45° angle. Having determined the propagation speed as the speed of light, the amplitude and frequency of a gravitational wave are what mainly characterise a gravitational wave. The frequency f, expressed in Hz, indicates the wave's oscillation and can span from $\sim 10^{-17}$ Hz if waves from a cosmological background to 1000 Hz if generated from the explosion of a supernova [4]. The amplitude h, often called strain, is a dimensionless number representing the wave size. Stated differently, taking two points separated by a small distance, the amplitude is twice the fractional change in distance between the two points due to the gravitational wave passage. Typical gravitational waves passing regularly through Earth are in the order of 10^{-21} or below [5].

Among the sources of gravitational waves that can be found are, for example, inspiralling binary systems (compact or not) and singular sources that show non-symmetric characteristics, i.e., supernovae whose explosion is not symmetric or non-

spherical spinning neutron stars (see Fig. 1.3).

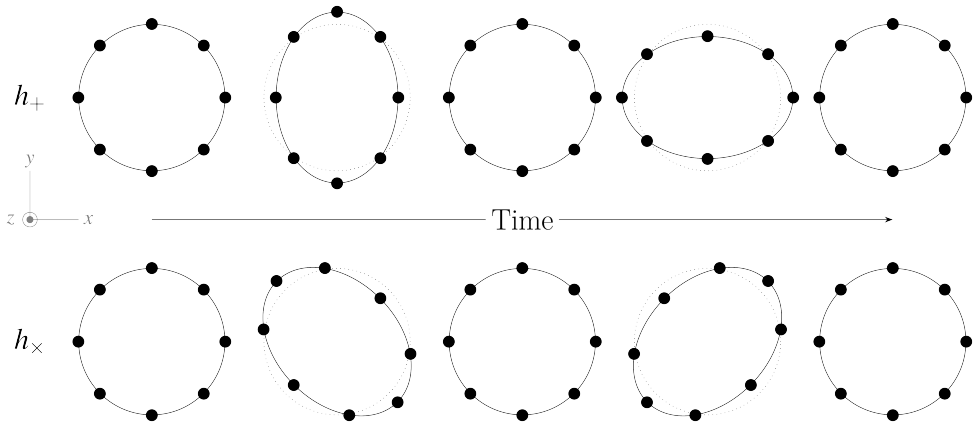

Figure 1.2: Displacements generated by a linearly polarized gravitational wave passing through a set of points circularly distributed. Top: plus polarized wave, bottom: cross polarized wave.

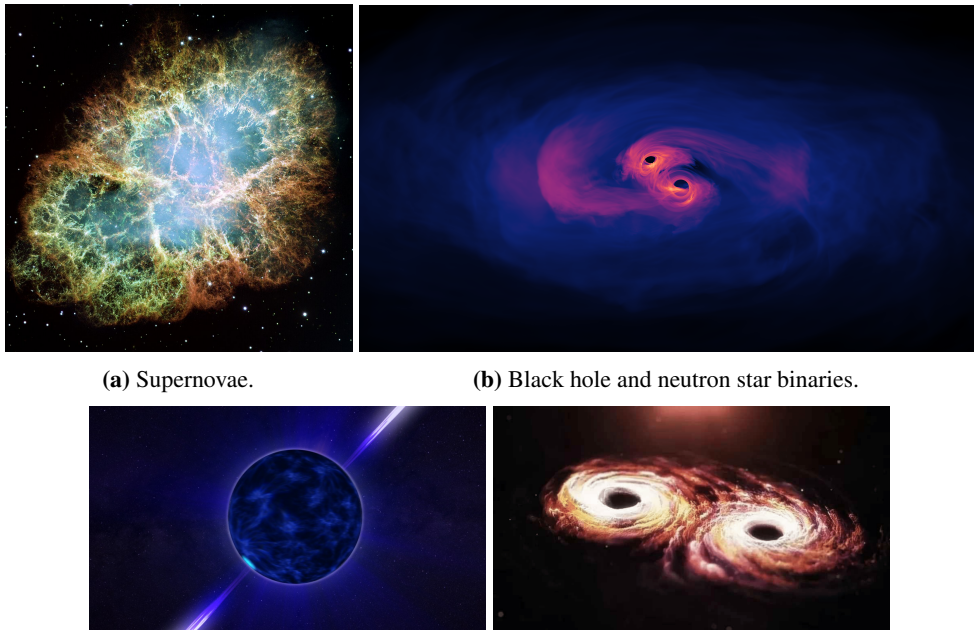

(a) Supernovae.

(b) Black hole and neutron star binaries.

(c) Spinning neutron stars.

(d) Supermassive black holes binary.

Figure 1.3: Some examples of gravitational wave sources. Credits: Fig. 1.3(a) NASA, ESA, Arizona State University; Figs. 1.3(b) and 1.3(c) NASA; Fig. 1.3(d) EPTA.

1.2 Gravitational waves detector

In the late 1950s, Joseph Weber pioneered using aluminium resonant mass bars to attempt to detect GW directly [6]. Although his initial attempts lacked sensitivity [7], they set the groundwork for future advancements in the field. Indeed, in the early 1960s, independent scientists began exploring optical interferometry as a promising alternative technique [8]. However, the development of laser interferometers for GW as we concept them today started in the 1970s when Rainer Weiss, building on Robert L. Forward's work [9], identified and calculated most of the background noises that could limit the detector sensitivity [10].

According to Weiss's work, laser interferometers for GW detection are essentially kilometre-long Michelson interferometers [11]. Light is sent to a beam splitter that bifurcates it into two orthogonal paths, commonly known as arms. Mirrors positioned at the end of each arm reflect light back to the beam splitter, where interference occurs. The optics are arranged so the beams travel equal distances in each arm and arrive at the beam splitter shifted by half the laser's wavelength (see Fig. 1.4(a)). This results in destructive interference, and the photodetector does not detect any signal. When a gravitational wave passes, it induces what is called a differential arm motion: one arm contracts while the other gets stretched and vice versa, as long as the wave passes (see Fig. 1.4(b)); consequently, the beams get a phase shift by travelling different distances, generating constructive patterns at the beam splitter, which then produces a signal at the photodetector.

In the early 1980s, while the scientific community focused on improving the interferometer's sensitivity, a detailed analysis of the orbital decay of pulsar PSR1913+16 aligned with general relativity[12], indirectly demonstrating the existence of gravitational waves. However, the scientific community had to wait until the late 2010s for direct detection using laser interferometry. Technological challenges were finally solved, allowing this type of detector to make the first direct detection of gravitational waves from the merger of two black holes in 2015 [13].

At the start of the fourth Observing Run (O4) in May 2023, the gravitational wave detector network will count five second-generation interferometers (2G-GWD) operating in different parts of the world: two overground with 4-km long arms detectors in the USA, known as Advanced LIGO Hanford and Advanced LIGO Livingston (aLIGO) [14]; one overground with 3-km long arms detector in Italy known as Advanced Virgo (AdVirgo) [15]; one overground detector with 600 m long arms in Germany known as GEO600 HF [16] and one with 3-km long arms underground detector in Japan known as KAGRA [17]. In almost a decade of operation, the global network of gravitational wave detectors has detected 90 events from diverse sources (see Fig. 1.5). This network has also facilitated the triangulation of the sources of gravitational waves, thereby restricting the region of the universe from which the signals originated [18].

1.3 Gravitational waves detectors sensitivity and noise sources

A simple kilometric-long Michelson interferometer, as presented earlier, is not sensitive enough to measure strains of 10^{-21} or below; that is why the current generation of

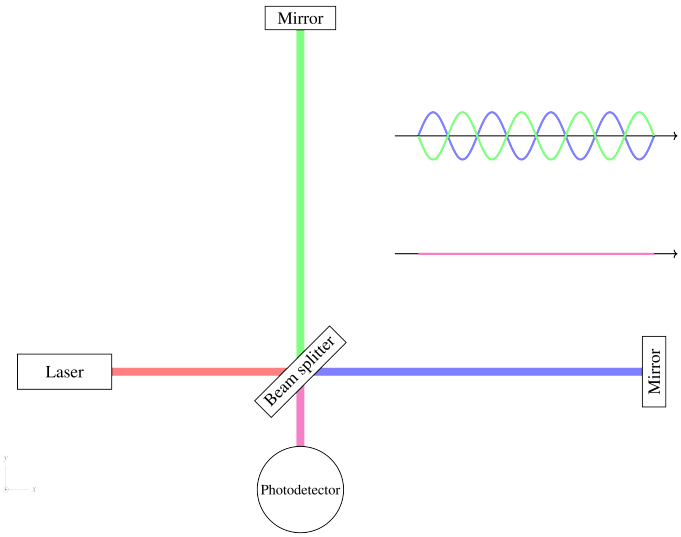

(a) No gravitational waves pass; the interferometer is at rest and no signal detected (magenta wave).

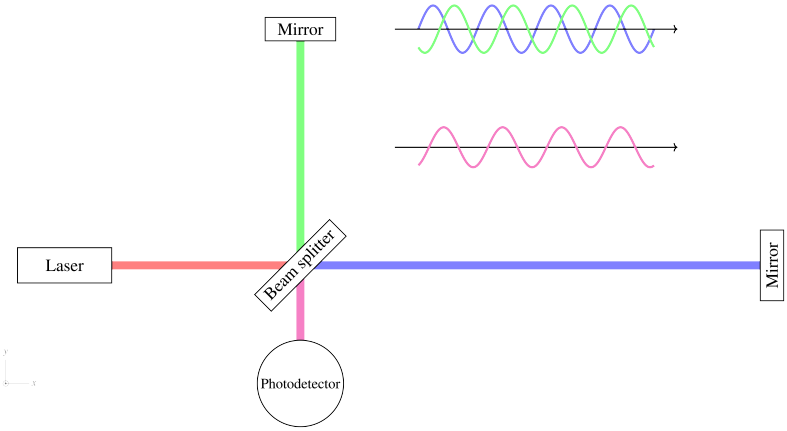

(b) A gravitational wave passes; the beam paths get shifted and a signal is detected (magenta wave).

Figure 1.4: Differential arm motion induced by the passage of a gravitational wave.

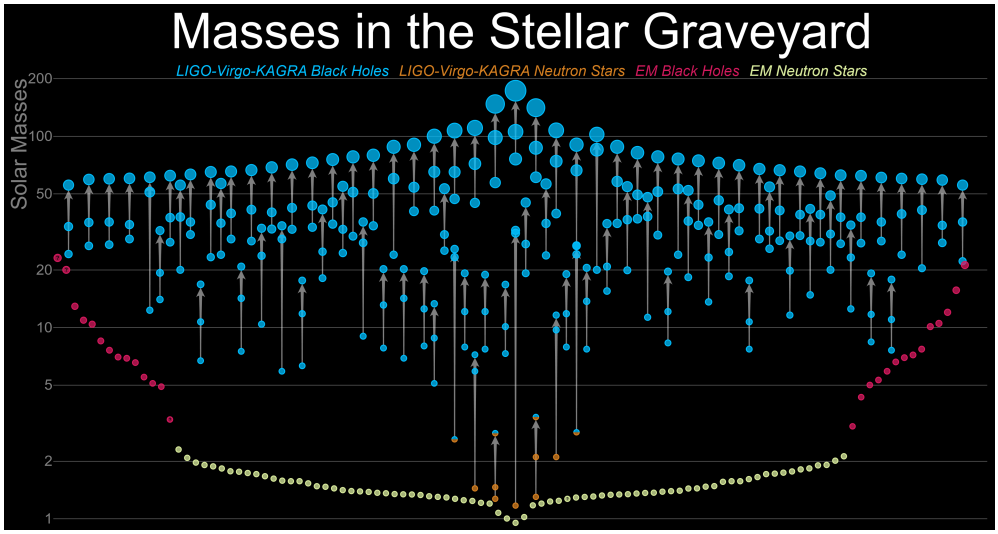

Figure 1.5: Events registered by LIGO, VIRGO and KAGRA in 10 years of operation. Credits: Aaron Geller / Northwestern

gravitational wave detectors adopt a series of solutions to overcome this lack of sensitivity [19].

The detector arms are Fabry-Perot Cavities (FPC) housing two mirrors, a partially reflective one at the beginning (Input Test Mass, ITM) and a highly reflective one at the end (End Test Mass, ETM) of the arms [20]. This configuration allows the "storage" of photons for several milliseconds as they bounce between the two test masses, effectively extending the light's interaction time with gravitational waves and the optical path length by approximately two orders of magnitude. Moreover, after the laser source and before the photodiode, Power Recycling Cavities (PRC) are installed to resonate the light from the interferometer and increase the power stored in the arm for better detection [21]. In addition to enhancing the sensitivity by adding optical cavities, the design of the interferometer and its subsystems has to mitigate the impact of noise sources that could reduce the detection sensitivity. Fig. 1.6 depicts, in amplitude spectral density across the frequency range, the most important noises in aLIGO.

Among the relevant sensitivity-limiting noise sources, we find quantum noise [23]. It sets the theoretical boundaries of the detector's performances and is associated with the quantum nature of light and spreading across the entire frequency spectrum. Its main contributors are the radiation pressure (photons impacting the mirrors and transferring momentum) and the shot noise (arising from aleatory fluctuations in photons' arrival time at the photodiode). Its contribution can be controlled by fine-tuning the lasers and optical cavities but limiting the maximum power injected into the interferometer [24].

The thermal noise [25], which impacts the sensitivity in the low and central frequency range, is correlated to the Brownian motion and the self-thermal excitation

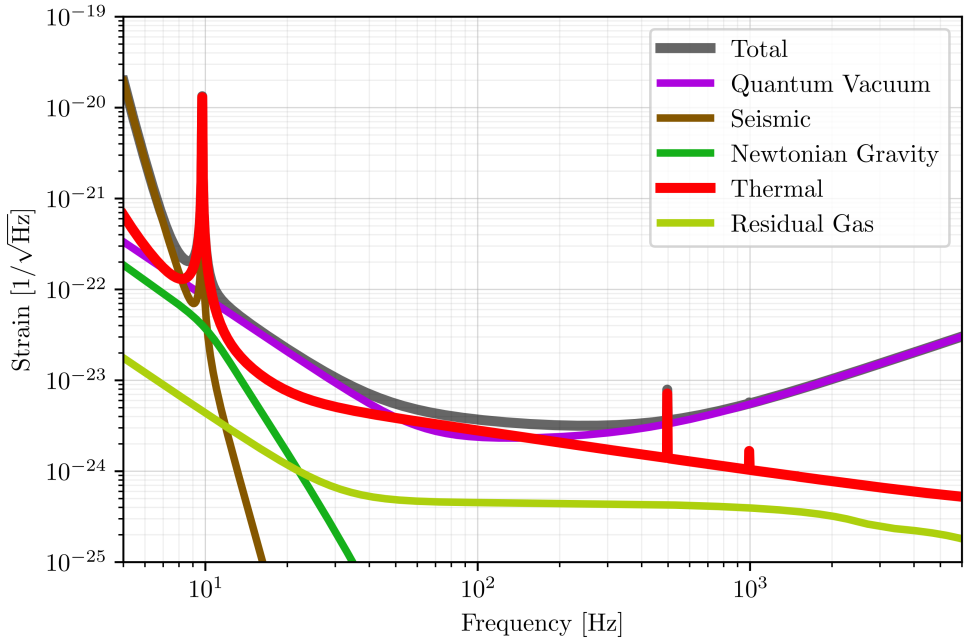

Figure 1.6: Amplitude Spectral Density (ASD) of the main noises of aLIGO in function of the frequency. The thermal noise curve (red) contains the thermal noises associated with the optics, their coatings and the suspension system. The quantum noise (purple), referred to as quantum vacuum, considers the shot noise and the radiation pressure noise. The residual gas noise (light green) is here represented as the sum of the damping noise slope (from 5 Hz to 50 Hz, which interests the tower vacuum) and the residual gas noise in the beampipes (from 50 Hz to 5kHZ). Graph generated using PyGWINC [22].

of the mirrors, their optical coatings [26], and the suspension system [27] since they are at a non-zero temperature. Since it is strictly dependent on the concept of thermal energy, it can be limited either through a material/coating selection that minimizes the mechanical/thermal losses or, as done in KAGRA, bringing the operational temperature of the components to 10-20 K to effectively reduce its contribution [28].

The low-frequency region of terrestrial gravitational wave detectors is affected by two noise sources: the Earth's seismic activity and Newtonian gravity. The former is attributable to the ground motion due to geological movements of the surface of the Earth. It can be mitigated by the suspension of the mirrors through a series of pendulums (i.e. quadruple pendulum suspension) and the adoption of dampening systems [29]. The latter is related to the attraction of the test masses by the distribution of masses surrounding them (buildings, the movement of the oceans, the wind, etc.) [30]. Filters and compensation systems can attenuate it, but its random nature makes any solution poorly effective. Last but not least is the residual gas noise. To allow the photons to travel unperturbed for kilometres in the FBC, essentially increasing their mean free path, the laser runs into 0.6-1.2 m diameter steel beampipes where Ultra High Vacuum (UHV) conditions are created. The resulting residual gas fluctuations

along the laser path could generate scattering if a photon hits a residual molecule, causing major beam losses [31, 32].

By design, most interferometers require an operating pressure in the main beampipes in the range or below of 1×10^{-9} mbar; this ensures residual gas noise levels $\sim$90% lower than the sum of all the other noises (see Fig. 1.6). Similarly to the radiation pressure contributing as quantum noise, residual gas molecules excite the motion of the mirrors, sensibly reducing the sensitivity at low frequencies [33]. That is why the mirrors and their suspension systems are enclosed in UHV vessels, often referred to as towers. UHV is also helpful in acoustically and thermally isolating the mirrors and ancillary equipment and preserving cleanliness from the dust of the optics, thus reducing the stray light noise. Although the residual gas noise can be mitigated from the early stage of design compared to other noises, it still poses significant technological and cost challenges, being the biggest and most expensive subsystem. Generating and maintaining UHV conditions in tens of thousands of cubic meters requires effort in selecting compatible materials, designing the vacuum and pumping system, and manufacturing, assembling, and operating the entire vacuum system.

1.4 The next generation of gravitational waves detectors

Since they are operational, GWDs have offered a new way to observe the universe. GWDs not only helped test general relativity and advance our understanding of black holes' physics but also marked a significant milestone in multimessenger astronomy with the detection of a signal from the merger of two neutron stars [34]. The merger, named GW170817, was accompanied by light emission in the electromagnetic spectra, allowing the location of the position in the universe and tracking the evolution of a newborn neutron star with space and terrestrial observatories [35]. Furthermore, by utilizing only the signal from GW170817, a new and independent measurement of the Hubble constant was achieved [36]. Post-O2 updates helped detect intermediate-mass black holes [37] and mergers involving objects in the mass gap [38].

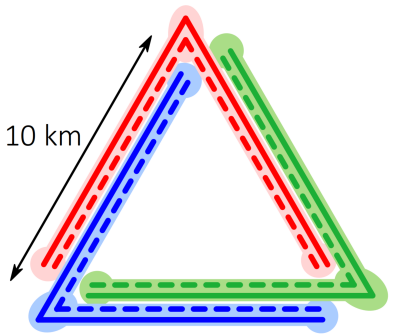

Figure 1.7: Schematic of the ET layout. The three detectors are marked in red, green and blue. The solid lines represent the ET-HF interferometers, the dashed lines the ET-LF ones. Figure taken from [39].

By the biennium 2028/2030, the 2G-GWDs will reach their nominal sensitivity [40], having given only a small glimpse of the gravitational universe. The breakthrough discoveries and the open questions left by the current generation stimulated the GW community to conceive a new generation of detectors (3G-GWD), aiming to enhance detection capabilities and explore much lower frequencies than the one probed today. Concepted to operate with a sensitivity one order of magnitude better than their predecessors (see Fig. 1.8), the Einstein Tele-

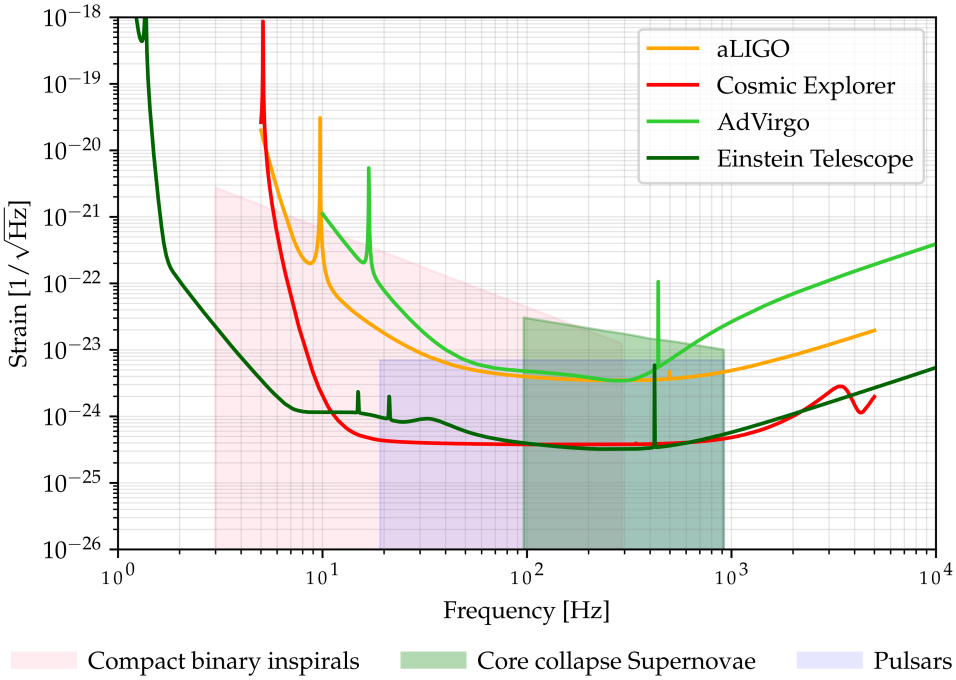

Figure 1.8: Sensitivity for aLigo, AdVirgo, Cosmic explorer and ET (design curve [39]). The areas represent the strain over frequency generated by some detectable astrophysical sources. Graph adapted from plots generated with the gravitational wave sensitivity plotter [41].

scope (ET) [39] in Europe and the Cosmic Explorer (CE) [42] in the US will enter the GWD network by 2040.

CE plans to implement two right-angled overground detectors: one with arms 40 km to focus on detecting GW from Black Hole - Black Hole (BHBH) mergers at the edge of the universe, and one with 20 to 40 km long arms fine-tuned to observe the final phase of Neutron Star - Neutron Star (NSNS) mergers [42]. ET, according to the 2020 Conceptual Design Report [39], envisions a single underground observatory hosting three detectors with 10 km long arms nested in a triangular shape (see Fig. 1.7). This ET configuration enables the retrieval of the polarization of a signal with just one observatory and the use of the detector in null-stream mode, a signal-free run that allows the spot of transient glitches in the detector, ensuring measurements are free of artefacts [43].

Although conceived with different designs, the science goals of the proposed 3G-GWDs overlap [39, 42]. Besides the possibility for a single observatory of detecting much feeble signals from BHBH, NSNS or Black Hole - Neutron Star (BHNS) mergers dating back to galaxies formation or first stars, and probe the evolution of a compact object through multimessenger astronomy, the full potential of the 3G-GWDs lies their networking and discovery potential, perhaps able to probe extreme gravity, fundamental physics phenomena or find unexpected events [44, 45].

1.5 The Einstein Telescope

As introduced in Section 1.4, the Einstein Telescope will be the next-gen European GWD. Contrary to the AdVirgo single detector, the ET reference design foresees three detectors arranged in a nested triangular shape. With the scope of operating at a sensitivity of a factor of ten better than AdVirgo, the ET arms were increased from 3 to 10 km per detector. Additionally, to extend the sensitivity over a much broader frequency range, each detector comprises two interferometers: one optimised for low frequencies (ET-LF) and one designed for detections at high frequencies (ET-HF). This double interferometer per detector concept allows the independent optimisation of the single interferometer performance without sacrificing the overall detector sensitivity given the overlapping of the two curves (see Fig. 1.9). The main technical design parameters of ET-HF and ET-LF are reported in Table 1.1 compared with the ones of AdVirgo.

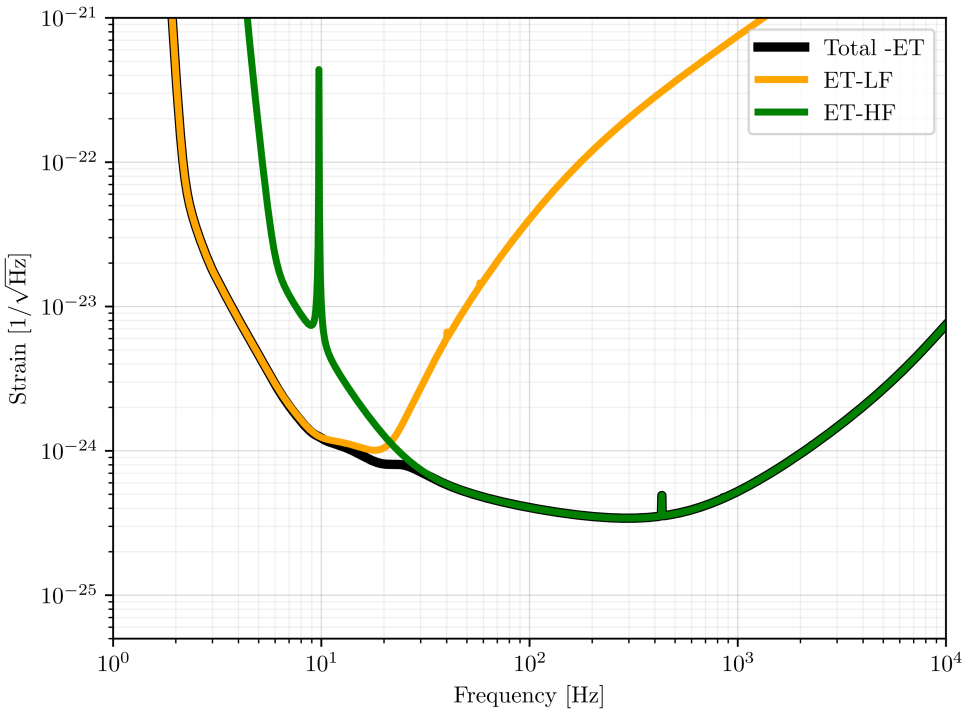

Figure 1.9: Sensitivity curves of ET-HF and ET-LF interferometer. The total ET sensitivity curve for one detector is obtained from the sum of the ET-LF and ET-HF curves. The cross-over frequency is at 35 Hz. Graph generated using PyGWINC[22] using June 2024 updated noise curves.

The ET-HF differs significantly from AdVirgo in performance, although it shares the same operating temperature, laser wavelength, mode, and mirror material.

To minimise the optics thermal noise and clipping losses (light lost outside the reflecting coating surface area) while storing 4.6 times more power than AdVirgo,

Table 1.1: ET-LF and ET-HF technical design parameters [39] compared with AdVirgo ones [46]. RoC = Radius of Curvature.

Parameter	ET-LF	ET-HF	AdVirgo
Arm length [km]	10	10	3
Beam pipe diameter [m]	1	1	1.2
Arm power [kW]	18	3000	650
Temperature [K]	10-20	290	290
Mirror material	Silicon	Fused silica	Fused silica
Mirror diameter [cm]	45	62	35
Mirror masses [kg]	211	200	42
ITM RoC [m]	5580	5070	1420
ETM RoC [m]	5580	5070	1683
Laser wavelength [nm]	1550	1064	1064
Beam shape	TEM_{00}	TEM_{00}	TEM_{00}
Beam radius at ITM [cm]	9	12	4.87
Beam radius at ETM [cm]	9	12	5.8
Beam waist [cm]	2.9	1.42	9.69
Beam waist position from ITM [m]	5000	5000	1363
Beam pipe total pressure [mbar]	10^{-10}	10^{-10}	10^{-9}

the ET-HF beam radius is adjusted to 12 cm, necessitating a 62 cm large mirror. Alternatively, for ET-LF, the thermal noise is reduced by running the main optics (ITM and ETM) at cryogenic temperatures (10-20 K); this choice drives the material decision for the mirrors to silicon. Although the silicon thermal and mechanical properties suit the needs of ET-LF, the mirror's dimensions are limited to 45 cm due to fabrication limitations. Because of the non-transparency of silicon at 1064 nm, the laser wavelength for ET-LF is set to be 1550 nm [39].

Decoupling the ET-LF and ET-HF systems allows the optimisation of the total ET quantum noise. To mitigate the radiation pressure, limiting at low frequencies, the ET-LF arm power is reduced to 18 kW; on the other hand, for ET-HF, the arm power is increased by a factor of about 170 to reduce the shot noise, limiting at high frequencies.

The optical baffles will play a critical role. As per the 2G-GWDs, conical optical baffles will be positioned strategically along the laser path to control the diffraction and back scattering of light caused by strayed photons escaping the reflection path and reaching other surfaces (e.g., the beam pipes' walls). To meet the stringent light scattering requirement, a minimum of 100 baffles per 10 km arm will be installed.

Similar to AdVirgo, a quadruple pendulum system will support the mirrors in ET to reduce seismic noise at low frequencies. However, the overall reduction will be

achieved by locating the detectors 200-300 meters underground. The two candidate sites for hosting the observatory are Sardinia in Italy and the Limburg region at the border between Belgium, Germany, and the Netherlands.

Significant improvements are also foreseen for the residual gas noise. As per the design, it is requested that the residual gas noise contribution in ET-HF and ET-LF should, at most, account for 20% and 7% of the sum of the other noises at the minimum strain (see Fig. 1.10). The request is for a tenfold improvement from the AdVirgo value, signifying a transition from 10^{-9} mbar to 10^{-10} mbar in ET-LF and ET-HF.

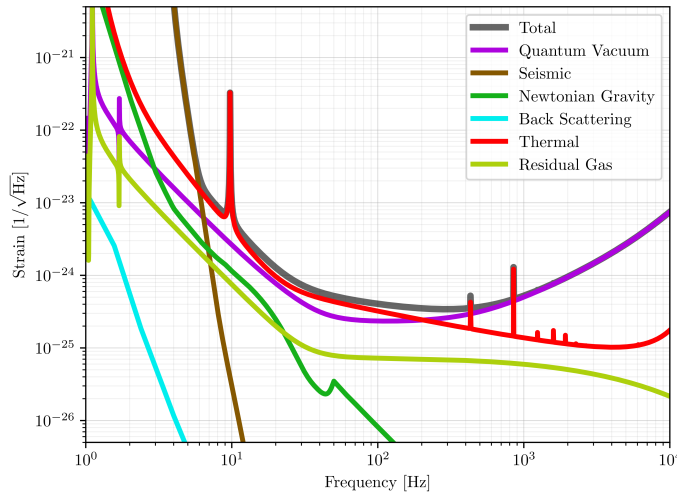

(a) ET-HF sensitivity curve. The thermal noise curve (red) contains the thermal noises associated with the optics, their coatings and the suspension system. The quantum noise (purple), referred to as quantum vacuum, considers the shot noise and the radiation pressure noise. The residual gas noise (light green) is here represented as the sum of the damping noise slope (from 5 Hz to 50 Hz, which interests the tower vacuum) and the residual gas noise in the beam pipes (from 50 Hz to 10kHZ). Graph generated using PyGWINC[22] using June 2024 updated noise curves.

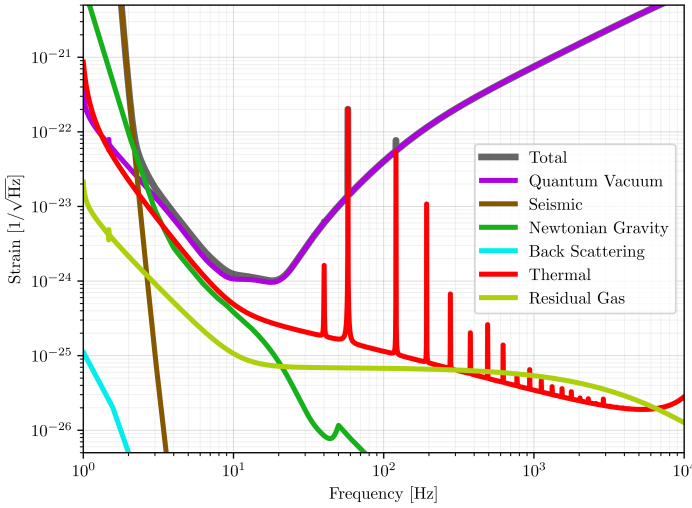

(b) ET-LF sensitivity curve. The thermal noise curve (red) contains the thermal noises associated with the optics, their coatings and the suspension system. The quantum noise (purple), referred to as quantum vacuum, considers the shot noise and the radiation pressure noise. The residual gas noise (light green) is here represented as the sum of the damping noise slope (from 1 Hz to ∼17 Hz, which interests the tower vacuum) and the residual gas noise in the beam pipes (from ∼17 Hz to 10kHZ). Graph generated using PyGWINC[22] using June 2024 updated noise curves.

Figure 1.10: ET-HF (a) and ET-LF (b) sensitivity curves and their noise contributions.

1.6 Statement of the Problem

The ET vacuum system is forecasted to burden the ET total budget for almost 1/3 (∼ 440 M€). Are there cheaper alloys or alternative designs and techniques to achieve UHV without compromising the beam pipe vacuum performance?

A preliminary cost estimation drafted in 2011 [47], scaling and adapting the vacuum system of Virgo to the ET dimensions and requirements [39], forecasted a total budget for the vacuum system of ∼ 510 M€ (∼ 32% of which attributed to the towers vacuum, the cryopumps and filter cavities costs). A more recent estimation inflates the cost of the ET vacuum system to about 570 M€ [48]. If projected to the total budget envisioned for the ET construction, esteemed to be of 1.7 B€ , the vacuum system cost will account for its 33% (see Fig. 1.11). If the tower and cryogenic vacuum costs are kept as forecasted from the first estimation, the beam pipe vacuum system alone will burden the ET budget for ∼440 M€.

Operating the 120 km of beampipe in the low $\times 10^{-10}$ mbar does not represent in itself a technological challenge since similar pressure requirements or lower is achieved in other large vacuum systems [49, 50]. However, given the size of ET, the cost of realising, commissioning, and operating the beam pipe vacuum system is a worrying problem.

Similar percentages of the impact for the beam pipe vacuum system cost are esteemed for Cosmic Explorer [42].

To reduce the overall project budget, cost-effective solutions must be explored to realise the beam pipe vacuum systems. This involves identifying and implementing

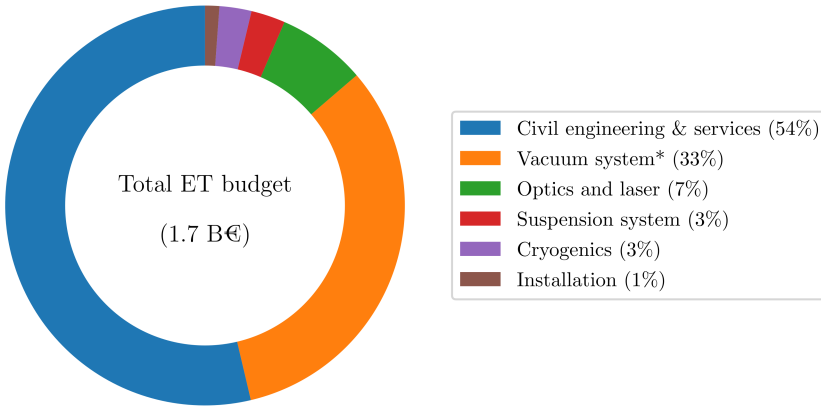

Figure 1.11: ET total budget broken down per subsystem percentage [48]. Following the civil engineering and technical infrastructure (HVAC, power distribution, etc.) covering 54% of the budget, the vacuum system (beam pipe, towers, cryogenic and filter cavities vacuum) burdens the budget for more than 30%. The 3% reported as cryogenics has to be intended as to be spent for the cryoplant and coolant piping. The voice installation accounts for the installation and contracting of the detector components.

materials and designs that lower costs without compromising the functionality and quality of a large vacuum system that lasts for 50 years [39].

In this regard, in 2019, a workshop was held to address the similar beam pipe vacuum budgetary issues faced by ET and CE [51]. The workshop brought together vacuum experts from gravitational wave detectors and particle accelerators to propose and discuss cost-effective solutions for the 3G-GWDs.

The experts identified three main areas for further research and development for cost optimization: beam pipe design, structural materials and coatings, and vacuum system layout.

Two beam pipe designs were discussed. The first was a traditional single-wall tubing, where a feasibility study was proposed to explore the use of thick pipes (1-2 cm). This option is especially relevant for the Cosmic Explorer since it is an overground infrastructure similar to LIGO. Using thick, bullet-proof pipes would alleviate concerns about vacuum incidents compared to the standard 3-4 mm thick pipes. The second proposed design was a nested system involving a thick outer tube containing a thin-walled inner tube. This design offers two main benefits: the bakeout for the inner tube is less demanding due to its reduced thickness (0.5 mm) and the vacuum insulation provided by the outer envelope, and during operation, the outer vacuum compensates for leaks in the thin-walled pipe. Despite these advantages, the nested system requires significant research and development in annular sector valves and integration/operation studies for baffles and pumping systems.

The workshop also focused on finding cheaper and low H_2 content structural materials as substitutes to the 304L currently adopted. The most promising materials discussed were mild steel and aluminium alloys. Studies highlighted the UHV compatibility of mild steel for its low H_2 outgassing rates and lower cost than AISI 304L. Mild steel was considered applicable in single-wall tubing and as the outer vessel for the nested system. Further vacuum characterizations of different mild steels were recommended, especially using commercial off-the-shelf products, as this could represent significant cost savings. Although aluminium alloys have outgassing rates one to two orders of magnitude lower than AISI 304L, they require greater thickness than mild steels for equivalent buckling performance. Therefore, aluminium alloys are considered mainly for the inner vessel of the nested system.

Low-water adsorption coatings, such as a-Si and magnetite conversion coatings for mild steels, were proposed to reduce bakeout efforts. These coatings could ease pumpdown operations after venting, despite not eliminating the need for a bakeout.

Variations in the vacuum system layout were also discussed. Non-evaporable getter (NEG) pumps were proposed as a primary source of UHV pumping for GWDs. The possibility of venting large volumes with ppb water-filtered air and using Titanium Sublimation Pumps (TSP) as a "sacrificial" pumping source for faster pressure recovery after venting were also discussed.

Following the LIGO-hosted workshop, an agreement was signed between the INFN, Nikhef (the two ET hosting institutes), and the CERN Vacuum, Surfaces and Coatings (VSC) group for the study of cost-effective technical solutions for the ET beam pipe vacuum system.

In particular, the VSC group is mandated to:

- Re-evaluate the baseline solution (proposed in the ET Conceptual Design Report (CDR) [39]) with minor modifications imposed by the new requirements.
- Design and test technical solutions that fulfil the ET requirements and are less expensive than the baseline.
- Manufacture, assemble and commission a pilot sector representative of the solution proposed for the ET beam pipe vacuum system.
- Write the Technical Design Report (TDR) of the ET beam pipe vacuum system, including cost estimations.

To fulfil the mandate, the VSC group, supported by the Mechanical and Materials Engineering (MME) group, divided the project into 8 work packages (WP), each covering different areas of development (see Fig. 1.12).

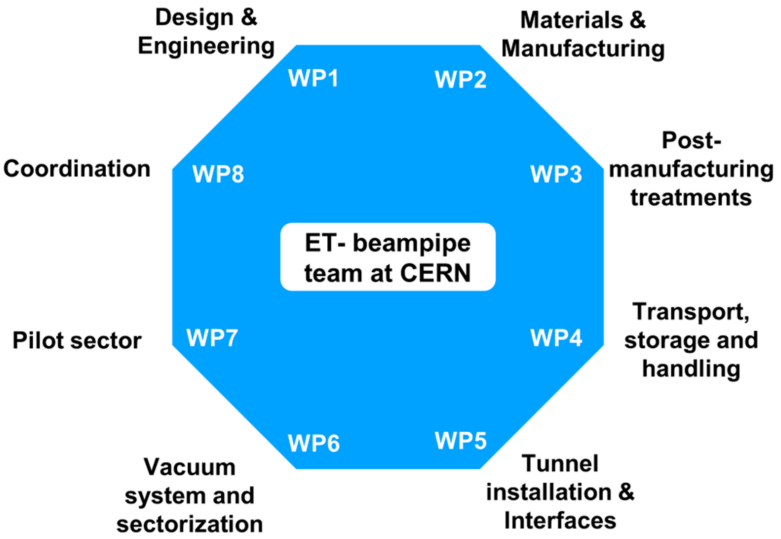

Figure 1.12: ET-beam pipe project at CERN work packages.

1.7 Objectives and Outline of the Thesis

This thesis aims to study the UHV compatibility of less expensive ferritic alloys as structural materials for constructing the ET beampipe. The results obtained will be used to optimise the beam pipe vacuum system design and its commissioning phase.

The work presented here falls in the broader mandate of the WP6 (Vacuum system and sectorization) of the CERN-INFN-NIKHEF collaboration, dedicated to:

1. Design the vacuum layout: sectorization, pumps and gauge positions.
2. Choice of sector valves and impact on integration.
3. Choice of the vacuum pumping system and study the impact on integration.
4. Choice of pressure measurement, control system and monitoring.
5. Outgassing measurement of proposed materials and treatments.

6. Cost estimation for the vacuum system.

To provide a comprehensive understanding of the research undertaken, this thesis is organized as follows:

-Part I-

Part I introduces the study's context, highlighting the research questions, objectives, and proposed solutions. It sets the foundation for the entire investigation.

-Part II-

Part II reviews the fundamental concepts of pressure-limiting sources in vacuum systems, focusing on the state-of-the-art techniques for the beam pipe vacuum in GWDs. This section provides the necessary context for understanding the materials examined in the study and explores design options for 3G-GWDs.

Chapter 2 covers the fundamental concept of outgassing in UHV systems. It details the primary sources of outgassing, the key species involved, and the mechanisms contributing to these limitations.

Chapter 3 explores the relationship between strain noise and residual gas within the beam pipe vacuum. The chapter includes a comprehensive review of the vacuum systems used in 2G-GWDs and analyses the conceptual design outlined in the ET 2020 CDR. It highlights critical challenges and introduces technical proposals from CERN aimed at reducing costs.

-Part III-

Part III presents and discusses the vacuum characterisation methods and experimental setups used in the study. It also details the selected materials and their preparation for testing.

Chapter 4 introduces the experimental methods and setups used to characterise the ferritic alloys in both baked and unbaked conditions. Alongside the system descriptions, this chapter provides the theoretical framework behind the measurements.

Chapter 5 presents the selected mild and ferritic stainless steels, providing a detailed account of their preparation for the tests.

-Part IV-

Part IV discusses the results of the vacuum characterisation campaign.

Chapters 6 and 7 collect mild and ferritic stainless steel results, respectively. In both chapters, results are organised by conditioning type and compared with those found in untreated austenitic stainless steels.

The best-performing grades from the three families analysed are used to produce

corrugated beam pipe prototypes. Chapter 8 examines the ultimate pressures achieved by the prototypes using a vacuum system designed to resemble a probable ET sector.

Chapter 9 summarises the findings from the characterisation campaign and offers insights into the beam pipe vacuum design.

-Part V-

Part V applies the results obtained in Part IV, considering the scientific requirements and technical infrastructure, to propose an updated ET beam pipe vacuum system design. A cost estimation is also provided.

Chapter 10 outlines the design of the ET beam pipe vacuum system. It reviews the scientific requirements and technical infrastructure, drawing preliminary considerations based on the established boundary conditions. The chapter includes designs, comments on the vacuum layout and commissioning phases, and an evaluation of performance and cost.

Chapter 11 is dedicated to a preliminary cost analysis of the proposed vacuum system based on the design presented in Chapter 10.

-Part VI-

Part VI summarises the key results from the study and the design efforts. It also makes final considerations and offers an outlook on future studies and potential next steps.

- Background -

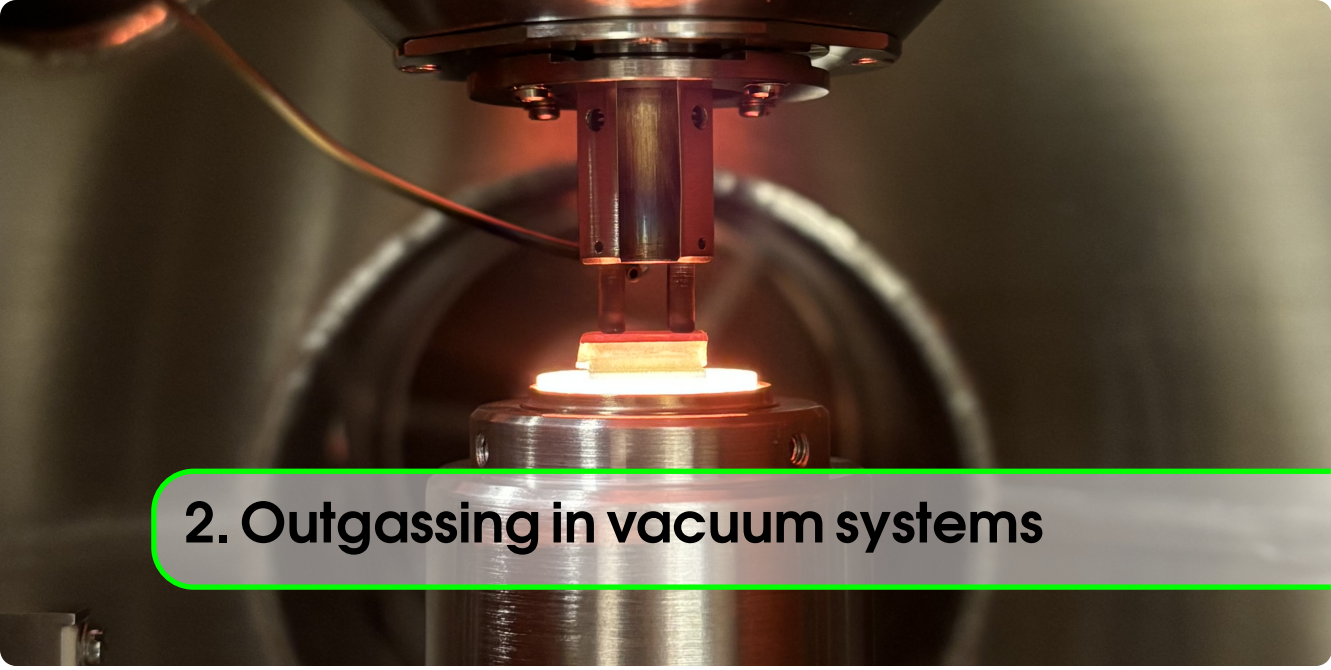

2. Outgassing in vacuum systems

> Nature abhors a vacuum. It is quite certain that in the bounds of nature, a vacuum, which is nothing, can find no place.
>
> -Jean Rey-

This chapter introduces the fundamental concepts of water vapour and hydrogen outgassing rates for typical metals used for UHV applications. The information given in this chapter will provide the reader with fundamental tools to understand the origin of the gas source in vacuum systems, their evolution and how to control them.

2.1 Gas sources in vacuum

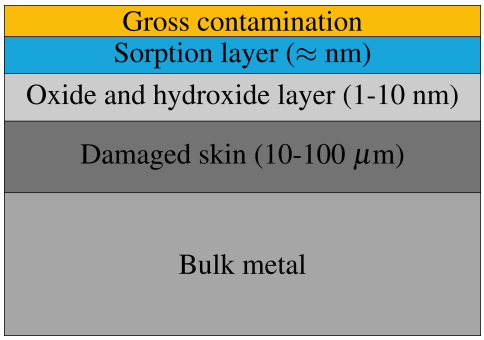

Figure 2.1: Schematic of the contamination layers. Figure adapted from [52]

In a leak-free all-metal vacuum system, the vacuum chamber walls represent the main gas source. The release of gas molecules is firstly ascribable to the nature of the interface between the volume to vacuum and the bulk of the material constituting the chamber. In a typical all-metal system, the layers covering the chamber's surface are depicted in Fig. 2.1.

After manufacturing and manipulation, the surface is usually contaminated by cutting fluids, oils, and grease. Underneath the gross contamination layer typically sits an interlayer (sorption layer) made of water vapour (due to air humidity) and hydrocarbons. These two topmost layers can be efficiently chemically removed by cleaning the vacuum components with solvents and/or detergent baths according to the nature of the bulk material used. The cleaning procedure to achieve a UHV-compatible surface often foresees ultrasonic agitation or recirculation of the cleaning bath, followed by rinsing with demineralised water to remove any residue or pollutant [53]. After the cleaning and drying of the vacuum component, a new sorption layer will form, although made only by airborne water vapour and light hydrocarbons.

Oxides, hydroxide layers, and any damaged skin layer covering the material's surface will likely contribute as gas sources. Characterised by crevices, dimples, and open/closed porosities, these layers can retain liquids or trap gases later released in vacuum. Chemical etching is generally performed to create a cleaner and more compact oxide than the native one (passivation).

Referring to Fig. 2.1, the last gas source is the bulk. Small O, N, C, and H atoms are trapped in the metal's bulk, along grain boundaries or near inclusions during the production steps or contained in the raw minerals [52]; secondary metallurgy refinement steps, such as Electron Slag Remelting (ESR) or Vacuum Oxygen Decarburization (VOD) help on reducing their content. The remnant quantity slowly diffuses towards the surface, where it recombines with another similar atom or with another species before being released in vacuum. The diffusivity for most dissolved gases at room temperature is imperceptible within human life, except for hydrogen. A hydrogen atom diffusing at room temperature in austenitic steel (Face-Centered Cubic, FCC), in terms of diffusion length, travels for about 6 μm [54] in a day, a C atom to move for the same distance takes more than 1×10^{19} years [55].

Once the gas molecule is adsorbed on the surface, its removal kinetics is described through its escape frequency [56]:

$$\nu = \nu_0 \exp\left(-\frac{E_d}{k_b T}\right) [s^{-1}] \tag{2.1}$$

Equation (2.1) considers a molecule as a simple harmonic oscillator, with a frequency ν_0. The average vibration frequency of a molecule can be deducted by the equivalence between classical (k_bT) and quantum mechanics ($h\,\nu_0$, with h = Planck's constant) for the energy of the oscillation, whereas E_d represents the kinetic energy to be reached by the molecule to break the bonding with the surface and get desorbed [52]. More practically, one can consider the reciprocal of Eq. (2.1), referred as mean sojourn time τ :

$$\tau = \frac{1}{\nu} \approx \tau_0 \exp\left(\frac{E_d}{k_b T}\right) \approx \frac{h}{k_b T} \exp\left(\frac{E_d}{k_b T}\right) \approx 10^{-13} \exp\left(\frac{E_d}{k_b T}\right) [s] \tag{2.2}$$

In other words, Eq. (2.2) represents the time a molecule spends at a given temperature and with a specific binding energy E_d before it gets released in vacuum. To achieve a good level of vacuum, limited by the desorption of particles bonded with an energy

E_d from the vessel's walls, by looking at 2.2 one can apply two strategies during a pumpdown[a] :

1. Increase the temperature of the walls for a given time during the pumpdown to reduce the sojourn time, accelerating the removal of the molecules. This operation is often referred to as bakeout.
2. Permanently reduce the temperature of the walls below room temperature, increasing the sojourn time. This condition can be achieved by cryogenic pumping.

Depending on whether the gas release is spontaneous or stimulated, the phenomena regulating the emission of gas in vacuum are named as follows [52]:

- **Degassing**: deliberate removal of gas from a surface or bulk (i.e. stimulated by heating at high temperatures).
- **Outgassing**: spontaneous removal of gas provoked by thermal vibration at room temperature.

When a vacuum vessel is properly surface conditioned and cleaned, the pumpdown process can start. During a pumpdown, the vacuum vessel can be schematised as an open system; therefore, the pressure evolution can be evaluated through a mass bass equation:

$$\frac{\mathrm{d}p}{\mathrm{d}t} V + S\, p + \frac{\mathrm{d}N_a}{\mathrm{d}t} = 0 \tag{2.3}$$

where:

- p is the pressure inside the vacuum vessel.
- N_a is the number of molecules adsorbed on the surface.
- $\frac{\mathrm{d}p}{\mathrm{d}t} V$ represents the change in the number of molecules in the gas phase.
- $S\, p$ is the gas leaving the system through pumping.
- $\frac{\mathrm{d}N}{\mathrm{d}t}$ is the change of molecules absorbed on the vessel surface.

Since a desorbed molecule is not necessarily pumped out but can stick and be re-absorbed on another free adsorption site, one can rewrite the third term of Eq. (2.3) as:

$$\frac{\mathrm{d}N}{\mathrm{d}t} = Q_{abs} - Q_{des} = \frac{\theta\, N_s}{\tau} - S_w\, p \tag{2.4}$$

where θ is the surface coverage, seen as the ratio between the occupied adsorption sites and the total amount of adsorption N_s; S_w is the wall pumping. For a complete analysis of the pressure evolution, together with Eq. (2.3), the variation in time of the coverage is to be also considered:

$$N_s \frac{\mathrm{d}\theta}{\mathrm{d}t} = S_w\, P - \frac{N_s\, \theta}{\tau} \tag{2.5}$$

[a]Pumpdown: a time-dependent process of removal of gas from atmospheric pressure to ultimate vacuum through pumping.

Therefore, the system of Ordinary Differential Equations (ODEs) to be solved to analyse a pumpdown can be composed by rearranging Eq. (2.3), Eq. (2.4) and Eq. (2.5):

$$\begin{cases} V \dfrac{\mathrm{d}p}{\mathrm{d}t} = -S\,p - S_w\,p + \dfrac{N_s\,\theta}{\tau} \\ N_s \dfrac{\mathrm{d}\theta}{\mathrm{d}t} = S_w\,p - \dfrac{N_s\,\theta}{\tau} \end{cases} \tag{2.6}$$

For the very first part of the pumpdown, the surface contribution is as negligible as the contribution of the wall pumping; therefore Eq. (2.6) reduces to:

$$V \frac{\mathrm{d}p}{\mathrm{d}t} = -S\,p \tag{2.7}$$

The ODE reported above Eq. (2.7) can be easily solved for:

$$p(t) = P_0\,\exp\left(-\frac{t}{\tau_s}\right) \tag{2.8}$$

where P_0 is the starting pressure and $\tau_s = \frac{V}{S}$ often referred to as characteristic pumping time.

2.2 Water outgassing rate

Once the atmospheric gas evacuation is completed, the adsorbed layer of water vapour is the main source contributing to the system's outgassing rate.

At this stage, the pumpdown curve is dominated by the surface characteristics; therefore, the surface coverage, wall pumping, and the sojourn time of water molecules on the surface are the driving parameters. Equation (2.6) can be rearranged and solved as second-order ODE in θ. Applying a series expansion for an approximate solution (where $\tau_p < \tau$ and $S << S_w$) for a boundary condition for $dP/dt = 0$ at $t = 0$, the solution can be written as [57]:

$$p(t) \approx \frac{N_s}{\tau\,(S_w + S)}\,\exp\left[-\frac{t}{\tau\,(1+\frac{S_w}{S})}\right] \tag{2.9}$$

The equation obtained re-describes the time that a water molecule spends on a surface from τ to $\tau\,(1+\frac{S_w}{S})$. It is worthwhile mentioning that the envelope of the exponential pressure decay shows a dependency of type 1/t as seen experimentally (see Fig. 2.2). The maximum pressure at each t can be calculated as:

$$\frac{\mathrm{d}p}{\mathrm{d}\tau} = -\frac{N_s}{\tau^2\,(S_w + S)}\,\exp\left[-\frac{t}{\tau\,(1+\frac{S_w}{S})}\right]\left[1 - \frac{t}{\tau\,(1+\frac{S_w}{S})}\right] = 0 \tag{2.10}$$

$$\rightarrow \tau = \frac{t}{1+(\frac{S_w}{S})}$$

Inserting the result of Eq. (2.10) in Eq. (2.9), one gets:

$$p(t) \approx \frac{N_m}{e\, t\, S} \tag{2.11}$$

Assuming one monolayer [b] of coverage, the maximum water outgassing rate per unit area at room temperature is [60]:

$$q_{max}(t) \approx \frac{N_s}{e\, t} \approx \frac{4 \times 10^{-5}}{e\, t\ [s]} \left[\frac{mbar\ l}{s\ cm^2}\right] \approx \frac{4 \times 10^{-9}}{t\ [h]} \left[\frac{mbar\ l}{s\ cm^2}\right] \tag{2.12}$$

The approximate relationship derived from the first principles fits the experimental data reasonably well; hence, one can deduce that water desorbs from the highest energy site at each time t [60] as seen in Eq. (2.10).

Although the calculation reported above agrees well with experimental values, a better definition of the coverage and energy distribution is needed to determine and precisely simulate the pumpdown curve of a vacuum system.

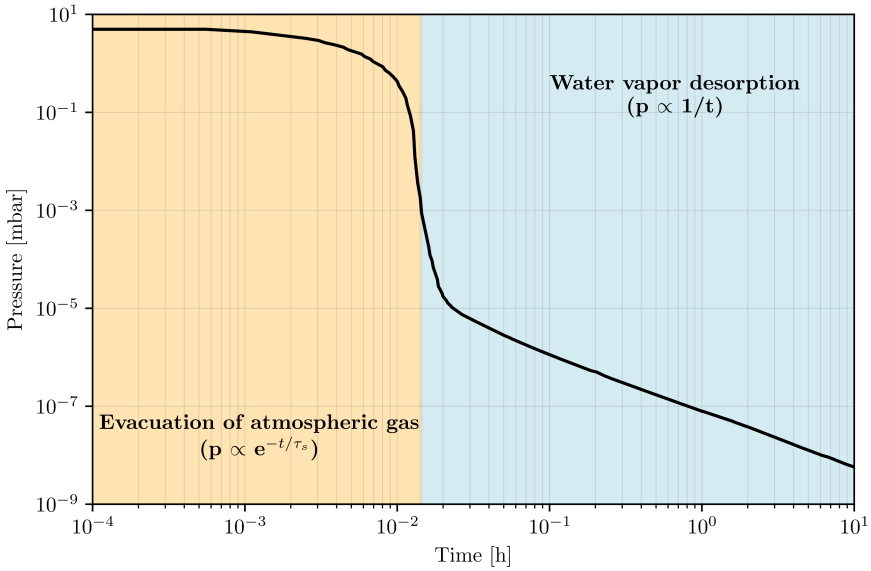

Figure 2.2: Pumpdown of a vacuum system in AISI 304L at 293K. The system was pumped with an effective pumping speed of S_{N_2} = 57 l s^{-1} and had an internal surface of 1000 cm^2.

2.2.1 Adsorption isotherms

One of the most used and verified approaches on water outgassing rate modelling foresees the use of adsorption isotherms [60–64].

[b] Monolayer (ML) = single, closely packed layer of atoms or molecules [58]. For a metallic surface, 1 ML $\approx 10^{15}$ molecules/cm^2 [59] $\approx 4 \times 10^{-5}$ mbar l s^{-1} at 293K.

Applying isothermal models does not require a precise definition of the geometrical arrangement and distribution of the desorbing species; it takes as input just the order of the process and the binding energy distribution of the molecules on the surface.

According to Horikoshi and Kanazawa [61–63], the adsorption of water vapour is fully reversible; hence, the surface and gas phase are considered in equilibrium, with the mean sojourn time of an adsorbed molecule exchanging with the gas phase much shorter than the time needed to observe a change in pressure [63]. Referred to as a quasi-static solution, the above-discussed condition can be resumed with the inequality, known as Kanazawa condition [61]:

$$\left| \frac{1}{p} \frac{\mathrm{d}p}{\mathrm{d}t} \right| << s \frac{A}{V} \frac{\bar{v}}{4} \tag{2.13}$$

where A and V are, respectively, the surface area and the volume of the vacuum chamber, and $\bar{v}$ is the average thermal speed of the water molecule at temperature T. The inequality of Eq. (2.13) is satisfied upon two additional assumptions:

- The surface is composed of sites (N_{sites}), each of them filled with one molecule, without dissociation [61].
- The sticking probability s of the surface (probability of the surface to capture an impinging molecule) is assumed constant and equally probable for all the sites [63].

Under these assumptions, the reversible isothermal model allows the surface coverage to be expressed as a function of temperature and pressure:

$$f(p,T) = \theta = \frac{N_a}{N_m} \tag{2.14}$$

with N_a representing the number of adsorption sites filled and N_m the total adsorption sites available in a monolayer. A new expression for a pumpdown curve is obtained by substituting Eq. (2.14) in Eq. (2.3) and applying a unit conversion to N_m:

$$\frac{1}{p} \frac{\mathrm{d}p}{\mathrm{d}t} V + S\, p + N_m\, k_b\, T \frac{\mathrm{d}\theta}{\mathrm{d}t} = 0 \tag{2.15}$$

Re-arranging Eq. (2.15) and applying the chain rule for $\dfrac{\mathrm{d}\theta}{\mathrm{d}t}$:

$$\frac{1}{p} \left[\frac{\mathrm{d}p}{\mathrm{d}t} + \frac{N_m\, k_b\, T}{V} \left(\frac{\mathrm{d}p}{\mathrm{d}t} \frac{\mathrm{d}\theta}{\mathrm{d}p} + \frac{\mathrm{d}\theta}{\mathrm{d}T} \frac{\mathrm{d}T}{\mathrm{d}t} \right) \right] = -\frac{1}{\tau_s} \tag{2.16}$$

More explicitly:

$$\frac{\mathrm{d}p}{\mathrm{d}t} = -\frac{\frac{p}{\tau_s} + \frac{1}{p} \frac{N_m\, k_b\, T}{V} \frac{\mathrm{d}\theta}{\mathrm{d}T} \frac{\mathrm{d}T}{\mathrm{d}t}}{\left(1 + \frac{N_m\, k_b\, T}{V} \frac{\mathrm{d}\theta}{\mathrm{d}p} \right)} \tag{2.17}$$

The general form derivated in Eq. (2.17) allows the calculation of the pumpdown curve for known isotherms and temperature evolutions as function of time.

Many adsorptions have been developed in the last century [65–67], based on the Langmuir isotherm [68]. They show similar behaviour although using different assumptions on the energy distribution functions. For a given binding energy distribution of adsoprion sites $\rho(E_d)$ having Langmurian behaviour $\theta_L(p,E_d)$, the isothermal expression is:

$$\theta(p) \;=\; \int \rho(E_d)\;\theta_L(p,E_d)\;dE_d \tag{2.18}$$

Langmuir isotherm

The Langmuir isotherm [68] is defined as first-order desorption. It assumes one constant binding energy for any coverage and that the rate of desorption and adsorption are proportional to the number of empty sites and occupied sites, respectively. The equilibrium between the adsorption and desorption reaction can be written as:

$$Q_{ads} - Q_{des} = 0$$

$$\frac{\theta\; n_m}{\tau} - (1-\theta)\; s_0\; p\; \nu = 0 \quad \text{with} \quad \nu = \frac{\bar{v}}{4\; k_b\; T} \tag{2.19}$$

where n_m is the number of sites in a monolayer per unit of surface area, s_0 is the sticking probability of an empty site, and ν is defined as the impingement rate of the molecule on the surface. The explicit form for the Langmuir isotherm can be found re-arranging Eq. (2.19):

$$\theta_L = \frac{a\; p}{1 + a\; p} \quad \text{where} \quad a = \frac{s_0\; \nu\; \tau}{n_m} \tag{2.20}$$

The derivative of Eq. (2.20) with respect to p is:

$$\frac{\mathrm{d}\theta_L}{\mathrm{d}p} = \frac{1}{(1 + a\; p)^2} \tag{2.21}$$

Figure 2.3 depicts the pumpdown curve of a fictitious vacuum system in which the surface obeys the Langmuir isotherm for different binding energies. As can be seen, by increasing the binding energy, the decrease in pressure slows down, starting to develop a linear slope in log p - log t graph.

It is worthwhile noticing that the convolution of the curves for different binding energies approximates the t^{-1} curve [63] seen experimentally, showing that to better simulate a real pumpdown behaviour, the density $\rho(E)$ must account for more than one energy.

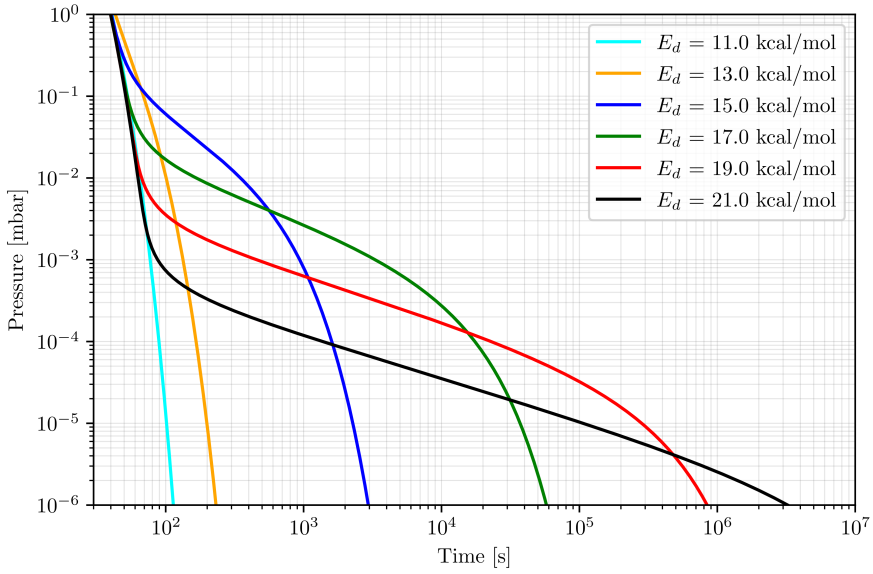

Figure 2.3: Pumpdown for a vacuum system with an adsorption layer following the Langmuir adsorption isotherm for binding energies from 11 to 21 kcal/mol. The system parameters used for the simulation are: $n_m = 3 \times 10^{15}$ molecules/cm^2, $\tau_0 = 10^{13}$ s, $s_0 = 1$, $P_0 = 4$ mbar, $A = 5000$ cm^2, $V = 20$ l, $S_{N_2} = 4$ l s^{-1} and $T = 293$ K.

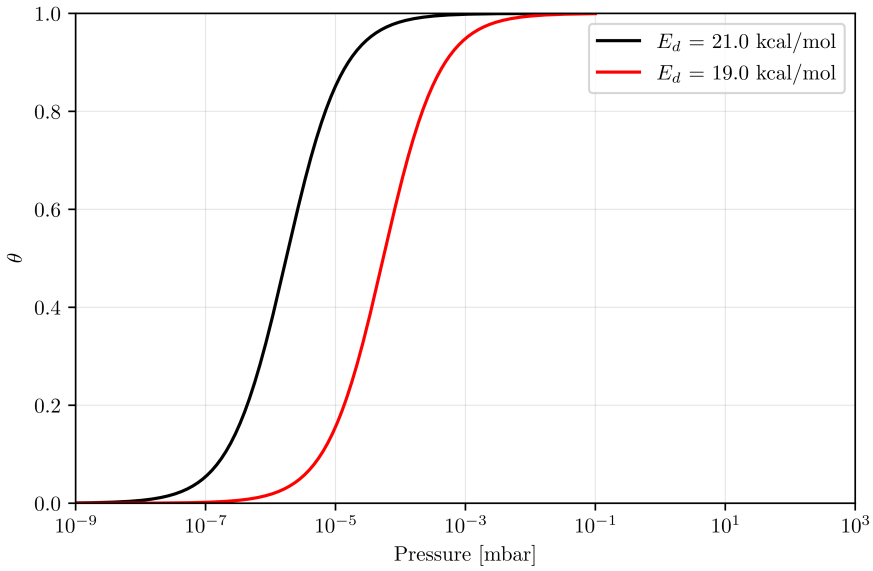

Figure 2.4: Coverage as a function of pressure for the last two pumpdowns of Fig. 2.3 following a Langmuir isotherm. As can be seen, the decrease in pressure is faster for lower binding energy. The isotherm parameters are: $n_m = 3 \times 10^{15}$ molecules/cm^2, $\tau_0 = 10^{13}$ s, $s_0 = 1$, and $T = 293$ K.

Temkin isotherm

To overcome the mono-energetic distribution of the Langmuir isotherm, the Temkin isotherm [66] assumes that the binding energy of all the molecules decreases linearly with increasing coverage in the adsorbent layer [63], i.e.:

$$E_d = E_0\,(1-\alpha\theta) \tag{2.22}$$

The energy distribution is defined as [69]:

$$\rho(E) = \begin{cases} \dfrac{1}{E_0 - E_1} & \text{if } E_1 < E_d < E_0 \\ 0 & \text{if } E_d < E_1 \text{ and } E_d > E_0 \end{cases} \tag{2.23}$$

where E_1 is the binding energy at coverage $\theta = 0$ and E_0 the binding energy at coverage $\theta = 1$. Being derived from the Langmuir isotherm, the coverage for a Temkin isotherm can be calculated by integrating Eq. (2.23) as shown in Eq. (2.18):

$$\begin{aligned} \theta_T(E) &= \int_{E_1}^{E_0} \frac{1}{E_0 - E_1}\,\frac{a\,p}{1+a\,p}dE = \int_{E_1}^{E_0} \frac{1}{E_0 - E_1}\,\frac{\dfrac{s_0\,\nu\,\tau}{n_m}\,p\,\exp\left(\dfrac{E_d}{RT}\right)}{1+\dfrac{s_0\,\nu\,\tau}{n_m}\,p\,\exp\left(\dfrac{E_d}{RT}\right)}dE \\ &= \frac{R\,T}{E_0 - E_1}\,\ln\left[1+\frac{s_0\,\nu\,\tau}{n_m}\,p\,\exp\left(\frac{E_d}{RT}\right)\right]\Bigg|_{E_1}^{E_0} = \\ &= \frac{R\,T}{E_0 - E_1}\,\ln\left[\frac{1+\dfrac{p}{p^*}\,\exp\left(\dfrac{E_0}{RT}\right)}{1+\dfrac{p}{p^*}\,\exp\left(\dfrac{E_1}{RT}\right)}\right] \end{aligned} \tag{2.24}$$

where $p^* = \dfrac{n_m}{s_0\,\tau_0\,\nu}$.

The main parameters of the Temkin isotherm are E_0, E_1, and n_m. Fig. 2.5, Fig. 2.6, and Fig. 2.7 show the effect on the pumpdown slope for different energetic and site distributions. Since E_1 governs the highly energetic sites exploited for high sojourn times, for increasing E_1, the pumpdown curve becomes less steep (see Fig. 2.5,). On the other hand, E_0 represents the low energetic sites; therefore, for lower values, only the initial part of the pumpdown decreases faster (Fig. 2.6). Changes in n_m shift the pumpdown curve towards lower or higher pressure, leaving the slope shape intact (Fig. 2.7). The construction of the isotherm allows its application for more complex surfaces. In the case of a non-uniform surface, the latter can be split into a number of uniform elements d_i, each of which follows a Langmuir isotherm and has assigned a constant binding energy [63].

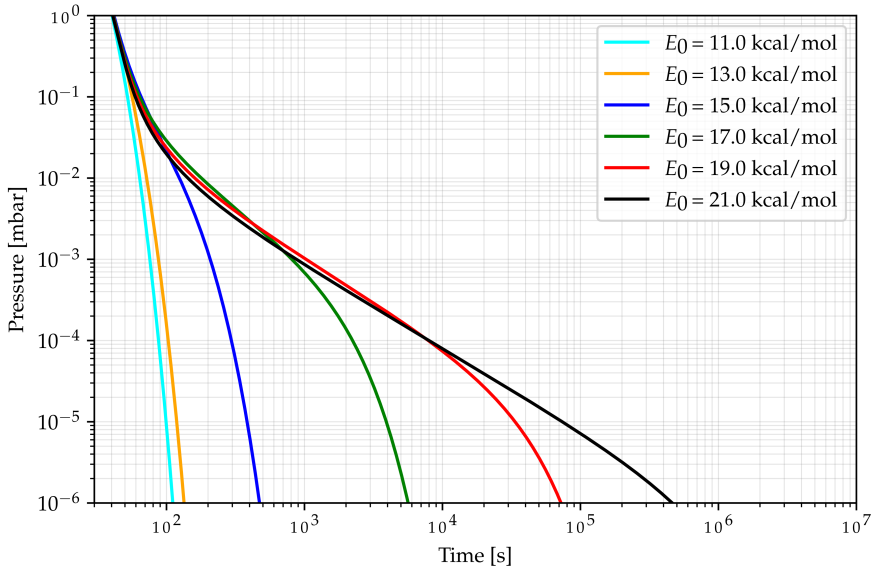

Figure 2.5: Pumpdown for a vacuum system with an adsorption layer following the Temkin adsorption isotherm for E_0 from 11 to 21 kcal/mol. E_1 is fixed at 10 kcal/mol. The other system parameters used for the simulation are the same as for Fig. 2.3.

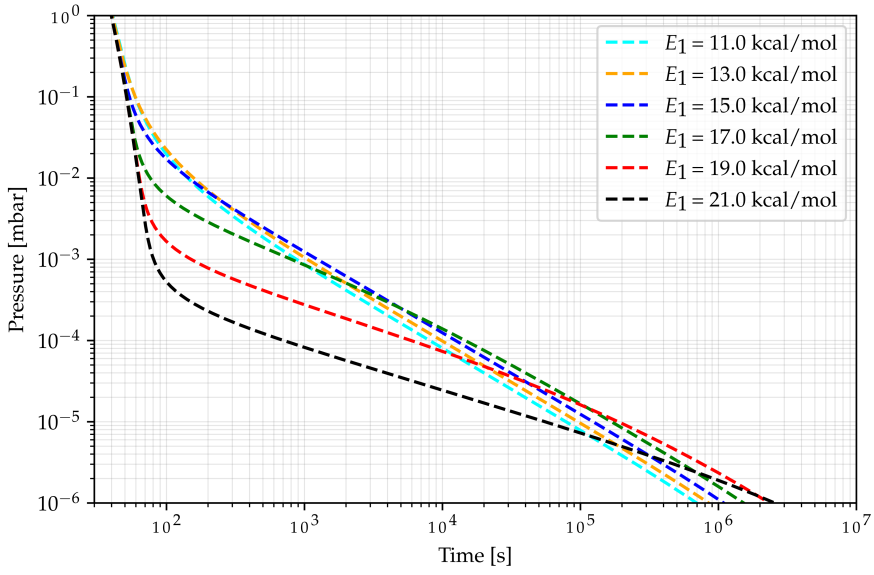

Figure 2.6: Pumpdown for a vacuum system with an adsorption layer following the Temkin adsorption isotherm for E_1 from 11 to 21 kcal/mol. E_0 is fixed at 22 kcal/mol. The other system parameters used for the simulation are the same as for Fig. 2.3.

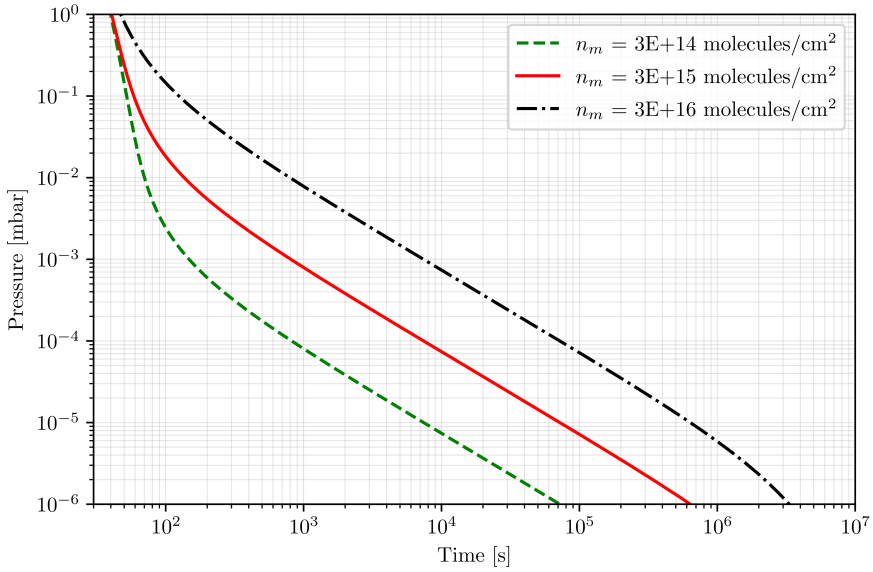

Figure 2.7: Variation of the pumpdown curve of a vacuum system following a Temkin isotherm for different n_m. The system parameters used for the simulation are: E_0 = 22 kcal/mol, E_1 = 10 kcal/mol $\tau_0 = 10^{13}$ s, $s_0 = 1$, $P_0 = 4$ mbar, $A = 5000$ cm^2, $V = 20$ l, $S_{N_2} = 4\,\mathrm{l\,s^{-1}}$ and $T = 293$ K.

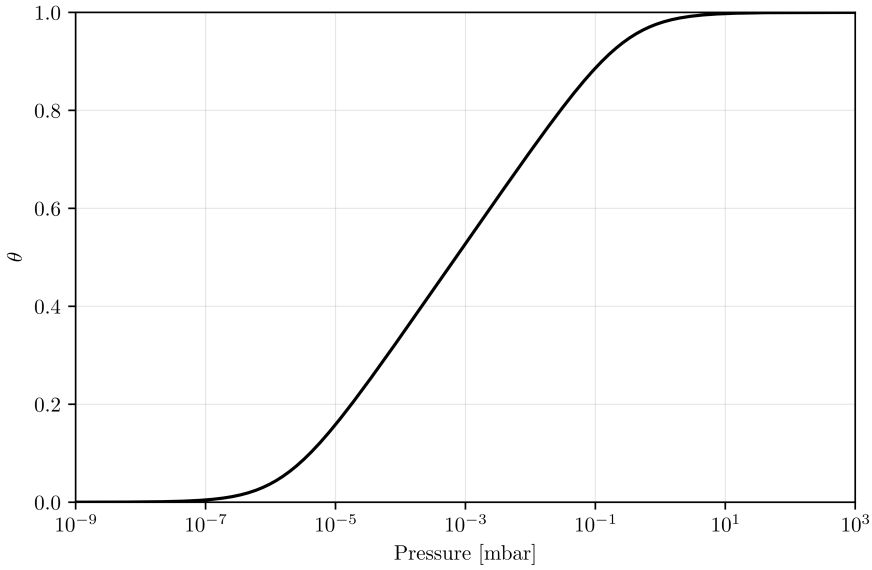

Figure 2.8: Coverage as a function of pressure for a system where the surface desorption obeys the Temkin isotherm. As can be seen, the central part of the curve shows a linear slope. The isotherm parameters are: E_0 = 21 kcal/mol, E_1 = 11 kcal/mol, $n_m = 3 \times 10^{15}$ molecules/cm^2, $\tau_0 = 10^{13}$ s, $s_0 = 1$, and $T = 293$ K.

As can be seen in Fig. 2.7, the central part of the pumpdown curve (otherwise the central part of the coverage (Fig. 2.8)) resembles well the t^{-1} behaviour seen experimentally (see Fig. 2.2). For the central part of the pumpdown, the following inequality is true [63]:

$$\exp\left(\frac{E_1}{RT}\right) << \frac{p^*}{p} << \exp\left(\frac{E_0}{RT}\right) \tag{2.25}$$

In the pressure range where the inequality is true, Eq. (2.24) can be reduced to [63]:

$$\theta_T = \frac{R\,T}{E_0 - E_1} \ln\left[\frac{p}{p^*} \exp\left(\frac{E_0}{R\,T}\right)\right] \tag{2.26}$$

Deriving Eq. (2.26) in p and substituting it in Eq. (2.17):

$$\left(\frac{1}{p} + \frac{1}{p^2}\,\frac{N_m\,k_b\,T}{V}\right)\,\mathrm{d}p = \frac{1}{\tau_s}\,\mathrm{d}t \tag{2.27}$$

Integrating on both sides and letting p vary from P_0 to p:

$$\ln\left(\frac{P_0}{p}\right) + \frac{N_m\,k_b\,T^2\,R}{V\,(E_0 - E_1)\,P_0}\,\left(\frac{P_0}{p} - 1\right) = \frac{t}{\tau_s}$$

For $\frac{P_0}{p} >> 1$ (otherwise for low pressures):

$$p = \frac{N_m\,k_b\,T^2\,R}{V\,(E_0 - E_1)}\,\frac{\tau_s}{t} \quad \rightarrow p \propto t^{-1} \tag{2.28}$$

As can be seen, applying the necessary approximation, it is possible to fit and simulate the pumpdown of a system knowing its geometrical and functional parameters by using a Temkin isotherm. The same considerations can be extended to a system subject to a change in temperature during the pumpdown, i.e., during a bakeout. Although the above-presented approach is very effective in simulating vacuum systems in ordinary conditions, it is based on a quasi-equilibrium condition; therefore, for situations where there is a sudden increase/decrease in pumping speed (i.e. opening or closing of an isolation valve), the thermodynamic equilibrium is not fulfilled anymore, and the Kanazawa inequality Eq. (2.13) is not valid [52].

2.3 Hydrogen outgassing rate

Once water vapour is strongly reduced by a long pumpdown or a bakeout, the outgassing process is dominated by the gases dissolved in the bulk [52]. As discussed in Section 2.1, in an all-metal system, only H atoms possess sufficient mobility to reach the surface, recombine, and be desorbed as molecular H_2 in vacuum within a reasonable time frame. The H atoms, whose sources are the metal ores or the tools and furnaces used for the primary/secondary metallurgy, are trapped during the liquid-solid

transition. The quantity of residual H in metals depends on the host microstructure's gas solubility.

If the gaseous hydrogen and the dissolved one are in equilibrium (H_2 (g) = 2 H (dissolved in the bulk), the hydrogen concentration in the bulk ($C_{eq,H}$) can be calculated with the Sievert's law [70]:

$$c_{eq,H}(P_{H_2}, T) = K_s(T)\,\sqrt{P_{H_2}} = K_0\,\exp\left(-\frac{\Delta H}{2\,k_b\,T}\right)\sqrt{P_{H_2}} \tag{2.29}$$

Where $K_s(T)$ is hydrogen solubility in the metal, K_0 is a pre-factor, ΔH is the enthalpy of solution, P_{H_2} is the hydrogen pressure in the gas phase often referred as dissociation pressure [52].

The absorption of hydrogen, for most of the materials used for constructing UHV vessels (Fe, Ni, Cu and their alloys), is an endothermic reaction [71]. This translates into a positive ΔH, and the solubility increases as temperature increases and vice versa. This condition has fundamental implications that can be seen in Fig. 2.9; for example, the solubility of H in iron drastically changes during the cooling from the liquid phase to room temperature. This allows H to be distributed in the metal along the grain boundaries, precipitates (carbides, nitrides, etc.), and in the lattice, forming the residual hydrogen content in the material. The typical hydrogen content in steels used for UHV applications is between 0.1 and 10 ppm wt. [52].

If the dissociation pressure from Eq. (2.29) is plotted in function of the temperature of the material, important information can be extracted. Taking as example 1 wt.

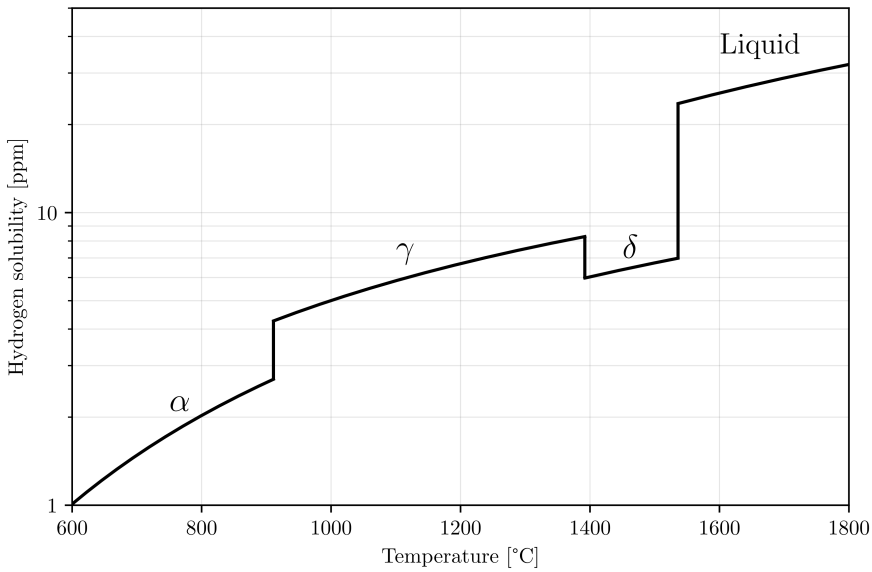

Figure 2.9: Hydrogen solubility in iron in function of temperature at P_{H_2} = 1 atm. As can be seen, the solubility is significantly reduced during cooling through the different allotropic forms of iron. The graph is adapted from [72].

ppm of hydrogen dissolved in austenitic stainless steel (see Fig. 2.10), it can be seen that for the typical pressures reached during vacuum operation, the hydrogen at room temperature will always be outgassed. The area above the curve in Fig. 2.10 represents the set of temperatures and hydrogen pressures where the hydrogen gets recharged in the material. The hydrogen pressure to recharge the material at room temperature should be over 10 bar. If compared with the 10^{-4} mbar (equivalent to 10^{-4} wt. ppm) of hydrogen partial pressure in the atmosphere [73], it is clear that the recharging of hydrogen in the material at room temperature is physically impossible. That is why, in ordinary vacuum operation, $c_{eq,H}$ is neglected with respect to the residual hydrogen content [52].

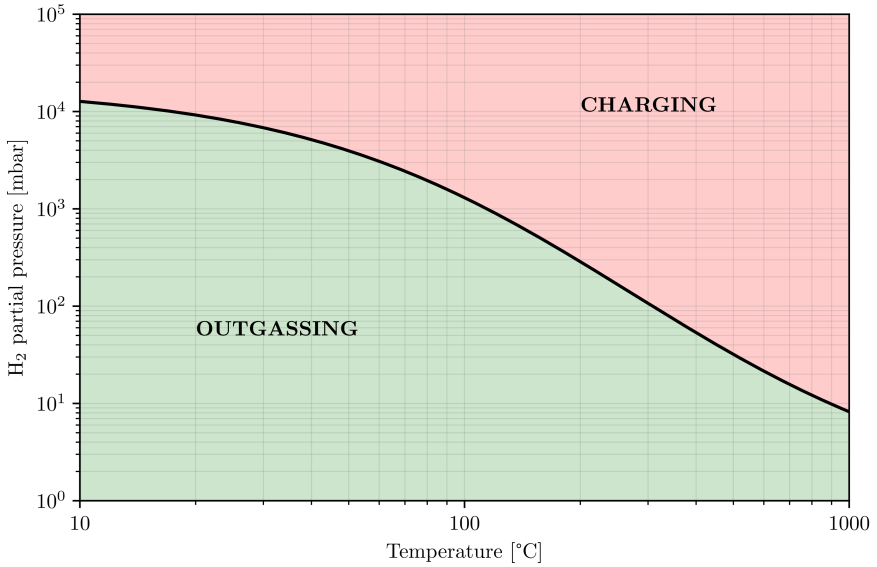

Figure 2.10: Equilibrium pressure in function of temperature for austenitic stainless steels containing 1 wt ppm [74] of hydrogen. Below the equilibrium pressure, hydrogen is outgassed; above, the hydrogen is charged in the material.

The desorption of the residual hydrogen from a solid can be schematised in two steps: the diffusion of the atom towards the surface and the following recombination with another atom to form the diatomic molecule to get desorbed. According to the nature of the metal solution (endothermic or exothermic), the bottleneck of hydrogen desorption could be the diffusion of hydrogen in the material or the rate of recombination on the surface, referred to as diffusion-limited and recombination-limited outgassing, respectively.

Experimental data reveals that diffusion is the limiting step for endothermal-type metals, proving the hypothesis that dissolution energy is higher than that of desorption; therefore, surface recombination is much faster than diffusion [52][75]. Although this is true for most of the hydrogen concentrations that can be found in UHV-compatible materials, Shipilevsky and Glebovsky [75] calculated the critical number of monolayer dissolved, above which the hydrogen outgassing rate is diffusion limited, and below

which it recombination limits the kinetics of desorption.

2.3.1 Diffusion limited outgassing

If the hydrogen outgassing is limited by bulk diffusion (Diffusion Limited Model, DLM), its value can be predicted by Fick's law. Considering one dimension [76]:

$$\frac{\partial c(x,t)}{\partial t} = D\,\frac{\partial^2 c(x,t)}{\partial x^2} \tag{2.30}$$

where D is the diffusion coefficient of H atoms in the metal: $D = D_0\,\exp\left(-\frac{E_d}{k_B T}\right)$ with D_0 a pre-factor and E_d is the diffusion energy, $c(x,t)$ is the concentration of atoms at position x and time t.

The general solution to Eq. (2.30) can be obtained by using the method of separation of variables:

$$c(x,t) = \Gamma(x)\,\Psi(t) \tag{2.31}$$

Substituting Eq. (2.31) in Eq. (2.30):

$$\frac{1}{\Psi(t)}\,\frac{\partial \Psi(t)}{\partial t} = \frac{D}{\Gamma(x)}\,\frac{\partial^2 \Gamma(x)}{\partial x^2} \tag{2.32}$$

Being both sides independent from each other, the ODE can be solved separately for the same constant ε:

$$\begin{aligned} &\frac{1}{\Psi(t)}\,\partial\Psi(t) = -\varepsilon^2\,D\,\partial t \\ &\rightarrow \Psi(t) = \exp\left(-\varepsilon^2\,D\,t\right) \end{aligned} \tag{2.33}$$

$$\begin{aligned} &\frac{1}{\Gamma(x)}\,\frac{\partial^2\Gamma(x)}{\partial x^2} = -\varepsilon^2 \\ &\rightarrow \Gamma(t) = A\sin(\varepsilon x) + B\cos(\varepsilon x) \end{aligned} \tag{2.34}$$

Therefore the general solution $c(x,t)$ can be written as:

$$c(x,t) = \Gamma(x)\,\Psi(t) = \left[A\sin(\varepsilon x) + B\cos(\varepsilon x)\right]\,\exp\left(-\varepsilon^2\,D\,t\right) \tag{2.35}$$

where A and B are integration constants. Given the linearity of Eq. (2.30), Eq. (2.35) can be written more generally as [76]:

$$c(x,t) = \sum_{m=1}^{\infty}\left[A_m\sin(\varepsilon_m\,x) + B_m\cos(\varepsilon_m\,x)\right]\,\exp\left(-{\varepsilon_m}^2\,D\,t\right) \tag{2.36}$$

where A_m, B_m, and ε_m are determined by the initial and boundary conditions. The initial concentration $c_0 = c(x,0)$ is assumed constant for the problems solved later

in the text. Having determined in Section 2.3 that the recombination and desorption of hydrogen from the surface are considered much faster than diffusion, the surface concentration $c(x_s,t)$ is considered in quasi-equilibrium with the gas phase so that it can be approximate using the Sievert's law Eq. (2.29):

$$c_w = c(x_s,t) \approx c_{eq,H}(P_{H_2},T)$$

Finally, the outgassing rate, defined as the flux of gas arriving at the surface via diffusion [52], can be written as:

$$q(t) = -D \left.\frac{\partial c(x,t)}{\partial t}\right|_{x=x_s} \tag{2.37}$$

The diffusion-limited outgassing rate is calculated below for typical vacuum situations.

Semi-infinite solid

It is here assumed a semi-infinite solid ($x > 0$) with the following initial and boundary conditions:

$$\text{initial condition: } c(x,0) = c_0 - c_w \tag{2.38}$$

$$\text{boundary condition: } c(0,t) = 0 \tag{2.39}$$

By substituting the boundary and initial conditions in Eq. (2.36), the concentration can be expressed as [76]:

$$c(x,t) = (c_0 - c_w)\, erf\left(\frac{x}{2\sqrt{D\,t}}\right) \tag{2.40}$$

where erf is the error function. Applying Eq. (2.37), the outgassing rate from a semi-infinite solid can be written as:

$$q(t) = (c_0 - c_w)\left(\frac{D}{\sqrt{\pi\, D\, t}}\right) = (c_0 - c_w)\left(\frac{D}{\sqrt{\pi}\,\lambda}\right) \tag{2.41}$$

The quantity $\sqrt{D\,t}$, called diffusion length and indicated with the letter λ, gives the distance travelled by an atom in a time t. As seen in Eq. (2.40), the outgassing rate is proportional to $t^{-1/2}$. This proportionality is also held for finite dimension slabs, whereas L (dimension of the slab) $>> \lambda$.

Slab approximation

Given a slab with thickness L, the initial and boundary conditions are expressed as:

$$\text{initial condition: } c(x,0) = (c_0 - c_w) \qquad 0 < x < L \tag{2.42}$$

$$\text{boundary condition: } c\,(0,t) = 0 \qquad x = 0, L \tag{2.43}$$

Applying the boundary conditions to Eq. (2.36), it can be easily found that:

$$x = 0 \rightarrow B_m = 0 \quad \text{and} \quad x = 0 \rightarrow \varepsilon_m = \frac{\pi\, m}{L} \tag{2.44}$$

Substituting Eq. (2.44) in Eq. (2.36) and applying the initial conditions:

$$(c_0 - c_w) = \sum_{m=1}^{\infty} A_m \sin\left(\frac{\pi\, m\, x}{L}\right) \tag{2.45}$$

Equation (2.36) is a Fourier series for sine and cosine; therefore the coefficient A_m can be determined as [77]:

$$A_m = \frac{2}{L}\int_0^L (c_0 - c_w)\, \sin\left(\frac{\pi\, m\, x}{L}\right) dx = \frac{2\,(c_0 - c_w)}{\pi\, m}\, \left[-\cos\left(\frac{\pi\, m\, x}{L}\right)\right]\Bigg|_0^L =$$

$$= \frac{4\,(c_0 - c_w)}{(2n+1)\,\pi} \quad \text{where} \quad m = 2n+1 \quad \text{with} \quad n = 0, 1, 2, \ldots \tag{2.46}$$

Therefore the concentration for a slab of thickness L, can be written as:

$$c(x,t) = \\ = \frac{4\,(c_0 - c_w)}{\pi} \sum_{n=0}^{\infty} \frac{1}{(2n+1)} \sin\left[\frac{(2n+1)\,\pi\, x}{L}\right] \exp\left[-\frac{(2n+1)^2\,\pi^2}{L^2}\, D\, t\right] \tag{2.47}$$

Differentiating Eq. (2.47) according to Eq. (2.37):

$$q(t) = \frac{4\,(c_0 - c_w)\, D}{L} \sum_{n=0}^{\infty} \exp\left[-\frac{(2n+1)^2\,\pi^2}{L^2}\, D\, t\right] \tag{2.48}$$

For $\lambda^2 > 0.05\, L^2$, as can be seen in Fig. 2.11, only the first term of Eq. (2.48) is relevant. Hence, the outgassing rate for a slab can be well approximated as [78]:

$$q(t) \approx \frac{4\,(c_0 - c_w)\, D}{L} \exp\left(-\frac{\pi^2}{L^2}\, D\, t\right) \tag{2.49}$$

Slab approximation and arbitrary thermal cycles

Besides reducing the water outgassing rate, the bakeout produces a reduction of the hydrogen outgassing. To evaluate the post-bakeout hydrogen outgassing rate at room temperature, Eq. (2.49) can be written as:

$$q \approx \frac{4\,(c_0 - c_w)\, D(T_{RT})}{L} \exp\left[-\frac{\pi^2}{L^2}\, D(T_H)\, t_H\right] \tag{2.50}$$

where T_H and t_H are the temperature and duration of the treatment respectively; T_{RT} is the room temperature. For an arbitrary thermal profile $T_H(t)$, the equation above can be generalised as:

$$q \approx \frac{4\,(c_0 - c_w)\, D(T_{RT})}{L} \exp\left[-\frac{\pi^2}{L^2} \int_0^{t_H} D(T_H(t))\, dt\right] \\ \approx \frac{4\,(c_0 - c_w)\, D(T_{RT})}{L} \exp\left(-\pi^2\, F_0\right) \tag{2.51}$$

$$\text{where} \quad F_0 = \frac{\int_0^{t_H} D(T_H(t))\, dt}{L^2} = \frac{\lambda^2}{L^2} \quad \text{Fourier number}$$

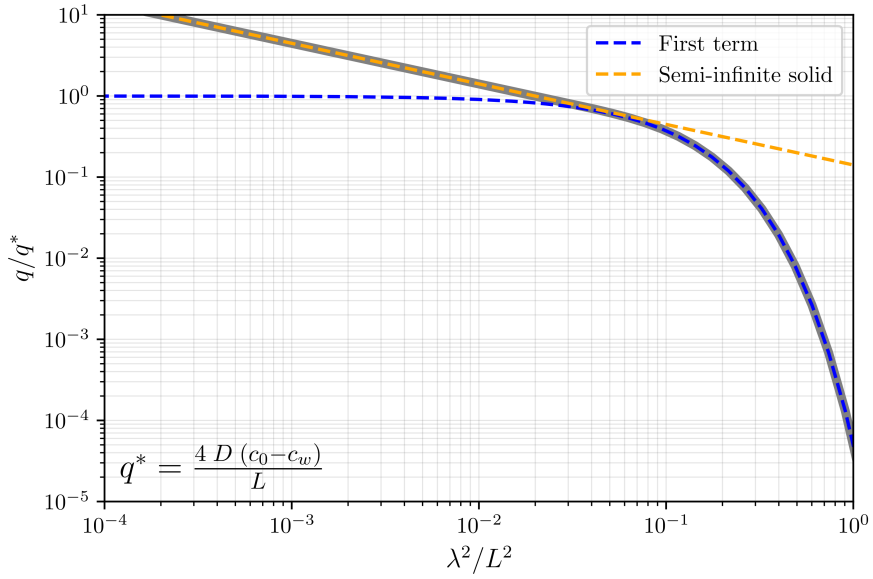

Figure 2.11: Outgassing rate from Eq. (2.49) normalised to the quantity q^*(grey line) plotted with its limits: the semi-infinite solid approximation (orange dashed line) and the first term of the summation (blue dashed line). As can be seen, the first term is a good approximation of the summation for $\lambda^2 > 0.05\,L^2$. The graph was produced assuming: D_0= 5.8 $\times$ 10^{-3} cm^2/s^2, E_d = 0.56 eV, T = 293 K and L = 3 mm.

The Fourier number indicates the amount of residual hydrogen depleted during the thermal treatment.

In case of multiple and identical heating cycles (i.e. a series of bakeouts) lasting t_H at a temperature T_H, the hydrogen outgassing rate after the (n+1) bakeout can be calculated as:

$$q_{n+1} = q_n \exp\left[-\frac{\pi^2}{L^2}\,D(T_H)\,t_H\right] \tag{2.52}$$

Equation (2.52) indicates that, after repetitive bakeouts at the same temperature and duration, the hydrogen outgassing rate is reduced by the same quantity [78].

Although the in situ bakeouts could reduce the residual hydrogen, the process is inefficient in attaining very low concentrations. To achieve low hydrogen contents, depleting the bulk down to what Sievert's law admits, austenitic stainless steels can be vacuum fired. The vacuum firing consists of a high-temperature thermal treatment (up to 1000°C) done in a vacuum furnace, where a hydrogen partial pressure of about 4×10^{-5} mbar can be attained at the end of the plateau of the heat treatment. The vacuum firing aims to increase the diffusion length of hydrogen while creating a gradient with the furnace partial pressure until $c_0 \approx c_w$ (furnace). The optimal temperature for the firing ranges is between 500°C and 1000°C, depending on the grade type. For temperatures lower than 500°C, the diffusion is too slow, while for temperatures higher than 1000°C, the steel might be subject to changes in the

metallurgical properties (i.e. abnormal grain growth or elements loss) [79, 80]. The duration of the treatment depends on the firing temperature and the thickness of the component (see Fig. 2.12). As can be seen, a temperature of about 900°C for 2-3 h is sufficient to reach diffusion lengths in the order or higher than the typical thickness of vacuum vessels ($\approx$ 2.5 mm). If this happens, the residual hydrogen content is reduced to the minimum value allowed by the steel's solubility and the lowest hydrogen partial pressure in the furnace during the treatment (concentrations as low as 0.1 wt ppm can be attained for an mm thick austenitic stainless steel sheet fired at 950°C for 2 h in a furnace with H_2 partial pressure of 10^{-5} mbar). For thick components, such as ConFlat flanges where the F_0 is much less than 3, hydrogen will only be partially reduced if the same recipe is applied; therefore, the outgassing rate can be approximated with the semi-infinite solid equation. However, even if the partial pressure is further improved in the furnace, it will not have any effect since $c_w << C_0$ (see Fig. 2.13).

Since in real applications, the vacuum firing is followed by an in-situ bake-out for the reduction of water vapour, using the models based on slab approximation shown above, the outgassing rate at room temperature can be calculated as follows:

$$q \approx \frac{4\,(c_F - c_w)}{L}\, D(T_{RT}) \sum_{n=0}^{\infty} \exp\left[-(2n+1)^2\, \pi^2\, F_0(T_{BO}, t_{BO})\right] \tag{2.53}$$

$$+ \frac{4\,(c_0 - c_F)}{L}\, D(T_{RT}) \sum_{n=0}^{\infty} \exp\left[-(2n+1)^2\, \pi^2\, F_0(T_{BO}, t_{BO} + F_0(T_{VF}, t_{VF})\right]$$

where: c_F is the concentration of hydrogen in the furnace, c_0 is the initial concentration of hydrogen in the material, c_w is the concentration of hydrogen in the gas phase of the vacuum system, $F_0(T_{BO}, t_{BO})$ is the Fourier number for the bakeout and $F_0(T_{VF}, t_{VF})$ is the Fourier number for the vacuum firing. Figure 2.13 depicts the hydrogen outgassing rate at room temperature after a vacuum firing at 950°C for 2 h and a bakeout at 150°C for 24 h. This vacuum firing recipe is used daily at CERN for austenitic stainless steels. For thicknesses below 5 mm, the outgassing rates below 1×10^{-14} mbar l s^{-1} cm^{-2} can be obtained. These results, two orders of magnitude better than the bakeout alone, are verified experimentally [52, 78].

Alternatively to the vacuum firing, austenitic stainless steels can be air-baked, obtaining similar outgassing rates. The air bakeout consists of heating the component in air at temperatures ranging from 200°C to 450°C Theoretically, the outgassing rate after air bakeout can be calculated via Eq. (2.54) assuming c_F at $\times10^{-4}$ mbar (hydrogen partial pressure in atmospheric air). However, the outgassing rates obtained with air bakeouts are lower than those attained by vacuum firing for the same temperature and duration [81, 82]. A possible explanation for the mismatch between the expected and the measured values can be ascribed mainly to the formation of a thick and mixed iron/chromium oxide layer [83] that acts as a barrier for H atoms.

Two large vacuum systems benefited from the air bakeout in the last century, the LIGO and VIRGO interferometers [84, 85]. LIGO opted to air-bake the AISI 304L coils at 455°C for 36 h before the forming of the ⌀1.2 m - 20 m long module; on the other end, VIRGO air-baked the ⌀1.2 m - 15 m modules in oven at 410°C for 72h.

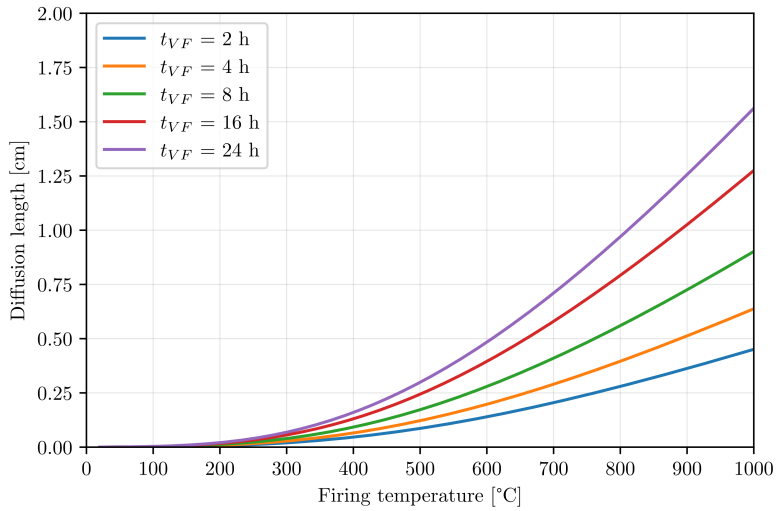

Figure 2.12: Diffusion length in function of the firing temperature and duration. As can be seen, a vacuum firing executed at temperatures around 900°C for 2 h corresponds to ≈ 2.5 mm of diffusion length. The parameters used for the graph are: $D_0 = 4.7\ 10^{-3}$ cm^2 s^{-1} and E_d = 0.56 eV.

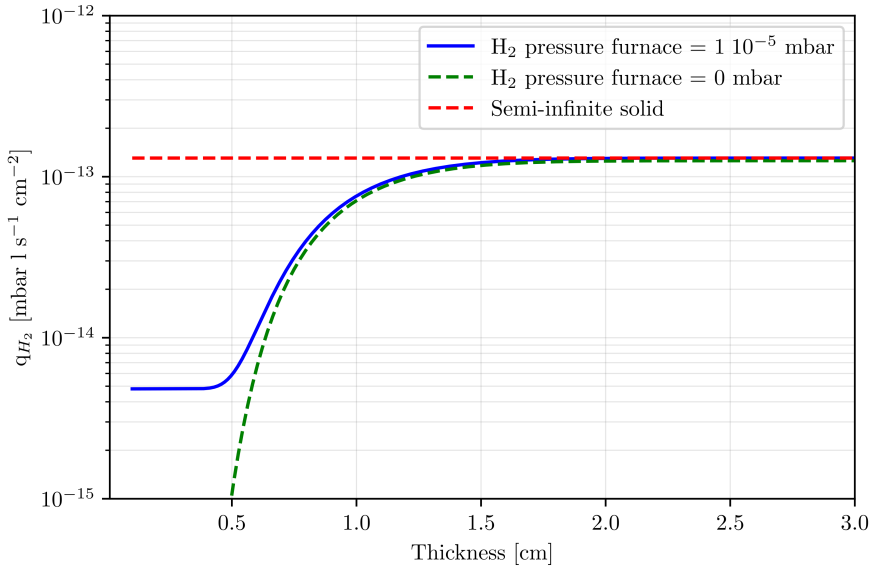

Figure 2.13: Hydrogen outgassing rate at room temperature in function of the thickness of an austenitic stainless steel component after a vacuum firing at 950°C for 2 h followed by a bakeout at 150°C for 24 h. The parameters used for the computation are taken from [52].

2.3.2 Hydrogen trapping

The above-described approximations are valid when hydrogen is mostly distributed around grain boundaries and in the lattice.

In reality, metals are often characterised by lattice defects, such as dislocations, vacancies, microcracks and precipitated phases (carbides, nitrides, etc.), to name a few. The origin of defects is attributed to particular manufacturing processes, such as cold working or precipitation of unwanted phases during steel production. The defects trap hydrogen to contents beyond the lattice solubility admitted by Sievert's laws due to a favourable energetic environment [86]. Apart from the increase in concentration, the traps hinder the effective diffusivity of hydrogen [87].

Given the presence of the traps, the total concentration of hydrogen in the material can be evaluated as follows:

$$C_{total} = c_L + c_T = N_L\,\theta_L + N_T\,\theta_T \tag{2.54}$$

where c is the concentration, N represents the number of sites, and θ represents the fractional occupancy of the lattice sites (c_L, θ_L, N_L) and trapping sites (c_T, θ_T, N_T). Like the desorption from the lattice, the desorption from trapping sites has an associated activation energy E_T, often called de-trapping energy.

Given the different types of trapping sites, the de-trapping energy can assume values higher or lower than E_a from the lattice. Since the nature of the materials leads to different E_a, the type of trapping sites in the literature, to generalise, are usually designated as reversible and irreversible sites. Reversible are all trapping sites for which a small fluctuation in thermal energy (typically around room temperature) is sufficient to cause a hydrogen atom to overcome the potential energy and jump from the trap to the lattice or a higher energetic site approaching an equilibrium. As can be imagined, the reversible traps concur with the lattice hydrogen content in the outgassing rate. On the other hand, irreversible sites are sites with energy significantly higher than hydrogen at a given temperature. Typically, to have a de-trapping from an irreversible site, the input temperature has to be sensibly higher than the room temperature. For most vacuum applications, the contribution from these deep trapping sites is neglected.

No absolute energy threshold is available to qualify trapping sites as reversible or irreversible. Several conventions are common in the literature [88–91]. In this manuscript, whether hydrogen de-trapping is going to be discussed, no speculation on the origin is going to be made, and the trapping sites are going to be defined as reversible or irreversible, simply if they have activation energy lower or higher than the lattice activation energy E_a, respectively.

In evaluating the impact of the traps on the diffusion of hydrogen, many theories have been developed in the last century [86, 92, 93]. One of the most known is the model developed by Oriani [86]. In his model, Oriani provides a solution to the generalised problem of McNabb and Foster [93], assuming a local equilibrium between the traps and the interstitial hydrogen to define the effective hydrogen diffusion content as:

$$D_{eff} = D\,\frac{c_L}{c_L + c_T\,(1-\theta_T)} \tag{2.55}$$

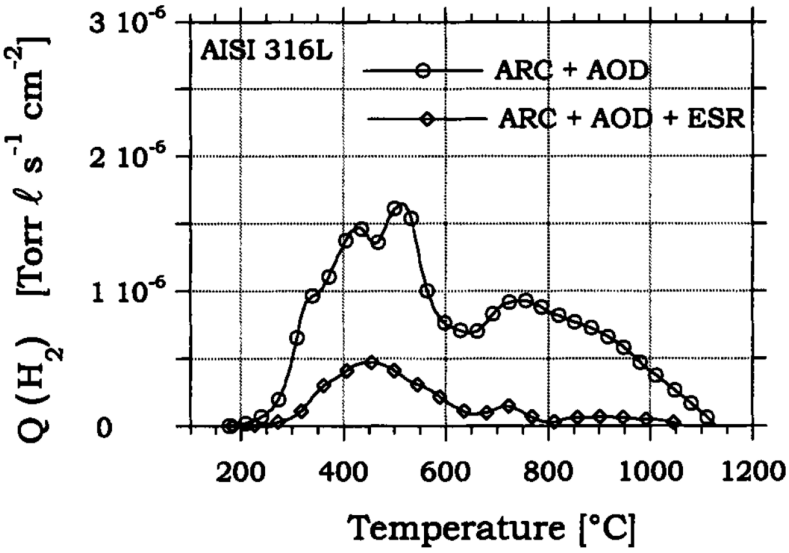

Figure 2.14: Hydrogen thermal desorption spectra of AISI 316L samples (thickness = 1 mm) solution annealed produced with different techniques: (ARC) Arc furnace melting, (AOD) Argon Oxygen decarburation, and (ESR) Electro Slag Remelting. The spectra where obtained using ramp rate β = 5 K min^{-1} [95]. The graph shows the influence of a refining process, such as the ESR, on reducing the trapping site and, therefore, the hydrogen content compared to the ARC+AOD sample.

For very low lattice and trap sites ($\theta_L, \theta_T << 1$) the equation can be simplified as:

$$D_{eff} = D \frac{1}{1 + \frac{N_T}{N_L} \exp\left(\frac{E_T}{k_b T}\right)} \tag{2.56}$$

Independently from the limits of applicability of the Oriani or other models, the de-trapping of hydrogen is a greatly observed phenomenon [91, 94] for both mechanical and thermal stimulation. One of the most common methods to thermally study hydrogen traps is Temperature Programmed Desorption (TPD). The TPD, typically carried out in vacuum, foresees the heating of a specimen from room temperature up to 1000°C, following a linear ramp rate β. A mass spectrometer near the sample tracks the evolution of the hydrogen spectra in the function of temperature (see Fig. 2.14). A common method to extract the binding energy for the different peaks/trapping sites characterising the hydrogen spectra, known as the Kissinger method, is to test the specimens with different ramp rates [96–99]. For first-order reactions, the maximum desorption of gas (peak) is obtained for a given β at a temperature T_p:

$$\frac{\mathrm{d}q(t)}{\mathrm{d}t} = 0 \tag{2.57}$$

Defining the outgassing rate with the slab approximation as in Eq. (2.49) and given

linear ramp rate:

$$\frac{\mathrm{d}q(t)}{\mathrm{d}t} = \frac{\mathrm{d}D(t)}{\mathrm{d}t} - D(t)^2 \frac{\pi^2}{L^2} = 0 \tag{2.58}$$

$$T = T_0 + \beta\, t \rightarrow D(t) = D_0\, \exp\left(-\frac{E}{k_b\,(T_0 + \beta\, t)}\right) \tag{2.59}$$

Where E is a general activation energy. By substituting the redefined diffusion coefficient into Eq. (2.58) and explicitating E for for T_{max}:

$$\log\left(\frac{\beta}{T_p^2}\right) = \log\left(\frac{k_b\, D_0\, \pi^2}{E\, L^2}\right) - \frac{E}{k_b\, T_p} \tag{2.60}$$

By doing measurements for different ramping rates and applying the linear regression by plotting $\log\left(\frac{\beta}{T_p^2}\right)$ in function of $\frac{1}{k_b\, T_p}$, it is possible to extract the activation energy of the trap or eventually the lattice (see Fig. 2.15).

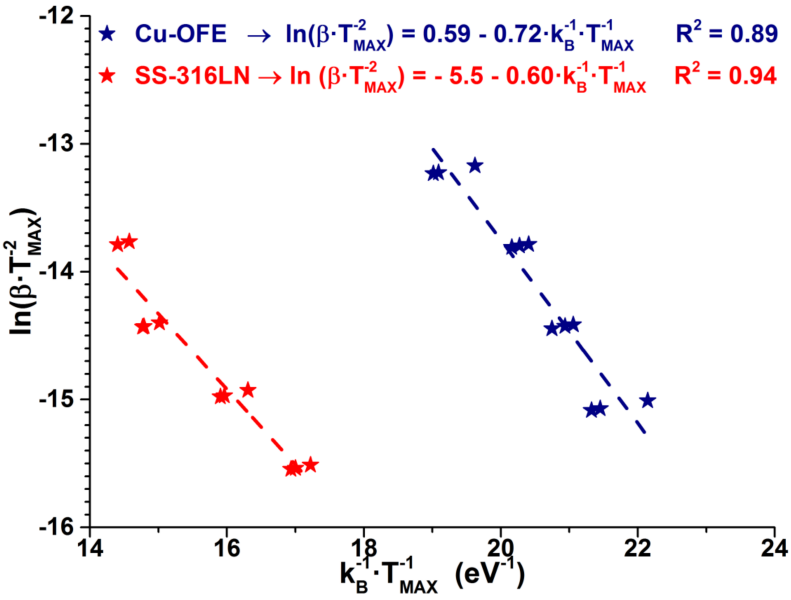

Figure 2.15: Linear regression for a AISI 316LN and Cu-OFE samples heated from 25°C to 950°C with β of 5, 10, 20 and 40 K min^{-1} with a TPD system. With T_{max}, the temperature at which the peak manifests is intended. The resulting lattice activation energies align well with literature values. Figure taken from [100]

Another possibility is to deconvolute the peaks by fitting them with Gaussian-shaped curves [94].

2.3.3 Recombination limited outgassing

When hydrogen diffusion in the material is faster than the recombination of atoms at the surface, the concentration of hydrogen near the surface is in the same order

as the bulk concentration; therefore, the hydrogen profile flattens spatially across the thickness [101]. For endothermal solution metals, as discussed in Section 2.3, this may happen in materials with very low hydrogen concentration or, as seen experimentally, in very well-degassed sub-millimetre thicknesses components (for which $F_0 > 10$ are easily attained) [102].

Baskes [101] formulated a model for the recombination outgassing (RLM, Recombination Limited Model), considering the incoming and outgoing fluxes [103, 104] on a metal surface and the bulk areas near the surface in contact with a hydrogen pressure. Considering a flux of hydrogen molecules striking the surface at an impingement rate ν (see Eq. (2.19)) and the dissociation of a molecule on the surface, the model was constructed under the following assumptions [101]:

- The rate of the process for which one atom gets adsorbed and the other one absorbed is far greater than the probability that both atoms are absorbed.
- The rate of desorption of a molecule generated by recombination from one atom from the bulk and one from the surface is far less than the rate of adsorption of a bulk atom.

Given the assumptions above, the outgassing rate in a recombination-limited endothermic solution metal can be written as [101]:

$$q(t) = 4\,(c_0^*)^{-2}\,\nu\,\alpha\,\exp\left[\frac{(E_s - E_d)}{k_b\,T}\right]c^2(t) = K_R(T)\,c^2(t) \tag{2.61}$$

where $c(t)$ is the bulk concentration at time t, ν is the impingement rate of molecular hydrogen on the surface, α is the sticking coefficient of hydrogen at zero coverage, c_0^* is an experimentally determined constant, E_s is the activation energy of the solution, E_d is the diffusion activation energy. The coefficient K_R takes the name of recombination rate constant and can experimentally be measurable with low-pressure permeation techniques [101][102]. The bulk concentration $c(t)$ can be determined as follows [105]:

$$L\,\frac{\mathrm{d}c(t)}{\mathrm{d}t} = -K_R(T)\,c^2(t) \tag{2.62}$$

$$c(t) = \frac{c_0}{1 + \left(\dfrac{K_R\,c_0}{L}\right)t}$$

Although the validity of the model presented in Eq. (2.61) has been proved for ion implantation in plasma experiments [106] and the evolution of the hydrogen outgassing rate during bakeout [102] for austenitic stainless steel, its application to extrapolate values at room temperature has to be taken carefully. The complexity of the metal surface (oxides and hydroxides contribution) and lack of clearly defined methodology for the measurement of K_R [107] may lead to several orders of magnitude in the difference in the measured values [105].

3. Beam pipe vacuum for GWD

> [Speaking about the difficulties found on building LIGO] Some of the really most difficult stuff is kind of the dumb stuff like vacuum - getting a good enough vacuum for the beams to go through [..]
>
> -Mike Zucker-

This chapter describes the relationship between strain noise and the residual gas in the GWD beam pipe. The 2G-GWDs beam pipe vacuum systems are presented, and their main features are resumed. The chapter then focuses on the ET beam pipe vacuum system, analysing the criticality of the 2020 conceptual design and discussing the potential cost-effective solutions explored by CERN in its project..

3.1 Strain noise induced by residual gas

As briefly introduced in Section 1.3, the residual gas pressure in the beam pipe induces a strain noise that could limit the detector sensitivity. Weiss and Whitcomb first modelled the relationship between gas density and optical path length fluctuations [31, 108]. The model considers a Gaussian beam (TEM_{00} mode) propagating over an axis z from 0 to L (L: length of the interferometer), crossed by a molecule *i* with an optical

polarizability α[c]. It is assumed that the interaction between the incident light and the molecule produces weak scattering and induces an electric dipole polarizing it. The result on the beam is a small distortion of the phase front and a small change in the average phase of the light phase [31].

Since the phase shift is directly proportional to the number of molecules crossing the beam, whereas the wavefront distortion is only proportional to the square root of that number, the latter effect is negligible in comparison to the former [31].

Assuming the beam radius variation along the direction of propagation is negligible:

$$\frac{\mathrm{d}\omega}{\mathrm{d}z} << 1 \rightarrow \omega_0^2 \approx \omega^2(z) \tag{3.1}$$

the mode amplitude phase shift ψ due to a molecule intercepting an incident beam can be estimated as follows [108]:

$$\psi = \frac{4\,k\,\alpha(\omega)}{\omega^2(z)}\,\exp\left(-\frac{2\,(x^2+y^2)}{\omega^2(z)}\right) \tag{3.2}$$

where:

- $k = \frac{2\pi}{\lambda}$, is the wavenumber with λ the laser wavelength.
- $\omega(z) = \omega_0\,\sqrt{1+\frac{z^2}{z_R^2}}$ is the beam radius along the propagation direction z.
- ω_0 the beam radius at the waist [109].
- $z_R = \dfrac{\pi\,\omega_0^2}{\lambda}$ the Rayleigh length.

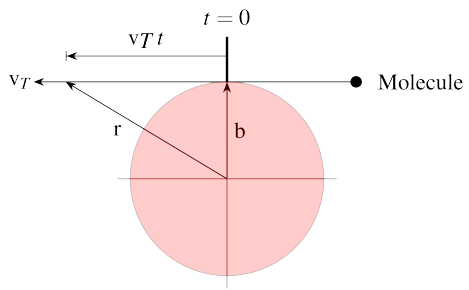

Figure 3.1: Schematic of the impact between the molecule and an incident Gaussian beam. Figure adapted from [108]

Considering a molecule crossing the beam with an impact parameter b (distance of closest approach to the beam axis), ψ can be rearranged in function of the molecule velocity in the direction transverse to the beam (see Fig. 3.1). Expressing the molecule position in radial coordinates (measured from the centre of the beam):
$r^2 = b^2 + v_T^2\,t^2$

$$\psi(t) = \underbrace{\frac{4\,k\,\alpha(\omega)}{\omega^2(z)}\,\exp\left(-\frac{2\,b^2}{\omega^2(z)}\right)}_{A(b)}\,\underbrace{\exp\left(-\frac{2\,v_T^2}{\omega^2(z)}\right)}_{u(t,v_T)} \tag{3.3}$$

[c] $\alpha(\omega) = (n_0-1)/2\,\pi\,\rho_0)$ where n_0 is the refraction index measured at angular frequency ω with ρ_0 density of molecules during the measurement.

From Eq. (3.3) one can see that the phase shift is characterised by an amplitude $A(b)$ and a pulse $u(t, v_T)$. Applying the Fourier transform to the pulse $u(t, v_T)$:

$$S_u(f, v_T) = \int_{-\infty}^{+\infty} u(t, v_T)\, \exp(-i\, \omega\, t)\, dt = \sqrt{\frac{\pi}{2}}\, \frac{\omega(z)}{v_T}\, \exp\left(-\frac{\omega\, \omega(z)}{8\, v_T^2}\right) \quad (3.4)$$

Assuming a Boltzmann distribution (in cylindrical coordinates), one can count the molecules crossing an infinitesimal surface $db \times dz$ having normal along ϕ (see Fig. 3.2), defining the pulse rate:

$$\frac{\mathrm{d}N(b, v_T, T)}{\mathrm{d}t} = \rho\, \frac{v_T^2}{v_0^3}\, \frac{1}{\pi\, \sqrt{\pi}} \exp\left(-\frac{v_z^2}{v_0^2}\right)\, \exp\left(-\frac{v_T^2}{v_0^2}\right) dv_T\, db\, d\phi\, dz\, dv_z \quad (3.5)$$

where:

- $v_0 = \sqrt{\frac{2\, k_b\, T}{m}}$, is the most probable thermal speed of the molecule with mass m.
- ρ is molecules density.
- v_z is the molecule speed component in the direction of the propagation of the laser.

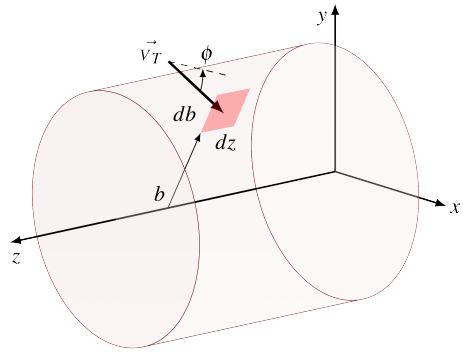

Figure 3.2: Schematic of the impact between the molecule and an infinitesimal surface $db \times dz$ of the Gaussian beam.
Figure adapted from [108]

It is now possible to define the power spectral density given by a pulse rate having an amplitude $A(b)$ as follows [32, 110]:

$$S_L(f) = 2 \int_{\substack{\text{all}\\ \text{pulses}}} \psi^2(f)\, \frac{\mathrm{d}N(b, v_T, T)}{\mathrm{d}t} = 2 \int_{\substack{\text{all}\\ \text{pulses}}} \left|A(b)\, S_u(f, v_T)\right|^2\, \frac{\mathrm{d}N(b, v_T, T)}{\mathrm{d}t} =$$

$$= \frac{16\, k^2\, \alpha^2(\omega)\rho}{\omega(z)\, v_0^3\, \sqrt{\pi}} \int_0^L dz\, \underbrace{\int_0^{2\pi} d\phi}_{2\,\pi}\, \underbrace{\int_0^{+\infty} \exp\left(-\frac{4\, b^2}{\omega^2(z)}\right) db}_{\frac{\omega(z)\, \sqrt{\pi}}{4}} \cdot$$

$$\int_{-\infty}^{+\infty} \underbrace{\exp\left(-\frac{v^2(z)}{v_0^2}\right) dv_z}_{\sqrt{\pi}\, v_0} \int_0^{+\infty} \underbrace{\exp\left(-\frac{v_T^2}{v_0^2} - \frac{\omega\, \omega^2(z)}{4\, v_T^2}\right) dv_T}_{\sqrt{\pi}\, v_0\, \exp\left(-\frac{\omega\, \omega(z)}{v_0}\right)} =$$

$$= \frac{2\,\rho\,(2\alpha k\pi)^2}{v_0} \int_0^L \frac{\exp\left(-\frac{2\,\pi\,f\,\omega(z)}{v_0}\right)}{\omega(z)}\,dz \tag{3.6}$$

Considering the position sensitivity and the two independent paths in the interferometer:

$$S_L(f) = \frac{4\rho(2\pi\alpha)^2}{v_0} \int_0^L \frac{\exp\left(-\frac{2\,\pi\,f\,\omega(z)}{v_0}\right)}{\omega(z)}\,dz \tag{3.7}$$

The formula obtained above represents the power spectral density in Hz^{-1} for a given gas density inside the beam pipe of an interferometer. The amplitude spectral density, elsewhere called strain sensitivity or strain noise $h(f)$ (see Fig. 1.6, Figs. 1.10(a) and 1.10(b)), is defined as the square root of the power spectral density [111]:

$$h(f) = \sqrt{S_L(f)} \tag{3.8}$$

The validity of the statistical model in Eq. (3.7) has been proved with the calibrated leak injections of Xe, N_2 and CO_2 (see Fig. 3.3).

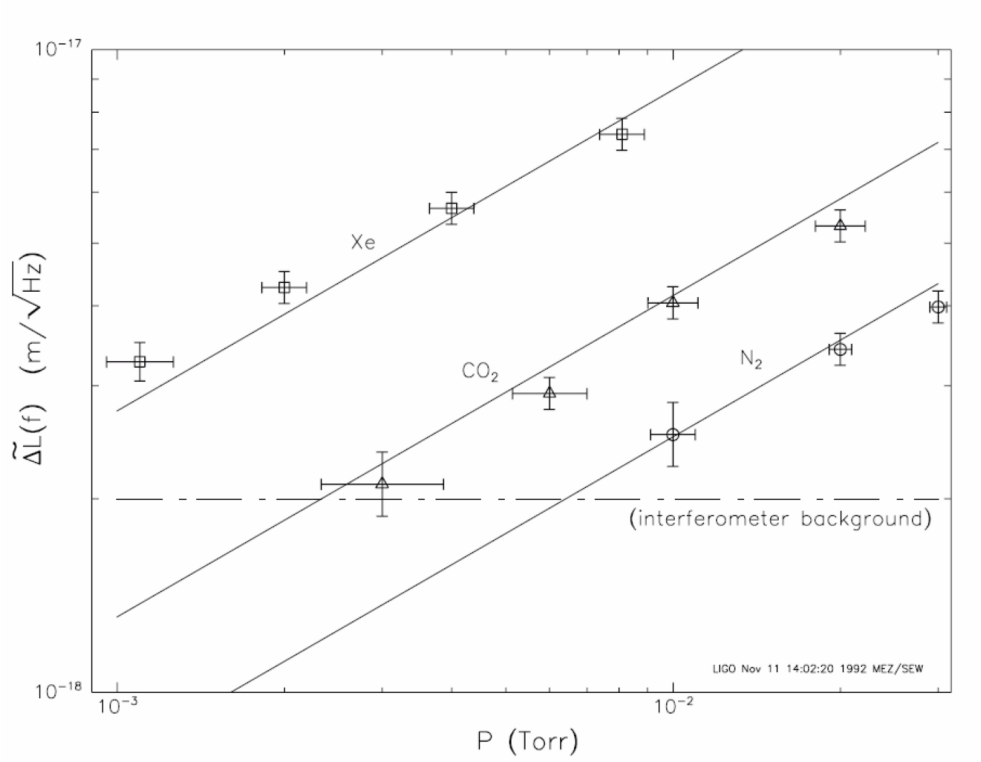

Figure 3.3: Displacement noise as a function of pressure for Xe, CO_2 and N_2 measured at the LIGO 40-meter interferometer. The solid lines are the displacement noise spectral density predicted by Eq. (3.7). The solid points are the measured values. Figure taken from [32].

Since the gas composition in the beam pipe is composed by i types of gases and the vacuum is typically assured by discrete distribution of pumps (lumped pumping), with

the density of the gases varying parabolically between two pumping groups, Eq. (3.7) for the total gas composition can be written:

$$S_L(f) = \sum_j \frac{4(2\pi\alpha_j)^2}{v_{0_j}} \int_0^L \rho_i(z) \frac{\exp\left(-\frac{2\,\pi\, f\, \omega(z)}{v_{0_j}}\right)}{\omega(z)}\, dz \tag{3.9}$$

Figure 3.4 depicts the variation of strain noise as a function of the frequency for ET-HF according to the pumping scheme, optical scheme/properties from ET CDR 2020 [39] and arbitrary gas loads.

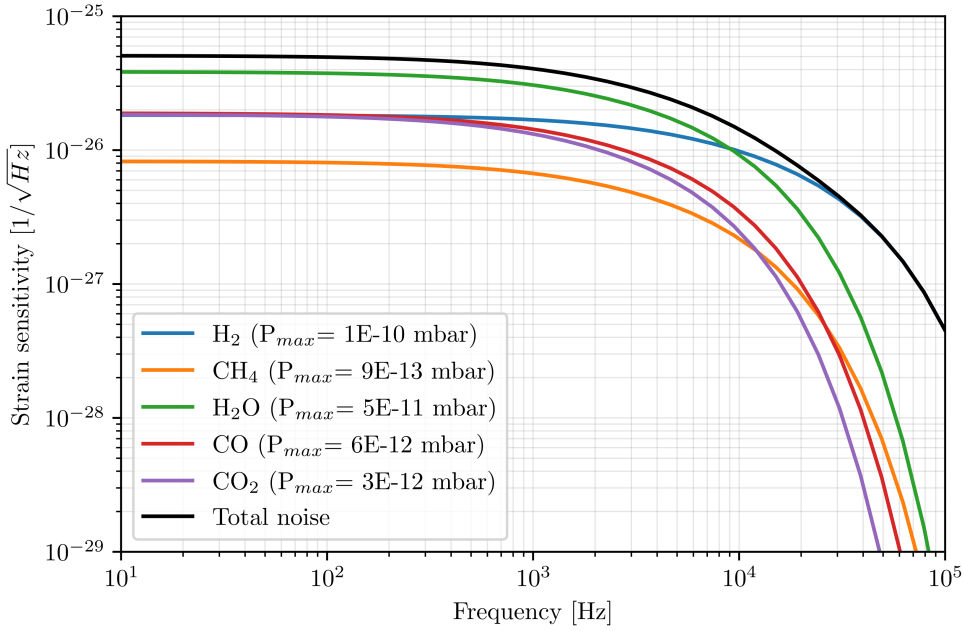

Figure 3.4: Strain noise as a function of the frequency for ET-HF according to pumping scheme (5000 l s^{-1} gas independent every 500 m) and optical scheme/properties from Table 1.1. The gas load assumed for the calculation are: H_2: 2×10^{-14} mbar l s^{-1} cm^{-2}, CH_4: 1×10^{-16} mbar l s^{-1} cm^{-2}, H_2O: 5×10^{-15} mbar l s^{-1} cm^{-2}, CO: 5×10^{-16} mbar l s^{-1} cm^{-2}, CO_2: 2×10^{-16} mbar l s^{-1} cm^{-2}). The optical polarizability for the gases of interest is reported in Table 3.1. The maximum partial pressures reached are reported in parentheses.

Mastering the residual gas composition inside the beam pipe is crucial for delivering low-strain noise. Considering α and v_0 of the typical residual gases in a baked UHV beam pipe (H_2, CH_4, H_2O, CO, CO_2 plus a heavy hydrocarbon (AMU 100) Table 3.1), it can be seen in Fig. 3.5 the impact of their partial pressure in the beampipe on the noise.

A key takeaway from this graph is that, for a given strain, the tolerance for partial pressure of heavy hydrocarbons (AMU 100 or higher) is orders of magnitude lower than for other UHV residual gases (H_2, CH_4, H_2O, CO, CO_2). This has substantial technological implications for the cleaning and handling the pipes during installation.

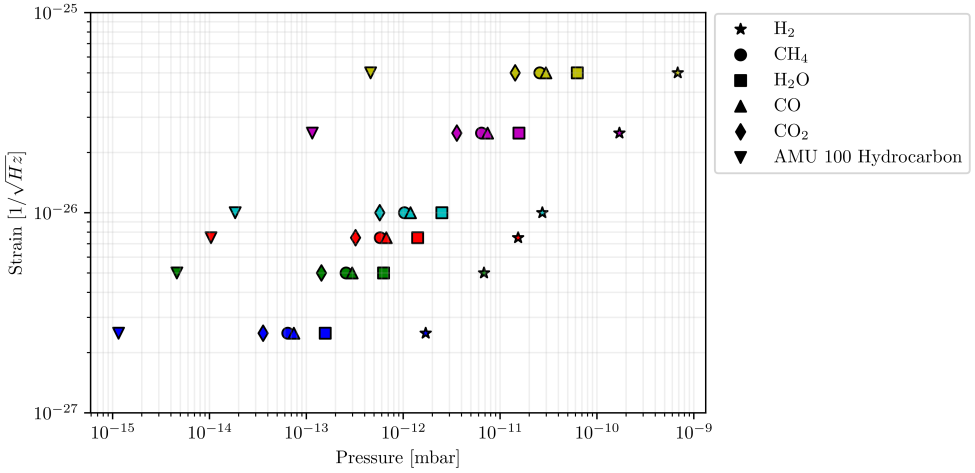

Figure 3.5: Strain noise as a function of the maximum partial pressure of the different gas species for ET-HF with optical scheme/properties from Table 1.1. As expected, the noise generated scales up with the ratio $\alpha/\sqrt{v_0}$ as indicated in Eqs. (3.7) and (3.8).

Table 3.1: Optical polarizability and most probable thermal speed for the main gases of interest for the beam pipe vacuum. The optical polarizabilities are taken from the NIST CCCBDB [112].

Gas	α [$\times 10^{-30}$ m^{-3}]	v_0 [m s^{-1}]	$\alpha/\sqrt{v_0}$ [$\times 10^{-31}$]
H_2	0.787	1561	0.2
CH_4	2.45	570	1
H_2O	1.5	520	0.7
CO	1.95	417	0.9
CO_2	2.51	333	1.4
AMU 100	11.4	221	7.7

Neglecting the typically low levels of CH_4, CO, and CO_2 in a well-baked UHV system, the primary gases contributing to noise are H_2 and H_2O. This underscores the challenge of selecting materials and treatments that can effectively minimize H_2 and H_2O levels without requiring a substantial increase in pumping speed, a more intricate pumping configuration, or an energy- and time-intensive bakeout process for water vapor removal. Given the significant contribution of heavy hydrocarbons and the scale of the experiment, delivering a thoroughly cleaned UHV system is far from trivial.

3.2 2G GWDs beampipe vacuum systems

All four 2G-GWDs adopted different manufacturing and pumping schemes to reach the targeted residual gas noise. Below is a brief resume of the beampipe vacuum layout and

materials used for aLIGO, AdVirgo, KAGRA, and GEO600. The description is done for one arm of each detector since the pumps are equally distributed along both optical path lengths. All the vacuum systems reported below have installed internal optical baffles for stray light noise reduction. However, they are not considered for this section. Gate valves, although not specified, have Viton sealing and are electro-pneumatically actuated.

aLIGO (113–117)

The aLIGO beam pipe vacuum system consists of two 2 km-long sectors. Each sector is delimited from the experimental areas (ITM and ETM) and the neighbouring ones by DN1250 gate valves. The sectors comprise 20 m-long modules consisting of a 19.4 m-long stiffened spiral welded tube with an internal diameter of 1.2 m (wall thickness of 3 mm) and a 60 cm-long 2.5 mm thick hydroformed bellow welded at one end.

Both the tube and the bellow are made of AISI 304L. To meet the stringent H_2 outgassing requirement of less than 3×10^{-14} mbar l s^{-1} cm^{-2}, the AISI 304L coils were air-baked at 455°C for 36 hours before being uncoiled to form the tubes. The bellow was air-baked separately. One of every twelve modules was equipped with a DN250 ConFlat (CF) pumping port, which was later completed at the interferometer site by installing the pumps shielded by a DN250 CF Viton sealed gate valve.

After being cleaned and leak tested, the beam pipe sections were joined on-site to form the vacuum sectors. Each sector was pumped down and baked separately before being put in communication by the opening of the middle DN1250 valves.

The volume evacuation of one vacuum sector was completed in 80 h using a dry roots blower baked by a large fore pump (effective pumping speed: ≈ 2000 m^3 h^{-1}) mounted at one extremity. Once the pressure reached $\approx 1\times10^{-2}$ mbar, two 2000 ls^{-1} Maglev Turbo Molecular Pumps (TMP) mounted at each extremity (backed by a dry pump) and 125K LN_2 cryo-pumps distributed every 250 m pumped down the sector to $\approx 1\times10^{-8}$ mbar in just over two weeks (400 h).

The vacuum sectors were then baked at 160°C for 3 weeks via direct joule effect, passing 1750 A DC, while it was insulated with 15 cm thick rock wool to attain a final water vapour outgassing rate $< 1\times10^{-11}$ mbar l s^{-1}.

Once the bakeout was finished, the cryopumps were substituted by a DN250 CF fitting with a DN63 CF flange for a Residual Gas Analyzer (RGA) installation, a port equipped with an inverted magnetron for UHV pressure monitoring, and a DN40 CF port for auxiliary operations.

For the initial LIGO, the UHV pumping was carried out by only three 2500 ls^{-1} Sputter Ion Pumps (SIP), all behind the DN1250 valves closer to the mirrors (two ITM, one ETM side). Given the more stringent requirements of aLIGO, 1200 ls^{-1} SIPs were added at 1750 m, 2000 m and 3750 m (where the cryopumps were placed) to meet the desired pressure. Specifically, the 1750 m and 2000 m SIPs were strategically placed near the beam waist, where the interferometer is more sensitive to pressure fluctuations.

From the pumpdown until the UHV regime, the pressure reading is deputed to capacitance gauges located in the sector and cold cathode gauges (Pirani and Inverted

Magnetron (IMG)) placed every 250 m. During the bakeout, a special instrumented pumping group was attached in the middle of each sector to monitor the gas evolution with an RGA.

AdVirgo (118)

The AdVirgo beam pipe vacuum system consists of one 3 km-long sector delimited from the experimental areas (ITM and ETM) by DN1000 gate valves. The sector comprises 15 m-long modules consisting of a 14.5 m-long stiffened longitudinal welded tube with an internal diameter of 1.2 m (wall thickness of 4 mm) and a 50 cm-long 2 mm-thick hydroformed bellow welded at one end.

As for aLIGO and AdVirgo, the tubes and the bellows are made of AISI 304L. To meet the stringent H_2 outgassing requirement of less than 3×10^{-14} mbar l s^{-1} cm^{-2}, contrary to what was done in the US, the modules were air-baked at 400°C for 5 days after manufacturing.

One of every twenty modules was equipped with two DN200 CF pumping ports for the intermediate (pumpdown and bakeout) and UHV pumping and a DN63 CF port for the instrumented module, which were later completed at the interferometer site by installing the pumps shielded by a CF Viton sealed gate valve of the respective sizes. The ports were spaced between 15 to 20 cm.

After being cleaned and leak tested, the beam pipe sections were joined on-site to form the vacuum sector. The volume evacuation of the sector was completed in about 3 days using a dry roots blower baked by a large fore pump (effective pumping speed: $\approx$ 1000 m^3 h^{-1}) mounted at one extremity via a DN100 CF manual Viton sealed gate valve. Once the pressure reached $\approx 1\times10^{-1}$ mbar, 1000 ls^{-1} Hybrid TMPs (backed by a dry pump) mounted every 600 m, pumped down the sector to $\approx 1\times10^{-6}$ mbar in just over one week.

The vacuum sector was then baked at 150°C for 1 week via direct joule effect, passing 2000 A DC, while it was insulated with 15 cm thick rock wool to attain a final water vapour outgassing rate $< 1\times10^{-11}$ mbar l s^{-1}.

Once the bakeout was finished, the UHV was carried out by a pumping group with an effective pumping speed of 3000 ls^{-1} composed by two Titanium Sublimation Pumps and a 200 ls^{-1} SIP, distributed every 600 m. For rough pumping and venting purposes, all the pumping modules were equipped with a DN40 CF all-metal angle valve for controlled venting and an IMG gauge for pressure control.

The instrumented modules dedicated to the pressure and residual gas monitoring were distributed every 300 m as for the UHV pumps and composed by an RGA (not all on during operation), a Bayard-Alpert (BA) gauges for the pressure monitoring during bakeout (only at the extremities and at the centre of the sector), capacitance and Pirani gauges for the rough pumping (same distribution as for the BA) and IMGs for the continuous monitoring of the pressure. Due to maintenance, all the instrumented modules were equipped with a DN40 CF all-metal angle valve for controlled venting.

KAGRA (119–121)

The KAGRA beam pipe vacuum system consists of one 3 km-long sector delimited from the experimental areas (ITM and ETM) by DN800 gate valves. The sector comprises 12.5 m-long modules consisting of a 12 m-long longitudinal welded tube with an internal diameter of 0.8 m (wall thickness of 8 mm) joined through flanges to a 50 cm-long 0.6 mm-thick hydroformed bellow at one end.

As for aLIGO and AdVirgo, the tubes and the bellows are made of AISI 304L.

Flanged connections were used because welding underground was impossible, especially in the harsh conditions of the KAGRA tunnel (95-99% humidity). The same restriction was applied for the bakeout, so the KAGRA tubes were only electropolished (to an R_{max} of 2.5μm) to reduce the pumpdown time.

Once cleaned, the modules were baked at 200°C for 20 h under vacuum, dry air vented (-40°C dew point), and temporarily sealed at the extremities for storage.

One of every ten modules had one DN250 CF pumping port, which was later equipped with a manual DN250 CF Viton sealed gate valve for the pumping group installation.

After being cleaned and leak tested, the beam pipe sections were joined on-site to form the vacuum sector.

The rough and intermediate pumping was done by a pumping group formed by a DN250 CF crossing hosting a 2300 ls^{-1} Maglev TMP backed by a dry multistage root pump shielded by a DN250 CF Viton sealed gate valve, a 1200 ls^{-1} SIP and a dry large fore pump ($\approx$ 600 m^3 h^{-1}). An additional pumping group distribution is one every 100 m.

The pressure monitoring is done via a wide-range gauge installed on all the pumping groups.

GEO600 (122)

The GEO600 beam pipe vacuum system comprises one 600m-long sector delimited from the experimental areas (ITM and ETM) by DN600 gate valves. The sector comprises 4.5 m-long modules consisting of 0.75 m-long AISI 316L hydroformed bellows with an internal diameter of 0.6 m (wall thickness of 0.8 mm) welded together to reach the desired length.

After being cleaned, the modules were wrapped with 20 cm thick rock wool and air-baked at 200°C for 48 h (the air was dried with silica gel) via direct joule passing 600 A.

The vacuum sector was evacuated through a 500 m^3 h^{-1} roots pump installed at the centre of and then pumped down by two 1500 ls^{-1} TMP (backed by dry scroll pumps), each located at the extremities. The TMPs are installed on the sector via DN200 CF Viton sealed gate valves.

Once at $<10^{-8}$ mbar, the vacuum sector was then baked at 250°C for 5 days via direct joule effect. The UHV pumping was still carried out using the pumps mentioned before.

The pressure and gas composition are measured at three points: one at each extremity and one at the centre. All the measuring points are equipped with an IMG

Table 3.2: Resume of the 2G-GWDs beam pipe vacuum systems parameters and performance. AB: Air-Baked, VB: Vacuum Baked

Parameter	aLIGO	AdVirgo	KAGRA	GEO600
Beam pipe length [km]	2×4	2×3	2×0.8	2×0.6
Beam pipe diameter [m]	1.2	1.2	0.8	0.6
Smallest module length [m]	20	15	12.5	4.5
Module profile	Straight	Straight	Straight	Corrugated
Welding	Spiral	Longit.	Longit.	-
Module material [AISI]	304L	304L	304L	316L
Module thickness [mm]	3	4	8	0.8
Module treatment	AB	AB	VB	AB
Treatment T [°C]	455	400	200	200
Treatment t [h]	36	120	20	48
Bakeout T [°C]	160	150	-	250
Bakeout t [weeks]	3	1	-	0.7
Vacuum sectors/arm	2	1	1	1
UHV pumps	SIP	SIP+TSP	TMP+SIP	TMP
UHV distribution [m]	See text	600	100	600
Ultimate pressure [mbar]	10^{-9}	10^{-9}	10^{-8}	10^{-9}
Main residual gas	H_2	H_2	H_2O	H_2

gauge and an RGA. The extremities also feature a Pirani gauges.

3.3 ET beam pipe vacuum system

3.3.1 ET beam pipe vacuum according to ET CDR 2020

A first draft of the ET beam pipe vacuum system was presented in the 2020 ET CDR [39].

Given the nested triangular shape of ET (see Fig. 1.7), the beam pipes of two interferometers will run parallel to each other as schematised in Fig. 3.6, hosted in a tunnel with an internal diameter of 6.5 m.

The ET CDR 2020 foresees an AdVirgo-like solution: straight 1-m internal diameter beam pipes with a wall thickness of 3-4 mm, made of AISI 304L stainless steel and externally stiffened by rings every 1 or 2 m. The envisioned 20-m-long modules will have a 2 mm-thick bellow at each end to compensate for the thermal expansion during bakeout. The modules welded in 500 m long sections will be assembled to build one vacuum sector 10 km long. As per AdVirgo, two DN1000 gate valves will isolate the experimental areas and cryotraps from the beam pipe vacuum.

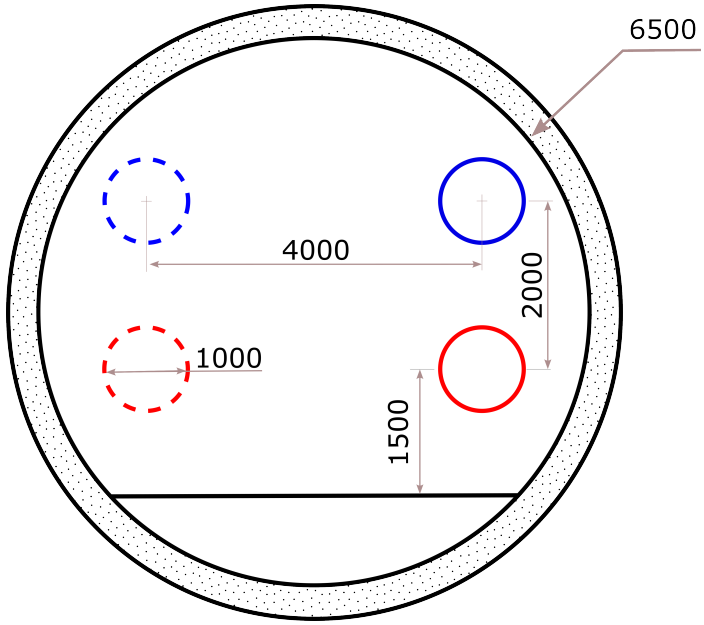

Figure 3.6: Schematic of the cross-section of the ET tunnel updated in 2023[d]. The two interferometers run parallel (blue and red). The beam pipes with the solid line represent the HF, and those with the dashed line represent the beam pipes for the LF. Dimensions in mm.

As illustrated in Fig. 1.8, ET requires a tenfold improvement in sensitivity to AdVirgo to achieve the desired science goals. According to the ET CDR 2020, this translates into a requirement on the strain sensitivity due to residual gas of $< 10^{-25}$ $1/\sqrt{\text{Hz}}$ for both ET-LF and ET-HF.

To ease the achievement of the desired strain sensitivity, the modules must be air-baked at 450°C for a week, followed by an in-situ bakeout at 150°C for 10 days to remove water. The bakeout is envisioned to be done via direct joule effect. With a 10-20 cm rock wool insulation wrapped around the tube, it is calculated that a current of 1250 A (60V DC) is sufficient to achieve 150°C. The total power for the bakeout of one beamline per arm is 2 MW (200 W/m).

According to the CDR, the pumping groups should be distributed every 500 m hosted in special recesses called "pumping rooms". Each pumping port, a DN250 CF, is foreseen to be equipped with a gate valve. The initial volume evacuation and intermediate pumping should be carried on by two 2000 ls^{-1} TMPs backed by dry pumps per pumping group. The UHV pumping, permanently installed on each pipe, should be maintained by three modules, each made by a 2500 ls^{-1} TSP (with its vessel) and a 300 ls^{-1} SIP. The combined three modules are calculated to give 5000 ls^{-1} of effective pumping speed. All the pumping groups, temporary and permanent, should be equipped with gauges for pressure monitoring for all the pumping stages. The RGAs are envisaged to be distributed at the extremities and in the middle of the 10 km pipe.

[d]Original drawing courtesy of Einstein Telescope Organization - Engineering Department.

Table 3.3: Beam pipe vacuum systems cost broken down, according to 2011 ET CDR [47]. The costs of HF and LF are adapted to the new beam pipe dimensions as per 2020 ET CDR[e] [39].

Category	Items included	Cost [%]
HF beam pipes	Installation, supports and thermal insulation	36.8
LF beam pipes	Installation, supports and thermal insulation	36.8
Pipe Factory	On-site production and air bakeout ovens	1.8
Sector (Gate) valves	Gate valves DN1000	2.8
Rough pumping	Roots and dry pumps	0.1
Intermediate pumping	TMPs, scroll pumps, gauges and valves	6.5
Baking supply	15kV - 50V	3.9
UHV pumping	TSPs, SIPs, gauges and valves	8.8
Gas monitoring	Gauges and RGAs	1.1
Controls	Hardware, software and cabling	1.3

3.3.2 Criticality of the AdVirgo approach on ET beam pipe vacuum

As can be understood from Section 3.3.1, as it was conceived in the 2020 ET CDR, the beam pipe vacuum system would have been at its core the AdVirgo system scaled to the new dimensions and adapted to meet the new requirements. What was presented was good as a first iteration step, although its realization, if analysed, raises some serious criticality.

First of all is the cost. As briefly discussed in Section 1.6, the sole beam pipe vacuum will burden the total budget for over 440 M€. If the cost of the beam pipe vacuum systems is broken down, as done in ET CDR of 2011 extrapolating AdVirgo costs, and adapted to the 2020 design[e], the leading cost voices are easily identified (see Table 3.3).

The beam pipes' construction, treatment, supporting system, and insulation have a more than 75% impact on the vacuum system budget. The second most impacting item is the pumping system.

Second, the production rate was a critical aspect not considered in scaling the AdVirgo approach. With a production rate of one 20-m module per day (considering forming, welding, cleaning, air-bakeout, and leak testing) of AdVirgo, realising the 6000 modules for ET will take more than 16 years. One mitigation strategy could be doubling the effort to speed up the production, but this dramatically increases the investment cost of tooling and production.

Third, but not less important, is the pumping system layout. As depicted in the 2020 ET CDR, the selected pumping groups will require recesses in the tunnel to host

[e]From ET CDR 2020, the HF and LF beam lines have the same internal diameter of 1 m.

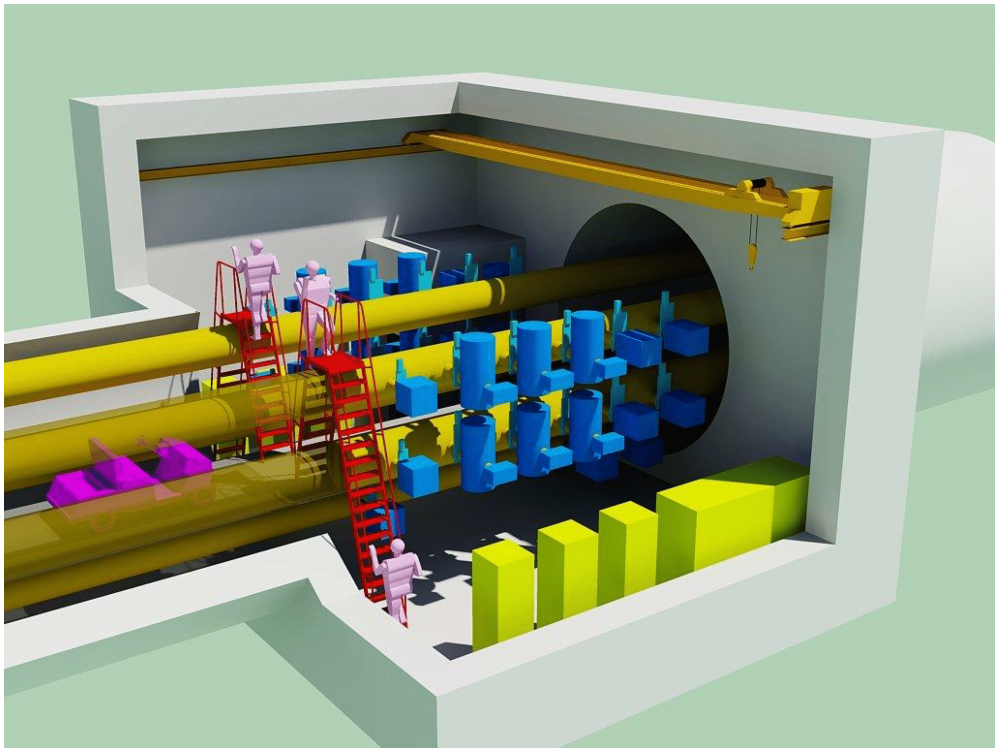

Figure 3.7: Pump rooms as per ET CDR 2020 [39]. In blue are the pumping groups; in neon yellow, the pumps control the power supplier for the bakeout.

the pumps and the high-voltage electrical transformers. This cost does not impact the beam pipe directly but has a non-negligible contribution to the civil engineering budget.

3.3.3 Possible cost reduction solutions

As introduced in Section 1.7, several cost-effective solutions were proposed for future development and studies for the 3G-GWDs. In addition to the options already discussed, the CERN team proposed two additional alternatives for the design and materials. The solutions that are more suitable for ET and considered by the CERN team are briefly introduced in the text below. The project takes the AdVirgo-like approach shown above as a baseline. The nested system discussed at the LIGO workshop was still in the conceptual phase when this thesis was written; therefore, it is not yet considered a viable solution in a short time.

BEAM PIPE DESIGN

Thick pipeline-like

The thick pipeline-like design could offer a cheaper alternative to the baseline design. Using mild steel as the raw material might allow the project to utilize an off-the-shelf solution. Additionally, the absence of stiffeners would simplify the production work-

flow. Despite the potential cost savings, its applicability for ET is not straightforward. The underground infrastructure and the arrangement of the beampipes make it difficult to handle the 1 cm thick modules. Furthermore, the thickness of these pipes would necessitate a significant amount of current for baking via the joule effect compared to the baseline design. Meeting the water outgassing requirements would mean lowering the bakeout temperature to below 150°C and increasing the duration.

There are also two other potential limitations: the joining of the modules would likely need to be done using flanged connections (similar to the KAGRA) and the UHV compatibility of the welding technology used for the pipes. Submerged Arc Welding, commonly used for large gas pipelines, is a concern in this context.

Corrugated pipe

The CERN team proposes using corrugated pipes as a cost-cutting solution. Unlike the hydroformed bellows used in GEO600, these are straight pipes mechanically deformed to produce corrugations. The corrugations can be either transverse to the module axis (circumferential) or spiral (helical). The corrugation heads/wheels can be integrated after the uncoiling process or in series with the welding station, creating a lean workflow.

This solution allows for a reduction in beam pipe wall thickness of a factor of two, therefore requiring less material and less current for the bakeout compared to the baseline design. Adopting this solution would also eliminate the need for stiffeners and bellows, as the entire structure can compensate for thermal expansions, and the corrugations act as a stiffening body.

For ET, spiral corrugations are preferred over circumferential ones because the valleys in circumferential corrugations can retain water during cleaning. With spiral corrugations, the tube can be rotated to drain the water efficiently. While this solution is very effective, it requires some effort in tooling development since no similar products are currently produced industrially.

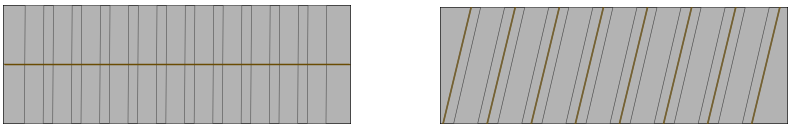

(a) Circumferential corrugations. **(b)** Helical corrugation

Figure 3.8: Schematic of a longitudinally welded pipe with circumferential corrugations (a) and a spirally welded pipe with helical corrugations (b). The brown lines represent the welding line.

MATERIALS

Mild steels

A potential alternative to AISI 304L for manufacturing the ET UHV beam pipes could be low-carbon steels [42, 51].

Commercially known as mild steel, it is widely used as a structural material due to its affordability and excellent mechanical properties. In vacuum technology, mild

steel is employed in systems operating within pressure ranges above 10^{-6} mbar [123, 124]. However, its broad adoption in a wider spectrum of applications is limited by several factors. Firstly, it is prone to corrosion [125], and its production process is primarily tailored for structural applications, often neglecting the surface finishing. Furthermore, its ferromagnetic properties pose a considerable limitation to application in particle accelerators and surface science equipment. Additionally, mild steel exhibits a significant CO outgassing rate [124] when exposed to high temperatures due to the high C content.

In the past, only a few authors have described the outgassing rate of mild steels, resulting in discouraging results compared to austenitic stainless steels. The water outgassing rates reported in the literature and textbooks often exhibit significant variability, sometimes differing by as much as three orders of magnitude [126, 127]. Furthermore, the lack of detailed information about the grade, surface conditions, cleaning procedures, or thermal treatments in these reports complicates the ability to conduct a thorough comparison. Scarce information could also be found for the hydrogen outgassing rate after bakeout. Indeed, the most complete results were reported for a C15E steel (S15C, according to JIS standard) after a bakeout at 300°C for 3 h [128], where mild steel showed values one order of magnitude higher than a 304L austenitic stainless steel baked at 150°C for 24 h [129].

Despite these discouraging results, a recent study has shown that mild steels could still be developed and applied in UHV environments [130, 131]. Indeed, using commercially available alloys, Park et al. measured a H_2 outgassing rate from mild steel that was 10 to 50 times lower than austenitic stainless steel subjected to a similar bakeout procedure (i.e., 150°C for 48 h). The same work gave a qualitative picture of the vacuum performance of low-carbon steels; however, the information is limited only to H_2 and H_2O outgassing rates.

The promising low outgassing rates of mild steel, in the same order of magnitude as an air-bake austenitic stainless steel, make it a valuable candidate as a substitute for AISI 304L. The advantages of using mild steel, in addition to those mentioned in the sections above, would be the elimination of the air baking step, simplifying the production and a raw material cost reduced by at least a factor of 3.5 ($\sim$ 1 €/kg for mild steel, $\sim$ 3.5 €/kg for AISI 304L without air bakeout [51]).

Ferritic stainless steels

Like mild steel, ferritic stainless steel could be a potential substitute for the austenitic stainless steel currently used for GWD. Characterized by a fully ferritic microstructure at room temperature, it is not commonly used in accelerators and surface science equipment due to its soft magnetic properties. The only reported study of a UHV application of ferritic stainless steel involved shielding a particle beam from an external magnetic field. Kamiya et al. report a H_2 content of 0.04 ppm weight in AISI 430, a ferritic stainless steel grade used to produce ISO flanges. This content, extracted via TPD measurements, is 12 times lower than that in AISI 316L [132]. In a related study, Kato et al. measured a H_2O outgassing rate after 100 hours of pumping for AISI 430, similar to that of AISI 304 [133]. Unfortunately, these studies did not directly

measure the H_2 outgassing rate. If these rates are found to be as low as those reported for mild steels, ferritic stainless steels will offer the same benefits as mild steel while also addressing the corrosion problems associated with low-carbon structural steels.

However, a potential drawback of ferritic stainless steel is grain growth in the Heat-Affected Zone (HAZ) of the welding line. This issue needs careful consideration, especially if the design involves a circumferentially corrugated pipe, as the loss in mechanical strength in the welding area could lead to cracking during corrugation forming. This problem might be mitigated by choosing a stabilized ferritic stainless steel grade (i.e. AISI 441, containing Ti and Nb to reduce the grain size in the HAZ during cooling).

BAKEOUT AND PUMPING SYSTEM

Low temperature bakeout

Given the size of the 3G-GWD beam pipes, the bakeout would require a significant amount of electrical power. At the 2019 LIGO workshop, a discussion was initiated to study the effect of a bakeout below 100°C, which is almost mandatory if a thick pipeline-like design is chosen. This lower-temperature solution could also be cost-effective for other thin-wall solutions. However, opting for a low-temperature bakeout would mean an increase in duration, and the efficiency of achieving the ultimate pressure post-bakeout would need to be tested.

PUMPING SYSTEM

UHV pumping with NEGs

As proposed at the 2019 LIGO workshop, the CERN team considers NEG-lumped pumps and SIPs as sources of primary UHV pumping. Compared to TSP, NEG pumps do not require a vessel to deposit the getter material, and the time before regeneration is significantly longer because the sorption capacity per regeneration cycle is several orders of magnitude higher. The installation of NEG pumps could be fully exploited if used to assist TMPs during bakeout.

II - Material & methods -

4. Experimental apparatus and methods

Operating in UHV is a question of fingerspitzengefühl.

-Ivo Wevers-

This chapter describes the experimental test benches and methods used for the UHV characterization of the selected steels in unbaked and baked conditions.

4.1 Throughput method

The outgassing rates of unbaked samples were measured using the throughput method [52, 134]. The measurement consisted of monitoring as a function of pumping time, the pressure in the test dome divided into two sides by the interposition of an orifice. The sample was placed on one side as a set of specimens inserted in a sample holder or as a connected vacuum chamber. On the other side of the orifice, a turbomolecular pumping group was connected through an all-metal right-angle valve (see Fig.4.1). The outgassing rate of the sample per unit of geometrical surface area tested is calculated as:

$$q_i = \frac{[C_i \cdot [(P_1 - P_{1,BGD}) - (P_2 - P_{2,BGD})]]}{A_{sample}} \quad \left[\frac{mbar \cdot l}{s \cdot cm^2}\right] \tag{4.1}$$

where C_i is the conductance of the orifice for the gas of interest (index 'i'); P indicates the measured pressures in the sample side, with index '1', and pump side, with index '2'. The index '*BGD*' stands for background, and it indicates the pressures recorded at

the same pumping time without the sample installed in the system. The subtraction of background pressures is required to remove the contribution of the austenitic stainless steel test dome and gauges to the total outgassing rate. The geometrical surface area of the sample is indicated as A_{sample}. During the measurements, the temperature was stabilised at 21±2°C. The orifice had a diameter of 0.8 cm, which results in C_{H_2O} = 7.4

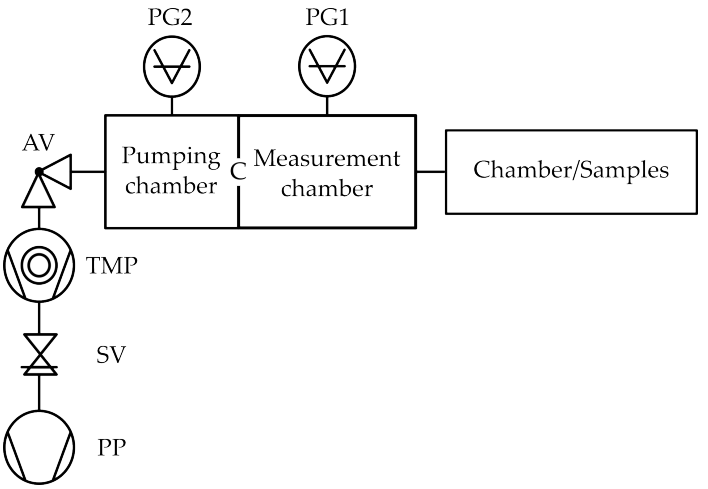

Figure 4.1: Schematic of the throughput system. TMP: turbomolecular pump; SV: electromagnetic safety valve; PP: primary pump; AV: right angle valve; C: orifice conductance; PG1 and PG2: pressure gauge 1 and 2.

ls^{-1}. The test dome had a diameter of 10 cm; it was connected to the sample holder or the sample chamber by a DN100 CF flange. The pressure measurement was performed by cold cathode gauges (Pfeiffer IKR070, estimated accuracy ±30%). The specific outgassing rate was monitored for approximately 100 h of pumping. The background measurements were repeated every time a new steel grade was tested.

4.2 Coupled accumulation-throughput method

The coupled accumulation-throughput method [52] was employed to measure the post-bakeout outgassing rate of the samples (see Fig.4.2). The all-metal measurement system consisted of a throughput system connected to the sample holder via a variable leak valve (VLV). Alternatively, the sample was the vacuum vessel to be measured connected directly to the VLV. Pumpdown, leak detection, and bakeout procedures were routinely conducted with the VLV left fully open. However, when performing an outgassing measurement, the VLV was fully closed, allowing the released gas to accumulate within the inner volume of the sample holder for a specified accumulation period. Subsequently, the VLV was gradually opened. The gas escaping from the sample holder was then detected using an RGA (Pfeiffer QMA 125) employing multiple ion detection (MID) and a BA gauge (SVT305 CERN [135], accuracy ±15%). The detection terminated when the pressure reached a reasonably stable value, and the VLV was closed for a new accumulation.

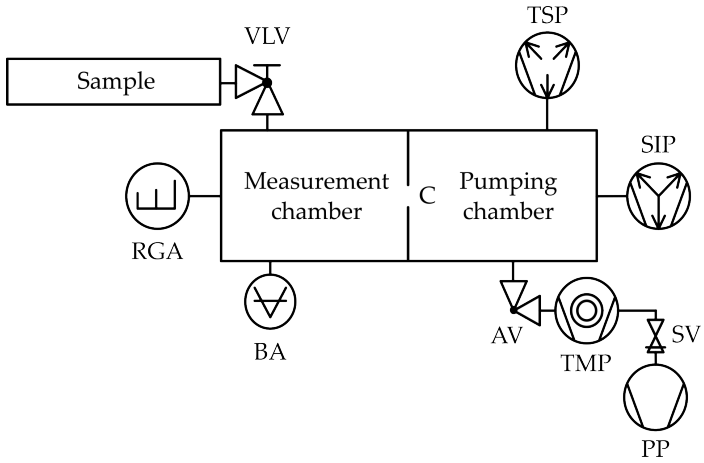

Figure 4.2: Schematic of the coupled accumulation – throughput system. TMP: turbomolecular pump; SV: electromagnetic safety valve; PP: primary pump; VLV: variable leak valve; AV: right angle valve; C: orifice conductance; BA: Bayard-Alpert gauge; SIP: sputter ion pump; TPS: Titanium Sublimation Pump; RGA: Residual Gas Analyser.

A TMP group ensured the required pumping speed during pumpdown and bakeout. To attain H_2 pressures in the low 10^{-11} mbar range, a SIP and a TSP were employed during the system operation. A 0.8 cm diameter orifice separated the pumping chamber from the measurement chamber where the RGA and BA gauge were installed. To avoid drift in the sensitivities, the RGA was regularly calibrated in situ against the BA gauge [136]. Unlike other accumulation techniques, this method provides outgassing rate values for specific gas species, assuming their partial pressure during accumulation varies linearly with time. This condition is met for gases with negligible sticking probabilities on sample holder surfaces, typically observed with hydrogen and methane. However, water vapour, prone to re-adsorption on sample surfaces, violates this linearity. H_2O molecules readsorb on the surfaces of the sample holder to attain equilibrium between accumulated gas and surface coverage. An advantage of this system is the absence of indirect gas pumping or cracking since no ion gauges are installed in the accumulation volume. Measurements are repeated for different accumulation times to confirm the measurement's linearity and increase its accuracy. The accumulated quantity of gas Q_{acc}, in the time interval t_a, is calculated using Eq.4.2.

$$Q_{acc} = S_c \cdot \int_{t_a}^{t_a+\Delta t} I_{RGA}(\tau) \times \alpha_{RGA}\, d(\tau) \quad \left[\frac{mbar \cdot l}{s}\right] \tag{4.2}$$

where Δt is the actual duration of the RGA recording, I_{RGA} is the ion current read by the RGA, α_{RGA} is the calibration factor relating current and pressure for the gas of interest, and S_C denotes the effective pumping speed at the level of the RGA. Assuming linearity, the specific outgassing rate q of the sample is computed as:

$$q_{acc} = \frac{Q_{acc} - Q_{BGD}}{A_{sample}} \quad \left[\frac{mbar \cdot l}{s \cdot cm^2}\right] \tag{4.3}$$

Q_{BGD} is the accumulated gas quantity measured without samples (background) after undergoing an identical bakeout cycle. If the sample is a vacuum vessel, Q_{BGD} accounts for the gas released from the VLV and flanges used for vessel closure. The sample's geometrical surface area was maximized to increase system sensitivity. To minimize other gas sources, all components that constitute the throughput system and sample holder were vacuum fired for 2 h at 950°C [52] prior to installation. The VLV was dismounted, and each stainless steel sub-component underwent the same vacuum firing treatment.

The sample holder was baked at 80°C and 150°C for 48 h. The throughput system and VLV underwent bakeout at temperatures ranging from 200°C to 350°C. The accumulation measurements started when the samples were at room temperature (21±2°C), 24 h after the end of the bakeout cycle.

4.3 Temperature programmed desorption system

Temperature Programmed Desorption (TPD) measurements were conducted to ascertain the diffusible hydrogen content in the selected steels. The TPD analysis was carried out using a commercial TPD workstation[137].

The system consisted of a testing chamber and a load-lock chamber, which were separated by a manual gate valve (GV). This GV maintained a UHV environment in the testing chamber, with a base pressure of approximately 1.5×10^{-9} mbar, while preserving the high vacuum conditions in the load-lock chamber, with a base pressure of about 1.5×10^{-7} mbar. This setup eliminated the need for a bakeout of the test chamber upon inserting a new sample. Cold cathode gauges were installed in both chambers to monitor pressure levels. Additionally, the testing chamber featured an RGA (Hiden 3F PIC) directly facing the sample to monitor gas evolution during measurements.

The samples, each having a surface area of 2 cm^2 and up 0.4 cm, underwent heating from 25°C to 940°C at a ramp rate of 5°C/min. To ensure measurement reproducibility, the background was re-measured after every ten samples. The accuracy of quantitative measurements was verified through regular in-situ calibration of the RGA. Hydrogen concentration calculation relied on sample weight, measured with a weight scale with a sensitivity of ±0.1 mg.

4.4 Water binding energy system

The water vapour binding energies on mild steel and ferritic stainless steel surfaces were conducted with the system depicted in Fig. 4.3. The measurements consisted of monitoring the pressure evolution as a function of the pumping time of chambers at different temperatures. The isothermal pumpdowns were then fitted with Eq. (2.17), assuming the coverage distribution follows a Temkin isotherm to extrapolate the binding energies (E_0, E_1) and the numbers of adsorption sites available in a monolayer per unit of surface (n_m).

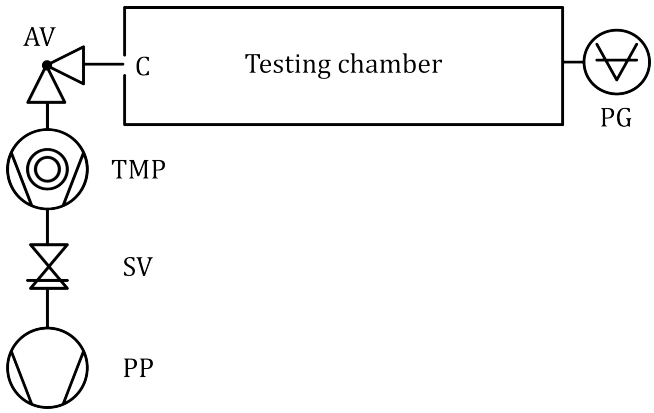

Figure 4.3: Schematic of the water binding energy system. TMP: turbomolecular pump; SV: electromagnetic safety valve; PP: primary pump; AV: right angle valve; C: orifice conductance; PG: cold cathod gauge.

The all-metal system used consisted of a simplified throughput; at one extremity of the testing chamber, a TMP group ensures the pumping during the pumpdowns; on the opposite side, a cold cathode gauge (Pfeiffer IKR070, estimated accuracy ±30%) was installed through a zero-length AISI 316LN vacuum fired flange. A 0.8 cm diameter (C_{H_2O} = 7.4 ls^{-1} at 21°C) orifice separated the testing chamber from the pumping group. The effective pumping speed for the fitting, given the position the measuring, is appropriately scaled with the conductance generated by the testing chamber and corrected for the testing temperature.

The measurement procedure foresaw a first pumpdown of the testing chamber until $P_0 \simeq 3\times10^{-5}$ mbar at room temperature; then the testing chamber was put in static vacuum (AV to pumping group close) and baked until the desired temperature following a ramp rate of 30°C/h. The AV was opened once the temperature was stable, and the testing chamber was pumped down for 10 days. At the end of the pumpdown, the entire system was baked at 120°C for 12 hours. Terminated the bakeout, the chamber was cooled to room temperature and vented to the laboratory atmosphere (21±2°C, relative humidity of about 50%) for 24 h before the next heated pumpdown was started.

4.5 Ultimate pressure system

Ultimate pressures after low-temperature bakeouts were investigated using a dedicated system. The sample, a mild steel vacuum chamber, underwent a series of consecutive bakeouts at 80°C, each lasting 48 h until the system's pressure limit was attained. The ultimate pressure at room temperature (21±2°C) was measured 24 h after the end of each bakeout, without intermediate air venting.
All the stainless-steel components of the system (see Fig.4.4) were vacuum fired at 950°C for 2 h to reduce their hydrogen outgassing rate. The sample was pumped through an orifice (C) with a diameter of 1 cm (9.2 ls^{-1} for N_2) by NEG cartridge that

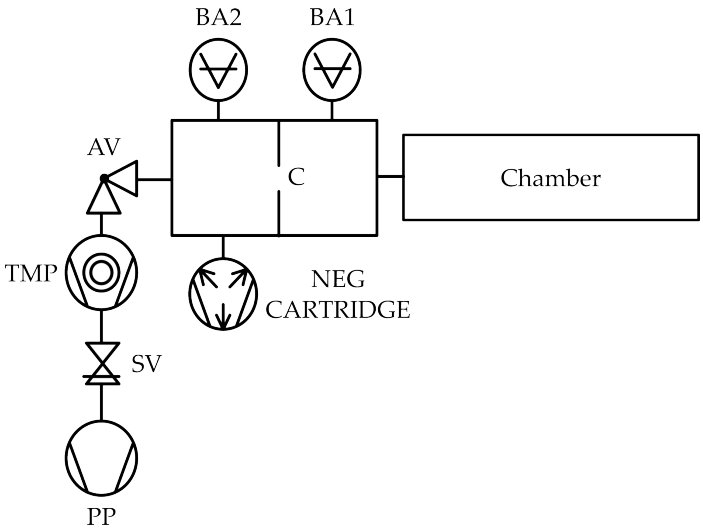

Figure 4.4: Schematic of the ultimate pressure system. TMP: turbomolecular pump; SV: electromagnetic safety valve; PP: primary pump; AV: right angle valve; C: orifice conductance; BA: Bayard-Alpert gauge; NEG: Non-evaporable Getter.

provided a 2000 ls^{-1} nominal pumping speed for H_2. A TMP group (effective pumping speed 120 ls^{-1} for N_2) was also installed to ensure pumping during bakeouts and to remove species that are not adsorbed by the NEG pump, i.e. rare gases and methane. The pressure measurements across the orifice were carried out by calibrated BA gauges (SVT305 CERN, accuracy ±15%). The sample was connected to the test system by a DN100 CF AISI 316LN vacuum fired flange welded at the extremity. During the bakeout of the sample, the rest of the system was baked at temperatures in the range of 200°C to 350°C, keeping the vacuum gauges always at the highest temperature. If the sample was not installed, the achieved pressure after bakeout in the dome where BA2 was installed was about 2×10^{-12} mbar mbar (N_2 equivalent).

4.5.1 LOLA

The original ultimate pressure system could not provide information about the gas composition or the evolution of specific outgassing rates during various bakeouts. To address these limitations, it was upgraded to a new version called LOLA (Low Outgassing Large Apparatus). The LOLA system combined the ultimate pressure system with an accumulation-throughput system (see Fig. 4.5). The pumping chamber was updated with the installation of a TMP group, a 75 ls^{-1} SIP and a NEG cartridge (2000 ls^{-1}, nominal pumping speed for H_2). The free port, left unused, was blanked with a vacuum fired flange. Despite the pumping group, the testing chamber was pumped through an orifice effectively pumped through an orifice (C) with a diameter of 1.3 cm (15.6 ls^{-1} for N_2). The pressure measurements across the orifice, while in pure throughput configuration, were carried about by calibrated BA gauges calibrated BA gauges (SVT305 CERN, accuracy ±15%).

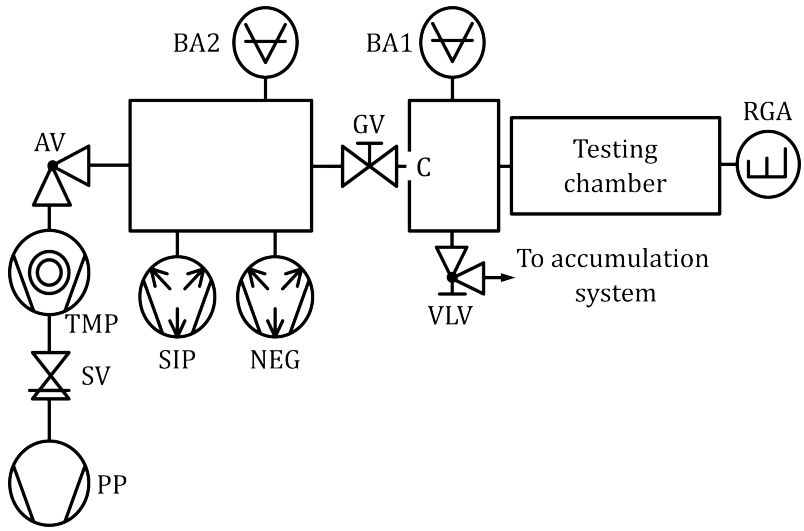

Figure 4.5: Schematic of LOLA. TMP: turbomolecular pump; SV: electromagnetic safety valve; PP: primary pump; AV: right angle valve; C: VLV: variable leak valve; orifice conductance; BA: Bayard-Alpert gauge; SIP: sputter ion pump; RGA: Residual Gas Analyser. NEG: Non-evaporable Getter.

The measurement dome was connected to the accumulation-throughput system via a VLV and to the pumping dome through an all-metal GV. Installing an RGA (Pfeiffer QMA 125) at the free extremity of the testing chamber made gas composition monitoring after each bakeout possible. The gas compositions, unless otherwise specified, were acquired with the RGA's secondary electron multiplier at 1600 V. To increase the measurement's resolution, the flanges connecting the sample — a 16-m long DN250 mild steel chamber — to the measuring system and the RGA were made in mild steel (S355J2+N, forged). To limit the H_2 outgassing rate contribution of all the non-mild steel components, all the stainless steel parts were vacuum fired at 950°C for 2 h.

Following the ultimate pressure system, the sample underwent a series of consecutive bakeouts at 80°C, each lasting 48 hours. Ultimate pressure, gas composition, and specific outgassing rates at room temperature (21±2°C) were measured 24 h, 48 h, and 72 h after each bakeout, respectively, without intermediate air venting. To achieve the lowest pressure and gas composition measurements, the RGA and BA gauges were turned off when not in use, with a 24-hour waiting period before commencing measurements. All instrumentation was turned off during accumulation mode, and the GV was closed to let the chamber accumulate.

During the bakeout of the sample, the throughput and accumulation throughput system were baked at temperatures in the range of 200°C to 350°C, keeping the BA gauges and RGA always at the highest temperature.

4.6 ET corrugated prototypes test bench

In addition to the UHV characterizations described above, three alloys from the austenitic stainless steel, mild steel, and ferritic stainless steel families were selected to produce corrugated prototypes DN400, 0.15 cm thick - 2 m long. Unlike previous tests, the ultimate pressure of the corrugated chambers after bakeout was evaluated with a pumping scheme scaled to that of a hypothetical ET section with an ad-hoc test bench (see Fig. 4.6). To reproduce the ET pressures for both intermediate and UHV pumping, the following equivalence was applied to scale the pumping speeds:

$$P_{max}\,(\mathrm{ET}^{\,\mathrm{f}}) = P_{max}\,(\text{prototype}) \tag{4.4}$$

The simulated pumping distribution scenario for the ET section included one 2000 ls^{-1} TMP every 1250 m for intermediate pumping, and a NEG and SIP able to provide 1500 ls^{-1} for H_2O and approximately 2500 ls^{-1} for H_2, distributed every 50 m for UHV pumping. Such a tight UHV pump distribution was chosen to meet laboratory-scale time to condition the system. After the scaling was applied, the orifice used to limit the pumping speed was 0.01 cm in diameter for the intermediate pumping (C2) and 1.3 cm in diameter for the UHV pumping (C1).

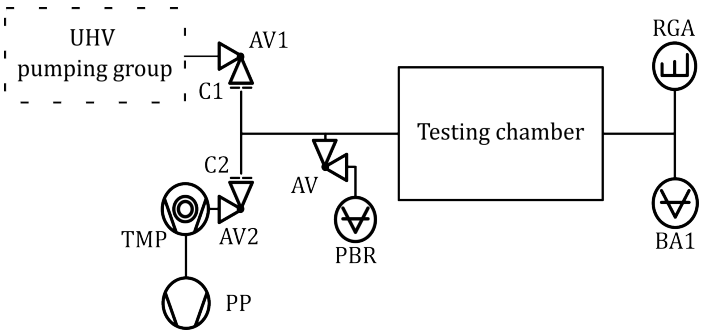

Figure 4.6: Schematic of the ET corrugated prototypes test bench. TMP: turbomolecular pump; SV: electromagnetic safety valve; PP: primary pump; AV: right angle valve; C: orifice conductance; PBR: Pirani/Bayard-Alpert gauge.

To simulate pumping conditions similar to those for ET, the two pumping groups were separated and mounted behind all-metal angle valves (AV1 and AV2). This configuration allowed the pumps to be isolated when unnecessary (e.g., the TMP after bakeout). The UHV pumping group (see Fig. 4.7) was equipped with a NEG cartridge (1000 ls^{-1} for H_2), a SIP + NEG cartridge (55 ls^{-1} + 200 ls^{-1} for H_2), a BA gauge (BA2, SVT305 CERN, accuracy ±15%), and a standard TMP group used only during the bakeout to support the activation of the NEG pumps. To ensure sufficient pumping speed behind AV1, the vessel containing the NEG cartridge and the connection to the SIP+NEG group were filled with NEG strips. After bakeout, the pressure achieved at BA2 was $<1\times10^{-12}$ mbar.

[f] between two pumping groups.

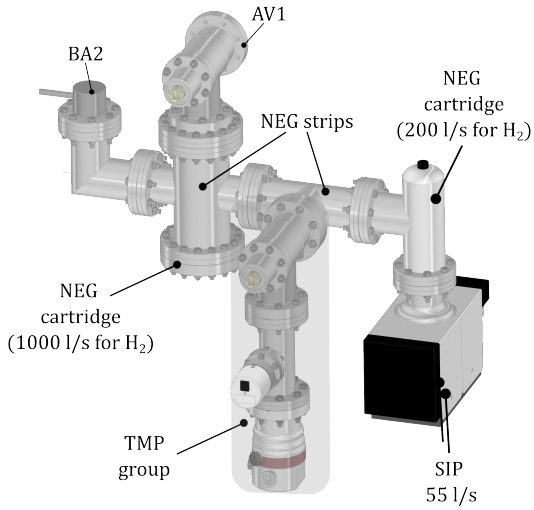

Figure 4.7: 3D model of the UHV pumping group of the test bench used to measure the corrugated chambers.

Instrumentation-wise, the pumpdown and bakeout were monitored with a Pirani/Bayard-Alpert combination gauge (Pfeiffer PBR 260, accuracy: ∼15% between 10^{-2}-10^{-8} mbar) mounted near the orifices. The ultimate gas composition and pressure were measured by an RGA (Pfeiffer QMA 125, secondary electron multiplier at 1600 V) and BA gauge (BA1, SVT305 CERN, accuracy ±10%) installed on the opposite side of the pumping groups.

During the testing chamber's bakeout, the instrumentation and fittings were baked at temperatures ranging from 200°C to 350°C. The gas composition and ultimate pressure measurements were started when the chambers were at room temperature (20±3°C) at least after 48 h the end of the bakeout cycle, respectively. To minimize the measuring systems' contribution to the ultimate pressure, all the stainless steel components except angle valves were vacuum fired at 950°C for 2 h. In addition, the DN400 closing flanges, before vacuum firing were machined to reduce their thickness to increase the hydrogen degassing efficiency of vacuum firing [78].

The ultimate vacuum of the corrugated prototype was tested following two separate conditioning and system configurations. The first configuration involved a week-long pumpdown followed by a week-long bakeout at 80°C. The second configuration included a bakeout at 150°C for 48 hours after venting the chamber. The purpose of the 150°C bakeout was to measure the ultimate pressure with a minimal background configuration, which is why the RGA was removed.

During the 80°C bakeout, an experimental use of the NEG during heating was tested. This test aimed to verify the benefit of increasing the pumping speed to shorten the bakeout duration, as proposed by SAES Getters [138].

Activating the NEG pumps during bakeout provides two benefits: first, it increases the pumping speed, which lowers the water vapour equilibrium pressure and accelerates its removal. Second, it reduces the water outgassing rate at room temperature due to the greater pumping speed for water provided by NEGs compared to other types of pumps, such as IPs, TSPs, and TMPs.

Let us assume an ET vacuum sector L meters long, pumped at the extremities by TMPs having pumping speed S (see Fig. 4.8(a)). The sector is pumped down at room temperature for 7 days and then baked for another week at 80°C and cooled down to room temperature, all while the TMPs continue pumping. The pressure at L/2, where it is at its maximum, will follow the green dashed curve depicted in Fig. 4.9.

If in the same sector, NEG pumps with pumping speed S_x, equally distributed at a distance x from the beginning of sector (see Fig. 4.8(b)), are activated during the bakeout (i.e. at 1/3 of its duration, see (Fig. 4.9)) a reduction of the equilibrium pressure will be attained. Additionally, despite stopping the activation during cooldown, the residual pressure at room temperature will be much lower than the layout with only TMPs due to the continued pumping effect of the NEG pumps.

If proven effective on the corrugated prototype, this technique will allow for a low-temperature bakeout of the beampipes without requiring months-long bakeouts to achieve low water pressures. This could potentially reduce both the cost and waiting time for vacuum conditioning.

However, the benefits of this approach should be evaluated by considering the cost, performance, and distribution of the NEG pumps to provide a fair comparison with a standard 150°C bakeout that lasts long enough to achieve the same ultimate water pressure.

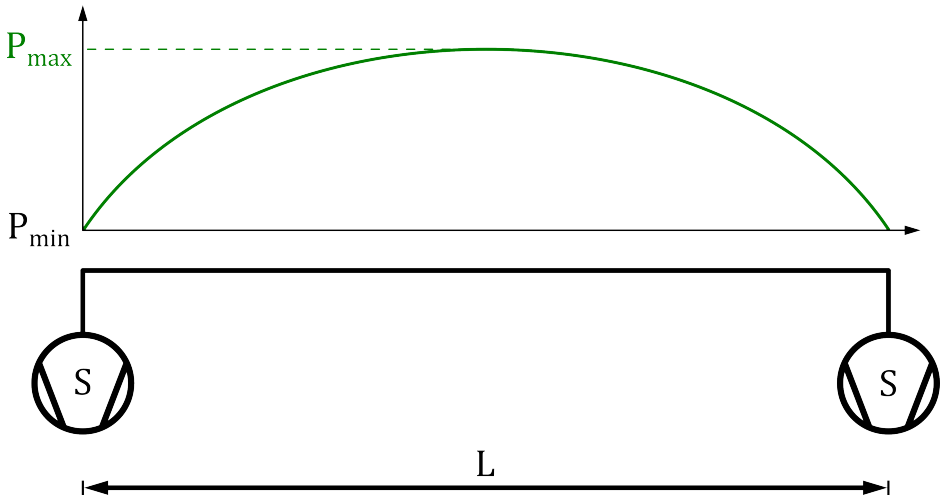

(a) Schematics of the pressure profile and pump distribution for a fictitious ET sector long L m. The pumps (TMPs) have a pumping speed of S and are positioned at the extremities of the sector.

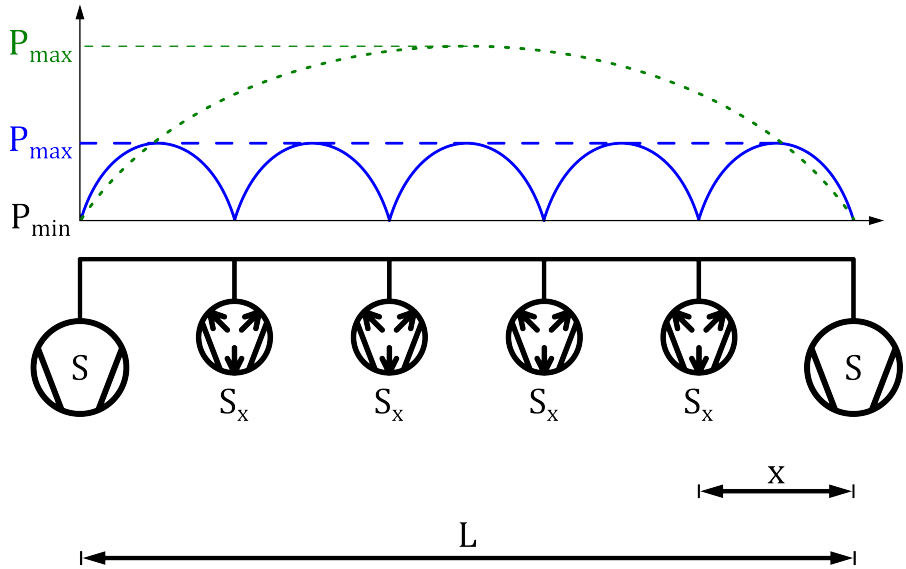

(b) Schematics of the pressure profile and pumps distribution for a fictitious ET sector long L m. The pumps have a pumping speed of S and are positioned at the extremities of the sector. Two TMPs with pumping speed S are positioned at the extremities of the sector, and several NEG pumps with pumping speed S_x are distributed equally every x meters from the beginning of the sector.

Figure 4.8: Schematics of the pressure profile and pumps distribution for a fictitious ET sector long L m, following pumpdown and bakeout cycles as per Fig. 4.9

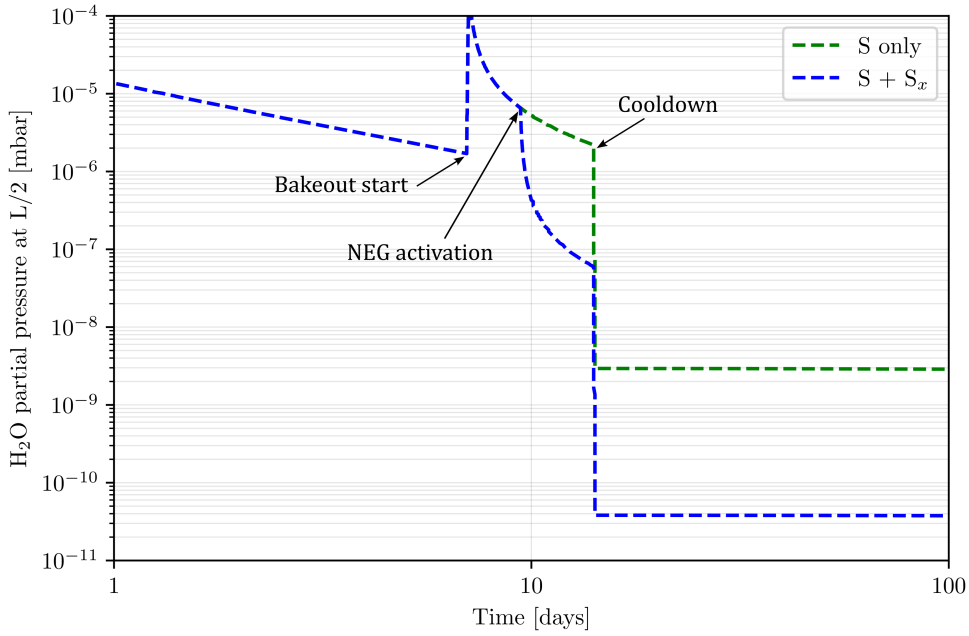

Figure 4.9: Temkin simulated pumpdown cycle at L/2 of a fictitious ET sector as depicted in Fig. 4.8. The pumpdown at room temperature is of 7 days; the bakeout is at 80°C, lasting another week. The green dashed line represents the pumpdown cycle as per Fig. 4.8(a) layout. The blue dashed line represents the pumpdown cycle as per Fig. 4.8(b) layout with the NEG pumps activated at 1/3 of the bakeout duration. The simulated room temperature is 20°C.

5. Materials and preparation

Engineering is the conscious application of science to the problem of economic production.

-Halbert Powers Gillette-

This chapter describes the alloys selected for the study and their post-manufacturing preparation for the UHV characterisation..

5.1 Materials and preparation

The mild steels and ferritic stainless steels selected for UHV characterization and their chemical compositions are summarised in Tables 5.1 and 5.2. These alloys were chosen from commercially available, off-the-shelf products to ensure representative, low-cost samples. They were compared with the baseline material, AISI 304L, both in their received condition and after vacuum firing at 950°C for 2 h. The purpose of vacuum firing AISI 304L was to evaluate outgassing rates analogous to those observed in air-baked austenitic stainless steel. To broaden the research, mild and ferritic stainless steels were brought from different suppliers in various shapes (tubes, blocks, sheets) and surface finishing.

Samples cut

Flat samples for the analysis were cut from blocks and sheets to the required dimensions using a bench shear or water jet. The decision behind the cutting methods was to avoid

Table 5.1: Chemical composition (wt.%) of the selected mild steels with the corresponding manufacturing process (MP), heat treatment (HT), and shape. AP: Acid Pickled, AR: As Rolled, CR: Cold Rolled, ERW: Electric Resistance Welded, HR: Hot Rolled, IF: Interstitial Free, N: Normalized.

	S355J+AR	S355J2+N	FB580	ULC-IF	ARMCO (grade 4)	S315MC	S355J2H	P355N
MP	HR	HR + Forged	HR	CR	CR	HR+AP	HR+ERW	HR+AP+ERW
HT	None	Normalization	None	None	None	None	None	Normalization
Shape	Block	Block	Sheet	Sheet	Sheet	Sheet	Tube	Tube
C	0.14	0.14	0.086	0.013	0.002	0.035	0.20	0.19
Mn	1.46	1.46	1.35	0.099	0.04	0.46	1.32	1.31
Si	0.20	0.20	0.045	0.005	0.003	0.039	0.17	0.16
Cu	0.06	0.06	0.009	0.008	0.008	0.19	0.08	0.13
Al	0.03	0.03	0.038	0.049	0.002	0.028	0.03	0.03
S	0.01	0.01	0.0012	0.0094	0.0018	0.0019	0.01	0.0001
P	0.01	0.01	0.0108	0.0093	0.004	0.0062	0.01	0.01
N	0.01	0.01	-	-	-	-	0.004	0.01
Cr	-	-	0.025	0.023	0.014	0.05	-	-
Ni	-	-	0.01	0.011	0.015	0.1	-	-
Ti	-	-	-	-	-	0.0018	-	-
Nb	-	-	-	-	-	0.0026	-	-
V	-	-	-	-	-	0.0037	-	-
Fe	Remainder	Remainder	Reminder	Reminder	Reminder	Remainder	Remainder	Remainder

Table 5.2: Chemical composition (wt.%) of the selected stainless steels with the corresponding manufacturing process (MP), heat treatment (HT), and shape. AISI 304L chemical composition values are to be intended as the maximum content allowed[139]. BA: Bright Annealed, CR: Cold Rolled, ERW: Electric Resistance Welded, RA: Recrystallization Annealed, SA: Solution Annealed.

	AISI 430	AISI 441	AISI 444	AISI 304L
MP	CR	CR	CR	CR
HT	BA	RA	RA	SA
Shape	Sheet	Sheet Tube (ERW)	Sheet	Sheet
C	0.041	0.015	0.011	0.03
Mn	0.39	0.385	0.3	2.0
Si	0.21	0.584	0.38	1.0
S	0.028	0.001	0.0014	-
P	0.0029	0.0029	0.0029	0.03
N	-	0.014	0.016	0.02
Cr	16.14	17.57	18.89	17-20
Ni	0.21	0.242	-	10-12.5
Mo	-	-	1.892	-
Ti	-	0.16	0.006	-
Nb	-	0.4	0.566	-
Fe	Remainder	Remainder	Reminder	Remainder

local heating of the samples and, therefore, modify the measurement output.

For specimens extracted from blocks, the external surfaces of the blocks were milled to remove the covering damaged oxide layer before final cutting.

For the S355J2H and P355N tubes, samples for TPD measurements were cut before they were turned into chambers.

Chambers preparation

The 16-m long tube measured with the LOLA system consisted of four 4-m long ϕ250 6 mm thick tubes in P355N tubes. The tubes were first cleaned and then joined together via circumferential TIG welding.

The three corrugated chambers were produced at the CERN main workshop. They were made of AISI 304L, S315MC, and AISI 441, with thicknesses ranging from 1.35 mm to 1.5 mm. Each chamber comprised three main sections, each 67.5 cm long. The sections of AISI 304L and S315MC were longitudinally welded via TIG welding, while the sections of AISI 441 were welded via laser. Laser welding was used for the ferritic stainless steel chamber to reduce the HAZ, minimize grain growth, and lower

Figure 5.1: Pictures of the corrugations steps for one AISI 304L section and final alignment for the butt welding for the final chamber production. Courtesy of Gilles Favre (CERN).

the risk of cracking due to the corrugations. The sections were then corrugated using a swagging machine (see Fig. 5.1) and welded together via TIG butt welding after being aligned. Before final welding, the corrugated sections in AISI 304L were vacuum fired at 950°C for 2 h. The final chambers were first visually inspected and finally controlled via penetrant testing, tomography and leak testing. As the ultimate step, DN400 CF AISI 316LN vacuum fired flanges were welded at the extremities.

To allow pumpdown, accumulation and ultimate pressure measurements of the tubes, DN100 CF AISI 316LN were welded at both ends and blank flanges were prepared. Before welding, the flanges were vacuum fired at 950°C for 2 hours. The part of the blank flanges exposed to the vacuum was thinned to increase the hydrogen degassing efficiency of vacuum firing [78].

Cleaning

Mild steel samples and tubes were then cleaned in solvent baths. The flat mild steel samples were first degreased through immersion in Topklean™ MC 20A, a mixture of halogen-free hydrocarbons, using ultrasonic and vertical agitation. They were then rinsed in modified alcohol baths at temperatures between 40-47°C with ultrasonic agitation and subsequently vapour rinsed. Finally, the samples were dried in a hot air convection oven at 60°C for 30 minutes before packaging.

A different approach was required for the mild steel tubes. The tubes underwent a 10-minute pre-cleaning immersion in Dowclene™ 1601, a mixture of 3-Butoxy-2-Propanol and Butoxy-1-Propanol, at 95°C. This was followed by spraying with the same cleaning agent at 95°C for 30 minutes. The tubes were then subjected to vapour rinsing with the cleaning agent at 90°C for 40 minutes. The final drying process involved placing the tubes in a hot air convection oven at 60°C for 30-50 minutes.

Instead, the austenitic and ferritic stainless steel flat samples and tubes were cleaned following the CERN UHV standard procedure[140]. This implied the use of a detergent

bath (NGL 17.40 spec. ALU III) at 45-55 °C for 15 min. with ultrasonic agitation, followed by rinsing with a raw water jet and by immersion and subsequent rinsing in demineralized water. The final drying step took place in a hot air convection oven at 60°C for 10-60 minutes before packaging.

The different cleaning methods employed for mild steels and stainless steels were necessitated by the rapid oxidation of mild steel specimens induced by the water content in detergent-based baths.

IV - Results and discussion -

6. Mild steels

Receiving money for something that was a pleasure to begin with is a little outrageous.

-Rainer Weiss-

This chapter summarises the results of the UHV characterisation of the selected mild steels. The results are discussed and compared with those of AISI 304L in as received condition for a direct comparison with a material compatible with the GWD application.

6.1 Water outgassing rate

6.1.1 Pumpdown of unbaked specimens

The measured pumpdown curves, representing the water vapor specific outgassing rate as a function of pumping time, are shown in Fig. 6.1. The specific outgassing rates recorded after 10 h of pumping are summarized in Table 6.1.
As shown in Figure 6.1, the pumpdown values of all mild steel samples are reasonably fitted by inverse power laws in which the exponents of time are around -1. This is the typical behaviour of metal surfaces as presented in Chapter 2 and interpreted by some authors [60, 141]. In terms of quantitative data, there is a significant dispersion ranging from 1.2 to 10 times higher values than AISI 304L. The lowest specific outgassing rates are reported for samples cut from blocks, while the highest ones are recorded for the S355J2H pipe. Scanning Electron Microscope (SEM) micrographs were taken for

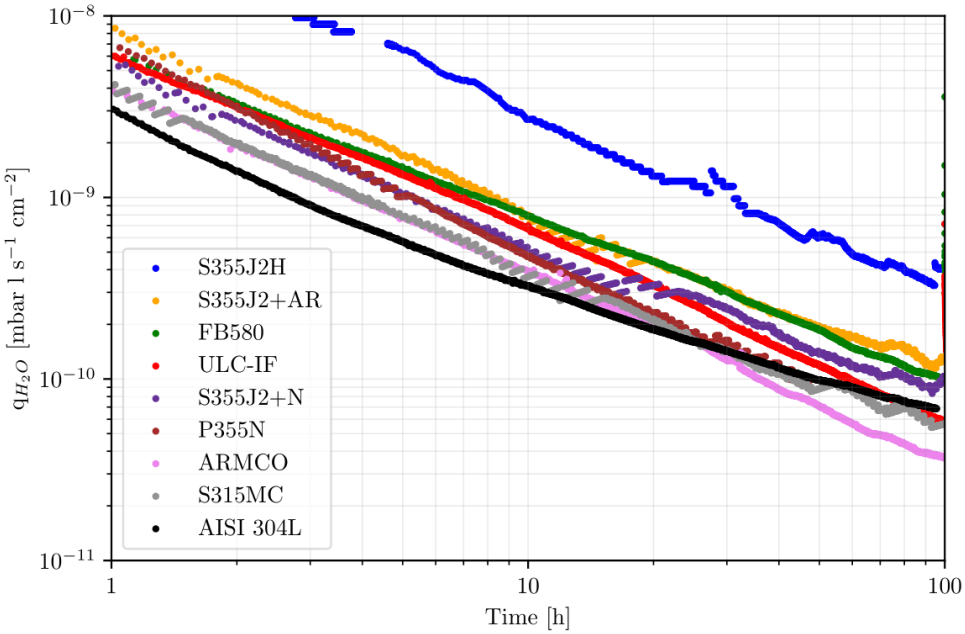

Figure 6.1: Pumpdown curves of the selected mild steels and AISI 304L at 21±2°C; the specific outgassing rate is plotted as a function of the pumping time. Background removed.

the S355J2H surface (see Fig.6.2). The S355J2H surface morphology appeared rough, characterized by cracks and small pores, and covered by particulates of a few μm size. Further, a SEM-FIB (Focused Ion Beam (FIB)) cross-section (Fig.6.3) displays a 10 μm thick oxide layer covering the S355J2H surface. The oxide exhibits significant cracks, partial detachment from the substrate, and pores that appear open to the surface, features not seen for the other mild steel samples (see Figs. A.2 to A.7 for comparison). The poor surface condition may be responsible for the high rate of water outgassing.

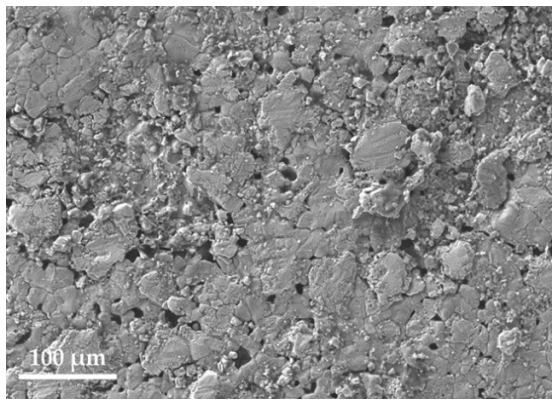

Figure 6.2: SEM micrograph of the surface of the S355J2H sample. Pores and adherent debris cover the surface.

Table 6.1: Water vapour specific outgassing rates of the selected mild steels and AISI 304L measured at 21±2°C. Background removed.

Steel	Tested samples [cm^2]	q_{10h} [mbar l s^{-1} cm^{-2}]	$q_0\, t_h^{-a}$
S355J2H	8821	2.7×10^{-9}	$2.6\times10^{-8}\, t_h^{-0.96}$
S355J2+AR	3536	8.1×10^{-10}	$8.0\times10^{-9}\, t_h^{-0.99}$
FB580	5956	7.9×10^{-10}	$6.9\times10^{-9}\, t_h^{-0.95}$
ULC-IF	6092	6.7×10^{-10}	$6.2\times10^{-9}\, t_h^{-0.97}$
S355J2+N	5780	4.9×10^{-10}	$5.1\times10^{-9}\, t_h^{-1.02}$
P355N	5938	4.7×10^{-10}	$6.8\times10^{-9}\, t_h^{-1.16}$
ARMCO	6050	3.9×10^{-10}	$4.0\times10^{-9}\, t_h^{-1.01}$
S315MC	5260	3.7×10^{-10}	$3.6\times10^{-9}\, t_h^{-0.92}$
AISI 304L	5260	3.3×10^{-10}	$1.96\times10^{-9}\, t_h^{-0.78}$

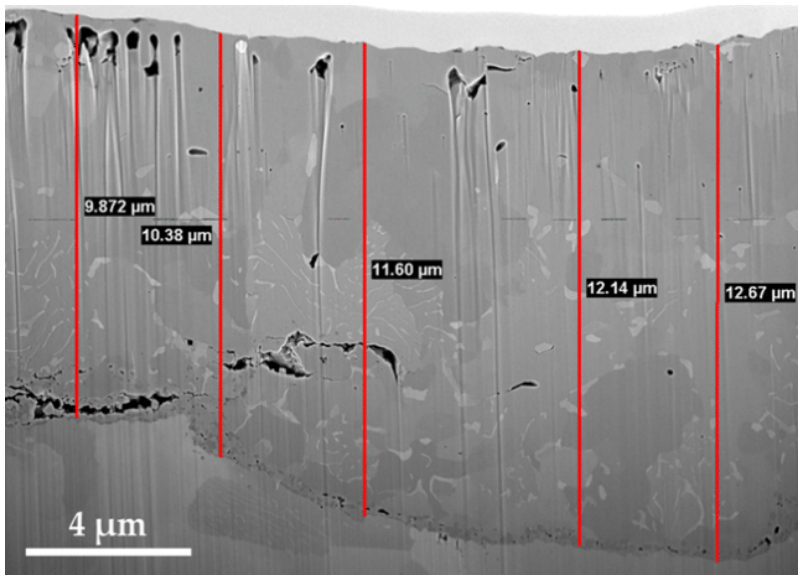

Figure 6.3: SEM-FIB cross-section micrograph of the S355J2H surface. The thickness of the oxide layer is highlighted by bars in five different positions.

6.1.2 Water vapour binding energies

The binding energy measurements were performed on a P355N vacuum chamber (6.3 cm inner diameter, 320 cm long, 6333 cm^2 internal surface area). The chamber was pumped down at 50°C, 100°C and 150°C for over 100 h following the procedure described in Section 6.1.2. The results obtained fitted with a Temkin isotherm (see Eq. (2.24)) and corrected to the pumping speed at the gauge position are reported in Fig. 6.4.

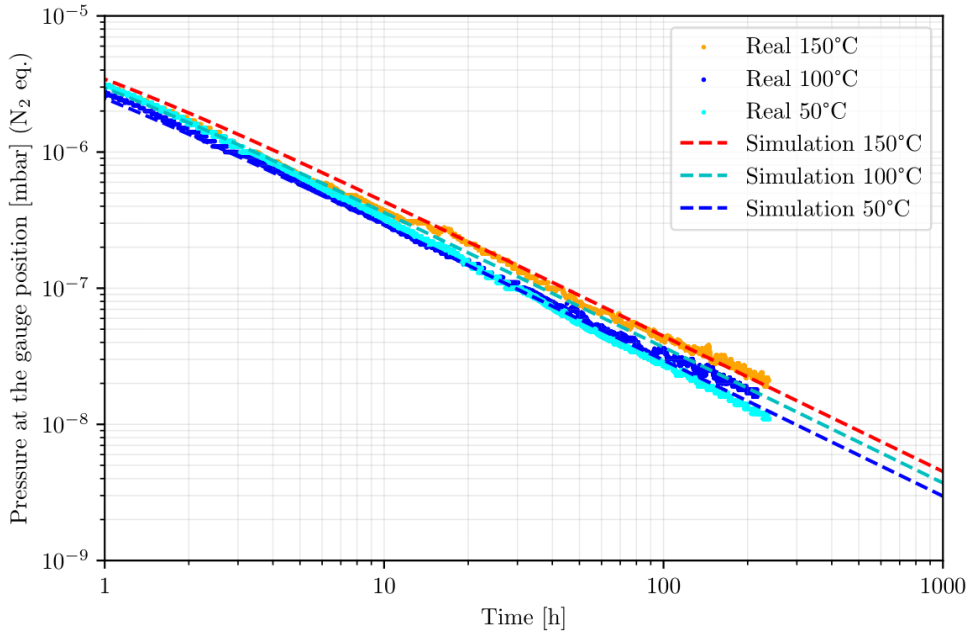

Figure 6.4: Pumpdown curves at 50°C, 100°C and 150°C of the P355N chamber measured with the binding energy system and their respective simulation using the Temkin isotherm (dashed lines). The system parameters used for the simulation are: $n_m = 9.8 \times 10^{15}$ molecules/cm^2, $E_0 = 1.5$ eV, $E_1 = 0.3$ eV, $\tau_0 = 10^{13}$ s, $s_0 = 1$, $P_0 = 1 \times 10^{-5}$ mbar, $A = 6333$ cm^2, $V = 9.97$ l.

The fitting parameters extracted with the modelling, after taking into account the gauge contribution to the effective pumping speed [g], are: $E_0 = 1.5$ eV, $E_1 = 0.3$ eV and $n_m = 9.8 \times 10^{15}$ molecules cm^{-2}. The parameters extracted were then used to simulate the pumpdown curves of the same chamber for 60°C, 48 h and 80°C and 48 h bakeouts.

The comparison between the simulated and experimental curves during bakeouts shows an overall good superposition and prediction of the ultimate pressure, as can be seen from Figs. 6.5 and 6.6.

[g]For the inverted magnetron gauge used, it is assumed a contribution to the pumping speed of 1 ls^{-1}.

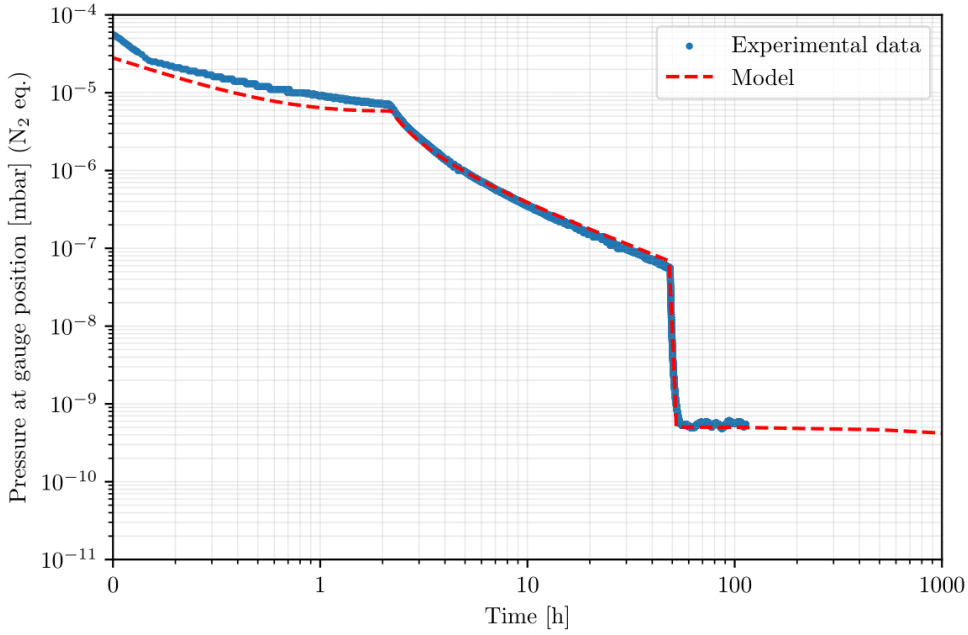

Figure 6.5: Comparison between experimental data and simulated (dashed line) bakeout at 60°C, 48h. The system parameters used for the simulation are: $n_m = 9.8 \times 10^{15}$ molecules/cm^2, $E_0 = 1.5$ eV, $E_1 = 0.3$ eV, $\tau_0 = 10^{13}$ s, $s_0 = 1$, $P_0 = 1 \times 10^{-5}$ mbar, $A = 6333$ cm^2, $V = 9.97$ l.

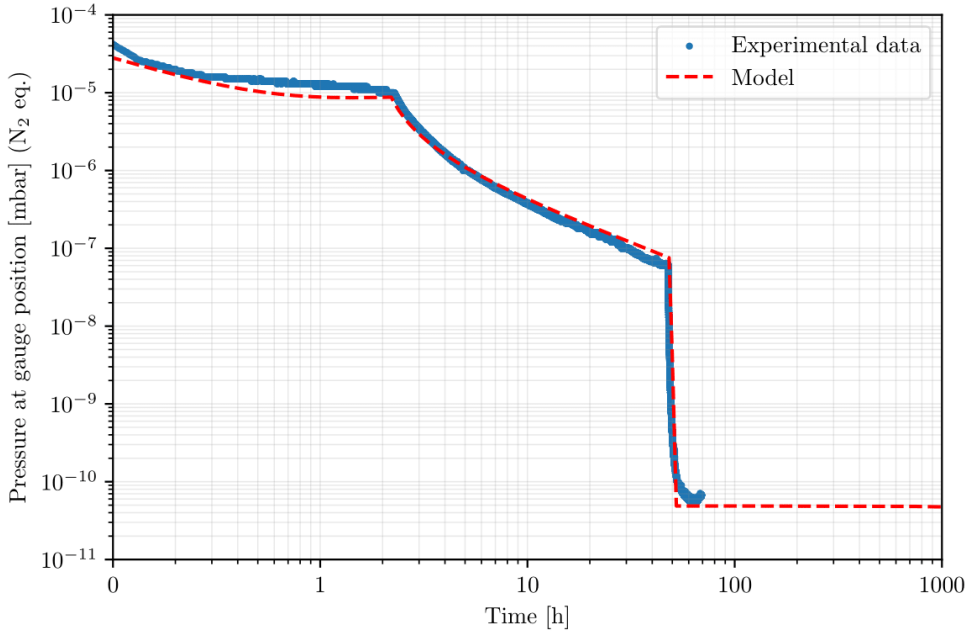

Figure 6.6: Comparison between experimental data and simulated (dashed line) bakeout at 80°C, 48h. The system parameters used for the simulation are: $n_m = 9.8 \times 10^{15}$ molecules/cm^2, $E_0 = 1.5$ eV, $E_1 = 0.3$ eV, $\tau_0 = 10^{13}$ s, $s_0 = 1$, $P_0 = 1 \times 10^{-5}$ mbar, $A = 6333$ cm^2, $V = 9.97$ l.

6.2 H_2 content and TPD profiles

The H_2 thermal desorption profiles, with the background signal removed, are shown in Figs. 6.7, 6.8 and 6.9(a). As the thicknesses of the mild steel samples were not the same, the H_2 desorption signals are represented normalised to the sample's weight. This choice can be argued. However, it is justified by the results reported hereafter. All raw data were smoothed for better visualization through a Savitzky-Golay filter [142] implemented in Python.

The signal obtained with AISI 304L samples can be fitted by a Fickian diffusion model that matches the broad peak with a maximum at 615°C (see Fig. 6.7). The obtained diffusion energy is 0.52±0.06 eV, i.e. a typical value for austenitic stainless steels [54, 143, 144]. Among the flat mild steel samples (see Fig. 6.8), we can identify

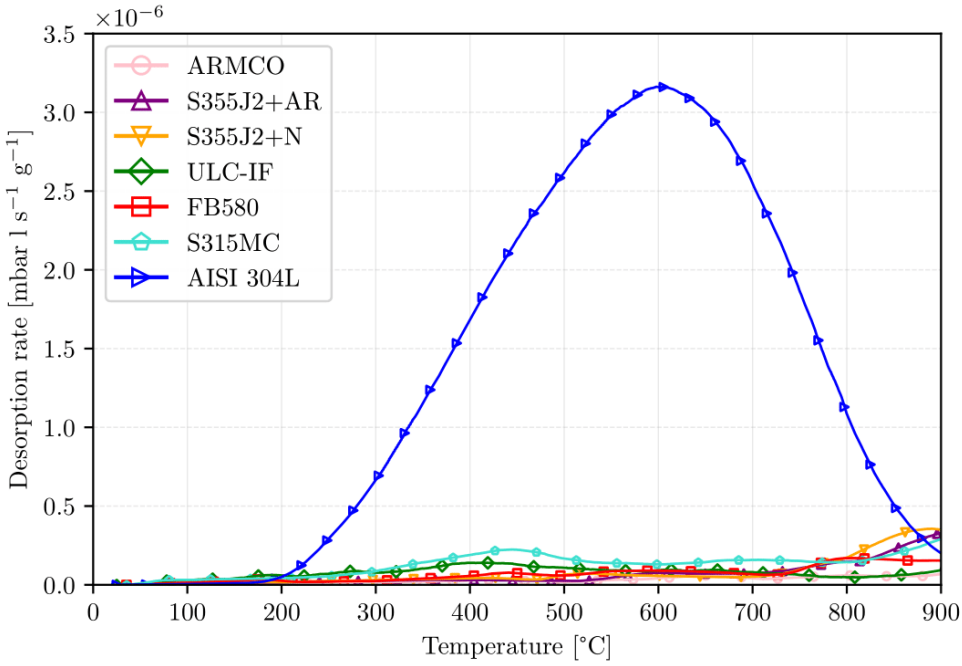

Figure 6.7: H_2 thermal desorption profiles of AISI 304L and flat mild steel samples. The background signal of the TPD system is removed.

a common peak/shoulder around 400–450°C. For the S355J2+AR, S355J2+N, ULC-IF, and FB580 samples, an additional concomitant peak/shoulder is observed between 520°C and 580°C. The S315MC shows the same trend as the previous samples but shifted to higher temperatures. The common presence of a shoulder for the signals of S355J2+AR, S355J2+N, S315MC, and FB580 is shown again around 780°C. Very distinctive and different from the flat samples and from the P355N samples, the latter characterised by a small peak around 270°C and a relatively flat profile, is the H_2 desorption profile of the S355J2H samples (see Fig. 6.9(a)). The desorption signal shows two small shoulders at 270°C and 380°C and a prominent and narrow peak at

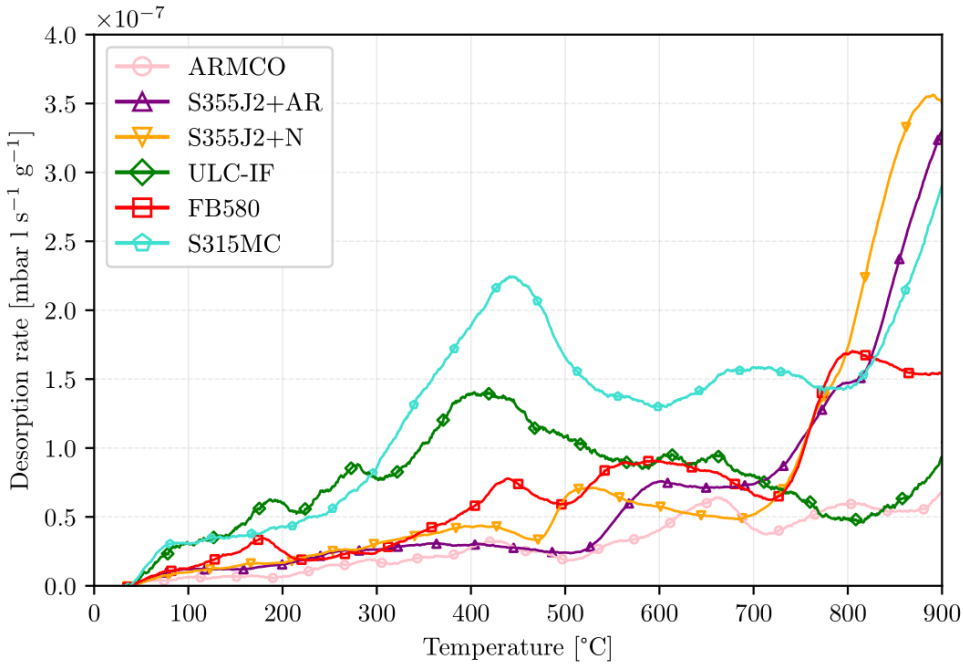

Figure 6.8: H_2 thermal desorption profiles of flat mild steel samples (vertical scale reduced x10 with respect to Fig. 6.7). The background signal of the TPD system is removed.

530°C. Contrary to all the other types of samples, the signal after the peak starts a descending slope around 740°C before ramping up again at 780°C. To identify the origin of the high peak at 530°C, samples of S355J2H taken from the same delivery batch were immersed in an HCl solution for 2 min to remove the thick oxide layer. Once etched, the samples show a significantly lower desorption signal (Fig. 6.9(b)). The desorption profile is characterized by a sharp peak at 170°C and a wide peak/shoulder at around 500°C.

The H_2 concentration in the measured samples is calculated by integrating the TPD signal up to 850°C and assuming uniform initial distribution in the volume of the samples. The results of the calculation are reported in Table 6.2. The selection of the integration range is arbitrary, justified by the observation that hydrogen released at temperatures above 850°C is tightly bound, rendering it non-diffusible within the temperature range relevant to GWD. As shown in Fig. 6.9(b), a significant quantity of hydrogen can be attributed to the oxide layer. Consequently, the calculated bulk concentrations have to be considered upper limits. The calculated hydrogen concentration in AISI 304L samples is 9.6 to 75 times higher than that evaluated for mild steel samples, the latter showing H contents always below 8 atomic ppm. As expected from their body-centred cubic structure (BCC), the mild steel samples have a much lower hydrogen concentration than AISI 304L, which is face-centred cubic austenite.

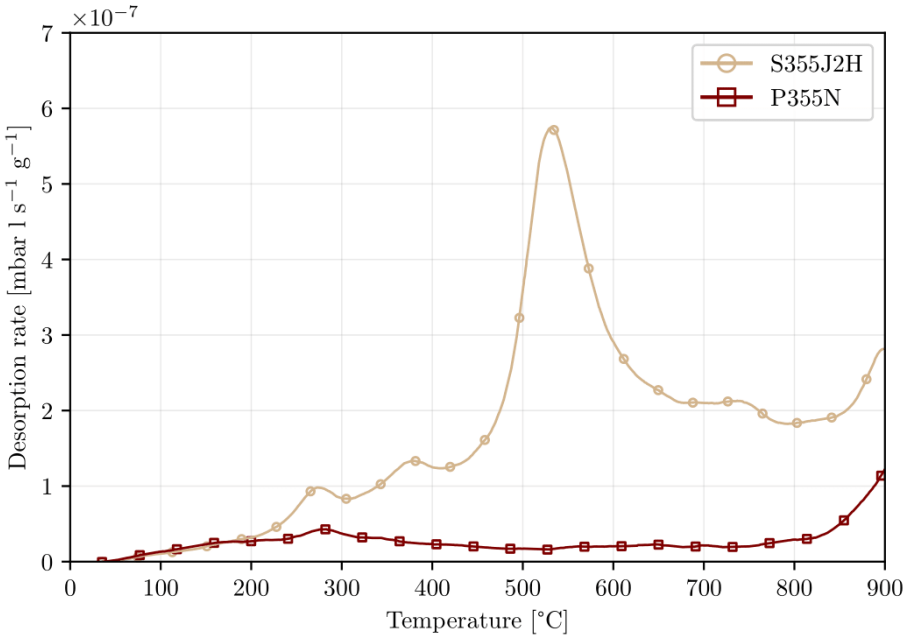

(a) H_2 thermal desorption profiles of mild steel samples from tubes. The background signal of the TPD system is removed.

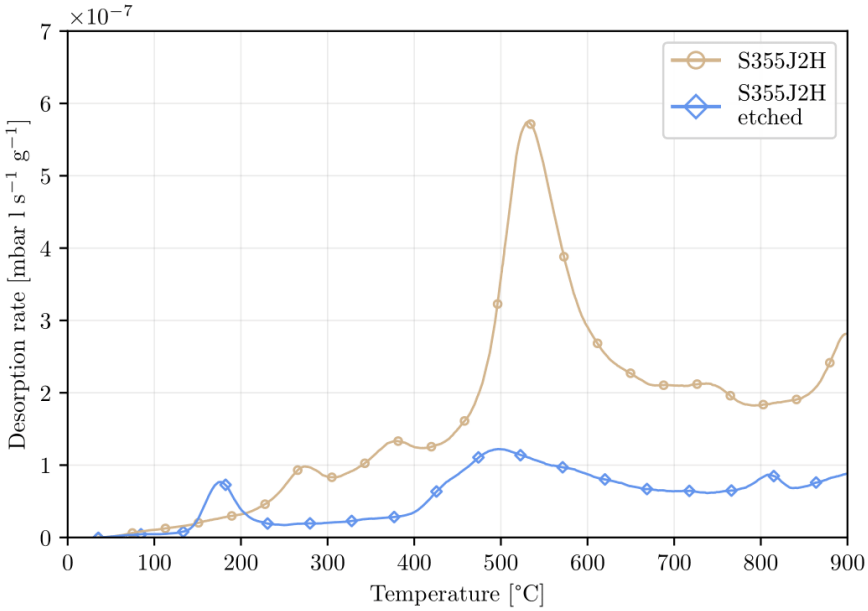

(b) H_2 thermal desorption profiles of S355J2H as received and after etching in a HCl solution. The background signal of the TPD system is removed.

Figure 6.9: H_2 desorption profiles of the selected mild steel tubes.

Table 6.2: Mild steels and AISI 304L hydrogen concentration obtained by integrating the TPD signals up to 850°C. The values reported are the average of at least three samples from the same batch. The background of the TPD system is removed. To convert atomic ppm to weight ppm, divide by 55.85 (molecular weight of iron).

Steel	H content [ppm at.]	Thickness [cm]
AISI 304 (as received)	75	0.3
S355J2H	7.8	0.4
S315MC	6.1	1.35
ULC-IF	3.7	0.69
FB580	2.8	2.1
S355J2H etched	2.7	0.4
S355J2+AR	2.0	0.3
S355J2+N	1.6	0.3
ARMCO	1.2	0.2
P355N	1.0	0.35

The different thicknesses and geometries of the tested samples do not allow a direct one-to-one comparison between the samples of mild steel; however, some general observations can be drawn. Given the shape of the peaks of the H_2 desorption profiles of the mild steels, it appears that they are primarily influenced by the de-trapping of hydrogen from grain boundaries, lattice defects, carbides, and precipitates rather than Fickian bulk diffusion typical of the austenitic microstructure [86, 145, 146].

Moreover, the shapes and intensities of the H_2 peaks are significantly influenced by the presence of thick iron oxides and hydroxides covering the samples. As can be seen from the etching of the S355J2H samples, hydrogen trapped in the oxide layers accounted for almost two-thirds of the total quantity of released hydrogen.

To further support the de-trapping desorption rather than bulk diffusion, S315MC and AISI 304L samples were analysed in two thicknesses, 0.15 cm and 0.3 cm. The results, reported in Figs. 6.10 and 6.11, show the peak position and intensity for the S315MC invariant to the thickness. On the contrary, the AISI 304L samples follow the Fickian desorption profile dependent on the thickness, which can be easily fitted with Eq. (2.49) using the binding energy presented above. An interesting feature observed for the S315MC samples is the appearance of the H_2 peak just after the last desorption shoulder of H_2O.

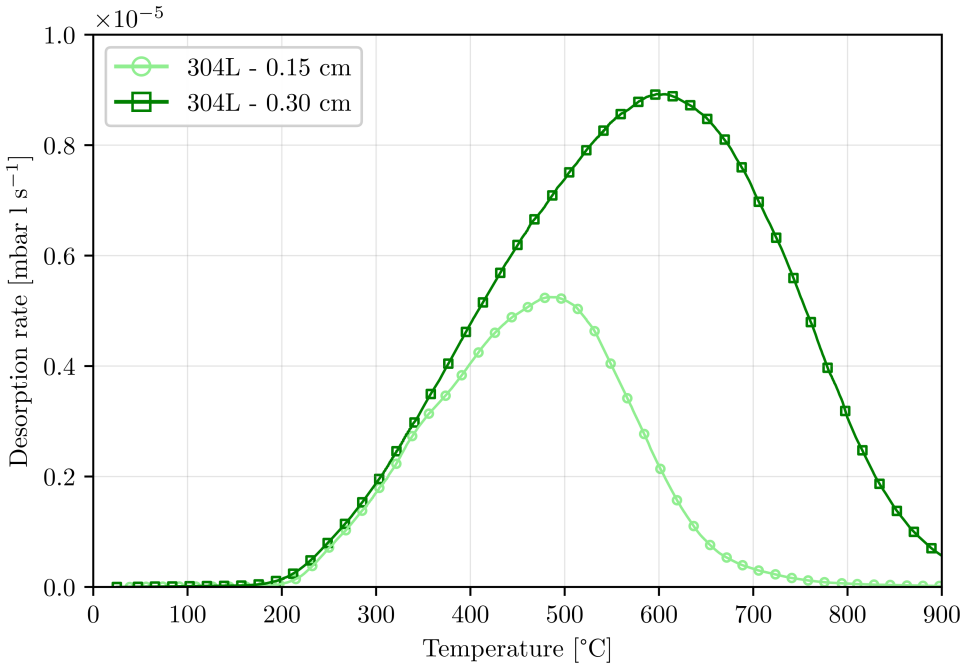

Figure 6.10: H_2 thermal desorption profiles of AISI 304L 0.15 cm and 0.3 cm thick samples. The background signal of the TPD system is removed.

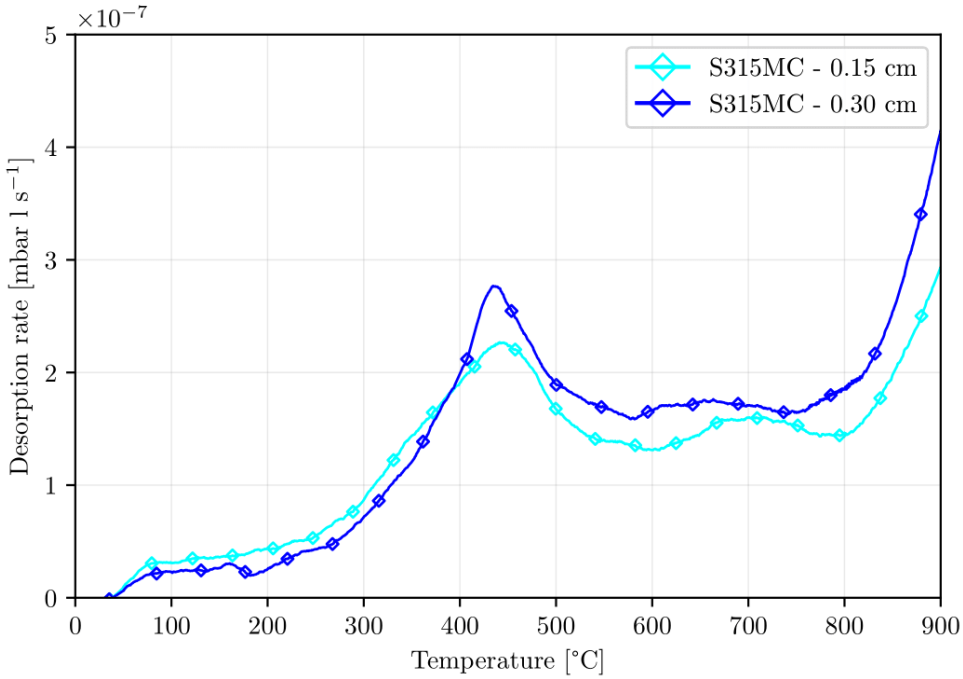

Figure 6.11: H_2 thermal desorption profiles of S315MC 0.15 cm and 0.30 cm thick samples. The background signal of the TPD system is removed.

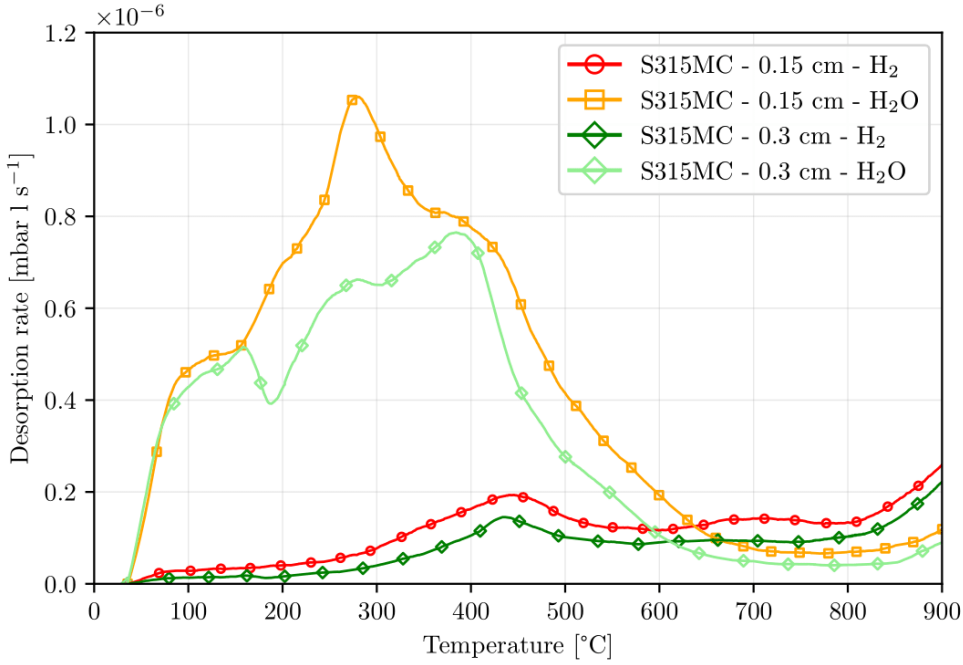

Figure 6.12: H_2 and H_2O thermal desorption profiles of S315MC 0.15 cm and 0.30 cm thick samples.

Furthermore, as depicted in Fig. 6.13 and Fig. 6.14, when heating the S355J2+N and S355J2+AR samples within the temperature range of 100°C to 450°C, a correlation becomes apparent between the peaks or shoulders of H_2 and those of CH_4, H_2O, CO, and CO_2. In this temperature range, water vapour is the leading gas; this result aligns with XPS measurements reported by the author [147] that indicate significant dehydration and dehydroxylation already taking place during a steady state at 80°C. Additionally, an intriguing overlap of peaks or shoulders of H_2, CO, and CO_2 is observed between temperatures of 500°C and 590°C. This latter temperature range coincides with the onset of Wustite (FeO) formation through the reduction of Hematite (Fe_2O_3) and Magnetite (Fe_3O_4)[148]. The shoulders observed between 700°C and 800°C in the hydrogen desorption profiles may potentially correspond to phase transformations within the steel samples, specifically from α-Fe + Fe_3C to α-Fe + γ-Fe. Similarly, the steeper shoulders observed between 800°C and 900°C could be attributed to a phase transformation from α-Fe + γ-Fe to γ-Fe [149]. The simultaneous increase in CO desorption further supports these observations.

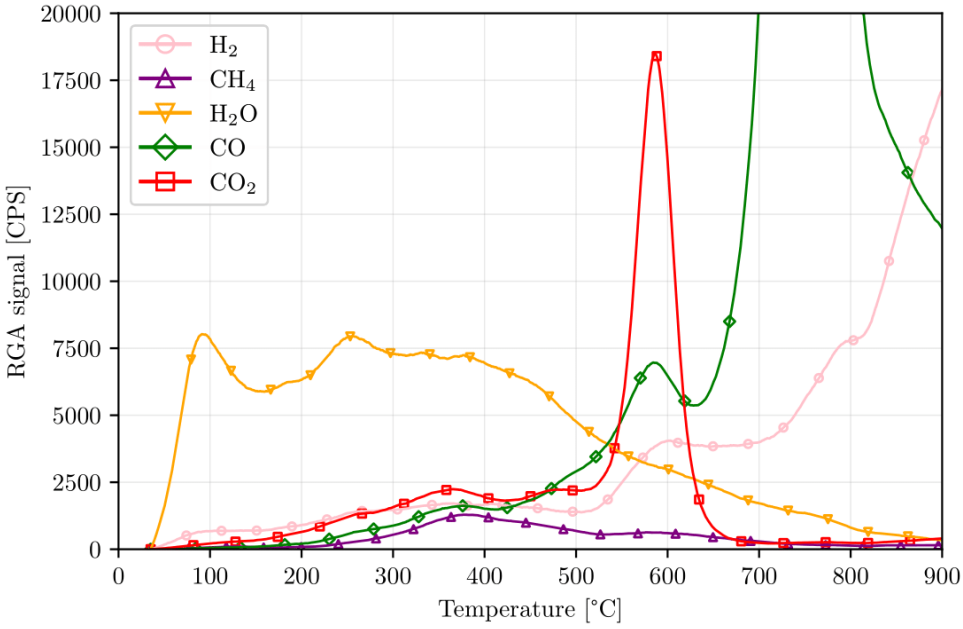

Figure 6.13: Thermal desorption profiles of a S355J2+AR sample. The background signal of the TPD system is removed.

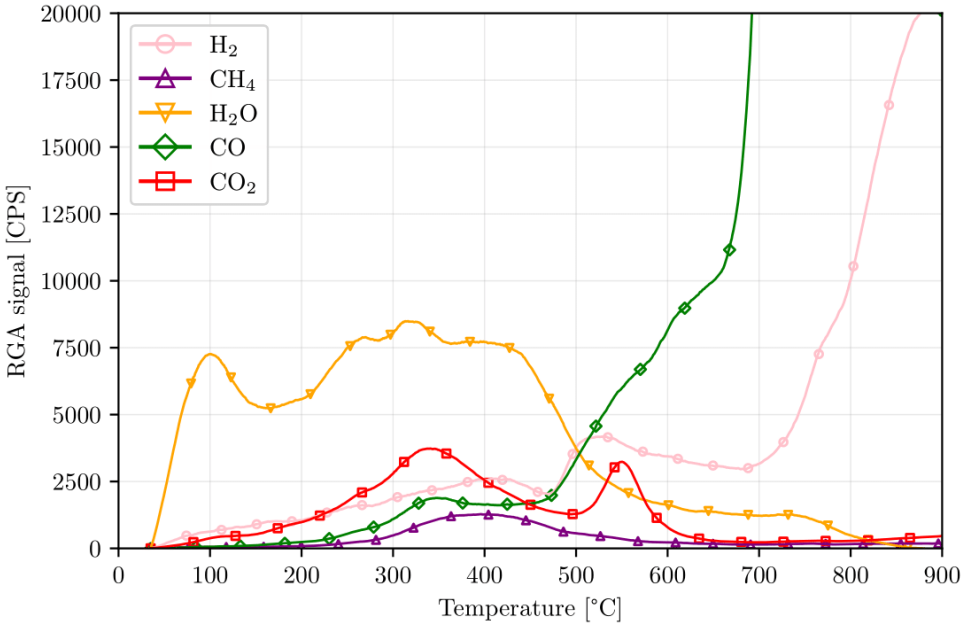

Figure 6.14: Thermal desorption profiles of a S355J2+N sample. The background signal of the TPD system is removed.

6.3 Outgassing rates of baked samples

6.3.1 H_2,CH_4,CO and CO_2 outgassing rates

The specific outgassing rates for H_2, CH_4, CO, and CO_2 are depicted in Figs. 6.15 and 6.16(a) to 6.16(c)) and reported in Table A.1 and Table A.2. The values were calculated with Eq. (4.3) from data obtained by accumulation according to the procedure described in Section 4.2. Measurements were taken for different accumulation times to verify the pressure linearity during accumulation.

After an 80°C, 48 h long bakeout, the measurements reveal H_2 as the leading gas, with the highest outgassing value equal to 7.0×10^{-14} mbar l s^{-1} cm^{-2} (see Fig. 6.15). The value measured for the P355N tube, despite being about one order of magnitude greater than the highest measured for the flat samples, is a factor of ten lower than what was measured for the AISI 304L. For the S315MC, the H_2 outgassing rate fell below the detection limit, defined as 50% of the background value.

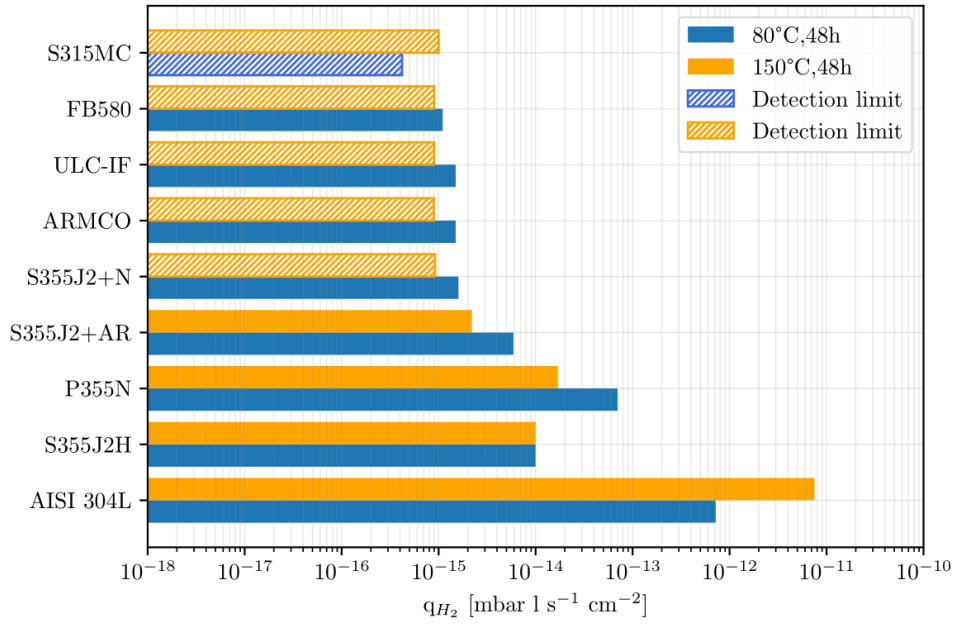

Figure 6.15: Comparison of H_2 specific outgassing rates reported in Tables A.1 and A.2. The system sensitivity (see definition in the text) normalised to the sample surface area is plotted as dashed columns when the measured values are below such a limit. The S355J2H outgassing data after 80°C,48h bakeout is taken from previous work from the author using the same accumulation system [150].

The measured specific outgassing rates of CH_4 and CO, ranging from 3.6×10^{-15} mbar l s^{-1} cm^{-2} and 2.3×10^{-17} mbar l s^{-1} cm^{-2}, are generally lower than those of the AISI 304L, with only a few instances showing similar values. In contrast, the specific outgassing rates of CO_2 were, especially those from the flat samples (see Fig. 6.16(c)), up to a factor of 3 higher than those of AISI 304L.

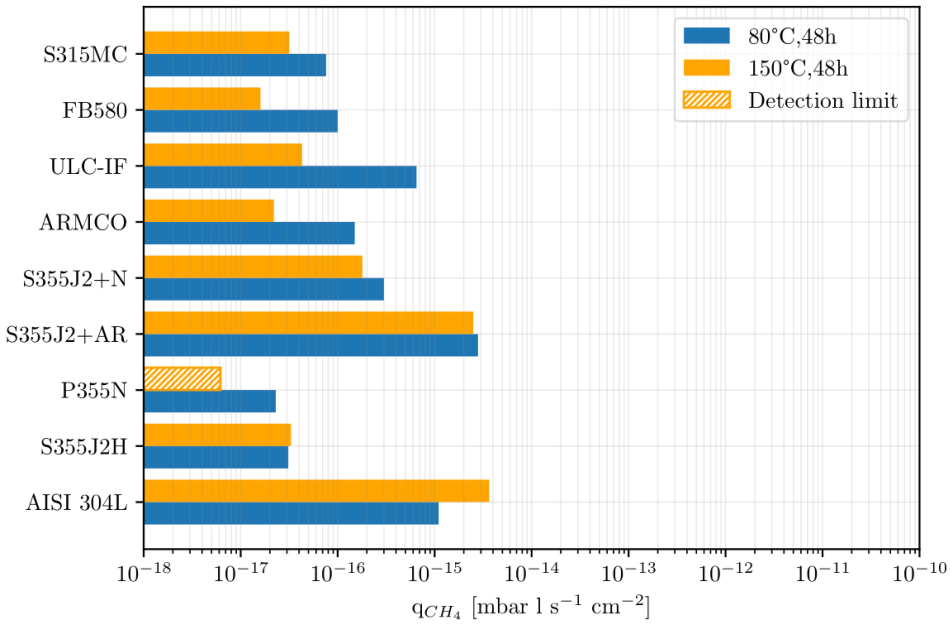

(a) CH_4 specific outgassing rates.

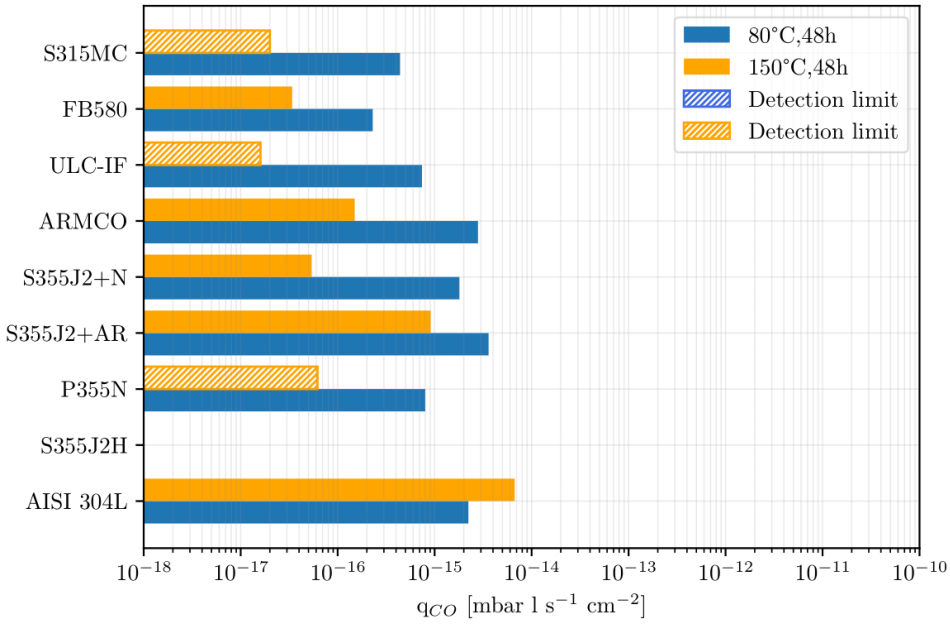

(b) CO specific outgassing rates.

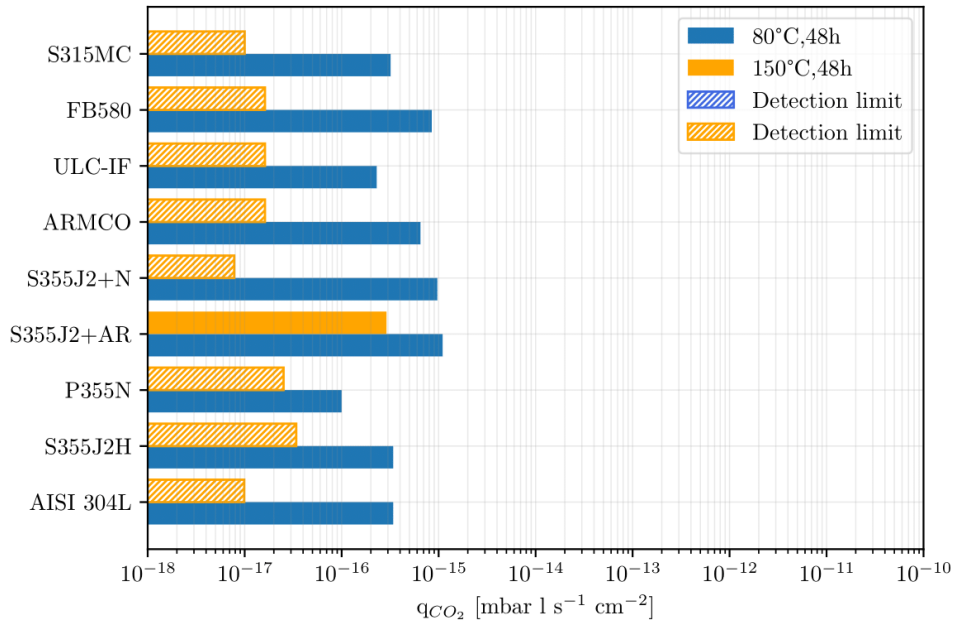

(c) CO_2 specific outgassing rates.

Figure 6.16: Comparison of CH_4, CO and CO_2 specific outgassing rates reported in Table A.1 and Table A.2. The system sensitivity (see definition in the text) normalised to the sample surface area is plotted as an orange-dashed column when the measured values are below such a limit. The S355J2H outgassing data after 80°C,48h bakeout is taken from previous work from the author using the same accumulation system [150].

The following bakeout at 150°C for 48 hours yielded striking results. While the H_2 specific outgassing rate of the S355J2H tube remained constant at 1×10^{-14} mbar l s^{-1} cm^{-2}, the S355J2+AR and P355N samples exhibited reductions by factors of 2.5 and 4, respectively. Interestingly, the AISI 304L showed an inverse trend compared to what was observed for the mild steels, increasing by one order of magnitude the outgassing rate passing from 80°C to 150°C. Additionally, for all other tested alloys, the total H_2 outgassing rate fell below the detection limit of the accumulation system. Similarly, CO and CO_2 show an important outgassing rate reduction. CH_4 outgassing rates showed little to no decrease for most of the steel grades when the bakeout temperature was increased from 80°C to 150°C.

Compared to the AISI 304L, baked for the same time and temperature, the mild steel samples show from two to four orders of magnitude lower H_2 specific outgassing rates, therefore attaining values measured for a few mm thick AISI 304L after vacuum firing (950°C, 2 h) [52] or air bakeout (390°C, 100 h) [85]. The hydrogen concentration ratios and the ratios of specific hydrogen outgassing rates in mild steels compared to austenitic steels don't align quantitatively. This mismatch might be because hydrogen in mild steel is mainly trapped within the material's bulk and surface oxide, thus not

participating in the diffusion process that causes outgassing at room temperature.

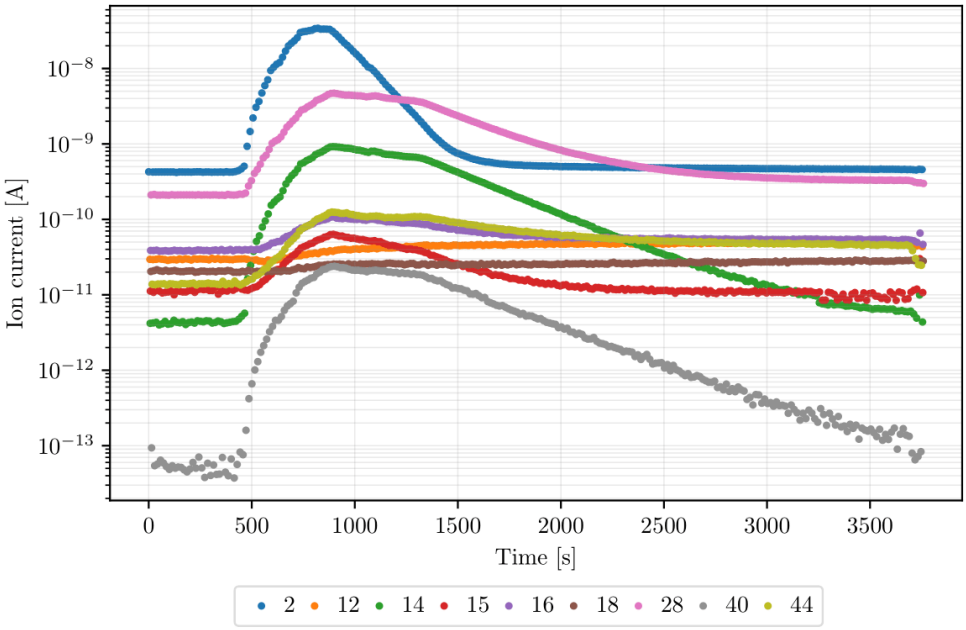

Figure 6.17: RGA scan of the accumulated gas for a S355J2H tube after 80°C, 48 h bakeout, showing the presence of N^+ (mass-14), N_2/CO (mass-28) and Ar(mass-40). Figure adapted from [150].

The CO specific outgassing rate of the S355J2H tube could not be accurately determined due to a significant virtual leak originating from the sample itself [150]. Fig. 6.17 illustrates that during the RGA measurement of accumulated gas, the increase in mass-28 signal correlates with rises in mass-14 and mass-40 signals, typical for N_2 and Ar. The mass-12 signal (C) could not be reliably used for calculating the CO contribution, as it may stem from fragmentation patterns of other gases like CH_4 and CO_2. Despite extensive leak detection efforts, no external leaks were found in the vacuum chamber or measuring system. The presence of virtual leaks suggests surface deterioration. Fig. 6.3 indicates porosities and cracks in the oxide layer likely responsible for an air in-leakage.

6.3.2 Ultimate pressure after low-temperature bakeout

The ultimate pressure measurements were performed on a P355N vacuum chamber (6.3 cm inner diameter, 320 cm long, 6333 cm^2 internal surface area). The results, with the background signal removed (equal to 1.5×10^{-11} mbar N_2 eq.) and expressed in N_2 equivalent, are reported in Fig. 6.18.

The P355N chamber was subjected to a series of consecutive heating steps at 80°C, each lasting 48 h, until the measured values were not too close to the background one and thus not allowing the calculation of a significant value. The chamber, as can be seen in Fig. 6.18, consistently exhibited a halving of the total pressure between each heating step. Based on the results of the initial cycle, it was decided to vent the P355N chamber to laboratory atmosphere conditions (temperature: 21±2°C, relative humidity of about 50%) for 24 h and proceed with a second cycle of bakeouts to observe if the same pressure reduction trend persisted.

As depicted in Fig. 6.18, following the initial heating step of the second cycle, the pressure was 2.4 times lower compared to that of the first cycle. The pressure reduction between steps in the second cycle closely resembled that of the first cycle. After completing four heating steps, the tube was again vented with air at room temperature for an additional 24 h before extending the measurement campaign to a third cycle. The ultimate pressure after the initial heating step between the second and third cycles did not exhibit the same decrease as observed in the first two cycles. However, the decay between the heating steps remained consistent with previous observations.

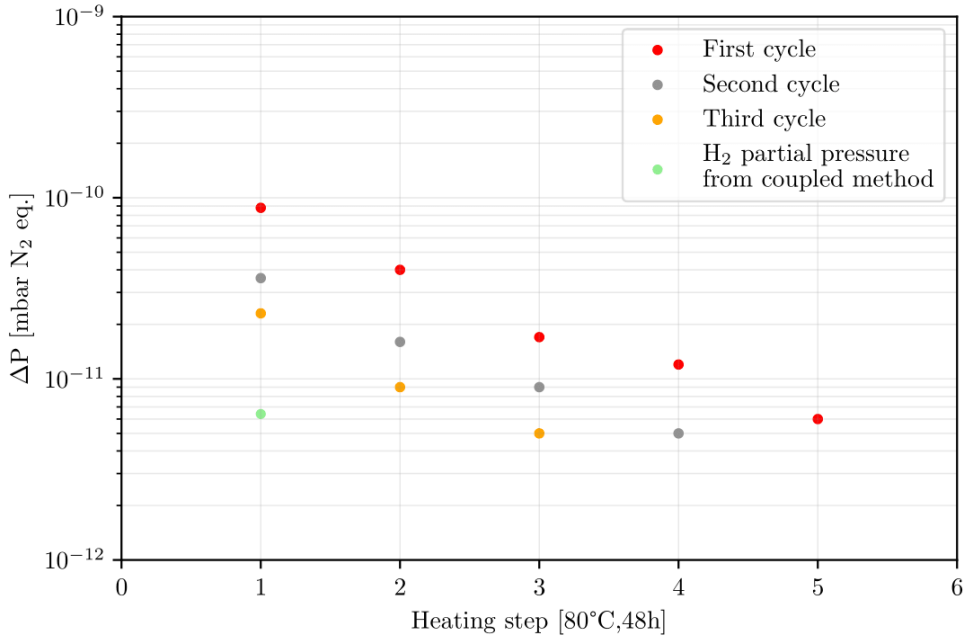

Figure 6.18: Ultimate pressure differences (ΔP) measured at 21±2°C. Background removed. The calculated H_2 partial pressure resulting from accumulation measurements is also shown at the first heating step.

The system was not equipped with an RGA to prevent undue contributions to the background signal, making it impossible to assess the gas species contributing to the total pressure directly. Nonetheless, valuable insights can be obtained from the specific outgassing rates measured using the coupled method for identical materials from the same production batch and subjected to identical cleaning procedures. For such materials, H_2 emerges as the dominant accumulated gas, while the contributions of CH_4, CO, and CO_2 are at least 87 times lower (see Table A.1). Assuming the same specific H_2 outgassing rate for the P355N vacuum chamber under examination, the N_2 equivalent pressure contribution would be 6.5×10^{-12} mbar. Considering that the difference between the measured pressure and the H_2 contribution is approximately one order of magnitude, the measured pressure can primarily be attributed to water vapour, considering that its outgassing rate cannot be determined by accumulation methods, as noted previously.

After the three cycles, i.e. in total 12 bakeouts at 80°C for 48 h, the specific H_2 outgassing rate of the P355N vacuum chamber was directly measured by the coupled method following an additional bakeout at 80°C for 48 h. The measured value was 7.5×10^{-16} mbar l s^{-1} cm^{-2}, nearly two orders of magnitude lower than the value of Table A.1, which was obtained after a single bakeout step at 80°C.

Given the ultimate pressures are dominated by water vapour, a simulation of the cycles was done to verify if the model could predict the results obtained experimentally.

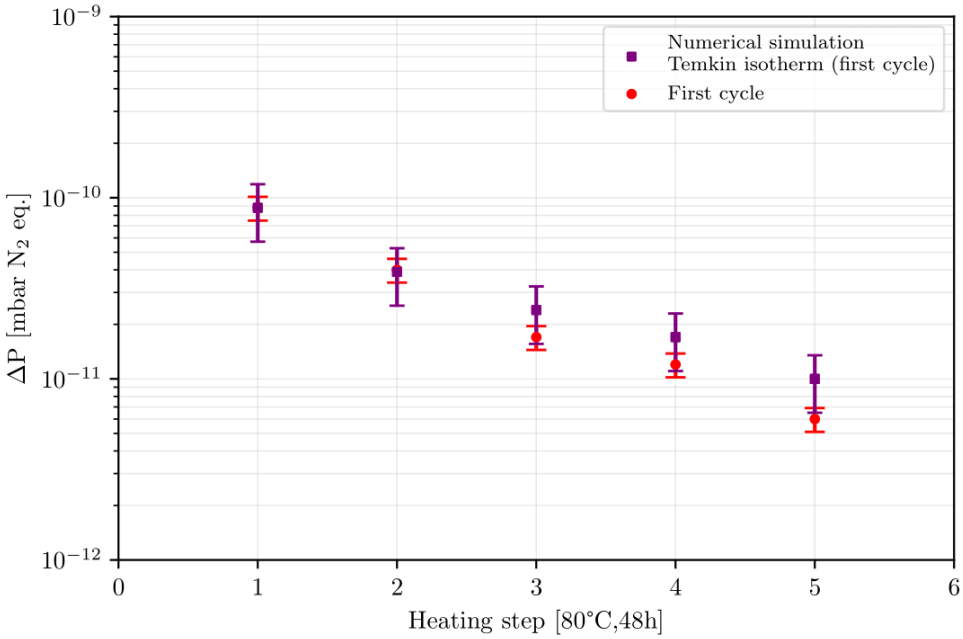

Figure 6.19: Comparison between first cycle experimental data and Temkin-based numerical simulation. The system parameters used for the simulation are: $n_m = 3.9 \times 10^{16}$ molecules/cm^2, $E_0 = 1.5$ eV, $E_1 = 0.3$ eV, $\tau_0 = 10^{13}$ s, $s_0 = 1$, $A = 6333$ cm^2, $V = 9.97$ l.

The numerical simulation, based on a Temkin isotherm, considered the energies extracted via the binding energy system and an arbitrary initial coverage of n_m = 3.9×10^{16} molecules cm^{-2} used to fit the first heating step. Considering the error associated with the ultimate pressure measurement at room temperature for the model (35%) and the gauge measurement for the experimental data (10%), as can be seen in Fig. 6.19, there is a good match between the two datasets. The goodness of the match also extends to the second and third cycles as demonstrated in Fig. 6.20.

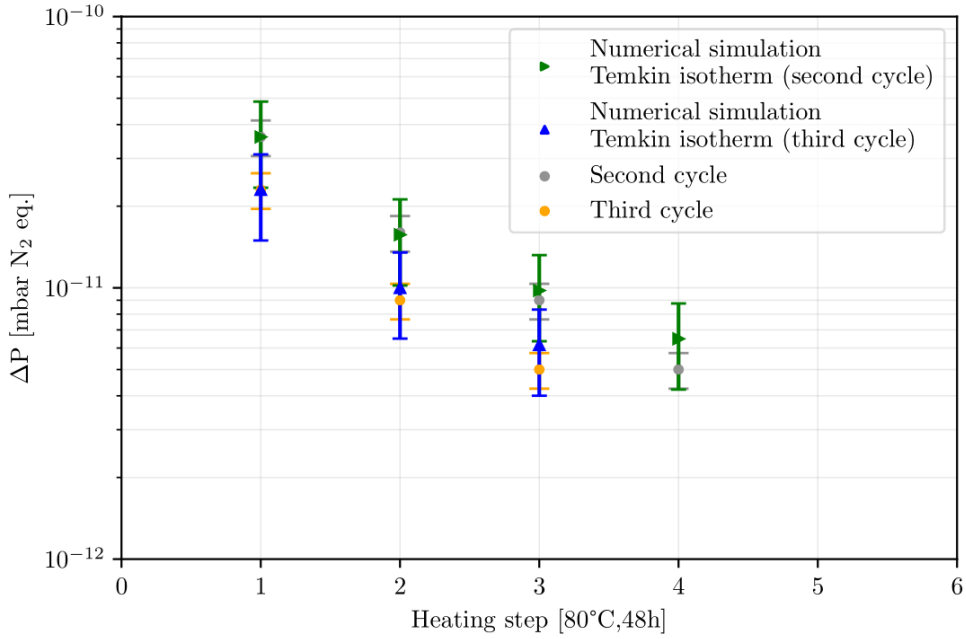

Figure 6.20: Comparison between second and third cycles experimental data and Temkin-based numerical simulation. The system parameters used for the simulation are: $n_m = 1.6 \times 10^{16}$ molecules/cm^2 (second cycle), $n_m = 1.05 \times 10^{16}$ molecules/cm^2 (third cycle), $E_0 = 1.5$ eV, $E_1 = 0.3$ eV, $\tau_0 = 10^{13}$ s, $s_0 = 1$, $A = 6333$ cm^2, $V = 9.97$ l.

Once the outgassing measurement was completed, the P355N vacuum chamber was disconnected from the accumulation system and stored in air on a laboratory's shelf for 6 months, protected only by plastic caps at the extremities. Afterwards, the same chamber was reinstalled again on the ultimate pressure system, and it underwent a fourth cycle of bakeouts. The objective of the measurement was to test the effect of the storage in air on the ultimate pressure with respect to the values recorded in the previous three cycles.

After the initial bakeout of the fourth cycle, the ultimate pressure matches that of the second cycle (see Fig. 6.21). Subsequently, a reduction by a factor of three is achieved after an additional bakeout, and a third bakeout results in an ultimate pressure comparable to the latest one measured six months before exposure to air.

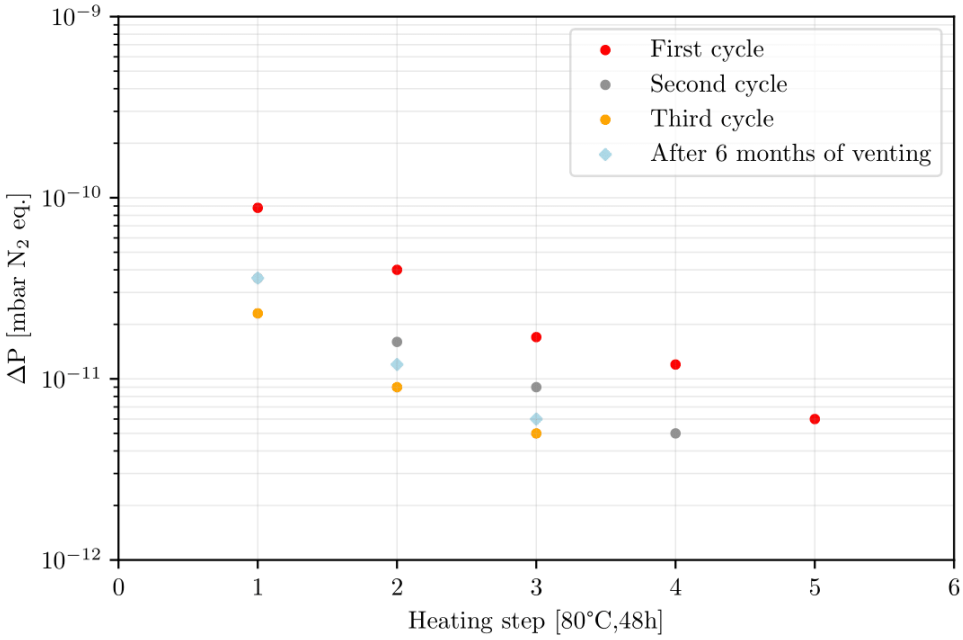

Figure 6.21: Ultimate pressure differences (ΔP) measured at 21±2°C, including a fourth cycle obtained after a 6-month exposure in air. Background removed.

The observed behaviours and trends across cycles can be attributed to surface modifications resulting from repeated bakeouts at 80°C.

The conditioning effect appears permanent within the specified time frame of air exposure, opening the way for further investigations.

6.3.3 Ultimate pressure after low-temperature bakeout: LOLA measurements

The ultimate pressure and accumulation measurements with the LOLA vacuum system were performed on a P355N vacuum chamber. The chamber subject of the study had an inner diameter of 20.71 cm, a length of 1600 cm, and an internal surface area of 10,400 cm^2 (later referred as DN250 - 16 m long chamber). The chamber was sealed at both ends with DN250-DN63 blank flanges made from S355J2+N, each flange exposing an area of 564 cm^2 to the vacuum.

Before being baked-out, the chamber was pumped down at 21±3°C for over 100 hours (see Fig. 6.22).

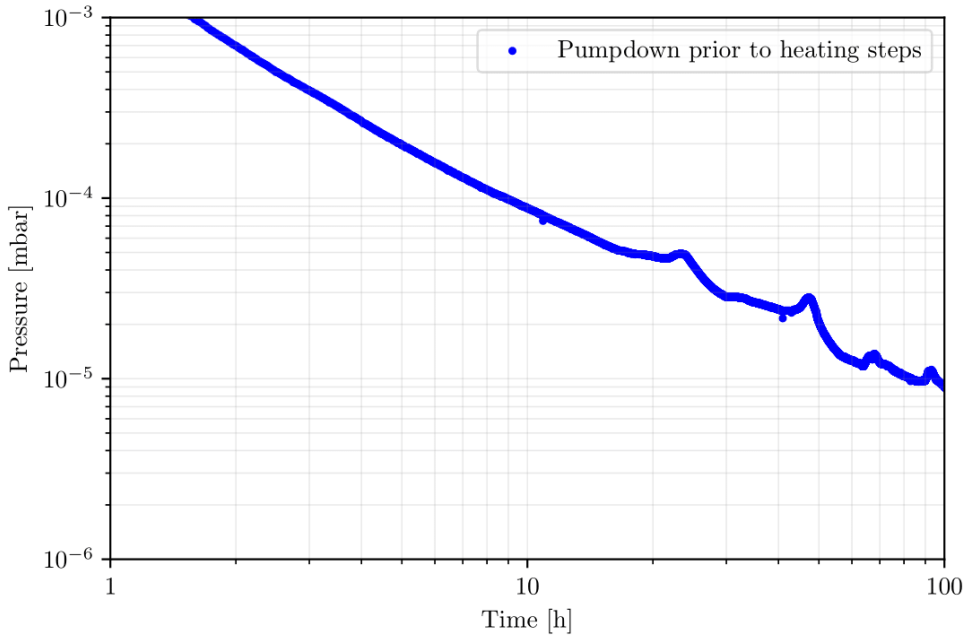

Figure 6.22: Pumpdown at 21±3°C of the DN250 - 16 m long chamber at 21±3°C. Pumping speed for H_2O: 19.5 ls^{-1}. The pressure wavering after 10 h of pumping is due to temperature fluctuations.

After the pumpdown vented to the laboratory atmosphere for four days, similar to the procedure used for the smaller P355N chamber (see Section 6.3.2), the 16 m long chamber and the mild steel flanges underwent ten consecutive heating cycles at 80°C, each lasting 48 hours. To speed up the measurement campaign, steps 5, 8 and 9 were arbitrarily skipped, making step 6 96 h long and step 10 144 h long.

Fig. 6.23 shows the ultimate pressures recorded at room temperature after each heating step and 24 h after switching off the BA gauges. Compared to the smaller P355N chamber, this larger chamber exhibited a slightly lower reduction in pressure after each heating step, with decreases ranging from a factor of 1.7 to 1.04, as opposed to the consistent halving observed in the former P355N chamber.

After each heating step, qualitative and quantitative gas composition measurements

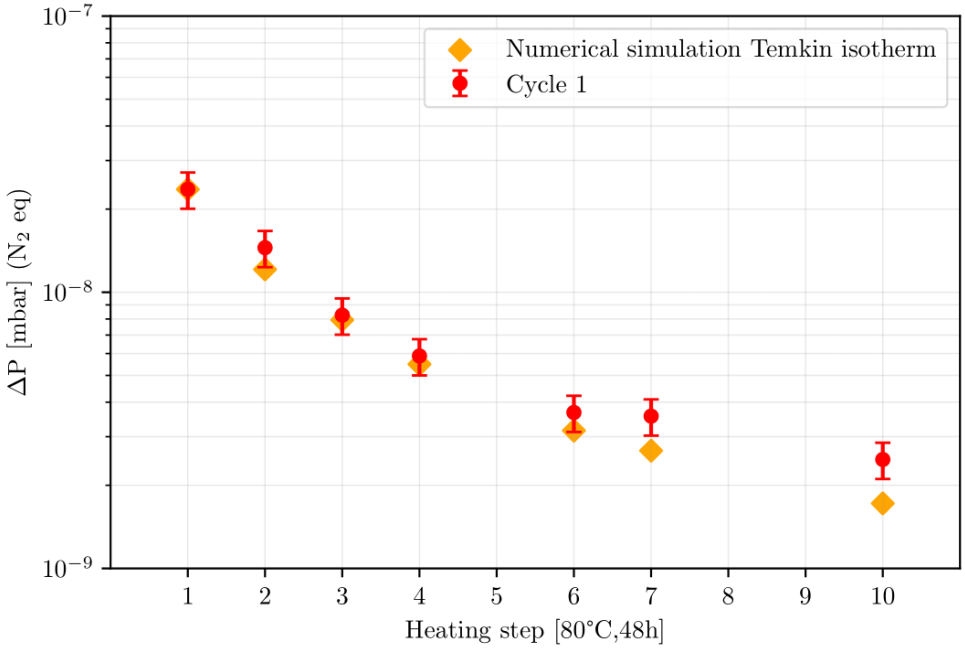

Figure 6.23: Ultimate pressure differences (ΔP) measured at 21±3°C. Background removed. The simulated pressures are based on a Temkin isotherm calibrated to the number of pumpdown sites and the chamber's real temperature after each heating step. The system parameters used for the simulation are: $n_m = 8 \times 10^{17}$ molecules/cm^2, $E_0 = 1.5$ eV, $E_1 = 0.3$ eV, $\tau_0 = 10^{13}$ s, $s_0 = 1$, $P_0 = 1000$ mbar, $A = 150128$ cm^2, $V = 538.5$ l.

helped assess the dominant gases. RGA spectra, taken 48 h after cooldown and BA gauges off since 24 h before, are reported in Fig. 6.24. The mass spectra reveal H_2O as the main source of gas, followed by H_2, CO, CO_2 and CH_4 throughout the conditioning cycle, confirming the ultimate total pressures at room temperature were dominated by water vapour.

Thanks to the accumulation system connected to the measuring chamber, each of the main gases' outgassing rates were quantified.

The accumulation measurement values, reported in Table 6.3 and Fig. 6.25, show interesting results. After the first three heating steps, the outgassing rates of CO and CO_2 are comparable to those of H_2, with rates ranging between 1.2×10^{-14} mbar l s^{-1} cm^{-2} and 5.9×10^{-15} mbar l s^{-1} cm^{-2}. From the fourth to the tenth heating steps, the outgassing rates evolution over the conditioning steps flattens with the H_2 outgassing rate stabilising around 2×10^{-15} mbar l s^{-1} cm^{-2} while those of CO and CO_2 around 4×10^{-16} mbar l s^{-1} cm^{-2}. After an initial halving, the outgassing rate of CH_4 decreased very slowly to 7×10^{-17} mbar l s^{-1} cm^{-2} at the ninth heating step. The values found generally align with those measured for other mild steel specimens (see Table A.1).

For the specific H_2O outgassing rates, calculated by subtracting the specific partial

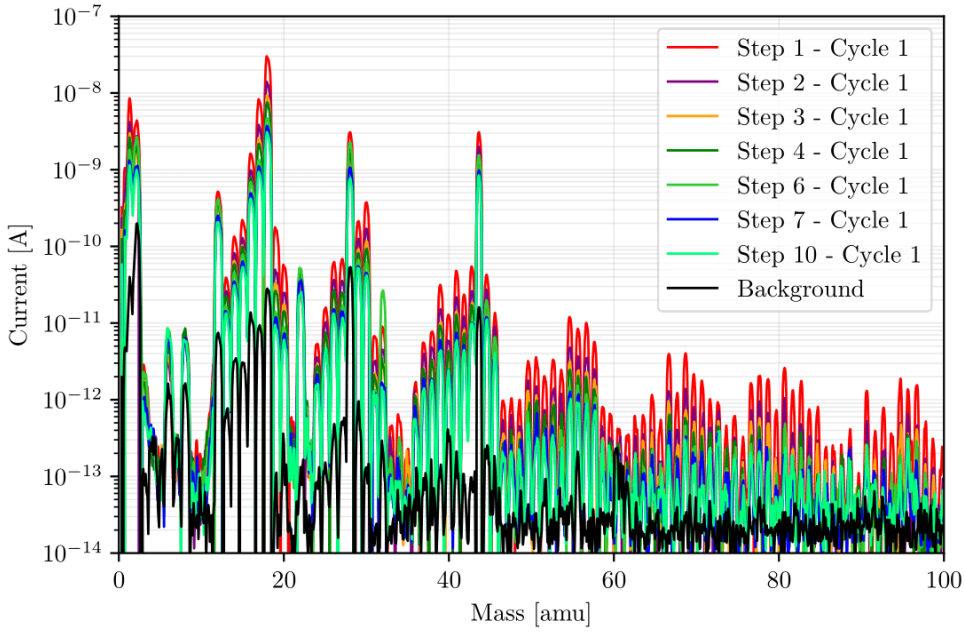

Figure 6.24: Gas composition measured at 21±3°C acquired 48 h after each heating step.

pressures of H_2, CH_4, CO, and CO_2 (converted to H_2O equivalents) from the total ultimate pressure values, the same considerations as for the ultimate pressures apply.

Given that the water outgassing rate drove the ultimate pressure, a tentative simulation of the experimental curve was performed using numerical simulation based on

Table 6.3: Specific outgassing rates of the DN250 - 16 m long chamber at 21±3°C after each heating step. Background removed.

Steps	Specific outgassing rates [mbar l s^{-1} cm^{-2}]				
	H_2 [$\times 10^{-15}$]	CH_4 [$\times 10^{-16}$]	CO [$\times 10^{-15}$]	CO_2 [$\times 10^{-15}$]	H_2O [$\times 10^{-12}$]
1	6.1	3.0	5.5	12	1.7
2	3.4	1.5	2.0	4.7	1
3	2.5	1.3	0.8	1.6	0.6
4	2.0	1.1	0.3	0.4	0.4
6	1.8	0.82	0.3	0.4	0.3
7	1.7	0.7	0.7	0.36	0.3
10	1.8	0.7	0.1	0.3	0.2

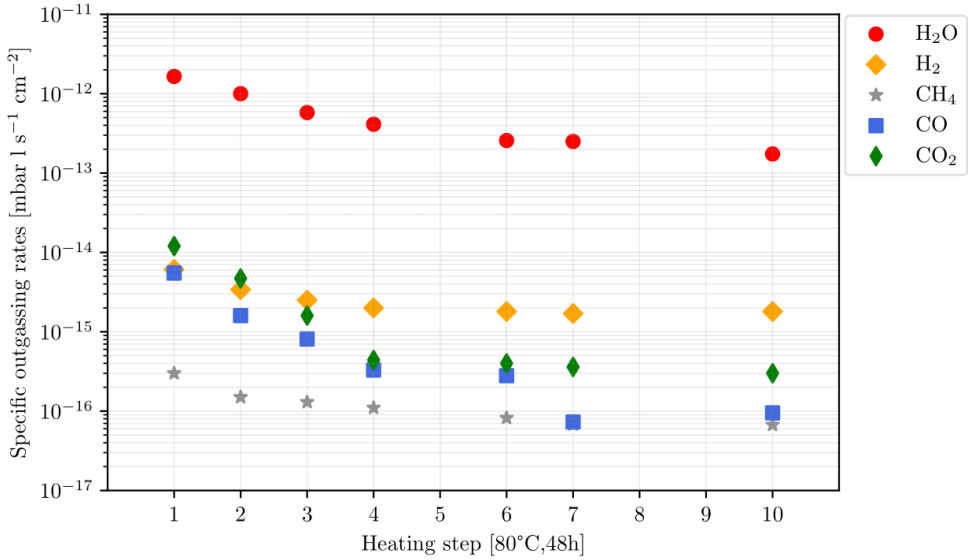

Figure 6.25: Specific outgassing rates as a function of the heating steps of the DN250 - 16 m long chamber at 21±3°C. Background removed.

Temkin isotherm. The numbers of molecules per unit of the surface were extracted from the room temperature pumpdown (see Fig. 6.22) while the binding energies are those extracted via binding energy. Contrary to the small ultimate pressure system, under the 3 cm thick insulation covering the chamber, controlling thermocouples were installed along the chamber's length that allowed the recording of room temperature fluctuations. Therefore, each simulated heating step, takes in input the real chamber temperature for a better comparison. The results, reported in Fig. 6.23, show a very good superposition between the simulated values and the experimental ones. A small deviation is observed for the last two steps, but the difference between the simulated and real values is a factor of 1.5 or lower.

After 10 heating steps, the chamber was vented for 7 days to the laboratory atmosphere (21±3°C, humidity of about 50%) and then re-pumped at room temperature for 100h. The pumpdown curve, reported in Fig. 6.26, superpose with that prior to the heating steps were applied. After 10 h of pumping, the pressure starts to oscillate following the temperature variations of the room. The chamber was re-vented (for 48 h) once the 100 h were hit, and a cycle of heating steps was started.

As depicted in Fig. 6.27, a similar behaviour was observed with the small mild steel chamber. Despite the pressure improvement compared to the first cycle, the pressure decreased just by about 27% (against the 60% observed in the previous measurements).

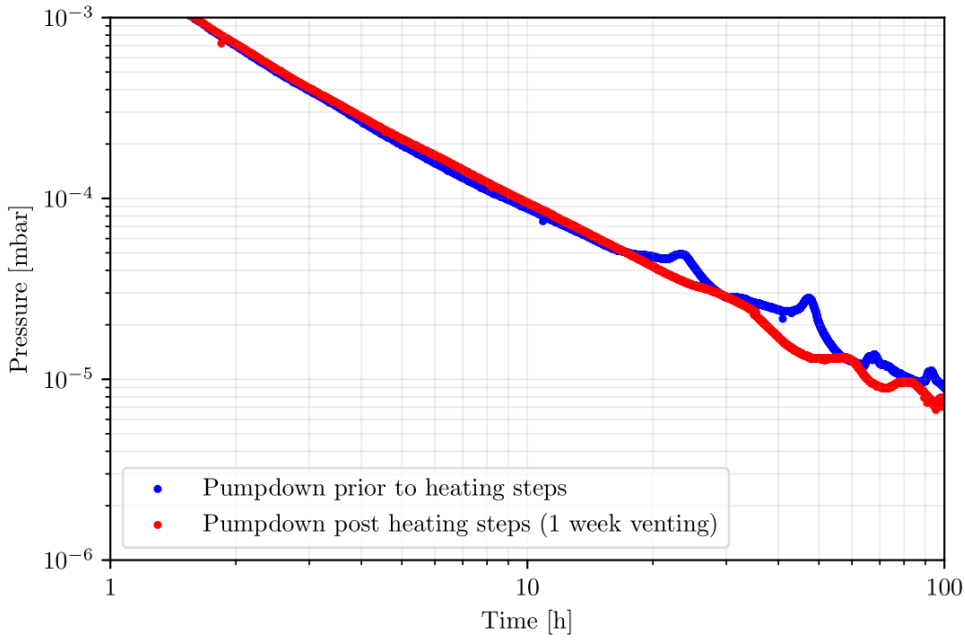

Figure 6.26: Pumpdown at 21±3°C of the DN250 - 16 m long chamber, after the 10 heating cycled and venting to the laboratory atmosphere. Pumping speed for H_2O: 19.5 ls^{-1}. As per the first pumpdown, the pressure wavering after 10 h of pumping is due to temperature fluctuations.

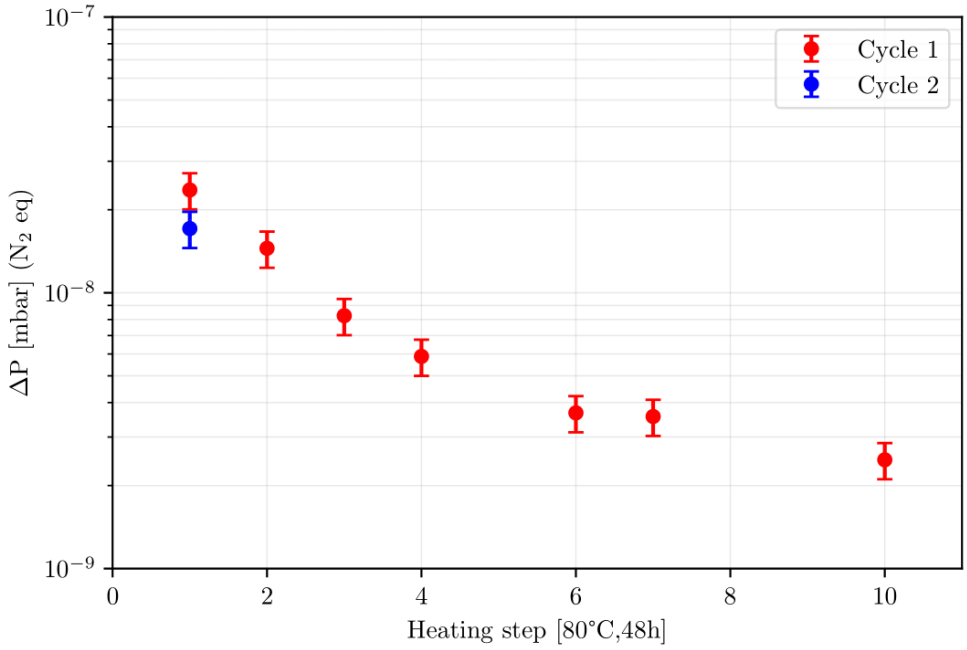

Figure 6.27: Comparison of the ultimate pressure differences (ΔP) measured at 21±3°C for the DN250 - 16 m long chamber, before and after the one-week venting. Background removed.

The RGA scans confirm once more that water is the dominant gas (see Fig. 6.28). An increase in signal for H_2, CH_4, CO and CO_2 is also observed. Unchanged, instead, are the signals for masses higher than 45 amu, The accumulation measurements further confirm the results of the RGA scans, as reported in Table 6.4.

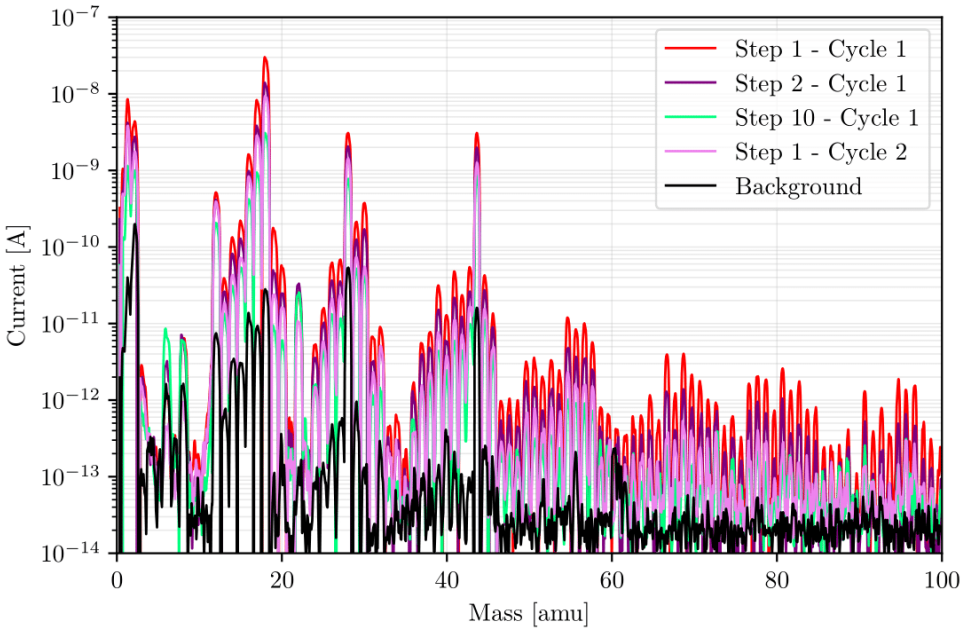

Figure 6.28: Comparison of RGA scans before and after venting of the DN250 - 16 m long chamber.

Table 6.4: Comparison of the specific outgassing rates of the DN250 - 16 m long chamber at 21±3°C before and after venting. Background removed.

Cycle	Step	Specific outgassing rates [mbar l s^{-1} cm^{-2}]				
		H_2 [$\times 10^{-15}$]	CH_4 [$\times 10^{-16}$]	CO [$\times 10^{-15}$]	CO_2 [$\times 10^{-15}$]	H_2O [$\times 10^{-12}$]
1	1	6.1	3.0	5.5	12	1.7
1	2	3.4	1.5	2.0	4.7	1
1	10	1.8	0.7	0.1	0.3	0.2
2	1	3.3	2.8	1.6	2.7	1.2

The specific outgassing rate of H_2, CO and CO_2, reached values similar to those of the second heating step of the first cycle. In contrast, the CH_4 outgassing rate surpassed the value registered for the first heating step.

With the data acquired, it is possible to try to draw some conclusions on the evolution of the H_2 outgassing rate throughout the heating steps applied. Having excluded a diffusion-limited outgassing rate due to the TPD spectras' shapes, a tentative fitting can be done with the recombination-limited model. If recombination limited, the hydrogen outgassing rate should be proportional to the number of heating steps, according to Eq. (2.61):

$$q \propto \frac{1}{N^2} \tag{6.1}$$

where N is the number of heating steps.

If fitted with a power law equation, the values reported in Table 6.3, show an exponent of 0.68. Therefore, it can be excluded that the hydrogen outgassing rate after the set of heating steps applied is limited by surface recombination.

Given the failure to fit the values with known outgassing limiting models and the increase observed after venting, it cannot be excluded the attribution of the H_2 outgassing to water desorption or, more in general, to the oxide layer. Since the setup could not further tackle the mechanism of H_2 desorption, it was decided to stop the measurement campaign at the first heating step of the second cycle.

From the RGA scans, it is worth highlighting the presence of hydrocarbons with molecular mass > 45 amu. The hydrocarbons were reduced by about one order of magnitude at the equivalent of 20 days of bakeout. Still, their presence after such conditioning is a worrying aspect, especially in the vision of the GWD application. Since the calibration factor for these gases is not available, a general observation can be done. If this chamber had been installed in the LHC and considered as partially baked due to the low temperature of the bakeout and the dominance of the water peak, it would barely be accepted for installation given the ratio H_2O peak/Mass > 44 amu peak slightly lower than 1000 [151].

A possible explanation for these high masses' presence might be their surface status. Before being welded to form the chamber, the 4-m long sections were unintentionally left in the snow for three weeks. The exposure to a harsh environment accelerated the passivation of the internal surface, leaving the large portions of the pipe covered by hydroxides/oxides patches as seen in Fig. 6.29. It is possible that the type of cleaning procedure applied together with the surface morphology, which might have retained some lubricant residue, did not result in a thoroughly cleaned chamber. In addition, the bakeout temperature is not high enough to thermalise the hydrocarbons, reducing the heavy masses slowly and inefficiently.

Figure 6.29: Internal surface aspect of the DN250 - 16 m long mild steel chamber before the first heating cycle was applied. Patches of hydroxides and oxides cover the surface.

To demonstrate that a prolonged low-temperature bakeout is less efficient at reducing heavy masses compared to a shorter, high-temperature bakeout, the chamber was baked at 150°C for 48 hours without being vented. As seen in Fig. 6.30, the 150°C bakeout reduced masses above 45 amu to nearly background levels. Compared to the 80°C bakeout held for time equivalent to 20 days (first cycle, last step), it was also more effective at reducing other species. Notably, the water's partial pressure was reduced to background levels.

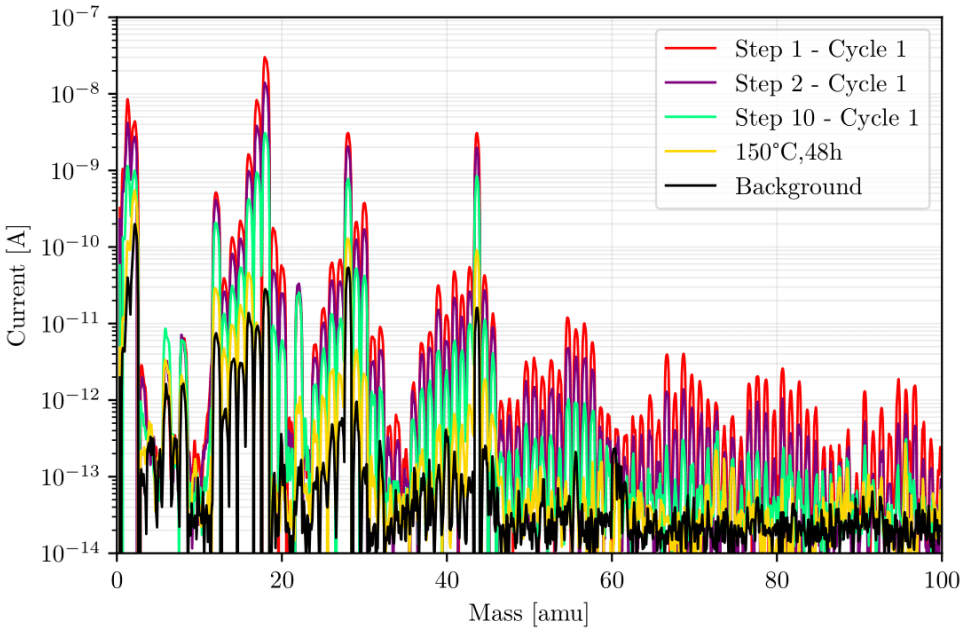

Figure 6.30: Comparison of RGA scans of the first and last steps of the two heating cycles applied.

The total pressure from the first heating step of the second cycle was reduced by more than two orders of magnitude. Compared to the last heating steps of the first cycle, with the 150°C 48 h long bakeout, a 34 times lower pressure was achieved within 1/5 of the time (see Fig. 6.31).

Unfortunately, the accumulation system's RGA stopped working while measuring the outgassing rates after the 150°C, 48 h bakeout. As a result, reliable data were unavailable to continue the comparison, concluding the measurement campaign.

During the system's decommissioning, an interesting feature was observed. The oxidised patches covering the pipe's surface darkened, transitioning from red rust/orange to a matte brown/dark grey. This could indicate dehydration of the hydroxides to form stable oxides.

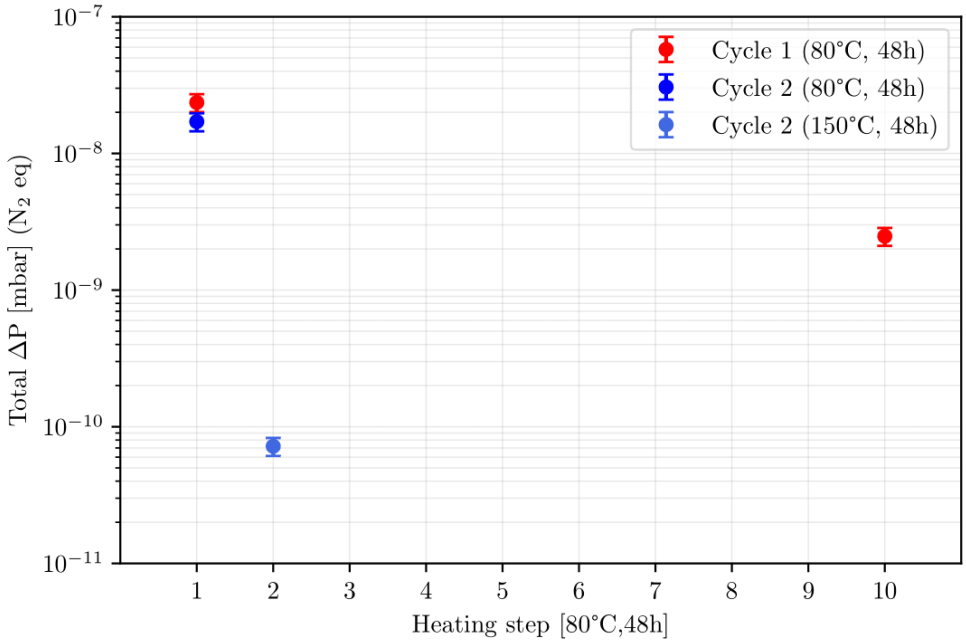

Figure 6.31: Ultimate pressure differences (ΔP) measured across the 1.3-cm diameter orifice at 21±3°C, including the 150°C, 48 h results. Background removed.

Figure 6.32: Internal surface aspect after the two heating cycles. Compared to Fig. 6.29, the oxide patches darkened in colour.

7. Ferritic stainless steels

Finding the right work is like discovering your own soul in the world.

-Thomas Moore-

This chapter summarises the results of the UHV characterisation of the selected ferritic stainless steels. As done also for mild steels, the results are discussed and compared with those of AISI 304L in as received condition for a direct comparison with a material compatible with the GWD application.

7.1 Water outgassing rate

7.1.1 Pumpdown of unbaked specimens

The measured pumpdown curves, representing the water vapour specific outgassing rate as a function of pumping time, are shown in Fig. 7.1. The specific outgassing rates recorded after 10 h of pumping are summarized in Table 6.1.

As shown in Fig. 7.1, the pumpdown values of all the ferritic stainless steel samples are reasonably well-fitted by inverse power laws with time exponents around -1. After ten hours of pumping, the outgassing rates of AISI 441 and AISI 444 are essentially in line with that of AISI 304L. This result was foreseeable considering the similar surface chemistry between the austenitic and ferritic samples.

Table 7.1: Water vapour specific outgassing rates of AISI 444, AISI 441 and AISI 304L measured at 21±2°C. Background removed.

Steel	Tested samples [cm^2]	q_{10h} [mbar l s^{-1} cm^{-2}]	$q_0\ t_h^{-a}$
AISI 441	4630	4.3×10^{-10}	$3.3\times10^{-9}\ t_h^{-0.86}$
AISI 444	9260	2.4×10^{-10}	$2.2\times10^{-9}\ t_h^{-0.91}$
AISI 304L	5260	3.3×10^{-10}	$1.96\times10^{-9}\ t_h^{-0.78}$

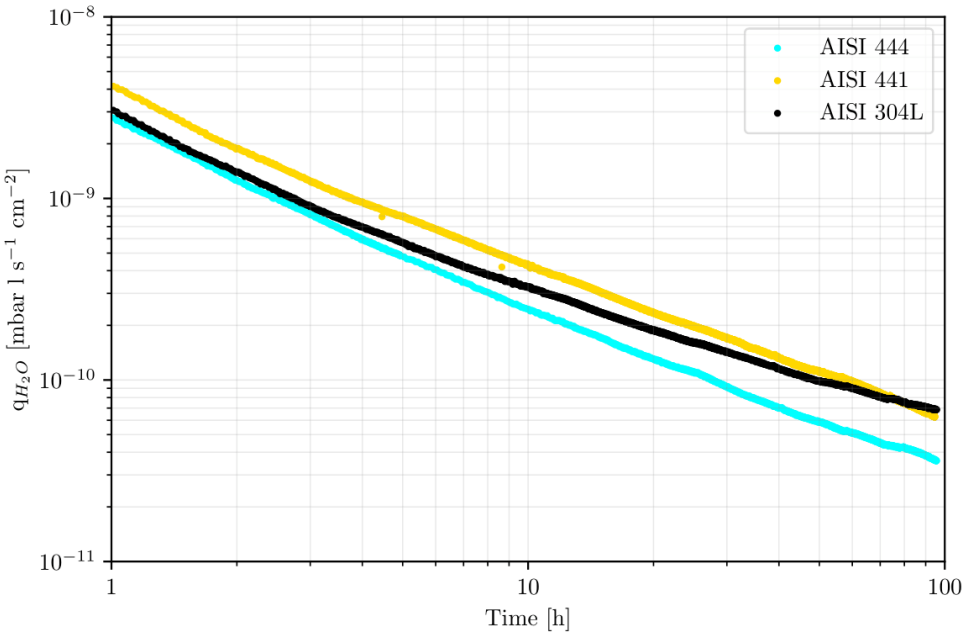

Figure 7.1: Pumpdown curves of the AISI 441, AISI 444 and AISI 304L at 21±2°C; the specific outgassing rate is plotted as a function of the pumping time. Background removed.

7.1.2 Water vapour binding energies

The binding energy measurements were performed on an AISI 441 vacuum chamber (7.6 cm inner diameter, 300 cm long, 7163 cm^2 internal surface area). The chamber was pumped down at 40°C, 80°C and 150°C for over 100 h following the procedure described in Section 6.1.2. The results obtained fitted with a Temkin isotherm (see Eq. (2.24)) and corrected to the pumping speed at the gauge position are reported in Fig. 7.2.

The fitting parameters extracted with the modelling, after taking into account the gauge contribution to the effective pumping speed [h], are: E_0 = 1.5 eV, E_1 = 0.2 eV and $n_m = 4.5\times10^{15}$ molecules cm^{-2}.

[h]For the inverted magnetron gauge used, it is assumed a contribution to the pumping speed of 1 ls^{-1}.

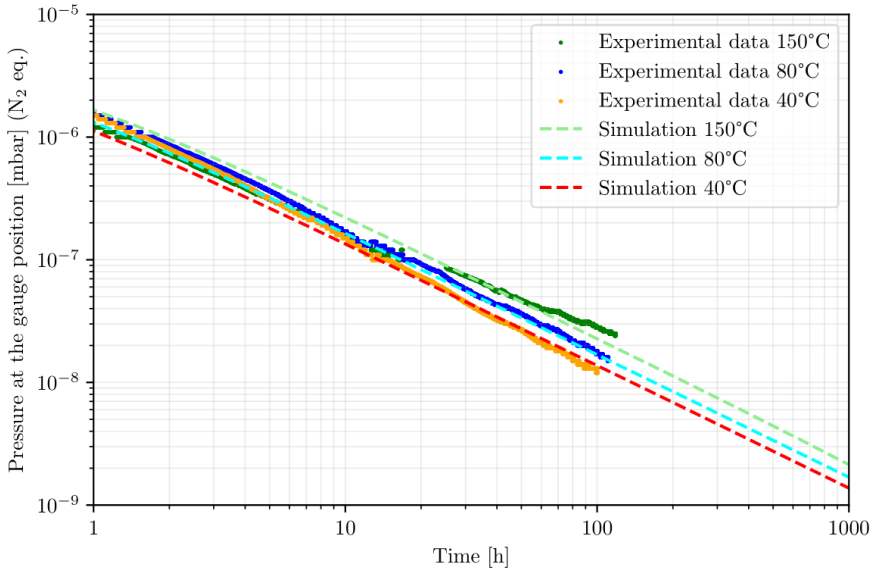

Figure 7.2: Pumpdown curves at 40°C, 80°C and 150°C of the AISI 441 chamber measured with the binding energy system and their respective simulation using the Temkin isotherm (dashed lines). The system parameters used for the simulation are: $n_m = 4.5 \times 10^{15}$ molecules/cm^2, $E_0 = 1.5$ eV, $E_1 = 0.2$ eV, $\tau_0 = 10^{13}$ s, $s_0 = 1$, $P_0 = 1 \times 10^{-5}$ mbar, $A = 7163$ cm^2, $V = 13.6$ l.

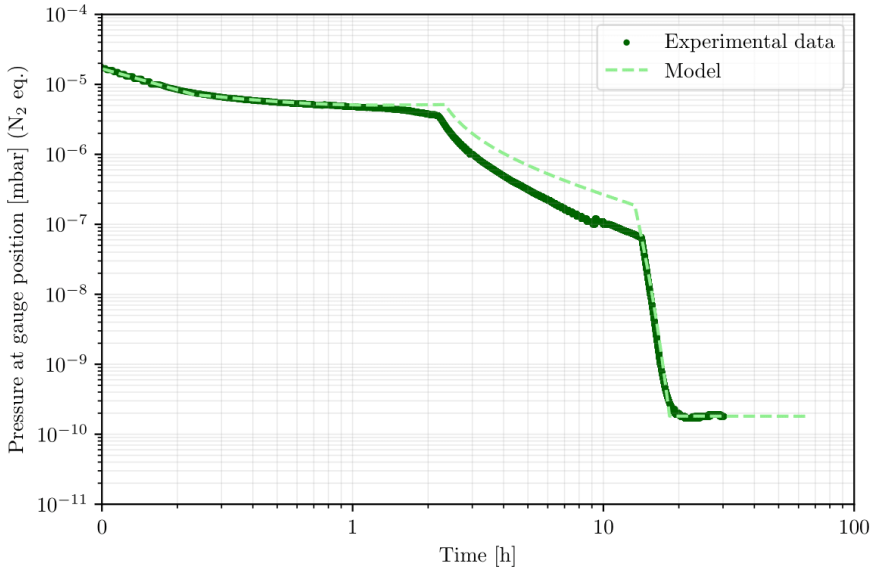

Figure 7.3: Comparison between experimental data and simulated (dashed line) bakeout at 80°C, 12h. The system parameters used for the simulation are: $n_m = 4.5 \times 10^{15}$ molecules/cm^2, $E_0 = 1.5$ eV, $E_1 = 0.2$ eV, $\tau_0 = 10^{13}$ s, $s_0 = 1$, $P_0 = 1 \times 10^{-5}$ mbar, $A = 7163$ cm^2, $V = 13.6$ l.

As done for mild steel, the values extracted were used to simulate the pumpdown curve and the ultimate pressure of the same chamber after a 80°C, 12 h bakeout. Despite a small discrepancy observed during the steady state, the comparison between the simulated and experimental curve during the bakeout shows an overall good superposition and prediction of the ultimate pressure, as seen from Fig. 7.3.

7.2 H_2 content and TPD spectra

The H_2 thermal desorption spectra, with the background signal removed, are shown in Fig. 7.4. All raw data were smoothed for better visualization through a Savitzky-Golay filter [142] implemented in Python. As per the 3 mm sample described in Section 6.2, the signal obtained with AISI 304L samples can be fitted by a Fickian diffusion model that matches the broad peak with a maximum at 480°C (see Fig. 6.7). The obtained diffusion energy is 0.52±0.06 eV, i.e. a typical value for austenitic stainless steels [54, 143, 144].

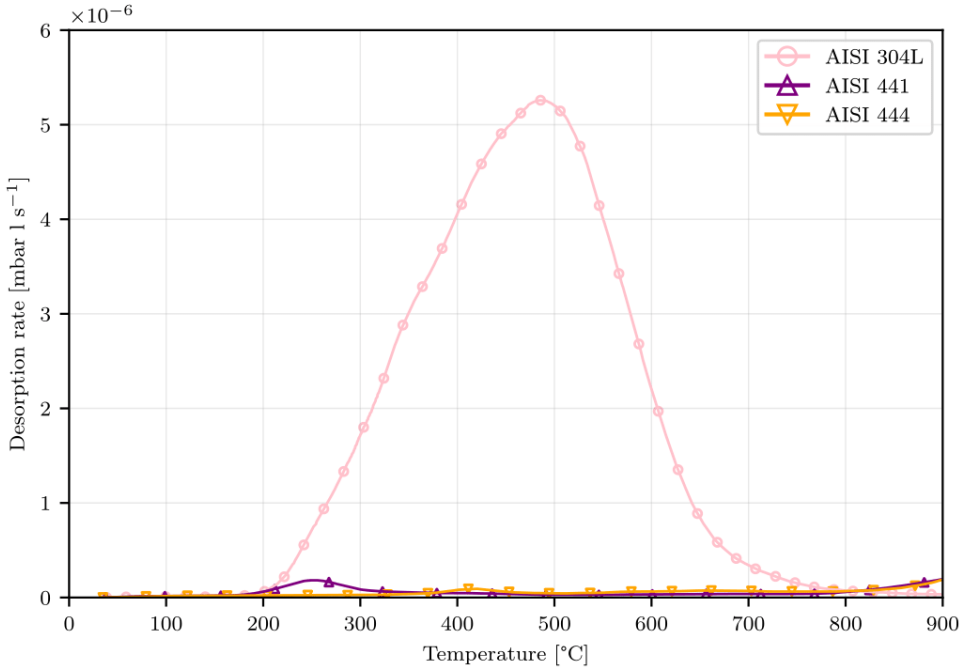

Figure 7.4: H_2 thermal desorption spectra of AISI 304L, AISI 441 and AISI 444 samples. The background signal of the TPD system is removed.

The H_2 spectra of the two ferritic stainless steels show similar features (see Fig. 7.5). The AISI 441 samples are characterised by a narrow peak around 250-260°C, followed by a shoulder at 420°C. Additionally, the spectra display a broad peak or shoulder between 530°C and 750°C before ramping up. Similarly, the AISI 444 samples exhibit the same peaks and shoulders, although the initial and highest peak is shifted to 420°C.

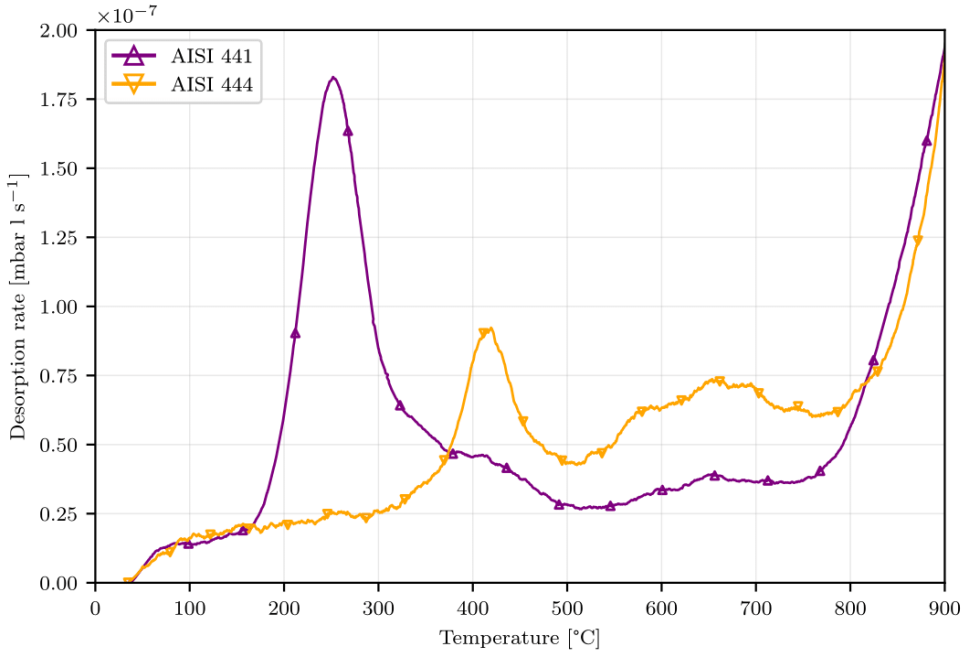

Figure 7.5: H_2 thermal desorption spectra of AISI 441 and AISI 444 samples (vertical scale reduced x30 with respect to Fig. 7.4). The background signal of the TPD system is removed.

As per the mild steel samples, the H_2 concentration in the ferritic stainless steel samples is calculated by integrating the TPD signal up to 850°C and assuming uniform initial distribution in the volume of the samples. The results of the calculation are reported in Table 7.2. The calculated hydrogen concentration in AISI 304L samples is 41 to 53 times higher than that evaluated for the ferritic stainless steel samples, the latter showing H contents always below 2 atomic ppm. As observed with the mild steel samples, this result was expected due to their ferritic BCC structure; the ferritic stainless steel samples have a much lower solubility for hydrogen than the austenitic FCC microstructure of the AISI 304L.

Given the shape of the peaks defining the ferritic stainless steel's H_2 TPD spectra, they appear not to follow a Fickian desorption. Most likely, as seen for the mild steels, the peaks might be influenced by de-trapping phenomena. A tentative extraction of the H_2 binding energy was performed using the Kissinger method. Fig. 7.6 shows the $\log\left(\frac{\beta}{T_p^2}\right)$ in function of $\frac{1}{k_b T_p}$ of AISI 441 samples heated with heating rates β of 5, 10, 15, 20, and 40 K min^{-1}.

Unfortunately, the great dispersion observed across the data leads to a poor linear regression. This behaviour, besides the measurement error of the system used (same as Fig. 2.15), suggests some hints on the desorption source. The Kissinger method assumes that the desorption energy, regardless of its source, is mono-energetic. The significant dispersion observed may be due to multiple sources with different energies.

Table 7.2: AISI 444, AISI 441 and AISI 304L hydrogen concentration obtained by integrating the TPD spectra up to 850°C. The values reported are the average of at least three samples from the same batch. The background of the TPD system is removed. To convert atomic ppm to weight ppm, divide by 55.85 (molecular weight of iron).

Steel	H content [ppm at.]	Thickness [cm]
AISI 304L (as received)	70	0.15
AISI 441	1.7	0.15
AISI 444	1.3	0.15

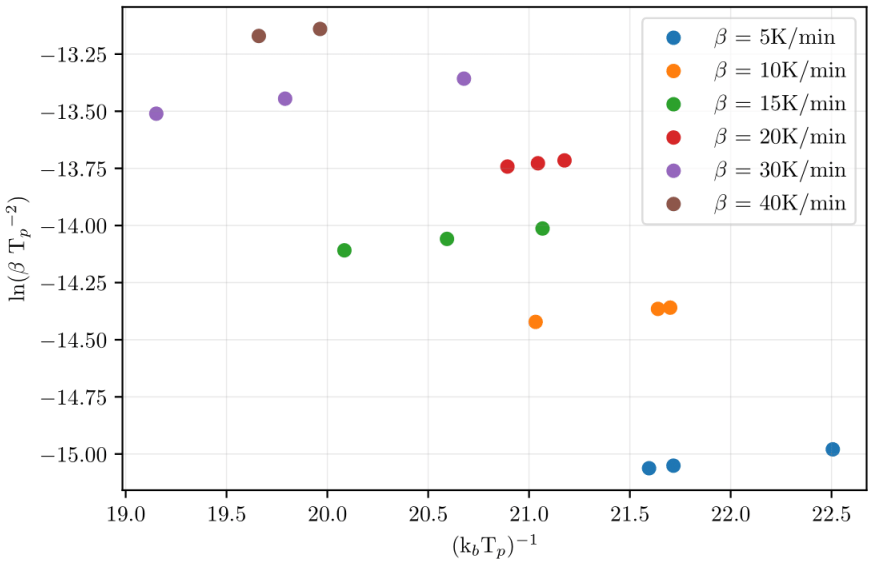

Figure 7.6: $\log\left(\frac{\beta}{T_p^2}\right)$ in function of $\frac{1}{k_b T_p}$ for AISI 441 samples heated with heating rates β of 5, 10, 15, 20, and 40 K min^{-1}. T_p, is the temperature at which the peak manifests.

This variability prevents precise determination of whether the peak is associated with lattice diffusion or de-trapping from dislocations or other defects.

Given that the AISI 441 was provided with a 2B finish, it is possible that the cold rolling induced dislocations, further emphasized by the subsequent skin passing (the final production step for finishing purposes), are responsible for the observed peak. In contrast, the AISI 444, which was provided with a 2D finish and not skin-passed, does not exhibit this peak. To support this hypothesis, 0.3 cm thick hot-rolled, skin-passed AISI 441 samples were tested. As depicted in Fig. 7.7, these 0.3 cm samples do not show the first main peak at around 250°C but only around 430°C, similar to the AISI 444. Despite the intensity of the peak, since it appears at low temperatures, it can be

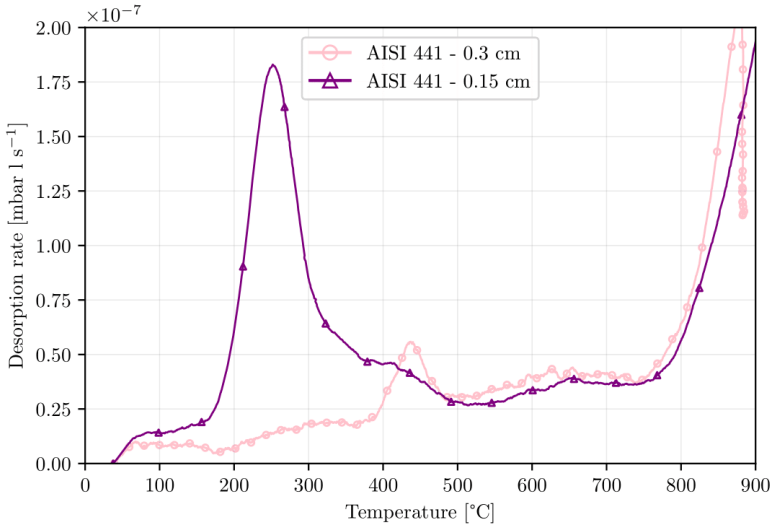

Figure 7.7: H_2 thermal desorption spectra of AISI 441 0.15 cm and 0.3 cm thick samples. The measurement of the 0.3 cm thick sample was manually interrupted at 850°C.

easily erased during a GWD's bakeout operation.

If we exclude the main peak around 250°C for the 0.15 cm thick samples, it can be confirmed that the peak position remains invariant with thickness for the ferritic stainless steel, as it does for mild steels. Furthermore, as observed with mild steels, both AISI 441 and AISI 444 show an interesting correlation between the water signals and the hydrogen signals (see Fig. 7.8).

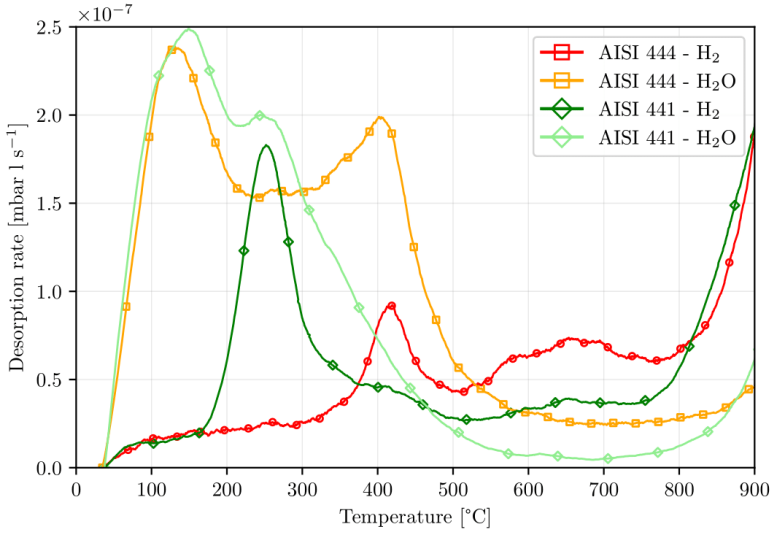

Figure 7.8: H_2 and H_2O thermal desorption spectra of AISI 441 and AISI 444 samples.

7.3 Outgassing rates of baked samples

7.3.1 H_2,CH_4,CO and CO_2 outgassing rates

The specific outgassing rates for H_2, CH_4, CO, and CO_2 are depicted in Figs. 7.10(a) to 7.10(c) and reported in Table A.3 Table A.4. The values were calculated with Eq. (4.3) from data obtained by accumulation according to the procedure described in Section 4.2. Measurements were taken for different accumulation times to verify the pressure linearity during accumulation.

After a 48-hour bakeout at 80°C, only AISI 444 showed a measurable H_2 outgassing rate. With more than 9000 cm^2 of surface tested, AISI 444 exhibited a H_2 outgassing rate of 1×10^{-15} mbar l s^{-1} cm^{-2}, more than 700 times lower than that of AISI 304L. Instead, the measured outgassing rates for CH_4, CO and CO_2 are from a factor of 1.8 up to a factor of 5 lower than those registered for the AISI 304L. For the AISI 441, the other values are systematically below the system sensitivity despite the CH_4 outgassing rate being one order of magnitude lower than that of AISI 304L.

The following bakeout at 150°C for 48 h made most outgassing rates from AISI 444 and AISI 441 fall below the detection limit. Where sensitive enough to be detected, especially the outgassing rates of CH_4, CO and CO_2 saw reductions from a factor of 4 up to a factor of 20.

Compared to the AISI 304L, baked for the same time and temperature, the ferritic stainless steel from two to four orders of magnitude lower H_2 specific outgassing rates, therefore attaining values measured for a few mm thick AISI 304L after vacuum firing (950°C, 2 h) [52] or air bakeout (390°C, 100 h) [85]. As per the mild steels, the hydrogen concentration ratios and the ratios of specific hydrogen outgassing rates in ferritic stainless steels compared to austenitic steels don't align quantitatively.

This mismatch might be because hydrogen in mild steel is mainly trapped within the material's bulk and surface oxide, thus not participating in the diffusion process that causes outgassing at room temperature.

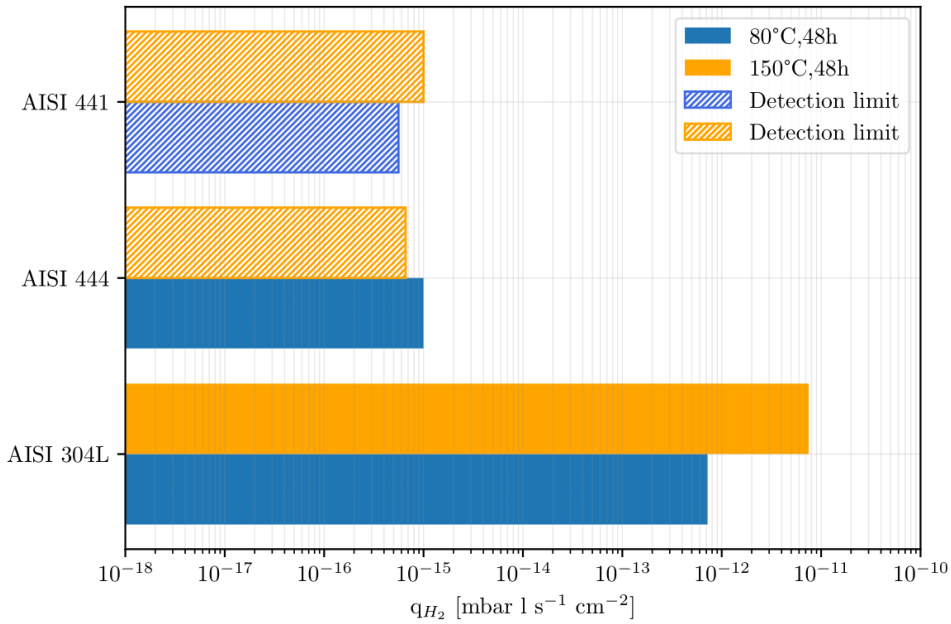

Figure 7.9: Comparison of H_2 specific outgassing rate reported in Tables A.3 and A.4. The system sensitivity (see definition in the text) normalised to the sample surface area is plotted as dashed columns when the measured values are below such a limit.

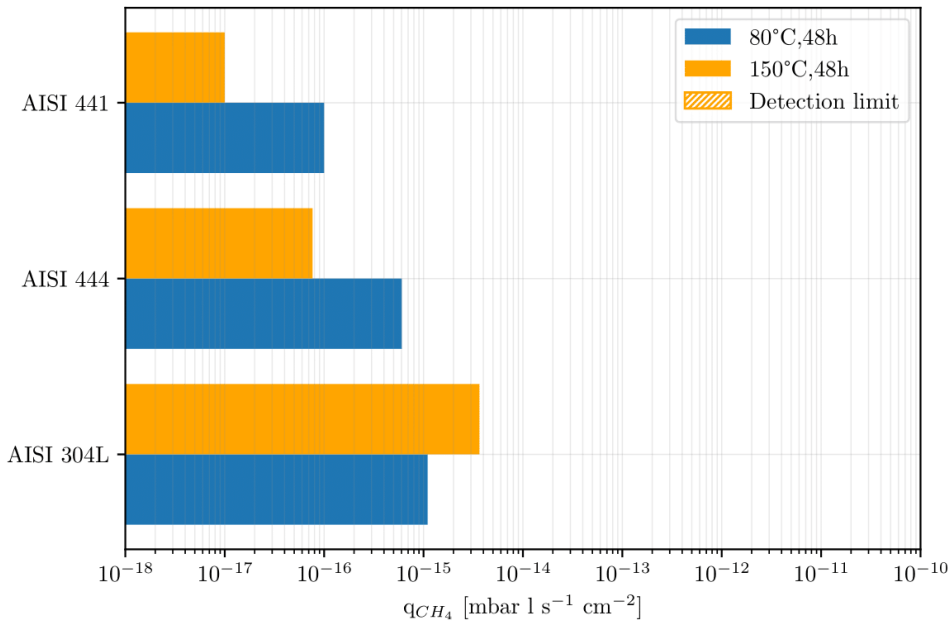

(a) CH_4 specific outgassing rates.

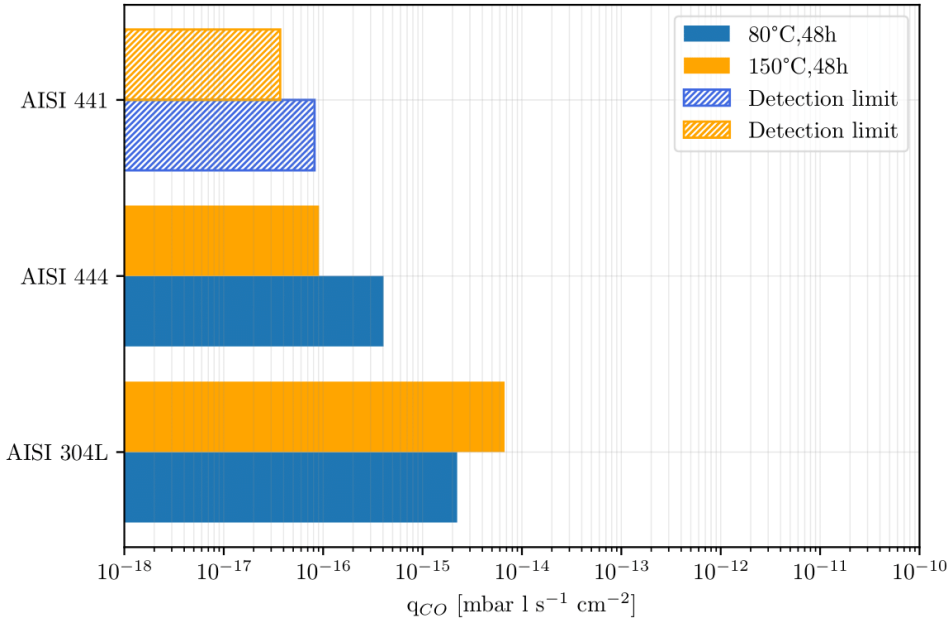

(b) CO specific outgassing rates.

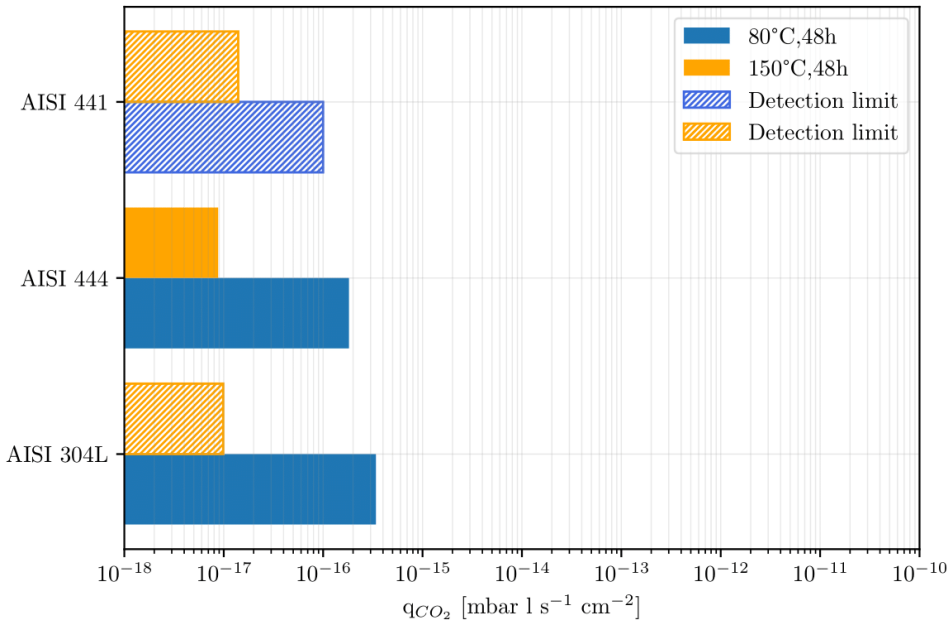

(c) CO_2 specific outgassing rates.

Figure 7.10: Comparison of CH_4, CO and CO_2 specific outgassing rates reported in Table A.3 and Table A.4. The system sensitivity (see definition in the text) normalised to the sample surface area is plotted as an orange-dashed column when the measured values are below such a limit.

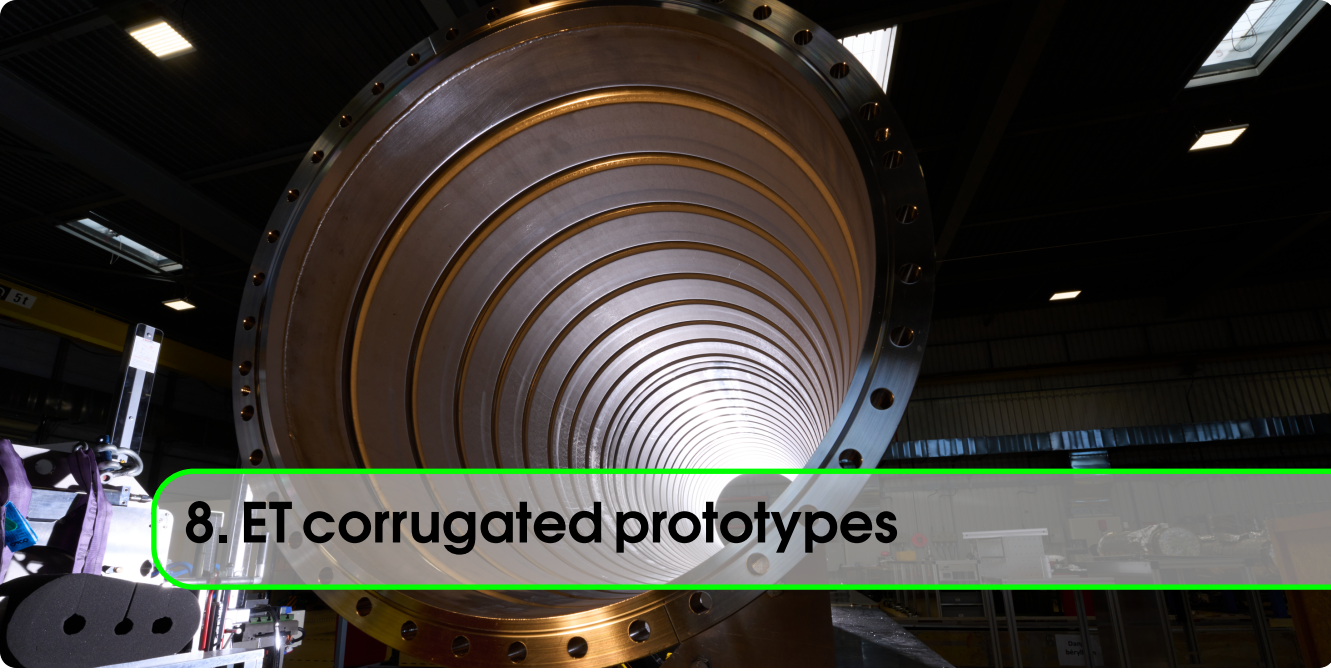

8. ET corrugated prototypes

There is no great genius without some touch of madness.

-Aristotle-

8.1 Ultimate pressures after bakeout

The ultimate pressures of the three DN400 - 2.1 m corrugated chambers (internal surface: 28800 cm^2) measured at 21±4°C after 80°C, 7 d and 150°C, 48 h bakeouts are reported in Fig. 8.1. To minimise the contribution of the DN400 closing flanges, they have been thinned to reach a wall thickness of 3 mm and then vacuum fired at 950°C for 2 h to reduce their H_2 outgassing rate.

All the measurements appeared dominated by the system background (instrumentation and fittings). Indeed, if the ultimate pressures are converted to outgassing rates[i], one can retrace back the instrumentation degassing rate of the BA and RGA, 2×10^{-9} mbar l s^{-1} and 8 $\times10^{-9}$ mbar l s^{-1} (H_2 eq.) respectively. The found values fall into the typically measured outgassing ranges [152]. The ultimate pressures measured can be, therefore, considered as upper limits. Consequently, considering the lowest background pressure, the resulting H_2 outgassing rates of the three chambers are lower than 8×10^{-14} mbar l s^{-1} cm^{-2}.

A factor of 1.6 improvement in the ultimate background pressure was observed

[i] pumping speed at the instrumentation: 31 ls^{-1} for H_2, N_2 to H_2 conversion factor: 2.19

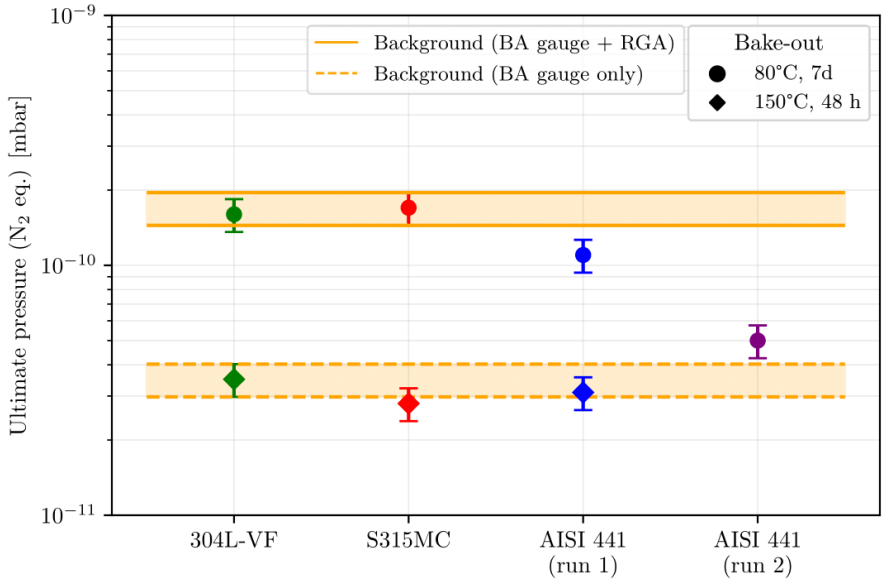

Figure 8.1: Ultimate pressures of AISI 304L-VF, S315MC, and AISI 441 corrugated chambers measured at 20±3°C after 80°C, 7 d and 150°C, 48 h bakeouts. The orange bands represent the background values. The error bars are given by the 15% measurement error of the BA gauge for both measurements and backgrounds.

after the 80°C bakeout of the AISI 441 chamber. The chamber needed to be baked twice at 80°C due to an unexpected power cut during the first conditioning. The bakeout was restarted (referred to as run 1) without venting the chamber from a base pressure of 1×10^{-6} mbar. Another bakeout at 80°C for 7 days was repeated (referred to as run 2) after a 150°C, 48-hour treatment, followed by four days of venting at laboratory atmosphere. This resulted in an additional factor of 2 improvement in the ultimate pressure. In both cases, the influence of the measurement temperature and an improvement in the instrumentation's outgassing rate cannot be excluded.

8.2 Water ultimate pressure after NEG-assisted low-temperature bake-out

The secondary objective of the corrugated chambers was to evaluate the residual water partial pressure after the 80°C week-long bakeout, executed experimentally using the NEG pumps during the treatment.

The three chambers were pumped down at room temperature for at least 6 days and baked out at 80°C for a week. At 1/3 of the bakeout duration, roughly 2 days after the start of the bakeout, the angle valve to the NEG pumps was open (see Fig. 8.2(a)), increasing the pumping speed seen by the system. After the opening, the valve is kept open until room temperature to carry on the UHV pumping.

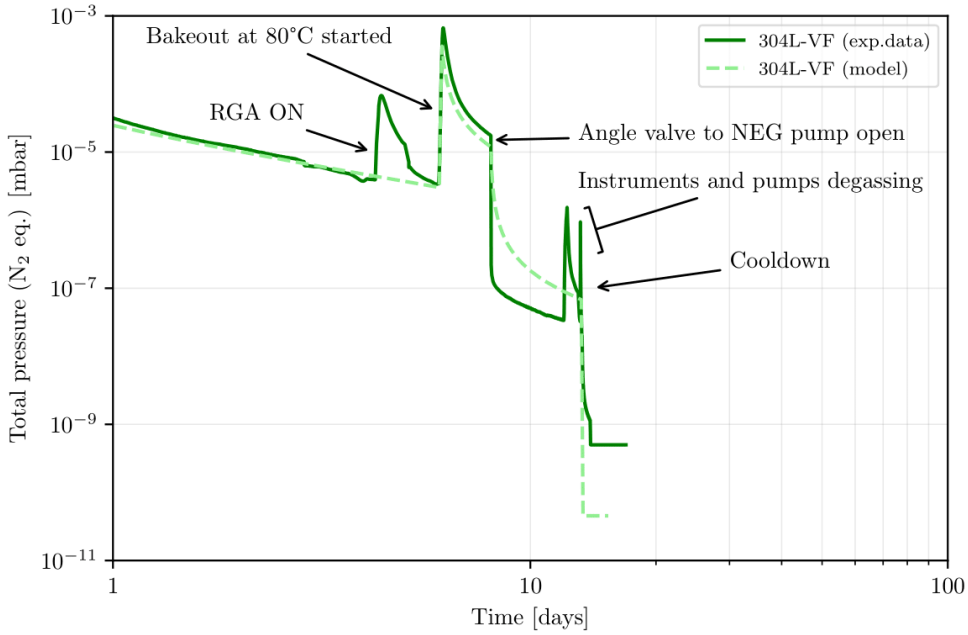

(a) AISI 304L-VF corrugated chamber pressure follow-up.

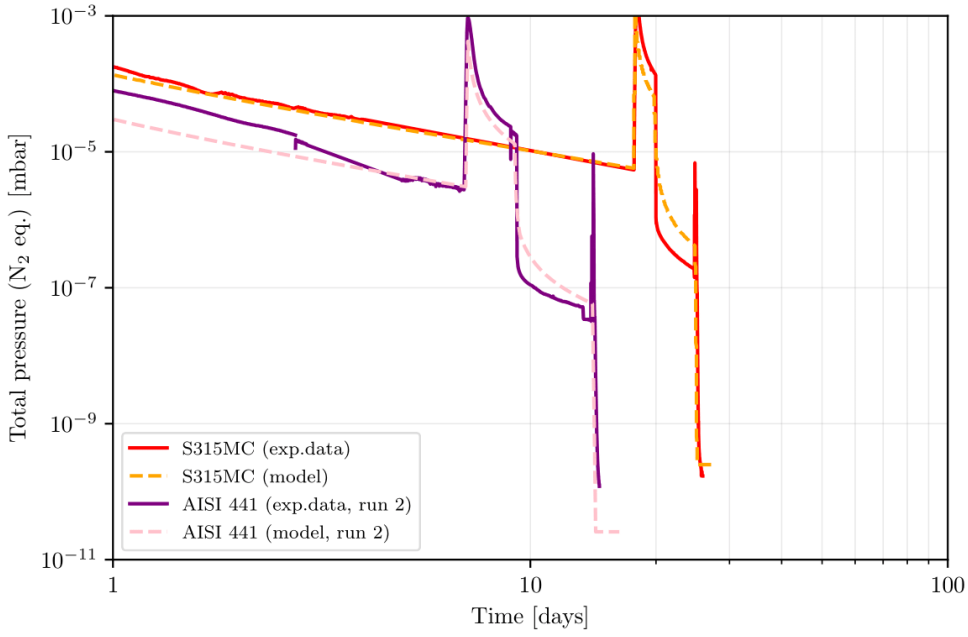

(b) S315MC and AISI 441 corrugated chambers pressure follow-ups.

Figure 8.2: AISI 304L-VF, S315MC and AISI 441 corrugated chambers pressure follow-ups from room temperature pumpdown until the end of 80°C, 7 days bakeout.The system parameters used for the numerical simulations are: $n_{m_{S315MC}} = 4.6 \times 10^{20}$ molecules/cm^2, $n_{m_{AISI441(\text{run 2})}} = 8.5 \times 10^{19}$ molecules/cm^2, $E_0 = 1.5$ eV, $E_1 = 0.3$ eV, $\tau_0 = 10^{13}$ s, $s_0 = 1$, $P_0 = 1000$ mbar, $A = 28800$ cm^2, $V = 266.9$ l.

The follow-up of the pumpdowns and NEG-assisted bakeouts for the three chambers compared with the isothermal model(corrected to real chambers' temperature) are reported in Fig. 8.2. Despite the instrumentation outgassing rates limiting the ultimate pressures for the three chambers, the model adheres quite well to the experimental data. As per the other simulations, the isotherm model relies on the Kanazawa approximation and, hence, assumes an instantaneous quasi-static equilibrium between the gas phase and the chamber's wall throughout the entire pumpdown process. As previously presented measurements show, this works quite well for almost all cases. As anticipated (see Section 2.2), during the sudden change in pumping speed, the Kanazawa conditions are lost due to the loss of thermodynamic equilibrium.

This effect can be seen on all three curves of Fig. 8.2 with a slight mismatch between the models and the experimental data during the first pressure drop. To better simulate the curves, a kinetic term has to be added to Eq. (2.6) to consider two flows: one emitted from the surface of the material defined by the equilibrium pressure corresponding to a determined coverage and the flow arriving to the wall given by the impingement rate ν, with the sticking coefficient considered equal for both flows. Another approach that could be used is the fine discretisation of the energy sites and the integration of the coverage distribution over the energy variation. This latter-explained method does not rely on the equilibrium between the chamber's wall and the gas phase.

Although these approaches provide a more adherent simulation, their influence on the prediction of ultimate pressure is negligible, helping only to simulate the transient phase better.

Given the impossibility of directly comparing the measured ultimate pressures with those forecasted by the models, a tentative comparison was made with the partial pressures measured with the RGA (see Fig. 8.3). The RGA used was not calibrated specifically for H_2O; therefore, in the absence of a measured H_2O calibration factor, it was estimated from the Relative Sensitivity Factor (RSF) between H_2O and N_2. With an RSF of 1.11 [153] and a measured sensitivity for N_2 of 11 A/mbar, the resultant calibration factor for H_2O corresponds to 12.1 A/mbar. The H_2O partial pressure calculated from the RGA spectra (see Fig. 8.3) and simulated at the measurement temperature are reported in Table A.5 and depicted in Fig. 8.4.

The ultimate water partial water prediction seems to be aligned with the measured value for the AISI 304L-VF while differing from a factor of 3.9 up to 10.4 for the mild steel and ferritic stainless steel, respectively. The uncertainties associated with this comparison are not easy to identify. Among the multiple sources of errors, one can point to possible instabilities of the RGA sensitivity due to the temperature fluctuations and cycles, simulation correctness at low partial pressures and unknown surface evolution during the treatment, to name a few. For this purpose, the pressures given by the model can be assumed as upper limits. Despite the comparison result, it has proven that increasing the pumping speed via NEG activation during bakeout effectively helps to reduce the duration of low-temperature bakeouts while meeting the typical water partial pressure requirements for GWD (see Fig. 3.4).

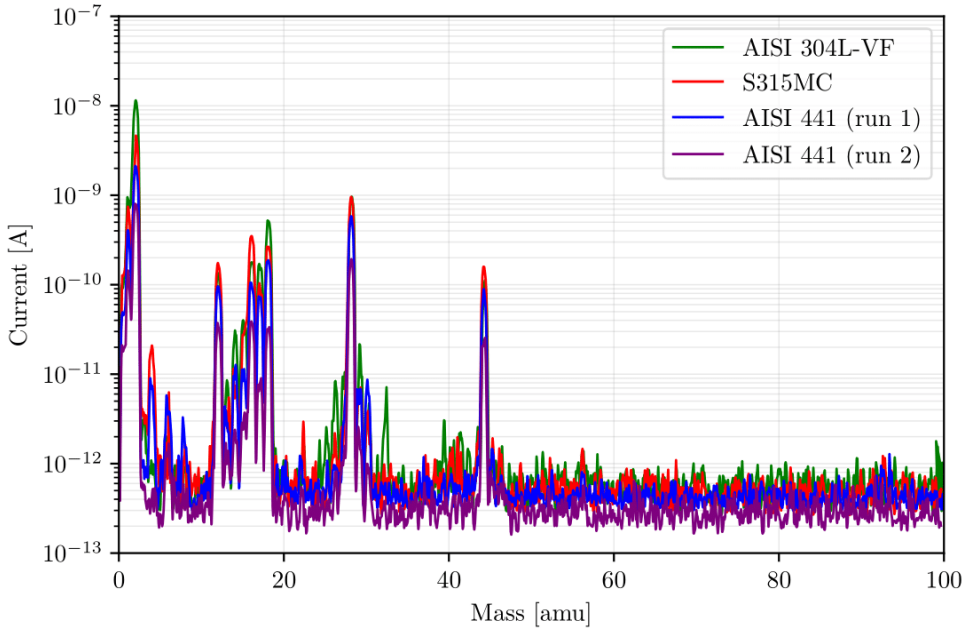

Figure 8.3: Gas composition measured at 20±3°C 48 h after the 80°C, 7 d bakeout with the BA gauge on. The AISI 304L-VF hydrogen signal, at the time of the reported bakeout, was largely dominated by the closing flanges erroneously not fired after manufacturing.

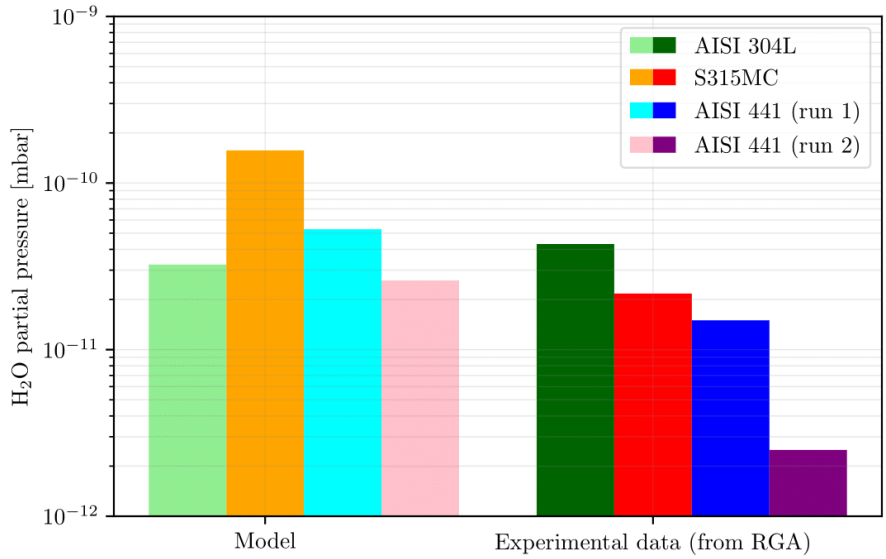

Figure 8.4: Graphical comparison of the modelled and measured ultimate water partial pressure for the three corrugated chambers baked at 80°C for 7 days.

9. Preliminary conclusions on materials

New discoveries in science and their flow of new inventions will continue to create a thousand new frontiers for those who still would adventure.

-Herbert Hoover-

In the first part of the work, the UHV of compatibility of mild and ferritic stainless steels was explored and analysed quantitatively.

The selected samples exhibited water vapour outgassing rates that followed the expected reciprocal function of pumping time before bakeout. Ferritic stainless steels showed outgassing rates comparable to those of austenitic stainless steels, while mild steel samples had rates of 1.3 to 9 times higher. These differences and the wide variation in values can be attributed to the morphology of the surface oxide layers, with thicknesses ranging from 1 nm to 10 µm, as revealed by SEM/FIB cross-sectional analysis.

Experimental studies on the water vapour binding energy of mild steel and ferritic stainless steel confirmed the accuracy of numerical simulation codes based on desorption isotherms. These simulations are crucial for optimizing the costs associated with conditioning the vacuum of GWD beam pipes.

TPD analysis, conducted up to 850°C, revealed that the hydrogen content extracted from mild steel and ferritic stainless steel samples was significantly lower—by 10 to 75 times—than that typically found in AISI 304L stainless steel. This reduction was expected due to the lower hydrogen solubility in the BCC structures characteristic

of the ferritic alloys studied. The TPD peaks indicated a more complex desorption process than in austenitic stainless steels, where hydrogen diffusion is the dominant factor. The shape and position of these desorption peaks and the concurrent release of carbon-containing molecules suggest that hydrogen release might be linked to de-trapping from either the metal or the oxide layer. Structural transformations, such as those introduced during manufacturing, may enhance this de-trapping, while chemical changes in the surface layer may also play a role. Although identifying the exact origin of these peaks lies beyond the scope of this study, their significant impact on outgassing rates warrants further investigation.

The bakeout temperatures chosen for this study were relatively low compared to the typical values used in UHV systems. This approach was selected as it represents the most practical and efficient method for baking out the beampipes of GWDs using the Joule effect, where an electrical current is applied to the vessel's walls. The study demonstrated that these lower temperatures do not present an issue for hydrogen outgassing. Specifically, the measured hydrogen-specific outgassing rates of the tested alloys, recorded at room temperature after a 48-hour bakeout at 80°C, were within the range of 10^{-14} mbar l s^{-1} cm^{-2}. These values are comparable to those observed in vacuum-fired or air-baked austenitic stainless steel vacuum chambers and meet the stringent requirements for future GWDs. Moreover, these results offer the advantage of avoiding costly and time-consuming high-temperature degassing treatments.

Despite the low outgassing rates exhibited by mild steel after bakeout, water vapour outgassing remains a concern, as it significantly influences the ultimate pressure after several days of bakeout at 80°C. However, a gradual decrease in the ultimate pressure was observed after a series of 80°C bakeouts, indicating a progressive reduction in the water vapour outgassing rate. This conditioning of the surface appears to be semi-permanent, with effects lasting for at least six months after exposure to air in a laboratory setting. The nature of this behaviour and its implications for the feasibility of using mild steel beampipes in GWDs will be explored in future studies. Furthermore, this work underscores the importance of surface quality, stability, and corrosion resistance in validating the feasibility of mild steel beampipes for next-generation GWDs.

Conversely, ferritic stainless steels present a ready-to-use solution, offering better water outgassing rates, better surface stability, and similarly low outgassing rates after bakeout compared to mild steels. The use of ferritic stainless steels for constructing next-generation GWD beam pipes, combined with the adoption of a corrugated pipe profile, would streamline the production process, reduce overall costs and production time, and facilitate meeting the stringent vacuum requirements necessary for the next generation of GWDs like the ET and CE.

Lastly, this work demonstrated the benefits of using NEG pumps during the bakeout phase. This approach effectively reduces the duration of low-temperature bakeouts while still meeting the stringent water partial pressure requirements for GWDs. Despite these positive results, further studies are needed to assess the adoption of this technique in larger prototypes with better sensitivity and more refined isothermal models.

V - Design of the ET beam pipe vacuum system -

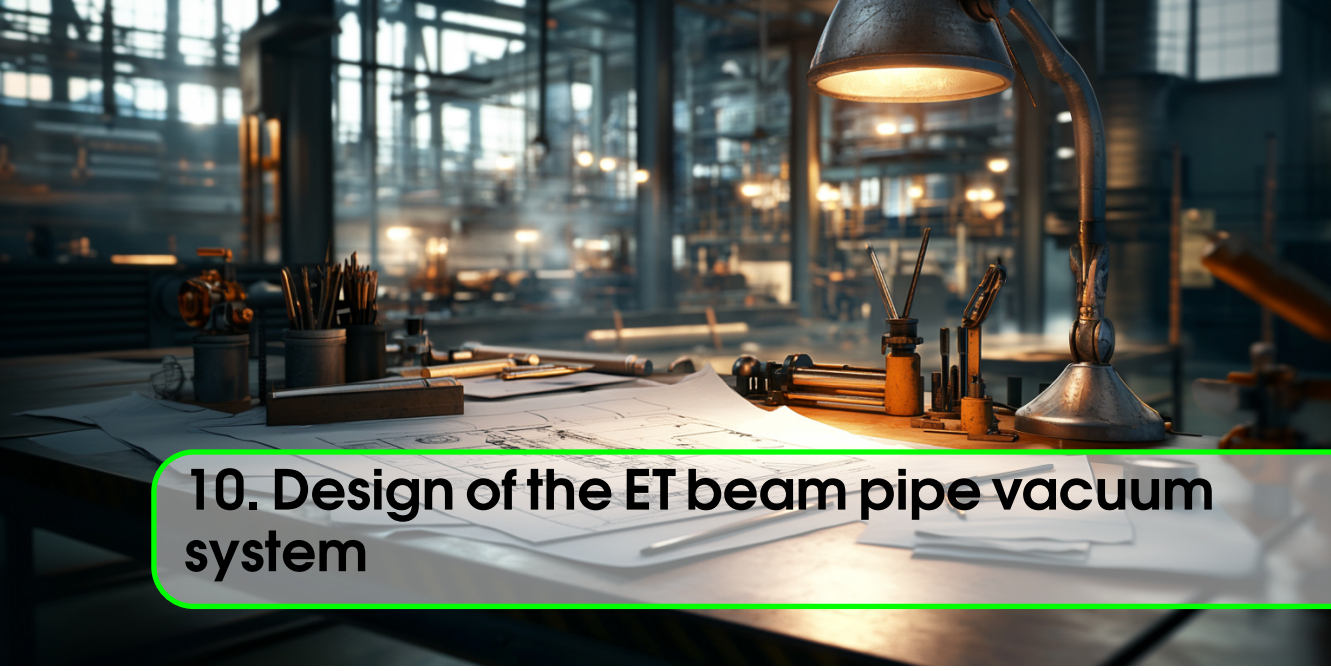

10. Design of the ET beam pipe vacuum system

Scientists investigate that which already is; Engineers create that which has never been.

-Albert Einstein-

In this chapter, the requirements and infrastructure information for the ET beam pipes are reviewed. Building on this foundation, preliminary considerations and assumptions for designing the ET beam pipe vacuum system are presented and discussed. The result of the assumptions will shape a new design of the ET beampipe vacuum system.

10.1 ET beam pipe requirements and technical infrastructure

As presented in Section 3.3, the 10 km tunnels hosting the beam pipes are 6.5 m large, with the 1 m in diameter beampipes arranged as in Fig. 10.1. For this design exercise, the presence and volume occupancy of the beam pipes and pumping groups supporting systems, the space needed for welding and cutting the pipes, and the presence of fire fighting equipment and auxiliary services are not considered. If the internal diameter of the tunnel is fixed, their presence will make the interaxle spacing between the HF and LF lines smaller than 4 m.

In 2024, the ET collaboration re-defined several requirements from scientific and engineering perspectives regarding the ET beam pipe [154]. The most important is the residual gas content in the beam pipe. Although no specific partial pressures are

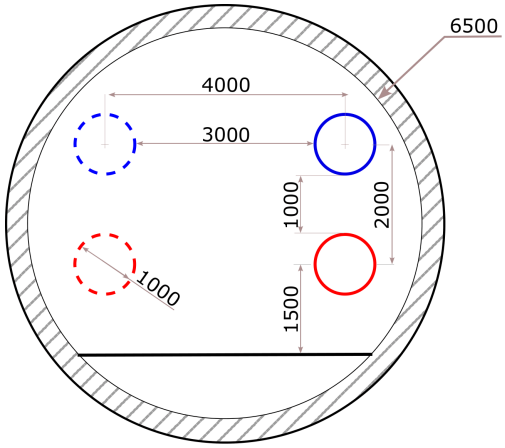

Figure 10.1: Schematic of the cross-section of the ET tunnel updated in 2023[j]. The two interferometers run parallel (blue and red). The beam pipes with the solid line represent the HF, and those with the dashed line represent the beam pipes for the LF. Dimensions in mm.

foreseen for the main gas species, a general yet stringent requirement for strain noise is set. ET-LF and ET-HF require strain noise to be lower than 1×10^{-25} $1/\sqrt{Hz}$. There is also a stringent partial pressure requirement for hydrocarbons with a mass higher than 100 amu, allowing a maximum partial pressure of 1×10^{-14} mbar.

During operation, minimal vibration and acoustic noise are required, as their presence induces unwanted stray light and environmental noise. In-depth analyses are ongoing to determine the acceptable threshold.

Specific maximum temperatures and humidity levels are set to ensure a safe environment for workers and preserve the structural integrity of the infrastructure. During bakeout, if access is permitted, the maximum tunnel air temperature is allowed to be 29°C. During standard operation, the temperature can reach up to 26°C. The humidity must not exceed 60%.

Lastly, the vacuum system's operational lifetime should be at least 50 years.

The requirements described above, whether already defined or given as a preliminary indication, can be translated into a set of technical consequences as summarised in Table 10.1.

The low-pressure requirement for heavy hydrocarbons directly impacts the cleaning methods and handling processes and indirectly affects the type of pumps used. To minimise the possible oil contamination from vapours backstreaming from backing pumps or leakages from the TMPs' bearings, all the fore pumps are assumed be dry, and the TMPs should be equipped with magnetic bearings (Maglev) to ensure an oil-free, clean vacuum.

Although not yet specified, the maximum vibration noise allowed during interferometer operations, similar to the constraints imposed by oil contamination, indirectly determines the types of pumps used in the UHV regime. To anticipate potential issues,

[j]Original drawing courtesy of Einstein Telescope Organization - Engineering Department.

Table 10.1: Technical implications on the ET beam pipe pumping system of the newly redefined scientific and technical requirements.

Requirement	Technical consequence
Low contamination levels	Only dry fore pumps and Maglev TMPs
Low vibration noise during operations	UHV pumping with chemical pumps only
Vacuum system lifetime of 50 years	Interlocks, gate valves on pumping ports, venting system

it is imposed that all pumps maintaining UHV pressures will be chemical pumps, such as evaporable and non-evaporable getters, including IPs, NEGs and TSPs.

The 50-year requirement for the vacuum system lifetime implies that all consumables (such as pumps, instrumentation, etc.) should ideally have a lifespan of at least 50 years. However, since guaranteeing such long lifespans for consumables is impossible, a mitigation strategy is necessary. This involves installing a gate valve on each pumping port, allowing for the safe replacement of faulty components without compromising the UHV conditions of the beam pipe. Interlocks and controlled venting systems are also envisioned to maintain the interferometer's operation and protect the UHV conditions. These systems will mitigate the detrimental effects of a possible vacuum breach.

10.2 Preliminary considerations and assumptions

10.2.1 Beam pipe material

Assumption

AISI 441 is assumed to be the structural material for the beam pipes, pumping modules, and all associated flanges. Additionally, all fittings and anti-chambers used to install the UHV pumping groups and optical baffles are also assumed to be made of AISI 441.

The parameters obtained from binding energy measurements are used to simulate the water outgassing rate during both room temperature pumpdown and bakeout, using Temkin-based isotherms.

The measured outgassing rates after bakeout, limited by the system's background, are assumed to provide a conservative estimate of the ultimate pressures. As discussed later in the text, the bakeout temperature and duration range from 80 to 150°C and 2 to 30 days. Due to the lack of data for some configurations, the outgassing rates after bakeout are assumed to be equal to those measured after a 150°C, 48h bakeout.

The vacuum properties and outgassing rates are summarised in Table 10.2.

Table 10.2: Vacuum properties and outgassing rates assumed for AISI 441.

Parameter	Value
n_m [molecules/cm^2]	4.5×10^{15}
E_0 [eV]	1.5
E_1 [eV]	0.2
τ_0 [s]	10^{13}
s_0	1
q_{H_2} [mbar l s^{-1} cm^{-2}]	1.0×10^{-15}
q_{CH_4} [mbar l s^{-1} cm^{-2}]	1.0×10^{-17}
q_{CO} [mbar l s^{-1} cm^{-2}]	3.7×10^{-17}
q_{CO_2} [mbar l s^{-1} cm^{-2}]	1.4×10^{-17}

10.2.2 Vacuum system sectorisation

Considerations

In the 2020 ET CDR, a single vacuum sector 10 km long was proposed, with no intermediate sectorization. This decision may be considered too risky. Smaller sectors, each less than an arm's length, would offer several advantages, among which:

- Flexibility during installation: Multiple vacuum sectors provide flexibility and save time during the installation phase. For example, while one sector is being installed, the neighbouring sector can undergo pumpdown, baking, or in-situ leak testing without waiting for the entire arm's installation to be completed. This multi-sector approach could reduce the number of conditioning equipment needed (such as rough pumps and mobile pumping groups), leading to significant cost savings.
- Vacuum quality check: The multi-sector approach would allow the possibility of accumulations in the beam pipe volume to check for small leaks and or qualitatively measure the outgassing rates' evolution over time.
- In a single-sector scenario, a major leak would compromise the entire arm vacuum, making 2/3 of the interferometer unusable due to noise during repair and recommissioning. Dividing the beam pipe into multiple sectors by gate valves allows the preservation of UHV conditions in unaffected sectors, enabling selective intervention in damaged areas. This results in faster and cheaper decommissioning and recommissioning due to each sector's shorter length than the entire arm (bakeout power and cost are directly proportional if a direct joule effect bakeout is used).

While vacuum sectors offer clear advantages, their implementation would require installing large DN1000 gate valves along the beam lines, significantly increasing the vacuum system cost, with each valve costing up to 200 k€. Additionally, the tunnel continuity would need to be interrupted by recesses to accommodate the sector valves, considerably raising the infrastructure costs.

Another drawback of sector valves is the local increase in the outgassing rate generated by the valve body and the gate sealant (typically Viton). To mitigate this issue, the valve body should be air-baked or vacuum-fired, the sealant material should be thoroughly degassed, and local additional pumps should be installed on the valve bodies.

Given that the project is still in the design phase, evaluating the number of sector valves and their distances for this exercise is based on achieving the best cost/benefit ratio.

Assumption and design criteria

The minimum sectorization that balances costs and risks is determined to be two sectors, each 5 km long.

To avoid placing the valve where the laser is at its minimum waist, which is more sensitive to pressure variations, and to increase system reliability in case of valve malfunction, we assume two sector valves are mounted 10 meters away from this sensitive point.

Therefore, the beam pipe is divided into three sectors: two outer sectors, each 4.99 km long, and one central sector, 20 meters long (see Fig. 10.2).

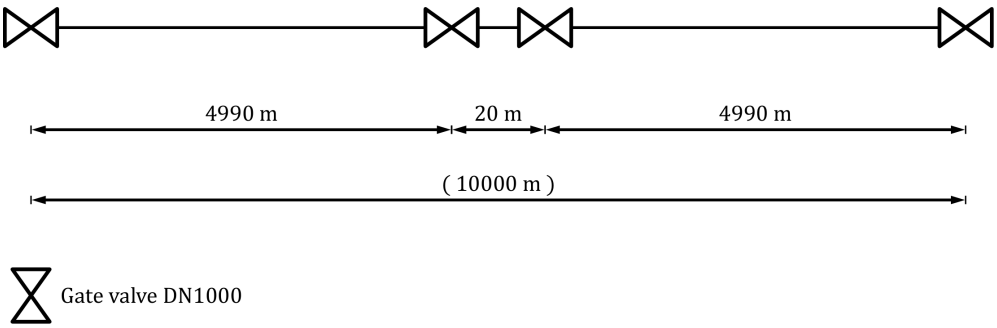

Figure 10.2: Schematic of the proposed sector length. The two valves DN1000 at the extremities delimit the beam pipe from the cryotraps and experimental areas. The central sector valves are 10 m equidistant from the midpoint of the beam pipe length.

To simplify the example for later development, it is assumed that one sector is commissioned with one valve open, allowing for a 5 km commissioning length. Meanwhile, the other sector is commissioned at its shortest length of 4.99 km.

Unless otherwise stated, all subsequent considerations and simulations will be applied to a 5 km sector.

10.2.3 Pumping port size, orientation and distribution

Boundary conditions

All the pumping ports should be equipped with a gate valve to ensure the interferometer's lifetime of 50 years.

Design criteria on ports orientation, distribution and gate valve type

Given the undeterminate space that has to be left in the tunnel to accommodate the beam pipe supporting system and the interaxle spacing between the ET-HF and ET-LF beamlines, it is designed beforehand to position the pumping ports on the bottom half of the beam pipes (see Fig. 10.3). This arrangement will leave more space at the centre, allowing the beampipe supporting system to be installed freely and allowing the safe movement of goods and personnel during operation. Locating the pumping ports/pumps on the bottom half of the beam pipes will eliminate the need for recesses, foreseen instead in the 2020 ET CDR.

The pumping ports are considered to be 20 cm long (taken from the inner surface of the beam pipe). The chosen length, considering the thickness of the flanges, can accommodate insulation thicknesses up to 15 cm without impeding access to the fastening of the flanged connection and allow easy installation/removal of the insulation.

Besides the port for the rough pumping assumed to be located in the first 10 m from the sector valve, as planned in the 2020 ET CDR, this design foresees pumping ports spaced 500 m.

The gate valves installed in front of the pumping ports are considered Viton sealed and electro-mechanic actuated. To minimise their outgassing rate contribution, the body and seal are assumed to be thoroughly degassed. Based on the results of previous studies done on heat-treated gate valves [155], it is assumed an H_2 outgassing rate coming from the valves of 1.2×10^{-11} mbar l s^{-1}.

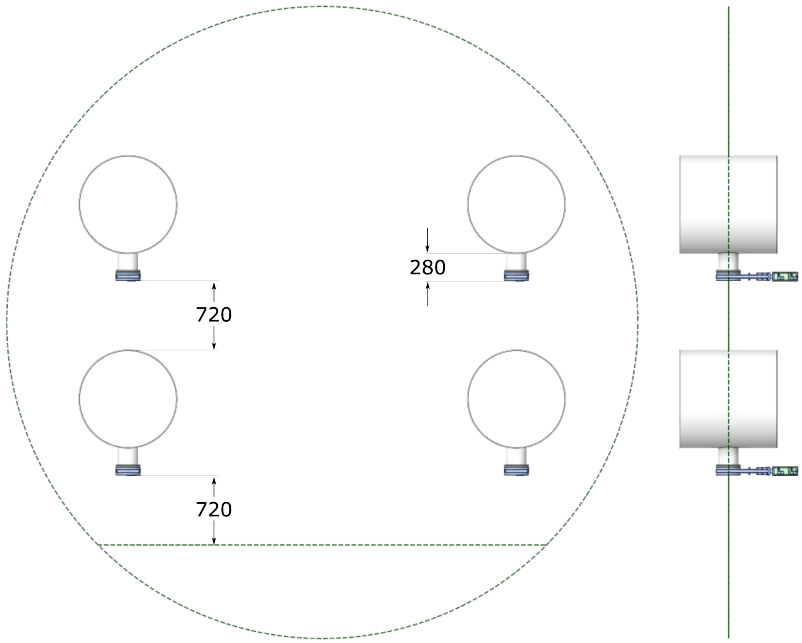

Figure 10.3: 3D schematic of the tunnel cross-section showing the beam pipes arrangement and the DN200 pumping ports and DN200 gate valves orientations. The dimensions are in mm.

Considerations on ports size

For this design exercise, four diameters are analysed: DN160, DN200, DN250, and DN320. Given the ratio diameter/length for the port, which is close to one, in this case, the size of the pumping port is primarily determined by the conductance of the port's aperture. The effective pumping speed S_{eff} per i gas of interest, is given by:

$$\frac{1}{S_{eff_i}} = \frac{1}{C_{port_i}} + \frac{1}{C_{valve_i}} + \frac{1}{S_i} \tag{10.1}$$

where C_{port} is the conductance of the port, C_{valve} is the conductance of the gate valve and S the pumping speed. Considering a pump with a gas-independent pumping speed of 2000 ls^{-1}, in Fig. 10.4 is plotted the effective pumping speed at the entrance of the pumping port as a function of the main gas species for the flanges sizes analysed.

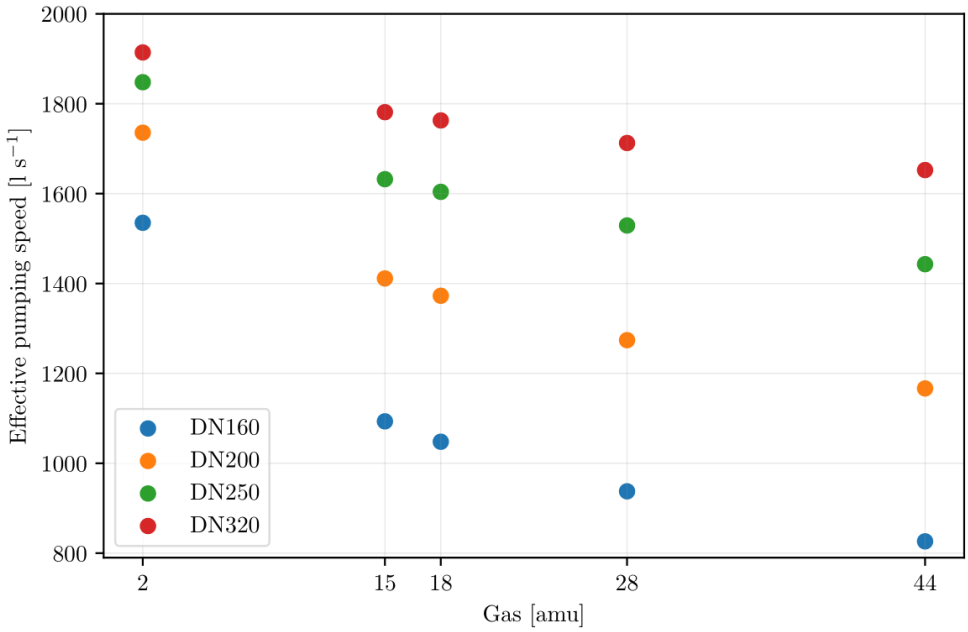

Figure 10.4: Effective pumping speeds for the main UHV gases of interest for DN160, DN200, DN250 and DN320 port sizes equipped with a 2000 l s^{-1} gas independent pump.

Assumption on ports size

A port size of DN200 has been selected to maximize effective pumping speeds while keeping the pumping groups at a manageable size. To efficiently use space, the valves will be mounted with their bodies parallel to the axis of the beam pipes. The DN200 valve has a width of 8 cm. Given these dimensions, the available space for positioning the pumping groups is 72 cm for both bottom and upper beamlines (see Fig. 10.3).

10.3 Rough pumping

Boundary conditions

The fore pump must be dry to reduce the possibility of heavy hydrocarbon contamination.

Design criteria

Similarly to what was done for the 2G-GWD (see Section 3.2), the rough pumping could be executed from one extremity of the beampipe. The pumping station's size and the beam pipes' arrangement make installation challenging and time-consuming. As a result, it is assumed that the pumping station is positioned near the centre of the tunnel and connected to the pumping ports via a flexible hose (see Fig. 10.5).

Given the interferometer layout, one rough pump is considered present at each vertex of the triangle. Installed on a hydraulic cart, the fore pump can be pivoted around the experimental caverns to pump the beamlines sharing the same vertex. Once the intermediate pumping begins, the gate valve connected to the rough pumping group can be closed, and the pumping station can be vented and installed in another neighbouring sector.

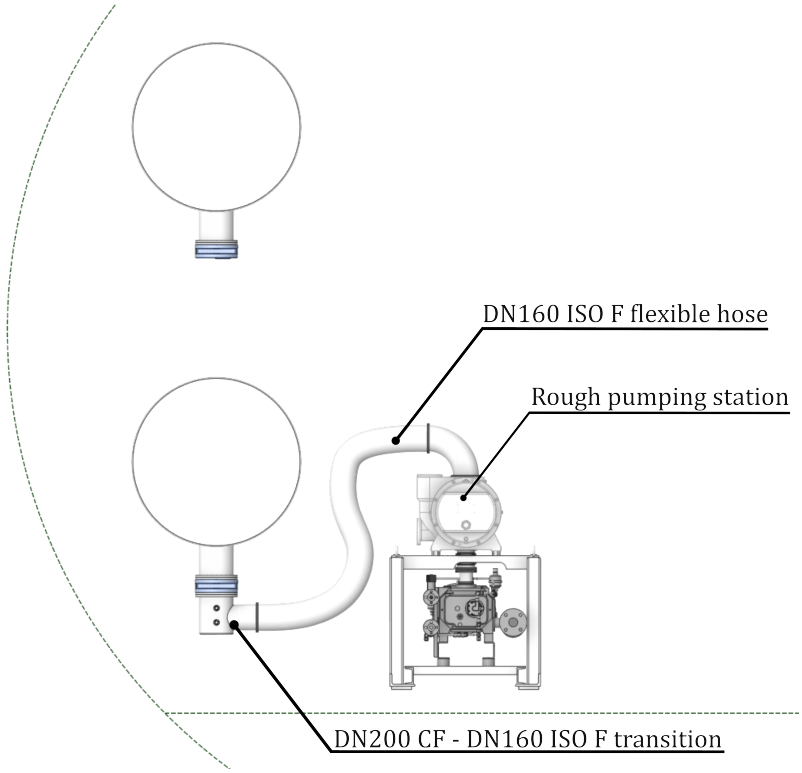

Figure 10.5: 3D schematic of the tunnel cross-section showing the rough pumping station connected to the beam pipe. The rough pumping station model, taken from the Pfeiffer Vacuum GmbH database (CombiLine WH 1800 P), is connected to a DN200 CF to DN160 ISO-F transition, represented as an instrumented pot, which allows for the installation of gauges and venting valves.

Considerations on the pump size

Considering three possible pumping groups - 4000 $m^3\ h^{-1}$, 2000 $m^3\ h^{-1}$ and 1000 $m^3\ h^{-1}$ (inlet port: DN250, DN160 and DN100, respectively) - backed by 600 $m^3\ h^{-1}$ and 300 $m^3\ h^{-1}$ screw pumps, respectively, and connected to the beam pipe pumping ports with a 2.5 m flexible hose and necessary fittings to link the roughing stations' inlet flanges to the gate valves (see Fig. 10.5), the pumpdown curve can be calculated using Eq. (2.7). Being in the laminar flow regime, the conductance of the beam pipe and of the connections are dependent on the geometry and on the pressure; therefore, the effective pumping speed to be inputted in the ODE is calculated as:

$$\frac{1}{S_{eff}} = \frac{1}{S_{pump}} + \frac{1}{C_{sector}} + \sum \frac{1}{C_{connections}}$$

with C_{sector} and $C_{connections}$ are computed as [156]:

$$C = p_{avg}\ \frac{\pi\, D^4}{128\, \eta\, L} \tag{10.2}$$

where D and L are the diameter and length of the component, η is the viscosity of air, and p_{avg} is the average pressure across the beginning and the end of the component. Despite the pumping station being capable of reaching x10-x100 better ultimate pressure, it is decided to stop at 0.1 mbar to avoid backstreaming of gas. The imposed ultimate pressure is low enough to start the TMPs and begin the intermediate pumping.

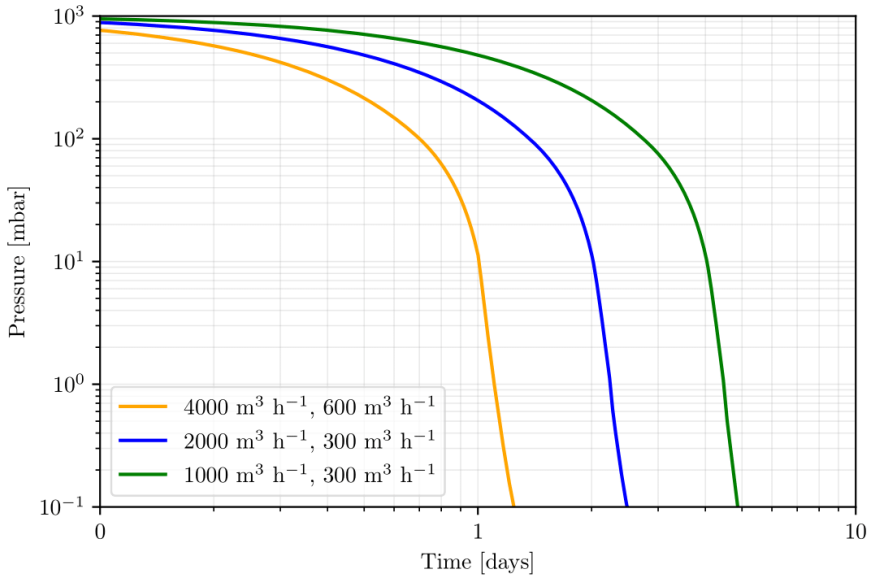

Figure 10.6: ET 5 km long sector pumpdown curve from 1000 mbar to 0.1 mbar for roughing stations with 4000 $m^3\ h^{-1}$, 2000 $m^3\ h^{-1}$ and 1000 $m^3\ h^{-1}$ nominal pumping speeds at 1 mbar. The curves are simulated using an air temperature of 20°C (η = 1.8×10^{-5} Pa s) and commercial products' pumping speed curves.

As shown in Fig. 10.6, the time needed to pump down the chamber to 0.1 mbar is about 5 days, 2.5 days, and 1.3 days for the smallest to the largest pump, respectively. Considering the weight (ranging from 0.9 to 2 tons), size, cost, and marginal gain in pump-down time, the best compromise is represented by the 2000 $m^3\ h^{-1}$.

Assumption

Therefore, the rough pumping station selected for this design exercise is a dry root pump with a nominal pumping speed of 2000 $m^3\ h^{-1}$ at 1 mbar, backed by a screw pump with a nominal pumping speed of 300 $m^3\ h^{-1}$.

10.4 Intermediate pumping

Boundary conditions

According to the requirements, the intermediate pumping should be performed using magnetically levitated TMPs backed by a dry roots pump.

Design criteria

The setup used for the rough pumping station cannot be replicated here, as the piping between the port and the pump would significantly reduce the TMPs' effective pumping speed. Therefore, the TMPs must be mounted directly on the gate valves, while the backing pumps can be placed on a mobile cart at the ground level. The connection between the TMPs and the pumping port should be made via a transition that allows the installation of a pressure gauge and a DN40 all-metal angle valve for controlled venting.

Air-cooled TMPs are preferred for easier infrastructure integration and general safety (considering direct joule bakeout, water sources should be avoided near electrical ones). Three pump sizes are considered for use: 800, 1500 and 2000 $l\ s^{-1}$ (nominal pumping speed).

As the TMP groups are foreseen to be used once in the interferometer's lifetime to optimise their use and cost, after the bakeout, the pumps could be removed and allocated to a neighbouring sector to proceed with the pumping phase.

Given the arrangement, the pumps must be easy to install and remove. To simplify temporary supporting systems and ease the handling of the pumps, the pump should not weight more than 50 kg (three operators can manually install it with minor tool assistance).

Assumptions on TMPs size

Given the factor of 1.5 in pressure evolution between the smallest and greatest size considered (see Fig. 10.7), the 800 $l\ s^{-1}$ TMP is assumed for this design exercise. On top of the vacuum properties, the selected size is lighter than the other two (20 kg against the 30 and 45 kg of the 1500 and 2000 $l\ s^{-1}$, respectively). The cost of the 800 $l\ s^{-1}$ is also 20% lower than the other two sizes here analysed. The backing pump here suggested to be used is a 40 $m^3\ h^{-1}$.

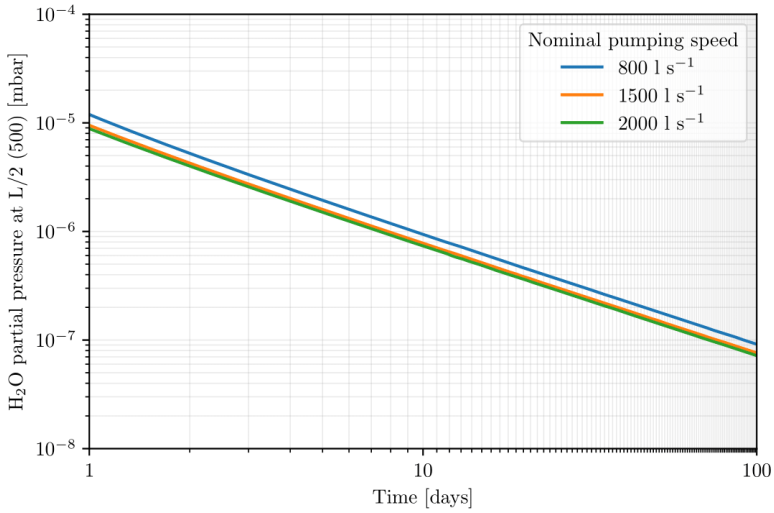

Figure 10.7: Isothermal-based (Temkin) simulation of a pumpdown of a 5 km long ET sector from 0.1 mbar using TMPs with nominal pumping speeds of 800, 1500 and 2000 l s^{-1}, spaced 1 km. The pumpdown curve represents the maximum pressure reached at the midpoint between two TMPs. The system parameters used for the simulation are: $n_m = 4.5 \times 10^{15}$ molecules/cm^2, $E_0 = 1.5$ eV, $E_1 = 0.2$ eV, $\tau_0 = 10^{13}$ s, $s_0 = 1$, $P_0 = 1 \times 10^{-1}$ mbar, T = 20°C.

Considerations on TMPs distribution

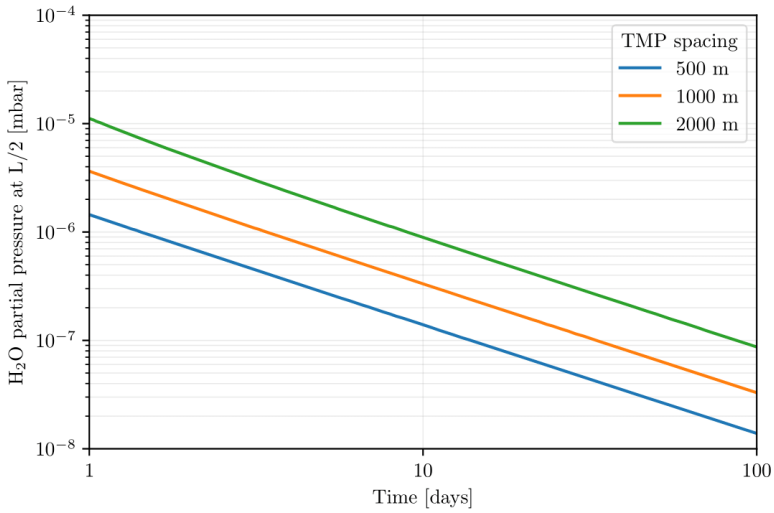

Figure 10.8: Isothermal-based (Temkin) simulation of a pumpdown of a 5 km long ET sector from 0.1 mbar using 800 l s^{-1} TMPs spaced 500, 1000, and 2000 m. The pumpdown curve represents the maximum pressure reached at the midpoint between two TMPs. The system parameters used for the simulation are: $n_m = 4.5 \times 10^{15}$ molecules/cm^2, $E_0 = 1.5$ eV, $E_1 = 0.2$ eV, $\tau_0 = 10^{13}$ s, $s_0 = 1$, $P_0 = 1 \times 10^{-1}$ mbar, T = 20°C.

The distribution of TMP groups is now analysed to optimise material use and cost. The spacing considered are 500 m, 1000 m, and 2000 m (see Fig. 10.8).

Despite the almost one order of magnitude better pressure between the 500 and 2000 m spacings, deploying pumps every 500 m is neither practical nor cost-effective in the context of ET. Given that the room temperature pumpdown using TMPs is anticipated to occur only once during the experiment's lifetime, reducing the number of TMPs and using them strategically across different beam pipes is more efficient. This approach lowers costs after commissioning for the entire ET and provides more flexibility during the pumpdown procedure.

Assumption on TMPs distribution

Considering the limited use of TMPs and the cost-saving aspect, the assumed distribution is one 800 l s^{-1} TMP every 2 km.

Assumption on bakeout starting pressure/time

As already pictured in Fig. 10.7, the difference in pumping speed between the analysed sizes had a small, if not negligible, effect on the ultimate pressure before bakeout. Additionally, as depicted in Fig. 10.9, the starting pressure of the bakeout does not affect the ultimate pressure achieved after the process. Therefore, the pumpdown time at room temperature, before the start of the bakeout, is arbitrarily foreseen to be carried out for 7 days. In this time frame, the in situ leak detections of the welded and flanged joints and the insulation material installation can be performed comfortably.

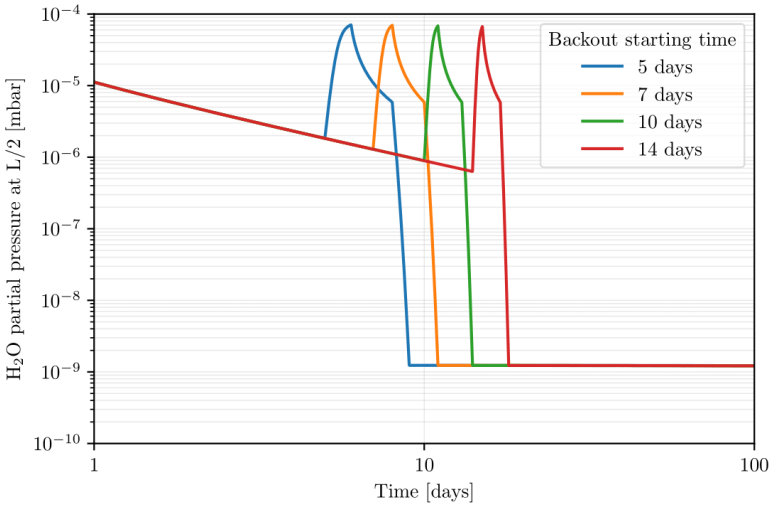

Figure 10.9: Isothermal-based (Temkin) simulation of the bakeout (100°C, 48 h) of a 5 km long ET sector after 5, 7, 10 and 14 days of room temperature pumping using 800 l s^{-1} TMPs spaced every 2000 m. The pumpdown curve represents the maximum pressure reached at the midpoint between two TMPs. The system parameters used for the simulation are: n_m = 4.5 $\times$ 10^{15} molecules/cm^2, E_0 = 1.5 eV, E_1 = 0.5 eV, τ_0 = 10^{13} s, s_0 = 1, P_0 = 1$\times 10^{-1}$ mbar, T = 20°C.

10.5 Bakeout

Boundary conditions

As per most of the 2G-GWD, the most efficient way to bakeout the ET beamlines is through the direct joule effect. The beam pipes must be insulated to minimise heat losses and control temperature uniformity. Due to the pumping port's design, the insulation's radial thickness should be equal to or less than 15 cm. The temperature in the tunnel during bakeout should be less than 29°C. As an expensive and energy-demanding activity, the bakeout of the beam pipes is foreseen to be executed just once in the interferometer's lifetime.

Design criteria on the bakeout temperature and duration

The bakeout temperature considered for ET ranges from 80 to 150°C for durations of 1 to 20 days. The decision to limit the duration to 20 days is to contain the intermediate pumping and bakeout phases in less than one month. The ramping up of the temperature and the cooldown should be done with 5°C/h ramps to allow uniformity in the temperature distribution and not induce leaks due to the sections' different thermal expansions.

Design criteria on the pumping scheme

The pumping schemes taken into consideration are two:

(**A**) Pumping with the TMP groups until the cooldown to room temperature. At room temperature, the pumping of H_2O is then continued by the getters (NEGs and IPs).

(**B**) Pumping with the TMP group meanwhile, after 1/3 of the bakeout duration, activate the NEG pumps until the cooldown. At room temperature, the pumping of H_2O continued by the getters (NEGs and SIPs).

In the case of a NEG-assisted bakeout, the pumps—except those eventually coupled with the TMPs groups—are foreseen to remain installed to continue the UHV regime. Removing the pumps will increase the risk of dust contamination or unwanted venting and reduce the delivery time and manpower use.

The NEG pumps should have enough capacity per single activation run to carry out 2/3 of the bakeout. Before cooldown, the pumps should be re-activated to exploit the maximum pumping speed and capacity for the UHV regime. To guarantee a reasonable effect of the NEG activation given the minimum spacing of 500 m and taking into account the reduction of the pumping speed due to conductances given by the fittings, the nominal H_2O pumping speed of the NEG pumps should be at least double that of the TMPs. Here, the NEG pumps are considered connected to the pumping ports via DN200 tees, allowing for the possibility of installing SIPs for UHV pumping. In layouts where a TMP and a NEG are not installed on the same port, the TMPs will be considered directly connected to the gate valves.

Consideration on pumping scheme

For the pumping scheme (**B**), NEG pumps with nominal pumping for water of 1500 l s^{-1} and spacing of 500, 1000, 1500 and 2000 m are considered. The water pressure

after bakeout, measured at half the spacing between the NEG pumps, is obtained by iterating the adsorption isotherm script over the temperature and time domains. The results are shown in Fig. 10.10.

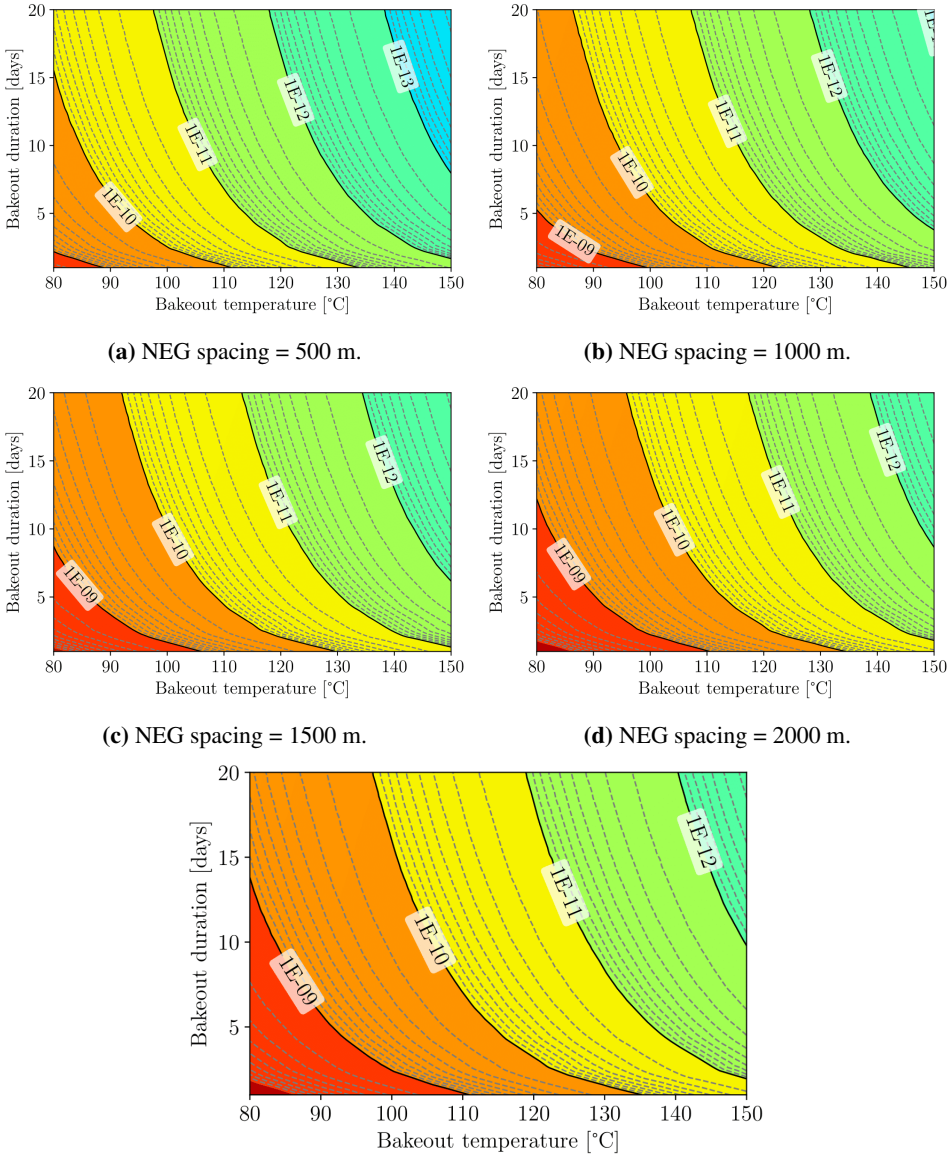

(a) NEG spacing = 500 m.

(b) NEG spacing = 1000 m.

(c) NEG spacing = 1500 m.

(d) NEG spacing = 2000 m.

(e) Only TMPs (No NEG pumping).

Figure 10.10: Maximum water ultimate pressure isobars, achieved between two NEG pumps, as a function of bakeout temperature and duration for various NEG spacings. The position of the mobile TMP groups is fixed to every 2000 m.

As expected, the 500 m spacing (see Fig. 10.10(a)) significantly reduces the bakeout temperature compared to the other spacings analyzed. For a target ultimate pressure

of 1 $\times 10^{-11}$ mbar, the 500 m spacing between getters allows achieving the desired pressure with bakeout temperatures ranging from 105°C to approximately 130°C, depending on the duration considered.

This new pumping scheme allows for some flexibility compared to the 150°C bakeout for 10 days proposed in the 2020 CDR. If the bakeout temperature is kept constant, the duration can be shortened to two days. Alternatively, if the duration remains fixed, the temperature can be lowered to 105°C.

While reducing bakeout time and temperature has clear benefits, adopting a denser spacing would require installing NEG pumps on every port. This introduces the need for a more comprehensive evaluation of cost-efficiency, factoring in the energy required for the bakeout process, the cost of thermal insulation, and the potential use of NEG pumps in the UHV regime. As demonstrated in Figs. 10.10(b) to 10.10(d), although less frequent spacing results in lower performance, it still offers efficient results at potentially reduced costs. From a vacuum pumping perspective, the most cost-effective scenario is achieved with the pumping scheme outlined in (**A**), though it necessitates maintaining a relatively high bakeout temperature.

Preliminary assumption on the pumping scheme

This assumption is based on specific considerations regarding the design. Given the presence of getter pumps optimized for the UHV regime, scheme (**B**) is proposed for the bakeout process. The NEG pump spacing of 1000 m is the preferred option due to its cost-effectiveness and operational efficiency. This configuration reduces bakeout temperature and duration while providing greater flexibility during the UHV phase. It also halves the cost of the pumping system compared to a 500-meter spacing and simplifies system integration by eliminating the overlap between TMPs and NEG pumps. The corresponding layout is depicted in Fig. 10.11.

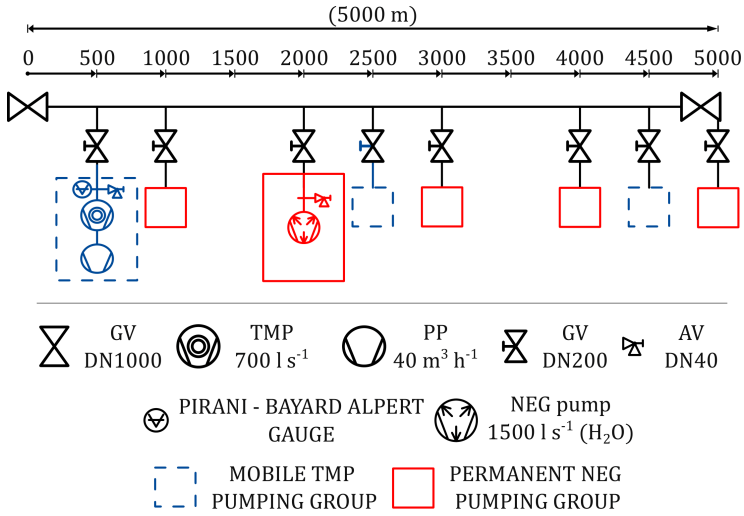

Figure 10.11: Intermediate pumping layout with the mobile TMP pumping groups (blue). spaced 2000 m and permanent NEG pumping groups (red) spaced 1000 m. AV: angle valve, GV: gate valve, PP: Primary pump, TMP: Turbomolecular pump.

Design criteria for the thermal insulation and electrical parameters of the bakeout

The current I to be provided to the beam pipes to keep them at the bakeout temperature T_{bo} is calculated from Ohm's law as:

$$I = \sqrt{\frac{Q_{term}}{R_{el}}} \quad [A] \tag{10.3}$$

where R_{el} is the electrical resistivity of the baked sector (dependent on the length, cross-section area and the material of the sector) and Q_{term} is the thermal energy needed to keep the material at T_{bo}.

The thermal energy Q_{term}, is calculated as:

$$Q_{term} = \frac{\Delta T}{R_{tot}} = \frac{T_{bo} - T_{RT}}{R_{conv} + R_{cond}} \quad [W] \tag{10.4}$$

where T_{RT} is the air tunnel temperature and:

- R_{conv} is the thermal resistivity due to convection. Dependent on the airflow in the tunnel is calculated as follows:

$$R_{conv} = \frac{1}{h_{air}\, A_{insu}} \quad \left[\frac{K}{W}\right] \tag{10.5}$$

  with h_{air} convection coefficient and A_{insu} the outer area of the tube considering the insulation thickness.

- R_{cond} is the thermal resistivity due to conduction. Dependent on the properties and thickness of the insulation it is calculated as follows:

$$R_{conv} = \frac{\log\left(\frac{R_{insu}}{R_{tube}}\right)}{2\,\pi\, k_{insu}\, L_{section}} \quad \left[\frac{K}{W}\right] \tag{10.6}$$

  where R_{tube} is the external radius of the beam pipe, R_{insu} is the external radius of the assembly pipe and insulation, k_{insu} is the insulation thermal conductivity of the insulation material, and $L_{section}$ is the length of the shortest sector baked.

The electrical power needed to bring one sector from T_{RT} to T_{bo} is calculated as:

$$Q_{ramp} = \frac{m\, c_p\, \Delta T}{3.6 \times 10^6} \quad [kWh] \tag{10.7}$$

where m is the mass of the sector and c_p is the specific heat of the steel. The electrical power to bake one sector at T_{bo} for a duration of t_{bo} hours can be finally calculated as follows:

$$Q_{bakeout} = \frac{L_{sector}\, V\, I}{d_{ps}}\, t_{bo} \quad [kWh] \tag{10.8}$$

where L_{sector} is the length of the baked sector (in this case 5 km), V is the voltage applied from the power supplier (fixed to 60 V), I is the current needed to bake the

tube at T_{bo} and d_{ps} is the distance between the power suppliers (here assumed regularly spaced every 500 m).

The cost of the power needed for the bakeout is computed as:

$$Cost_{el} = Cost_{kWh}\,(Q_{bakeout} + Q_{ramp}) \quad [€] \tag{10.9}$$

with $Cost_{kWh}$ the cost of the current in €/kWh, here assumed equal to 0.5.

The bakeout is here simulated in calm air conditions (h_{air} = 5 W m^{-2}K^{-1}) with the temperature of air in the tunnel of 20°C.

Given the absence of literature-reported values of the electrical resistivity as a function of the temperature for AISI 441, it is assumed to be equal to that of AISI 316L [157], thus:

$$\rho = 7.09 \times 10^{-7} + 7.95 \times 10^{-10}\,\Delta T \quad [\Omega\, m] \tag{10.10}$$

Due to the scarcity of cheap and fire-resistant material, only mineral wool is currently considered as insulation material. The thermal conductivity and cost of the insulation, averaged from the products available in the market, vary as follows:

- k_{insu} = 1.01 × 10^{-10} ΔT^3 + 2.50 × 10^{-7} ΔT^2 + 8.79 × 10^{-5} ΔT + 3.48 × 10^{-2} [W m^{-1}K^{-1}].
- 4 × $t_{insulation}$[cm] + 8.4 [€/m^2].

Consideration on thermal insulation and electrical parameters of the bakeout

From Eq. (10.9), the cost of the bakeout process is primarily driven by the insulation cost. To minimize costs and simplify integration, the insulation thickness should be limited, and its overall quantity should be reduced. One potential solution is using pre-made insulation shells that can be removed after the bakeout is complete and then transported and installed on the next sector.

From Eq. (10.8), it can be observed that the cost of the bakeout increases linearly with time. This suggests that higher-temperature bakeouts, performed for shorter durations, are more cost-effective than lower-temperature bakeouts over longer periods (see Fig. 10.12).

However, as illustrated in Fig. 10.13, a higher bakeout temperature results in a slightly elevated insulation surface temperature.

Assumption on bakeout temperature and duration

Given the linear relationship between bakeout cost and duration, and considering the chosen NEG distribution, the bakeout process is assumed to occur at 150°C for 2 days. This duration allows the temperature to stabilize along the entire length of the beam pipe.

The maximum ultimate pressure reached between the two NEG pumps after the full treatment is approximately 2 ×10^{-12} mbar. The sorption capacity required by the NEG pump—calculated by multiplying the area between the pumping curves with and without getters by the effective pumping speed for water—is 632 mbar l. For the selected type and size of the getter, this represents only 20% of the total capacity per sorption cycle. Thus, the pump is sufficient for the planned cycle and may not even need activation at the end of the bakeout.

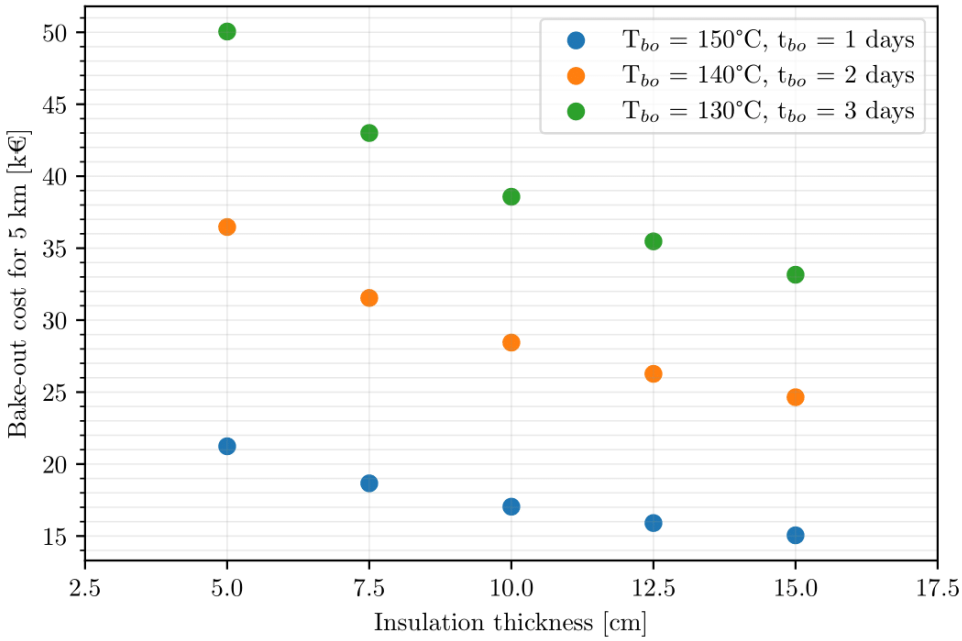

Figure 10.12: Electricity cost for the bakeout of a 5 km sector as a function of the insulation (mineral wool) thickness, temperature and duration.

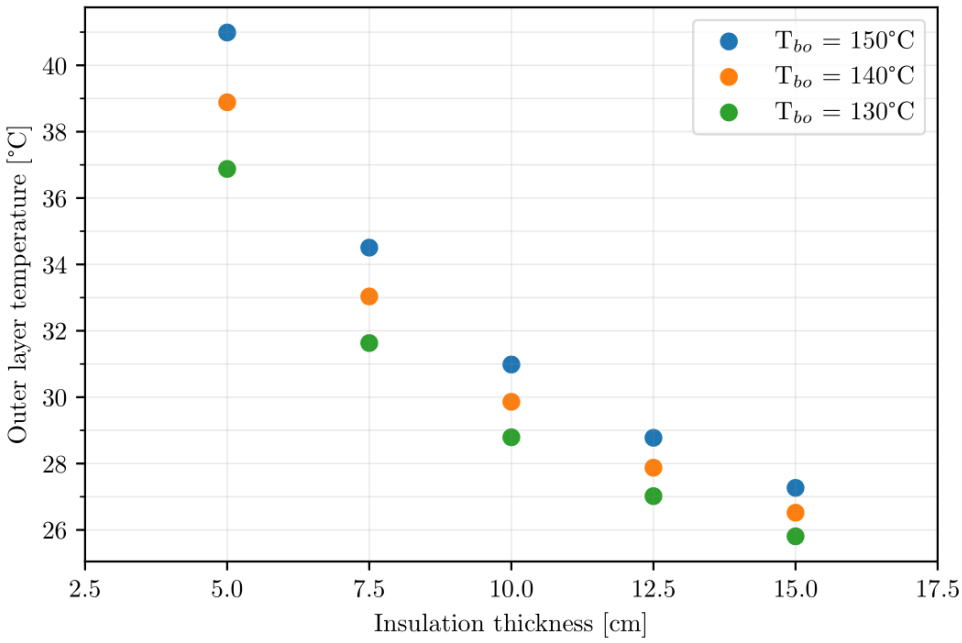

Figure 10.13: Insulation external temperature as a function of the bakeout temperature and insulation (mineral wool) thickness.

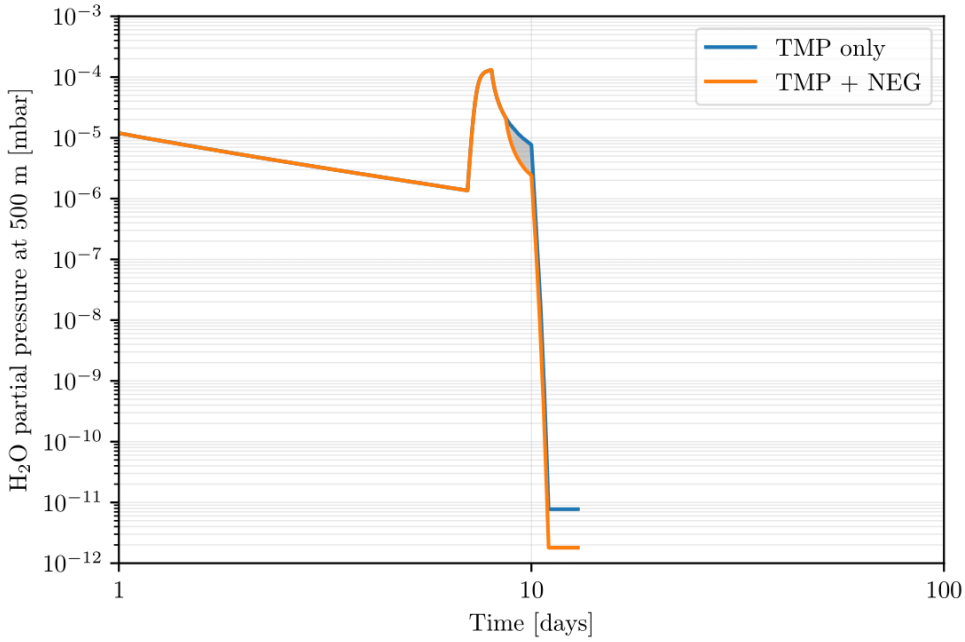

Figure 10.14: Pressure evolution curve with and without the NEG-assisted bakeout. The area in grey represents the sorption quantity taken from the NEG, spaced every 1000 m, during the bakeout. If converted in seconds and multiplied by the NEG effective pumping speed for water, it gives the 632 mbar l.

10.5.1 Final estimation of thermal insulation and electrical parameters

Rotating insulation across different sectors makes using thinner insulation less practical. The optimal insulation thickness, which balances minimizing thermal power emission, bakeout costs, and energy consumption, is 10 cm.

Based on these assumptions, the electrical and thermal parameters are calculated and summarized in Table 10.3 for a 4 mm thick straight pipe and a 1.5 mm corrugated pipe, both covered with 10 cm of mineral wool insulation.

A simple 2D model of the infrastructure can be simulated using COMSOL to quantify the impact of bakeout on tunnel air temperature. A surface temperature of 31°C is assigned to the outer layer of the insulation, with a convective heat flux to the surrounding air (h_{air} = 5 W/m^2·K) and radiation from the insulation to the ambient air, as well as from the tunnel walls to the surrounding rock [k]. The emissivities used are $\varepsilon_{insulation}$ = 0.05 and ε_{rock} = 0.95.

Time-dependent simulations were carried out for a 5 km sector. The average temperature in the tunnel and the temperature distributions, simulated for one to four beam pipes being baked simultaneously, are shown in Fig. 10.15. Assuming an initial tunnel temperature of 20°C (although it is likely 3 to 5°C lower), it can be concluded that baking up to two pipes at 150°C would not raise the tunnel temperature above

[k] ρ_{rock} = 2500 kg/m³, c_{rock} = 800 J/kg·K, k_{rock} = 2 W/m·K [39]

Table 10.3: Electrical and thermal parameters of a 150°C, 48 h direct joule effect bakeout for 1-m internal diameter 4 mm thick straight pipe and a 1.5 mm thick corrugated pipe. The electrical power and the bakeout cost include the ramp-up and cooldown phases.

Parameter	Straight pipe (4 mm)	Corrugated (1.5 mm)
Sector length [km]	5	5
Insulation thickness [cm]	10	10
Bakeout temperature [°C]	150	150
Ramp up duration [days]	1	1
Bakeout duration [days]	2	2
Cooldown duration [days]	1	1
Thermal power [W/m]	208	207
Insulation surface temperature [°C]	31	31
Current [A]	1800	1097
Electrical power [$\times$ 10^4 kWh]	6	3.4
Bakeout cost [k€]	30	17

29°C, even in calm air conditions.

Additionally, when baking two parallel pipes, one pipe can be used as a return cable for the other. This method increases the efficiency of the bakeout process and reduces costs by eliminating the need for a thick return cable or bus bar.

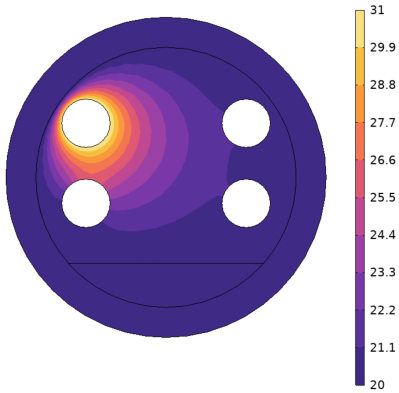

(a) One sector baked at 150°C for 2 days. Average temperature at the end of the bakeout = 22°C.

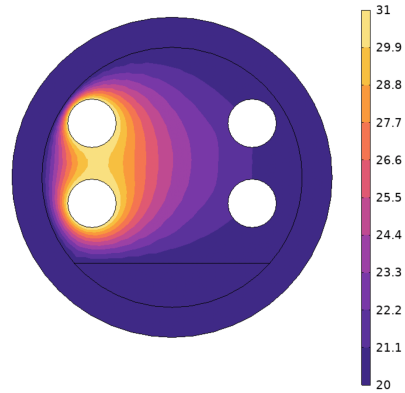

(b) Two sectors baked at 150°C for 2 days. Average air temperature at the end of the bakeout = 23.2°C.

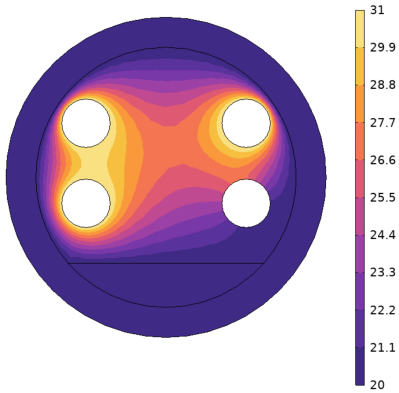

(c) Three sectors baked at 150°C for 2 days. Average air temperature at the end of the bakeout = 24.9°C.

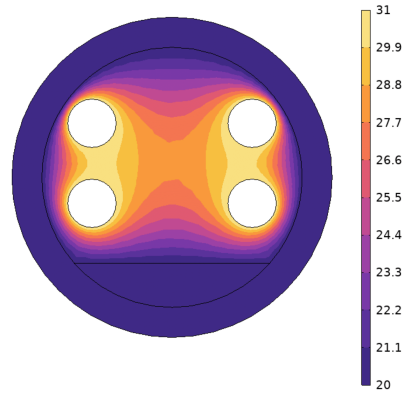

(d) Four sectors baked at 150°C for 2 days. Average air temperature at the end of the bakeout = 26.2°C.

Figure 10.15: Temperature distribution and average air temperature in the tunnel after 2 days of bakeout at 150°C, with one to four sectors baked simultaneously.

10.6 UHV pumping

Boundary conditions

The residual gas noise must be lower than 1×10^{-25} $1/\sqrt{Hz}$.

Design criteria

The position of the NEG pumps is locked by the bakeout design to 1000 m. Commercially available cartridges that can achieve the target nominal pumping speed for water of 1500 ls^{-1} are characterized by pumping speeds and sorption capacities for other gases of interest, as detailed in Table 10.4.

Table 10.4: Nominal and effective pumping speed of the NEG pumps selected for the HV and UHV pumping. The effective pumping speeds are calculated considering the assembly shown in Fig. 10.19(b). SAES kindly provided the nominal pumping speeds and sorption capacity.

Gas	Nominal pumping speed [$l\,s^{-1}$]	Effective pumping speed [$l\,s^{-1}$]	Sorption capacity [mbar l]
H_2	2100	1555	30058
H_2O	1500	857	3458
CO	880	568	345.8
CO_2	880	521	345.8

The selection of the SIPs specifically included pumping CH_4 and noble gases (He, Ar, etc.) through sputtering, which will be made among those equipped with triode cathodes and will depend on their pumping speeds at low pressures. Notably, the pumping speeds of SIPs at pressure ranges of $\times 10^{-10}$ mbar to 1×10^{-11} mbar are lower than the nominal speed achieved at 1×10^{-5} mbar, as shown in Table 10.5. The

Table 10.5: Percentage of pumping speed relative to the nominal N_2 equivalent for various gases in sputter ion pumps, as a function of the equilibrium pressure in the system. [158]

Pressure	H_2	CH_4	H_2O,CO, CO_2	He,Ar
1×10^{-10} mbar	36%	58%	37%	11%
1×10^{-11} mbar	60%	87%	58%	15%

design of the UHV pumping system must also consider the outgassing rates from the beam pipe body, optical baffles, large sector valves, and gate valves installed in front of the pumping groups. The outgassing rates considered for dimensioning the UHV system are resumed in Table 10.6.

Consideration on the UHV pumping

Considering the outgassing rates reported in Table 10.6, and the ultimate pressure of water after bakeout with only NEG pumps spaced 1000 m apart, the pressure profiles

Table 10.6: Specific and total outgassing rates budget for the different components and gas species. The baffles and their support are assumed to be distributed with a spacing of 100 m and contributing with an area of 5810 cm^2 [159]. The outgassing rate for the DN1000 sector valve is taken from VIRGO experimental measurements [160].

Gas	Beam pipe, fittings, baffles [$\times 10^{-17}$ mbar l s^{-1} cm^{-2}]	DN200 gate valves [$\times 10^{-11}$ mbar l s^{-1}]	DN1000 sector valves [$\times 10^{-7}$ mbar l s^{-1}]
H_2	100	1.2	5
CH_4	1	-	-
CO	3.7	-	-
CO_2	1.4	-	-

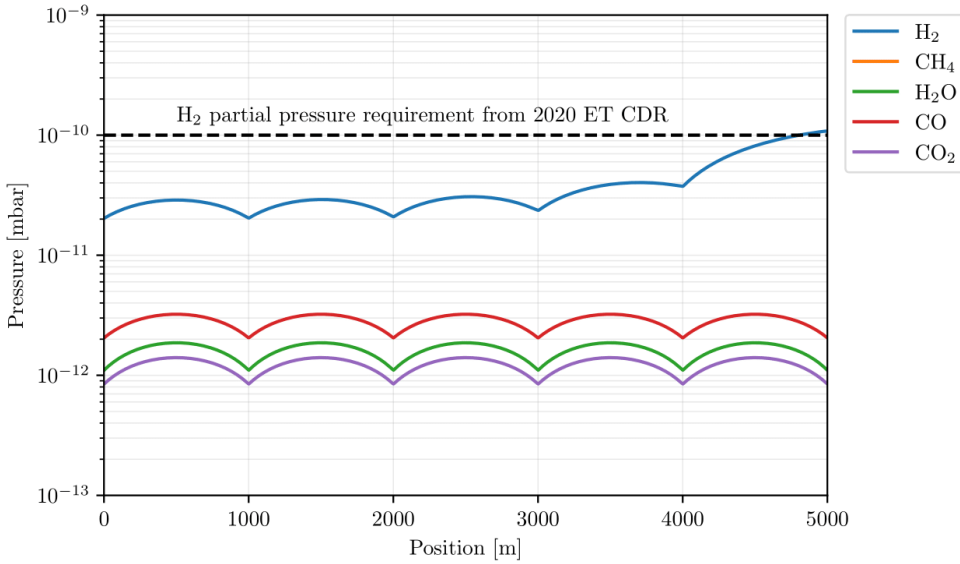

Figure 10.16: Pressure profiles for the main gas of interest considering the outgassing reported in Table 10.6 and only the presence of NEG pumps spaced 1000 m. CH_4 signal is out of scale due to the absence of SIPs.

along the vacuum sector are shown in Fig. 10.16. As can be seen in Fig. 10.16, the presence of the NEG pumps alone is sufficient to keep the pressures of H_2 and H_2O below the value suggested in the 2020 ET CDR by nearly one order of magnitude. The low outgassing rates from the baffles, fittings, and DN200 gate valves do not significantly affect the uniformity of the pressure profile. However, the high outgassing rate of the sector valves causes irregularities in the pressure profiles that exceed the recommended threshold.

Two potential solutions can address this issue. The first involves mitigating the gas load by installing specific NEG pumps on the sector valve body to reduce the high

pressure. The second option would be to explore more effective heat treatments to degas the valve's subcomponents.

For the SIP distribution, the pumps are assumed to be mounted in the same positions as the NEG pumps, spaced 1000 m apart. Three SIP sizes are considered: 200, 300, and 500 l s^{-1} (nominal pumping speed for N_2 at 1×10^{-5} mbar). Given a maximum pressure of 3×10^{-11} mbar for H_2, the effective pumping speeds, considering the conductance chain and Table 10.5, are listed in Table 10.7.

Table 10.7: Effective pumps for the considered SIPs at the equilibrium pressure of 1×10^{-11} mbar.

Gas	SIP 200 l s^{-1} [ls^{-1}]	SIP 300 l s^{-1} [ls^{-1}]	SIP 500 l s^{-1} [ls^{-1}]
H_2	71	106	175
CH_4	110	161	255
H_2O	71	105	169
CO	71	104	166
CO_2	70	102	162

The final maximum pressures are summarised in Table 10.8.

Table 10.8: Maximum pressures, in mbar, for the different configurations of NEG+SIPs considered.

Gas	NEG+SIP 200 l s^{-1} [ls^{-1}]	NEG+SIP 300 l s^{-1} [ls^{-1}]	NEG+SIP 500 l s^{-1} [ls^{-1}]
H_2	1.0×10^{-10}	1.0×10^{-10}	1×10^{-10}
CH_4	3.0×10^{-12}	2.2×10^{-12}	1.5×10^{-12}
H_2O	1.8×10^{-12}	1.7×10^{-12}	1.7×10^{-12}
CO	3.0×10^{-12}	2.9×10^{-12}	2.8×10^{-12}
CO_2	1.3×10^{-12}	1.3×10^{-12}	1.2×10^{-12}

The results show that the CH_4 pressure improves by a factor of two when comparing SIP sizes 200 and 500 l s^{-1}. However, the effect on other gases is negligible.

Assumption on the UHV pumping

Considering the slight pressure differences between the selected SIPs, their respective weights (51, 69, and 120 kg) and ease of integration, it is assumed that 300 l s^{-1} SIPs will be used every 1000 m. The final assembly of the pumping group is depicted in Fig. 10.19.

NEG cartridges, similar to those used on the beam pipes, are assumed to be installed directly on the valve bodies to reduce the gas load from the sector valves. The resulting

pressure profiles for the relevant gases are shown in Fig. 10.17, with the maximum values listed in Section 10.6.

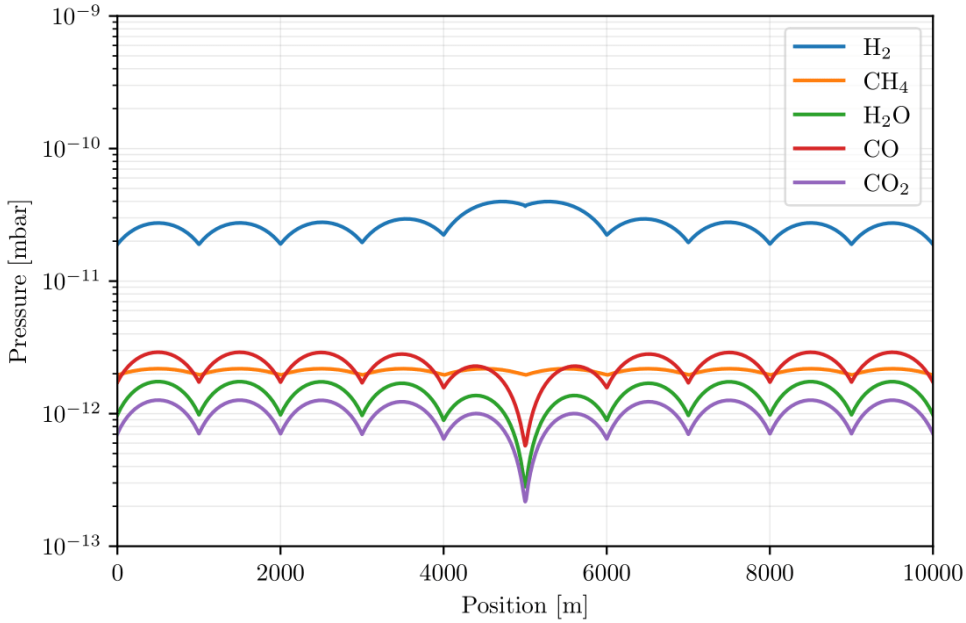

Figure 10.17: Pressure profiles along a 10 km arm, assuming 2000 l s^{-1} NEG and 300 l s^{-1} SIP pumps spaced 1000 m. The presence of 2000 l s^{-1} NEG pumps on the sector valve bodies reduces by a factor of 2.5 the maximum H_2 partial pressure compared to the pressure profile of Fig. 10.16.

Table 10.9: Maximum pressures, in mbar, considering NEG pumps and SIPs spaced 1000 m on the beam pipes and one 2000 l s^{-1} mounted on the bodies of the central sector valves. The pumping speeds for the NEG cartridges mounted on the sector valve bodies are taken from the nominal values reported in Table 10.4.

Gas	Pressure [mbar]
H_2	4.0×10^{-11}
CH_4	2.1×10^{-12}
H_2O	1.7×10^{-12}
CO	2.9×10^{-12}
CO_2	1.3×10^{-12}

With the assumed size and distribution of the UHV pumping groups, the maximum strain noise due to residual gas, calculated using Eq. (3.9) is $2.65 \times 10^{-26}\ 1/\sqrt{Hz}$ and $2.53 \times 10^{-26}\ 1/\sqrt{Hz}$ for ET-HF and ET-LF, respectively. The values achieved are one order of magnitude below the required limit (see Fig. 10.18).

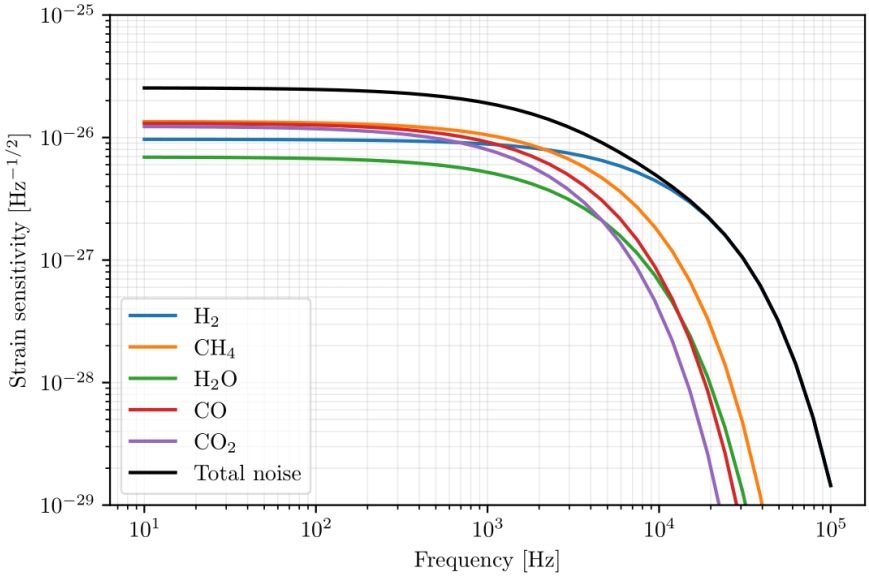

(a) Residual gas strain noise as a function of frequency for ET-LF for the different gases and as total quantity, using the above-described pumping schemes and gas loads.

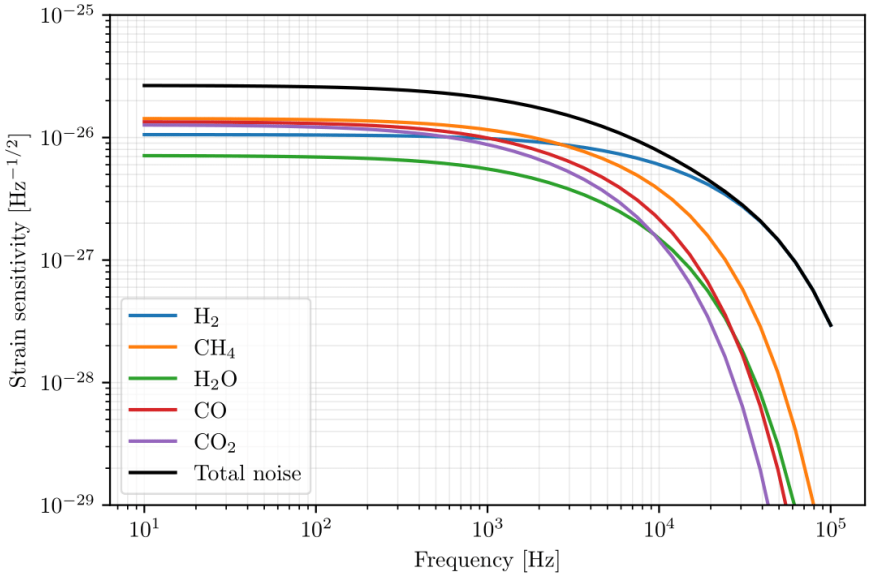

(b) Residual gas strain noise as a function of frequency for ET-HF for the different gases and as total quantity, using the above-described pumping schemes and gas loads.

Figure 10.18: Residual gas noises as a function of frequency for ET-LF and ET-HF.

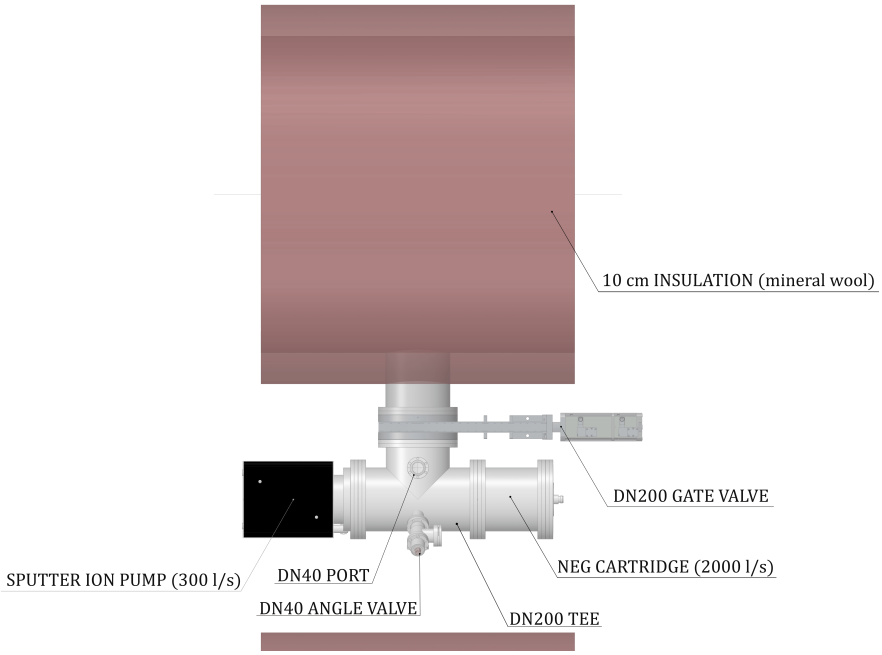

(a) Lateral view of the proposed UHV pumping group. The DN200 tee is equipped with two additional DN40 ports, one for the installation of the instrumentation and the other tapped by a DN40 valve, which can be used for the pumping of the modules during reactivation of the pumps or conditioning of the modules in case of substitution or reparation.

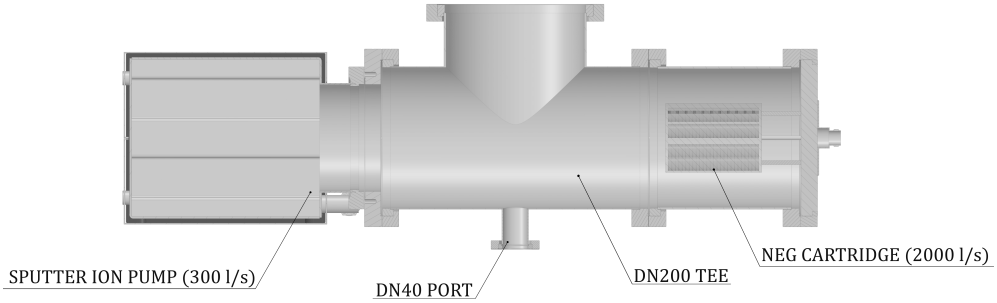

(b) Cross section of the proposed UHV pumping group.

Figure 10.19: 3D model of the proposed UHV pumping group. The SIP 3D model is courtesy of Agilent Technologies. The angle valve 3D model is courtesy of VAT.

10.7 Gas monitoring

Considerations on gas monitoring

Gas monitoring is mandatory to ensure the vacuum's quality throughout the conditioning to the UHV regime and the evolution of the pressure during the experiment's lifetime. If for the rough and intermediate pumping stages, a combi gauge Pirani/Bayard-Alpert or Capacitance/Pirani/Bayard-Alpert gauge is enough to track the pumpdown from 1000 mbar to 5×10^{-10} mbar, a not-so-obvious choice is that of the type of gauge for the UHV regime. As depicted in Fig. 10.20, the total pressure,

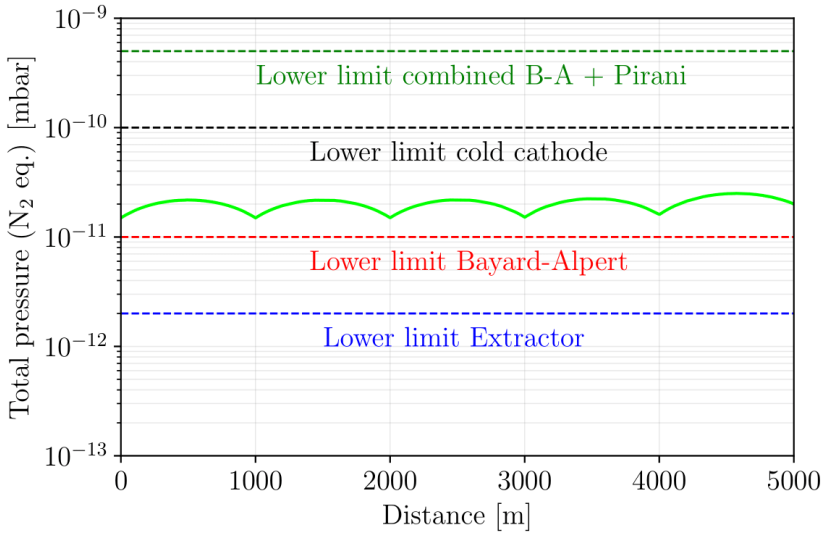

Figure 10.20: Total pressure profile along a vacuum sector and the respective lower limits of different commercially available gauges. The total pressure is calculated by converting the partial pressures to N_2 equivalent values. Conversion factors gas to N_2: H_2: 0.43, CH_4: 1.53, H_2O: 1.11, CO: 1.01, CO_2: 1.53.

expressed in N_2 equivalent mbar, read by a potential gauge given the partial pressures reached with the proposed pumping scheme yield to a maximum 2.5×10^{-11} mbar. This operational range cuts off most of the cold cathode and combination gauges. Therefore, the low pressures at which ET is foreseen to operate in the UHV regime narrow the selection of the gauge towards, if not exclusively, the Bayard-Alpert gauges or derivations (extended ranges or extractor gauges).

The measurement of the partial pressures at the UHV regime is deputed to the RGAs. Given the pressure reported in Fig. 10.17 and the detectability of the heavy hydrocarbon, a minimum detectable partial pressure of 5×10^{-15} mbar would be required. Due to the objectives mentioned above, the range of masses should be from 0 to 200 amu.

Assumption on gas monitoring

For the proposed pumping scheme, it is foreseen to adopt a combination of Capacitance / Pirani/Bayard-Alpert gauges for the roughing and intermediate vacuum. The gauges

should be mounted on the transitions to connect the pumps to the DN200 gate valves (see Fig. 10.5 and Fig. 10.11).

For the UHV regime, is here assumed the presence of Bayard-Alpert gauges able to detect pressures (with a measurement error up to 40%) down to 1×10^{-11} mbar. Choosing a standard Bayard-Alpert gauge over the Extractor relies on much better reliability and stability over time and the benefit of a much more robust design and lower price (40-60% lower depending on the required sensitivity).

The distribution assumed here is one BA gauge spaced every 1000 m and mounted on the UHV pumping group (see Fig. 10.21). Distributing the gauges every 500 m, will increase the overall cost of the vacuum system while not adding value to the pressure measurement. The pressure at 500 m can be calculated analytically by knowing the beampipe's conductance and the pumping point's pressure.

The same distribution is foreseen for the RGA since a similar conclusion can be drawn per the BA gauges.

To ensure the measurement's reliability and repeatability, all instrumentation before and during the interferometer's lifetime must be calibrated ex-situ or, in case of urgency, in situ using an Ar-calibrated leak with the SIP turned off.

In case of leaks, the BA gauges and the ion pumps can be used as interlocks for the sector valves.

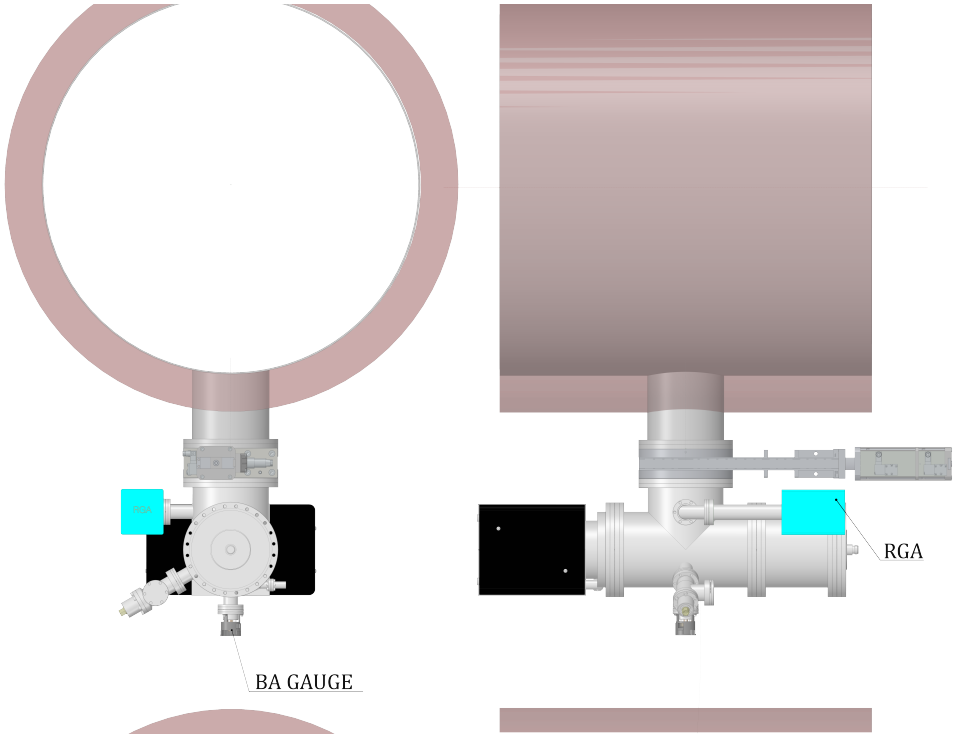

Figure 10.21: 3D assembly of the proposed BA gauge and RGA mounting on the 1000 m spaced UHV pumping groups.

10.8 Operational aspects

10.8.1 Vacuum quality check after bakeout

The total and partial pressure reached after the bakeout should be checked at least two days after the sector reaches the tunnel temperature.

Alongside the pressure measurement in a dynamic vacuum, accumulations should be done by isolating the sector. Given the installation and the types of pumps assumed, the sole purpose of the accumulation is to check on the presence of Ar. For obvious reasons, the SIPs must be turned off during the accumulations.

10.8.2 Air leaks: impact on the operation and detection

A leak detection campaign must be initiated if the pressures do not conform to the expected values. Given the sector's dimensions and the dynamic of leak detection, the leak test campaign must concentrate on the weakest points known to develop leaks due to thermal expansions: welded joints and flanged components. Specific tooling (clam shells) could be easily implemented to deliver Helium directly around the joint to confine the gas spreading in the tunnel. Similar equipment can be developed to leak-test the tube's welding line. However, the complexity of the tooling and the leak test procedure strongly depend on the welding profile (longitudinal vs. spiral).

Although air leaks, whether real or virtual, could negatively affect the interferometer's performance, the vacuum system has been designed to function even in the presence of high leak rates.

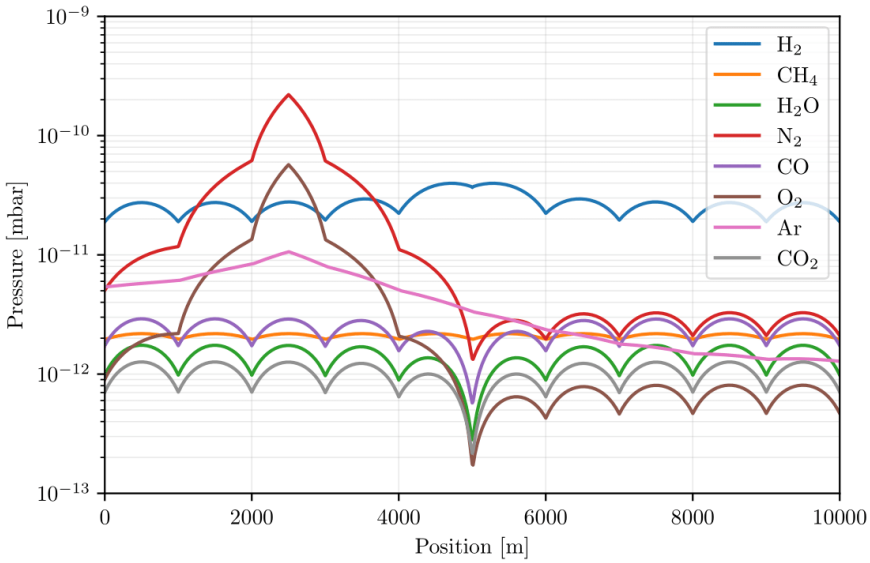

Figure 10.22: Partial pressures profile in case the presence of a leak 1×10^{-7} mbar l s^{-1} localised at 2500 m. The optical polarizability for N_2, O_2 and Ar are taken from [112]. The outgassing rates for N_2, O_2 and Ar are arbitrary assumed as $q_{N_2} = 3.7\times10^{-17}$ mbar l s^{-1} cm^{-2}, $q_{O_2} = 1\times10^{-17}$ mbar l s^{-1} cm^{-2} and $q_{Ar} = 1\times10^{-18}$ mbar l s^{-1} cm^{-2}.

In Fig. 10.22, is depicted the case of a localised air leak with a throughput of 1×10^{-7} mbar l s^{-1}. Despite the high leak rate, the low starting pressures and the strategic distribution of the pumping modules keep the strain noise a factor of two far from the interferometer upper limit (see Fig. 10.23).

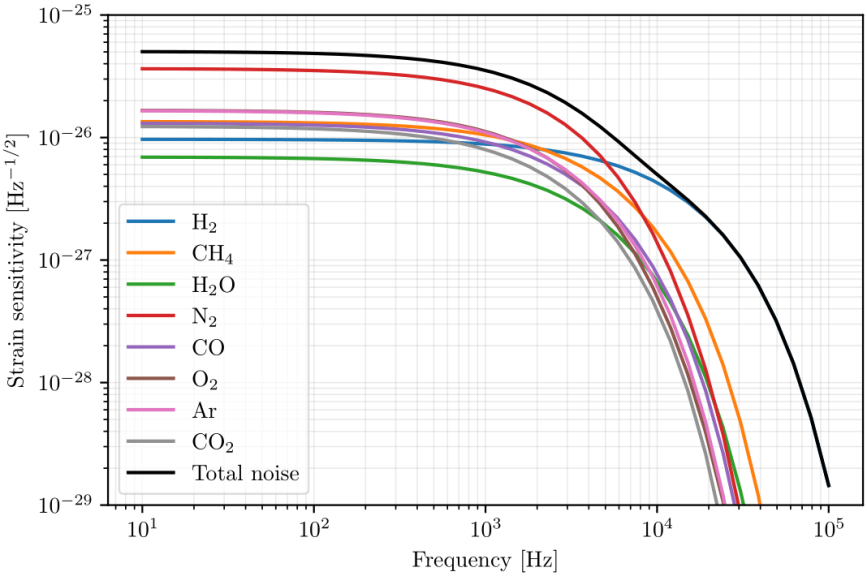

Figure 10.23: Strain noise as a function of frequency for an air leak of 1×10^{-7} mbar l s^{-1} in ET-LF. Similar results apply to ET-HF.

Although the system can operate with high leak rates, it is strongly recommended that the leaks be repaired, as their size could increase over time and saturate the getter pumps very fast.

10.8.3 Pumps sorption capacity and regeneration rate

As shown, getters offer several advantages, such as high pumping speeds in compact designs, minimal power requirements (only SIPs need power), and vibration-free operation, to name a few.

Since they rely on chemical pumping, they require no maintenance compared to mechanical pumps. However, they have a limited sorption capacity before reaching saturation. Once saturated, pumps like NEGs can be reactivated (with over 100 reactivation cycles possible if the gas load is modest), or they may become irreversibly conditioned and require the getter replacement, as with SIPs.

In the pessimistic case where the NEG pumps see the outgassing of the tube, gate valve and sector valve combined, the time needed until the reactivation is higher by several orders of magnitude than the experiment's lifetime as reported in Table 10.10.

Table 10.10: Gas loads and time after saturation of the NEG pumps distributed every 1000 m. The total gas load is calculated in the pessimistic case where the NEGs pump the outgassing rate of 1000 m of pipe, the baffles, the DN200 gate valve and that of the DN1000 gate valve (see Table 10.6).

Gas	Outgassing rates [mbar l s^{-1}]	NEG sorption capacity [mbar l]	Time before reactivation [s (years)]
H_2	1.3×10^{-7}	30058	2.3×10^{11} ($\simeq 7.3\times10^{3}$)
H_2O	9.4×10^{-10}	3458	3.7×10^{12} ($\simeq 1.2\times10^{5}$)
CO	1.1×10^{-9}	345.8	3.1×10^{11} ($\simeq 1\times10^{4}$)
CO_2	3.1×10^{-10}	345.8	1.1×10^{11}($\simeq 3.5\times10^{4}$)

Therefore, theoretically, the NEG pumps do not require any further care after the activation at the end of the bakeout.

10.9 Summary of the ET vacuum system design

The technical parameters resulting from the design exercise above are summarised in Table 10.11. As designed, one ET beam pipe sector is conditioned from atmospheric pressure to 2.5×10^{-11} mbar (N_2 eq.) in 13 days.

Table 10.11: Summary of the technical parameters resulting from the design exercise above, using beam pipes

Parameter	Straight pipe (4 mm)
Shortest sector length [m]	4990
Longest sector length [m]	5010
Pumping port size [DN]	200
Pumping port spacing [m]	500
Rough pumping spacing [m]	one sector
Rough pumping ultimate pressure [mbar]	1×10^{-1}
Rough pumping duration [days]	2.5
Intermediate pumping spacing [m]	2000
Intermediate pumping (RT) [days]	7
Bakeout temperature [°C]	150
Ramp up duration [days]	1
Bakeout duration [days]	2
NEG pumps at activation temperature [days]	1.3
Cooldown duration [days]	1
Insulation thickness [cm]	10
Thermal power [W/m]	208
Insulation surface temperature [°C]	31
Current [A]	1800
Electrical power [$\times$ 10^4 kWh]	5.2
UHV pumping spacing [m]	1000
P_{H_2} (max) [mbar]	4.0×10^{-11}
P_{CH_4} (max) [mbar]	2.2×10^{-11}
P_{CO} (max) [mbar]	1.7×10^{-12}
P_{CO} (max) [mbar]	2.9×10^{-12}
P_{CO_2} (max) [mbar]	1.3×10^{-12}
Strain noise ET-LF [$1/\sqrt{Hz}$]	2.54×10^{-26}
Strain noise ET-HF [$1/\sqrt{Hz}$]	2.65×10^{-26}

11. Preliminary cost estimation

The difficulty lies not so much in developing new ideas as in escaping from old ones.

-John Maynard Keynes-

In this chapter, the requirements and infrastructure information for the ET beam pipes are reviewed. Building on this foundation, preliminary considerations and assumptions for designing the ET beam pipe vacuum system are presented and discussed. The result of the assumptions will shape a new design of the ET beampipe vacuum system.

11.1 Cost per assembly

The preliminary cost estimation is based on 2024 market prices. The costs are extracted by averaging prices from at least two manufacturers. Whether the prices of some components were unavailable, the assumed cost is based on an educated guess.

This preliminary cost collection concerns only the hardware/software associated with the pumping groups, sectorisation and bakeout (excluding leak detectors). It does not include the cost of producing, cleaning, and installing the supports and beam pipes.

The electricity needed for the bakeout is calculated using 4 mm straight AISI 441 beam pipes.

Assembly	Subcomponent	Unitary cost	Comment
Sector vales	DN1000 gate valve	200	Includes cost of the heat treatment.
	Controls and cables	1.7	
	Subtotal [k€]	**201.7**	
Pumping ports	DN200 gate valve	6.8	Includes cost of the heat treatment.
	Subtotal [k€]	**6.8**	
Rough pumping group	Roots pump	65	Includes mobile cart.
	DN200 CF - DN160 ISO KF transition	1.5	
	DN160 ISO-KF elbow	0.5	
	DN160 bellow	1.7	3.5 m long.
	Gauge	1.2	
	Controls	3	
	Subtotal [k€]	**72.9**	
Intermediate pumping group	DN200-DN40 CF tee reducer	2	
	Gauge	1.2	
	DN40 CF angle valve	0.8	
	Turbomolecular pump (800 l s^{-1})	20	
	Electromagnetic HV valve	3.6	Cost for two units.
	DN25 KF bellow	0.9	4 m long.

Intermediate pumping group	DN25 KF cross	0.15	
	Gauge	1.2	For foreline control.
	DN25 KF HV manual angle valve	0.35	
	DN25-DN40 KF conical transition	0.05	
	Backing pump (multi-stage roots)	8	
	Accessories	0.2	Clamps, seals, blank flanges.
	Controls	5	
	Mobile cart	1	
	Subtotal [k€]	**44.45**	

UHV pumping group	DN200 CF custom tee	2.9	Includes cost of the heat treatment.
	DN40 CF angle valve	1	Includes cost of the heat treatment.
	DN40 CF blank flange	0.1	Includes cost of the heat treatment.
	DN40 CF elbow	0.2	Includes cost of the heat treatment.
	BA gauge	1	
	RGA	20	
	NEG pump (2000 l s^{-1})	20	
	SIP (300 l s^{-1})	8	
	Subtotal [k€]	**53.2**	

Free ports	DN200 CF blank flange	0.55	Includes cost of the heat treatment.
	Subtotal [k€]	**0.55**	

Bakeout	Mineral wool (10 cm thick)	154	Cost per km.
	Electricity	6	For a bakeout at 150°C for 2 days. Cost per km (0.5 €/kWh).
	Thermocouples beam pipe	0.4	One thermocouple/100 m. Cost per km.
	Power supply (up to 3000A)	70	
	Power supply cables	1.5	Power supply - tube Cost per km.
	Heating collars, jackets and thermocouples	1.2	Per pumping port.
	Bakeout PLC racks	25	One rack for two pumping ports.

Controls and softwares	PLC rack	4	Per pumping port.
	SIP controller	3	Controls up to 4 SIPs. Fixed.
	SIP cable	0.5	
	NEG controller	3	Controls up to 2 NEGs. Mobile.
	NEG cable	0.3	
	BA controller	3	Controls up to 4 BAs. Fixed.
	BA cable	0.5	
	SCADA server	5	For the whole vacuum system.

Ancillary components	Gaskets, screws, nuts, etc.	100	Per beam line.
	Subtotal [k€]	**1200**	

11.2 Preliminary cost estimation

The preliminary cost estimation of the ET beam pipe vacuum system presented in this chapter is based on the design and considerations presented previously.

The bakeout of two parallel sectors is assumed simultaneously (see Fig. 10.15(b)). This arrangement would allow using one beam line as the returning cable of the parallel one. In addition, it is arbitrarily chosen to process 6 sectors simultaneously (two per 10 km arm).

As a consequence of the assumption and based on what was anticipated with the design criteria:

- The intermediate pumping groups will be moved to other vacuum sectors after the bakeout. This approach will reduce the depreciation cost of the pumping group and reduce the cost of the intermediate pumping stage.
  → It is assumed to use 2 sets of 3 intermediate pumping groups per arm. Therefore, a total of 12 intermediate pumping groups are foreseen.
- The insulation is assumed to be used in a shell form. As per the intermediate pumping groups, the shells can be moved to a neighbouring sector once the bakeout is finished. The same consideration is applied to the thermocouples, cables, heating elements for the pumping ports, bakeout PLC racks and power suppliers.
  → It is assumed to use a total length of insulation of 30 km.
- NEG pumps do not require power after activation; therefore, the accounting for the controllers and cables follows the same logic as the mobile intermediate pumping groups.
  → Being the NEG pumps spaced 1000 m (plus those pumps located on the bodies of the gate valves) and activating two sectors per arm simultaneously, it is assumed the presence of 15 controllers and 15 cables for the whole beam pipe vacuum.

Given the conditions above, the bakeout and controls costs are pre-calculated in Tables 11.2 and 11.3.

Table 11.2: Summary of the bakeout costs.

Subcomponent	Quantity	Cost [k€]	Total cost [k]€
Mineral wool (10 cm thick)	30	154	4620
Electricity	120	6	720
Thermocouples beam pipe	30	0.4	12
Power supply (up to 3000A)	15	70	1050
Power supply cables	15	1.5	22.5
Heating collars, jackets, ..	120	1.2	144
Bakeout PLC racks	36	25	900
		Subtotal [k€]	**7468**

Table 11.3: Summary of the controls and software costs.

Subcomponent	Quantity	Cost [k€]	Total cost [k]€
PLC rack	228	4	912
SIP controller	27	6	162
SIP cable	108	0.5	54
NEG controller	15	3	45
NEG cable	15	0.3	4.5
BA controller	27	3	81
BA cable	108	0.5	54
SCADA server	1	5	5
		Subtotal [k€]	**1318**

The preliminary cost estimation is summarised in Table 11.4.

Table 11.4: Summary of the ET beam pipe vacuum system cost, according to the design proposed. The total cost of UHV pumping groups also considers the presence of the NEG pumps on the central sector bodies.

Assembly	Quantity	Cost [k€]	Total cost [k]€
Sectorisation	48	201.7	9682
Pumping ports	228	6.8	1550
Rough pumping groups	3	72.9	219
Intermediate pumping groups	12	44.45	533
Free ports	120	0.55	66
UHV pumping groups	108	53.2	5746
Bakeout	-	-	7468
Controls and software	-	-	1318
Ancillary components	-	-	1200
		Grand total [k€]	**27783**

The proposed design offers substantial cost savings compared to the estimates from the 2011 CDR and the 2020 ET cost book, as shown in Table 11.5.

If we update the previous estimates to explicitly account for the 20 cm mineral wool insulation required for 120 km of beam pipes—previously included in the general production and installation costs—the savings introduced by adopting the proposed design and an improved operational strategy become even more significant, with reductions ranging from 40% to 80%.

Table 11.5: Preliminary cost comparison between the proposed pumping layout and those presented in the 2011 ET CDR [47] and 2020 ET cost book [39]. The costs from the 2020 cost book are calculated from Table 3.3.

Source	Cost estimation [M€]	Thermal insulation [M€]	Final cost estimation [M€]
Proposed design	28	-	28
2011 CDR	35	34	69
2020 cost book	108	34	142

VI

- Conclusion -

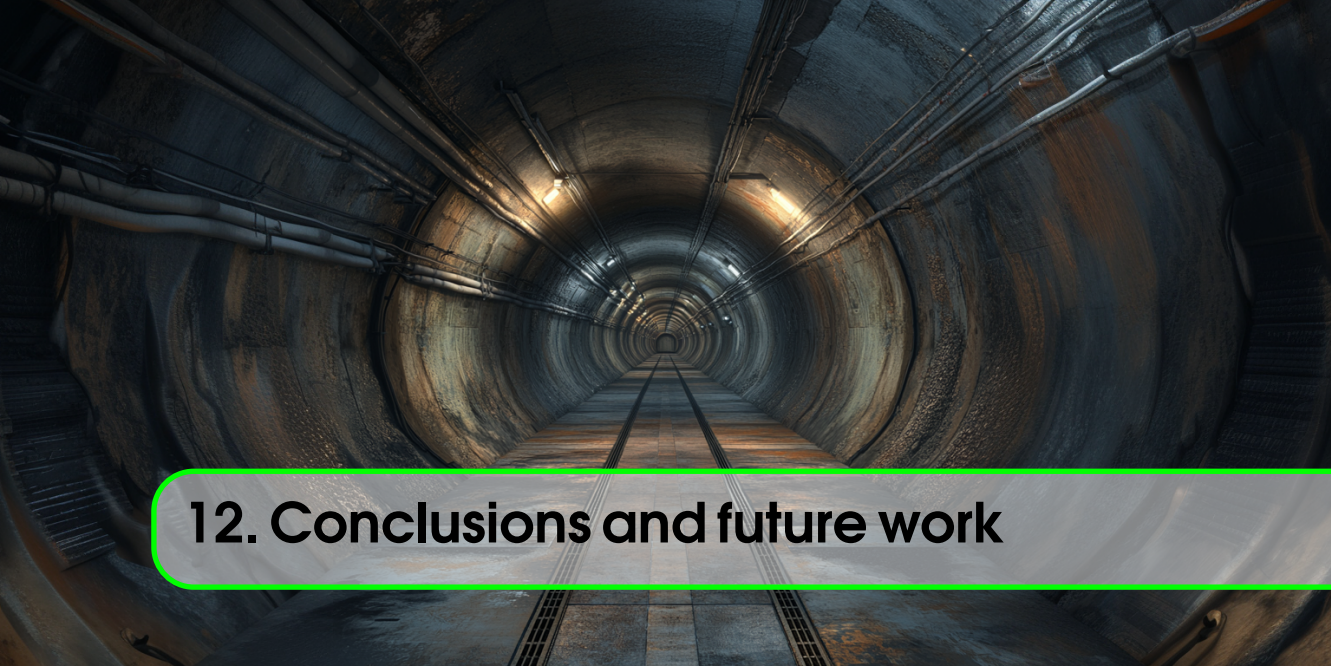

12. Conclusions and future work

I have been impressed with the urgency of doing. Knowing is not enough; we must apply. Being willing is not enough; we must do.

-Leonardo da Vinci-

In this concluding chapter, the study results are summarised, the research question addressed, and an outlook on future works and analysis is given.

12.1 Conclusions

The next generation of gravitational wave detectors will offer a new perspective on the universe, enabling us to deeply probe one of the most elusive fundamental forces: gravity. One of the major challenges in this quest is designing and constructing unprecedentedly large, highly efficient interferometers. A critical yet often underestimated component in this design is the beam pipe of the detector's arms, which, if not carefully designed, could significantly impact the experiment's budget.

In my research, I demonstrated that cheaper alternative steels, such as mild and ferritic stainless steels, are compatible with UHV applications, proving their suitability for constructing the beam pipes of GWDs. Notably, in as-received conditions, the outgassing rates of the tested ferritic alloys outperform the austenitic stainless steels currently used in GWDs by several orders of magnitude. This finding has significant cost implications, as it eliminates the need for high-temperature, time-consuming heat

treatments to meet the strict requirements of 3G-GWDs.

Extensive testing was performed to close the knowledge gap between these ferritic alloys and traditional austenitic stainless steels. Additionally, custom models were developed to predict the water outgassing rate based on bakeout temperature and duration. These models were experimentally validated on both small specimens and larger, sector-scaled prototypes, demonstrating their applicability and allowing for further refinement in even larger mockups.

Moreover, the research indirectly validated the effectiveness of a new thin-walled, corrugated beam pipe design. If industrialised, this design could lead to substantial cost savings due to several optimisations: less material use compared to straight beam pipes, lighter overall weight, production efficiency, and the elimination of the need for expansion bellows due to the geometric advantages of the corrugated profile.

The need to save energy during the bakeout phase through low-temperature solutions stimulated the exploration of alternative uses of NEG pumps to shorten the duration of the treatment without compromising the ultimate water partial pressure targeted by the project. The solution,proposed a decade ago by NEG manufacturers, was proved to work on a larger-scale prototype for the first time.

The results from the UHV characterisation campaign were then used to redesign the ET beam pipe vacuum system. Considering strict boundary conditions and applying a rationalised set of design criteria with redundancy, the new design could potentially save 60% to 80% of the forecasted budget for the vacuum system's hardware (excluding beam pipe production). Moreover, it would enable the delivery of over 1/4 of the entire beam pipe vacuum system in less than 15 days.

In summary, this work demonstrated that by carefully selecting the structural alloy and the proper design of the vacuum system, the ET beampipe vacuum system could be produced, installed, and conditioned at a fraction of the original cost while surpassing the originally forecasted scientific requirements.

12.2 Outloook

Hydrogen outgassing evolution

Despite having proven the low hydrogen outgassing rate of the ferritic alloys, the mechanism governing its desorption is yet to be determined. In future studies, the effort should be directed either at testing large amounts of surfaces or to more ad hoc designed experiments to discriminate specifically the hydrogen signal and the hydrogen-lattice/hydrogen-surface interactions.

Water outgassing rate modelling

The successful water binding energy study campaign on ferritic alloys immediately yielded usable results. Although extensively tested, the models require further fine-tuning, especially during transients (e.g., a change in pumping speed).

Test of alternative insulation materials

As seen from the bakeout's design and cost analysis, the current selection of affordable, high-temperature materials is quite limited. Mineral or glass fibres are readily available,

but unless they are properly jacketed, they pose unresolved safety risks, particularly related to dust production during installation and handling. In the future, exploring alternative, potentially more sustainable materials should be a priority and thoroughly tested.

Automated optimisation of the vacuum system parameters and updated costs

In the future, the scripts developed for the simulations, and set of inputs/boundary conditions will be integrated into an algorithm to simulate the best cost optimisation in terms of layout, parameters and material quantity. Together with this development, a more mature and complete costing evaluation will be done, including additional hardware (i.e., leak detectors and venting units) and considering the workforce for the vacuum system installation.

12.2.1 The ET Pilot Sector @ CERN

Most of the proposed work will be tested at CERN's ET Pilot Sector (ET-PS). As the final part of the agreement between CERN, INFN, and NIKHEF, the ET-PS will serve as a full-scale testbed for the beam pipe vacuum system. Its primary goal is to evaluate the design, fabrication, installation, and commissioning of the beam pipes and their support systems.

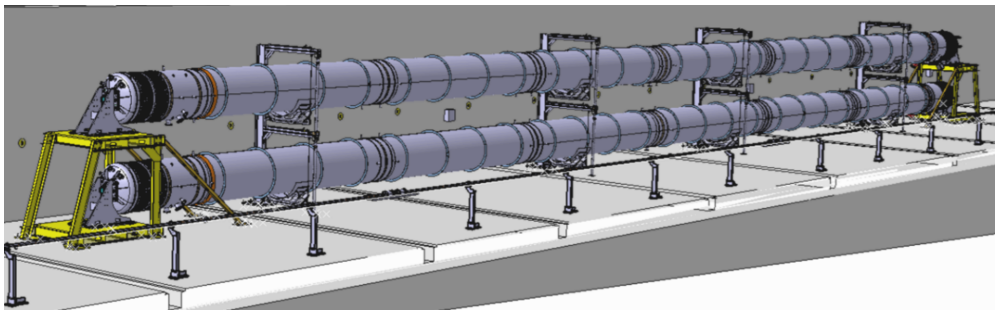

Figure 12.1: 3D model of the ET pilot sector (ET-PS). Credit:CERN

The preliminary tests and validations with the ET-PS will cover several key areas:

- Installation and alignment of supports and beam pipes.
- In-situ welding and assembly procedures.
- Leak detection during fabrication and assembly.
- Integration of thermal insulation, instrumentation, and vacuum components.
- Pumpdown time and vacuum operation.
- Bakeout temperature distribution and efficiency, using the direct joule effect.
- Measurement of ultimate partial pressures and outgassing rates.
- Validation of the vibration transmission matrix, particularly for optical baffles.
- Efficiency of dust contamination reduction methods during installation and operation.

Additionally, it will allow for comparing several technical choices regarding their feasibility.

The ET-PS installation will accommodate up to two beam pipes stacked vertically, each with an internal diameter of 1 m and a length of 36 m.

The testing activities will begin in Q1 2025, starting with two 4 mm thick, externally stiffened straight beam pipes made of AISI 441.

VII - Literature & Appendix -

A. Appendices

A.1 SEM - SEM/FIB micrographs of the selected alloys.

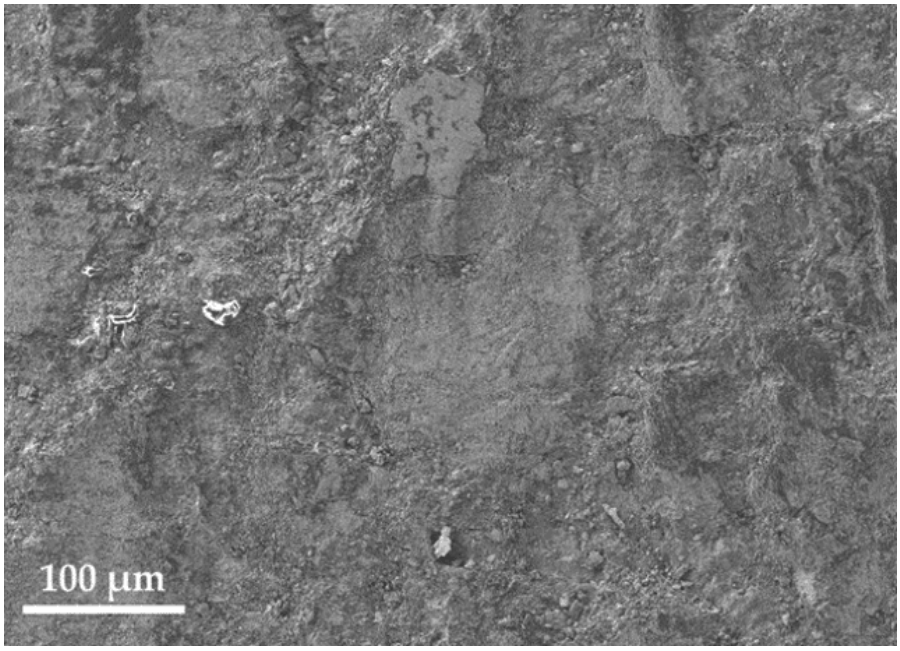

Figure A.1: SEM micrograph of the surface of the S355J2H sample.

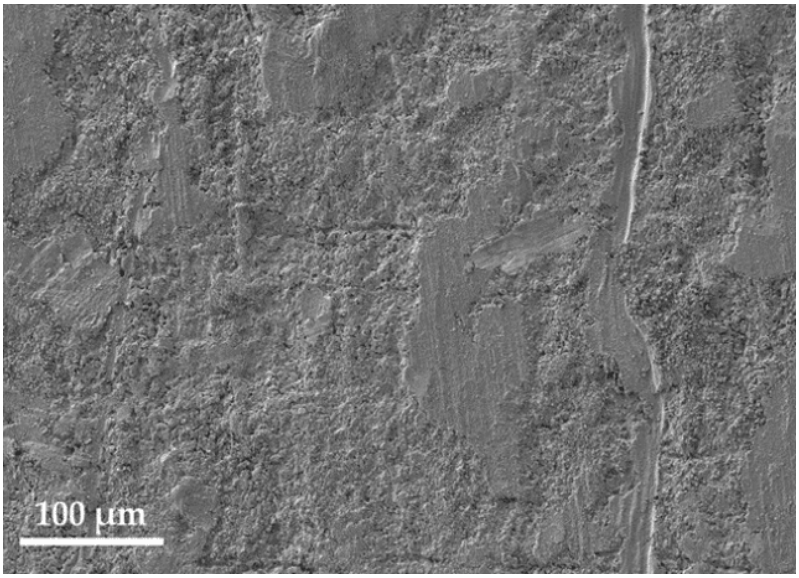

Figure A.2: SEM micrograph of the surface of the P355N sample.

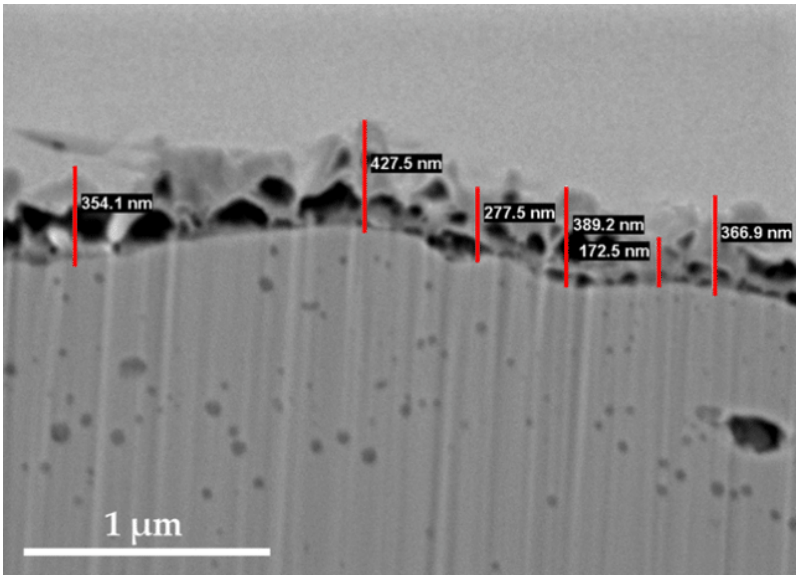

Figure A.3: SEM-FIB cross-section micrograph of the P355N surface highlighting an oxidated spot. The thickness of the oxide layer is highlighted by bars in six different positions.

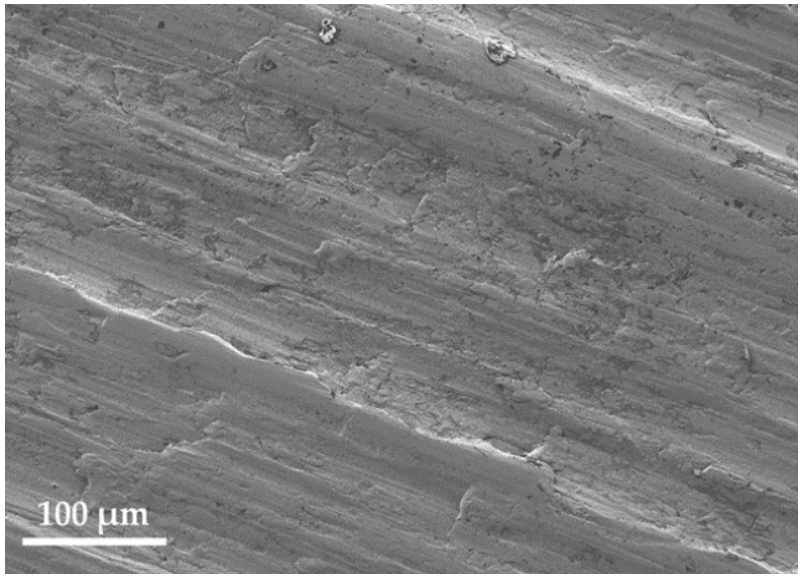

Figure A.4: SEM micrograph of the surface of the S355J2+AR sample.

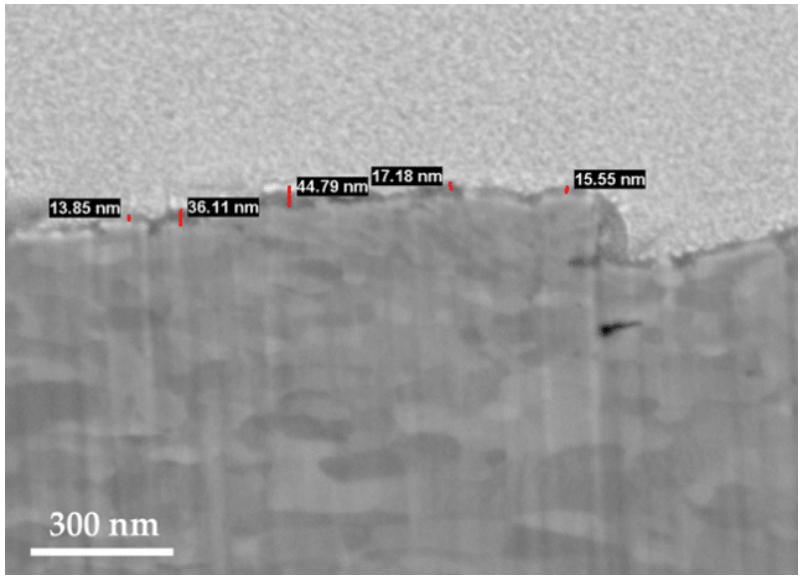

Figure A.5: SEM-FIB cross-section micrograph of the S355J2+AR surface highlighting an oxidated spot. The thickness of the oxide layer is highlighted by bars in five different positions.

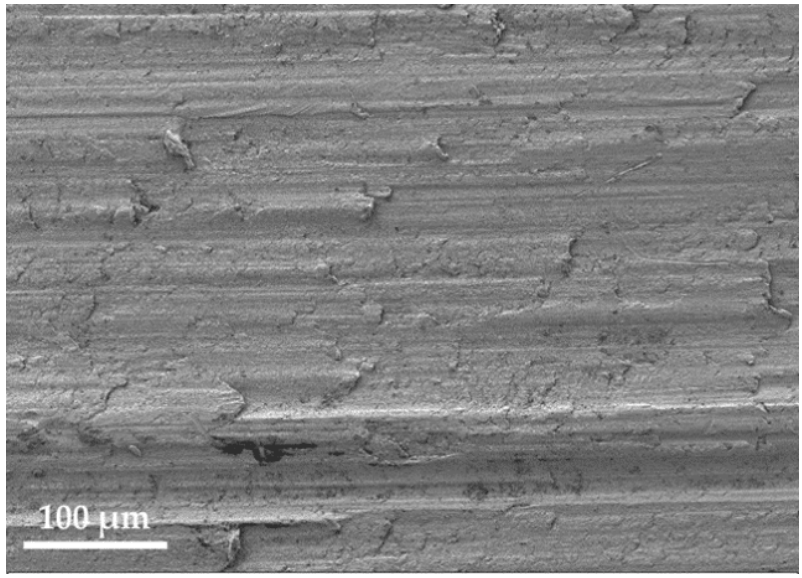

Figure A.6: SEM micrograph of the surface of the S355J2+N sample.

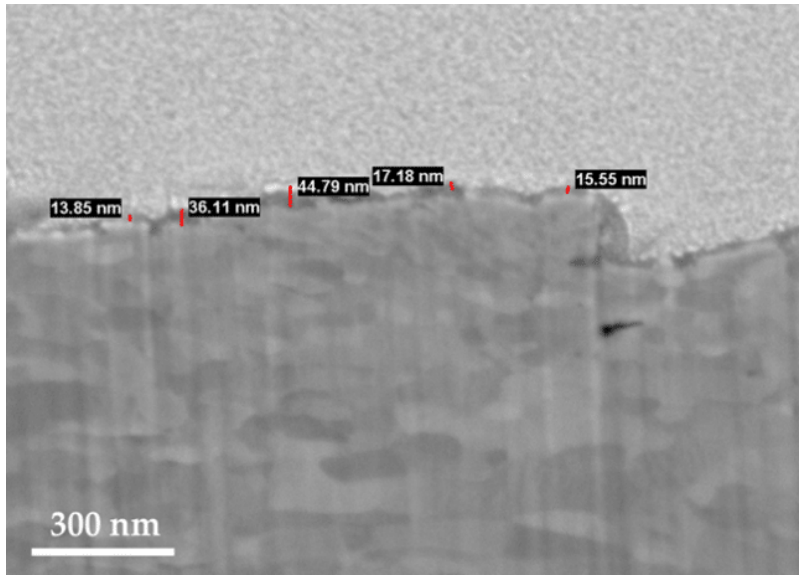

Figure A.7: SEM-FIB cross-section micrograph of the S355J2+N surface highlighting an oxidated spot. The thickness of the oxide layer is highlighted by bars in four different positions.

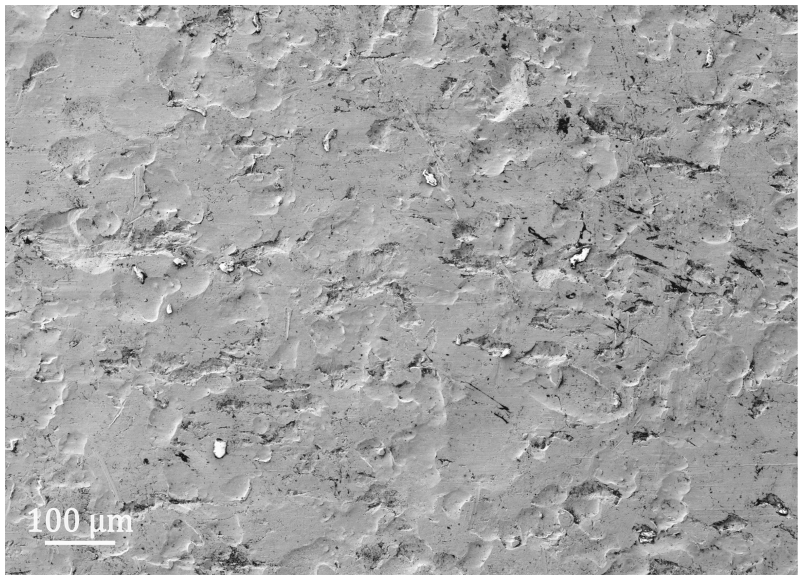

Figure A.8: SEM micrograph of the surface of the ARMCO sample.

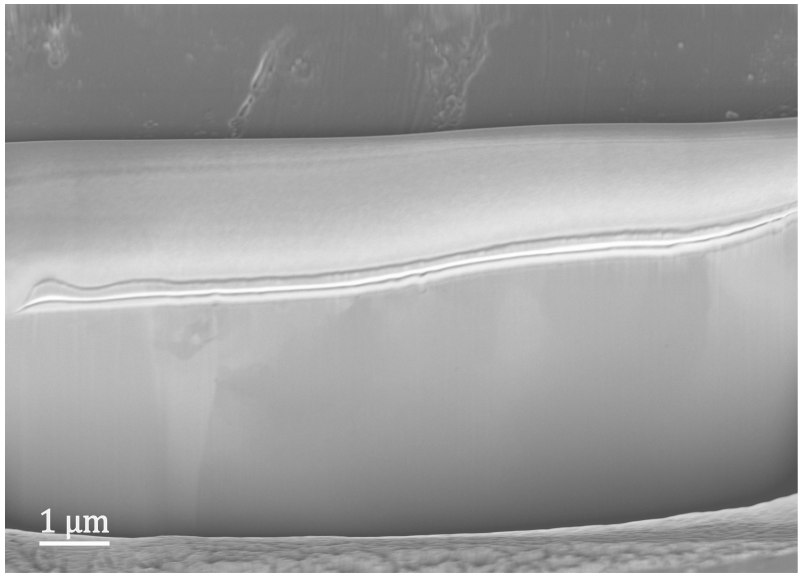

Figure A.9: SEM-FIB cross-section micrograph of the ARMCO surface.

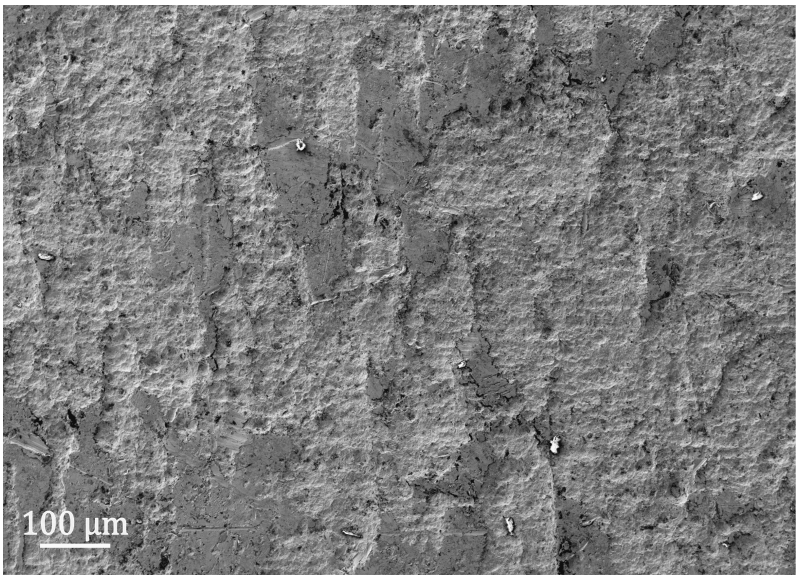

Figure A.10: SEM micrograph of the surface of the FB580 sample.

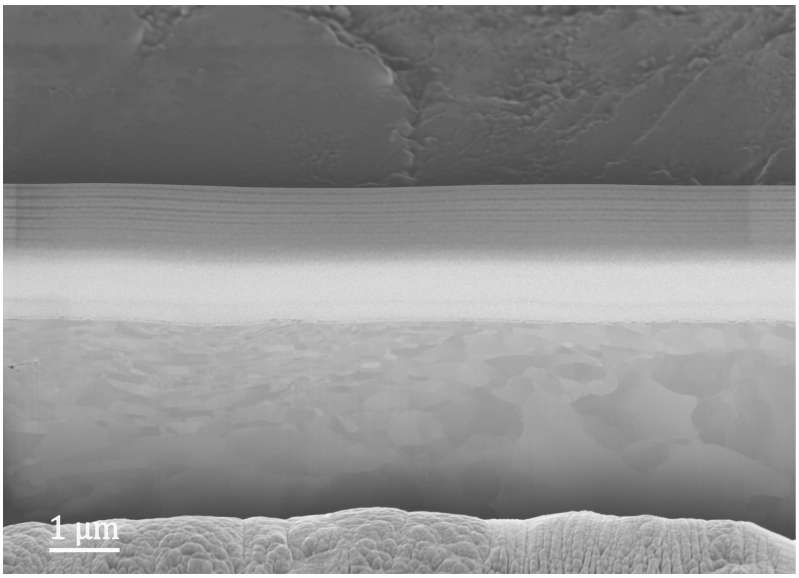

Figure A.11: SEM-FIB cross-section micrograph of the FB580 surface.

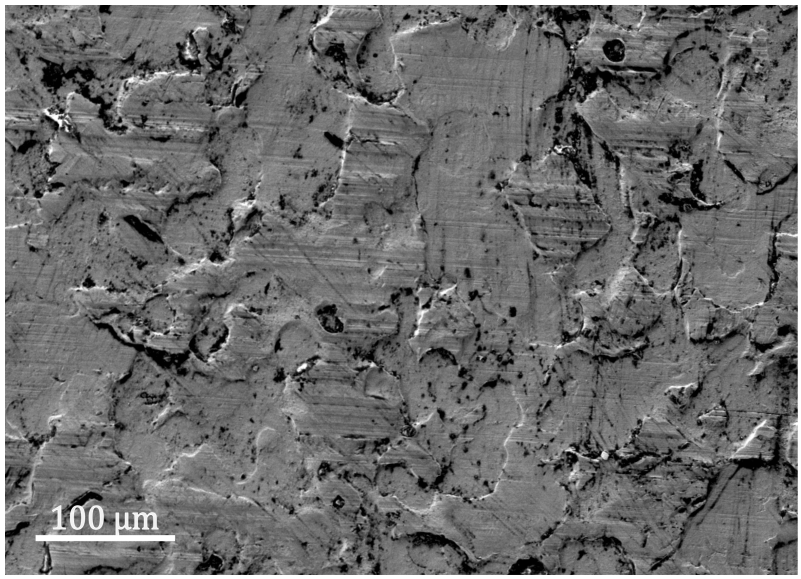

Figure A.12: SEM micrograph of the surface of the ULC-IF sample.

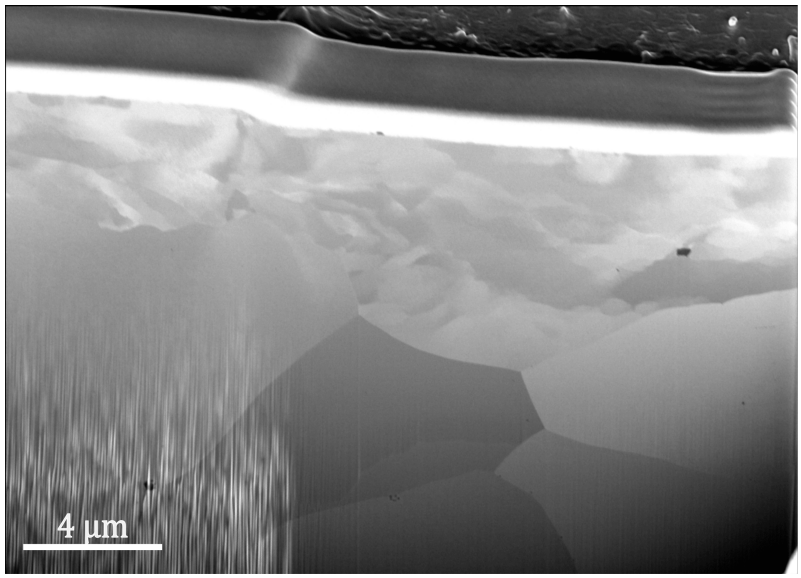

Figure A.13: SEM-FIB cross-section micrograph of the ULC-IF surface.

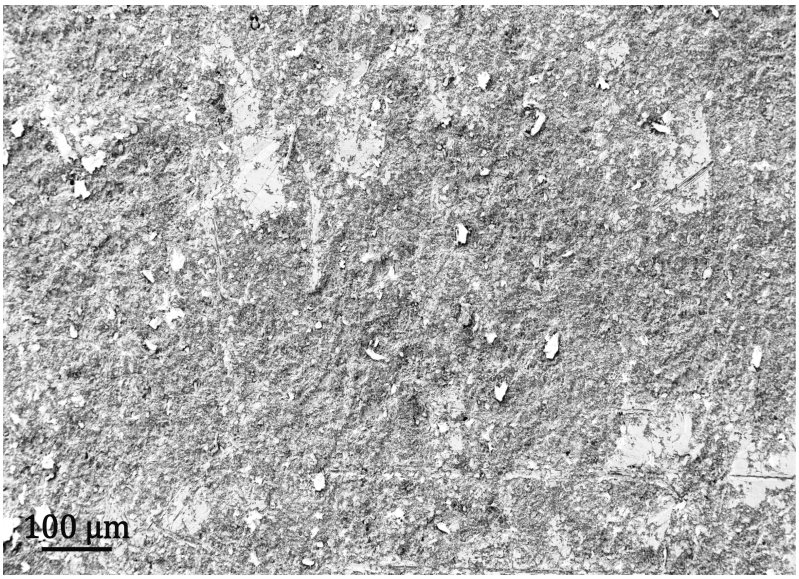

Figure A.14: SEM micrograph of the surface of the S315MC sample.

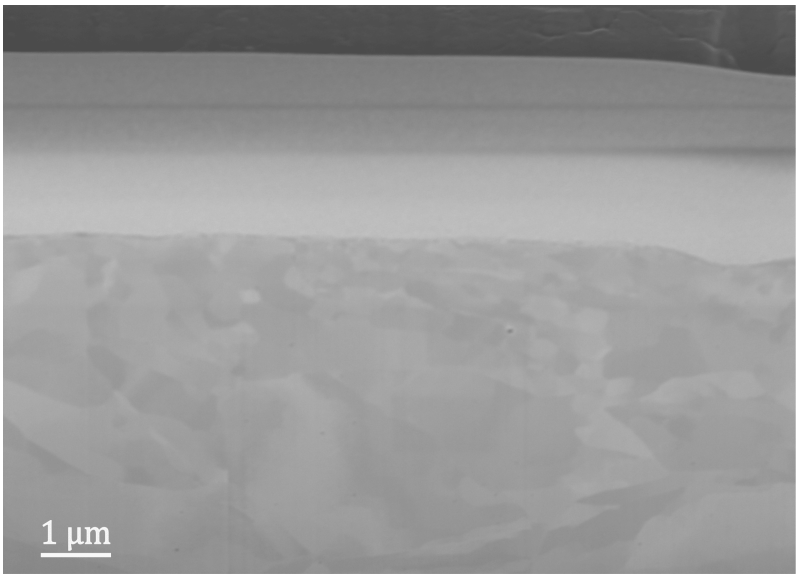

Figure A.15: SEM-FIB cross-section micrograph of the S315MC surface.

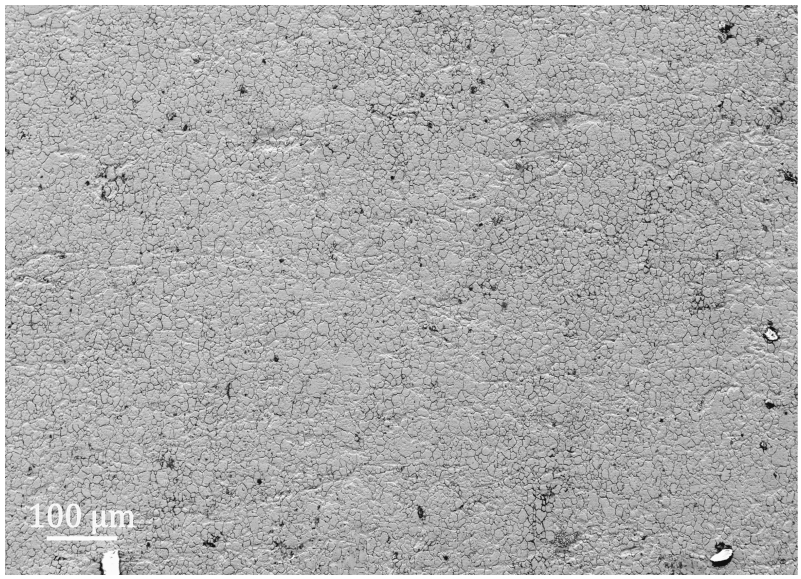

Figure A.16: SEM micrograph of the surface of the AISI 304L sample.

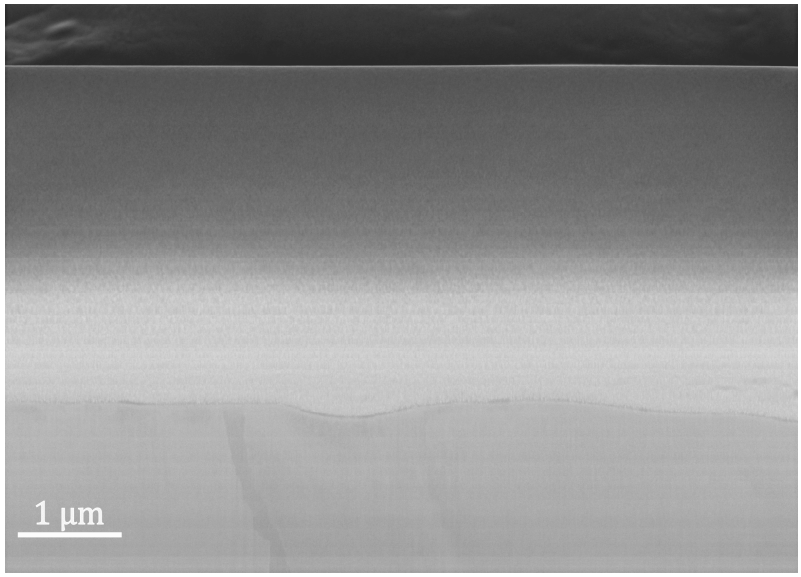

Figure A.17: SEM-FIB cross-section micrograph of the AISI 304L surface.

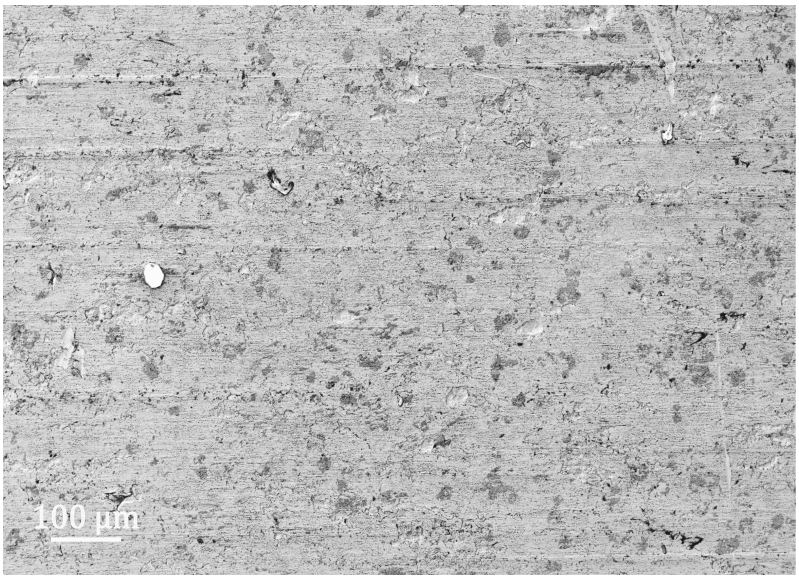

Figure A.18: SEM micrograph of the surface of the AISI 444 sample.

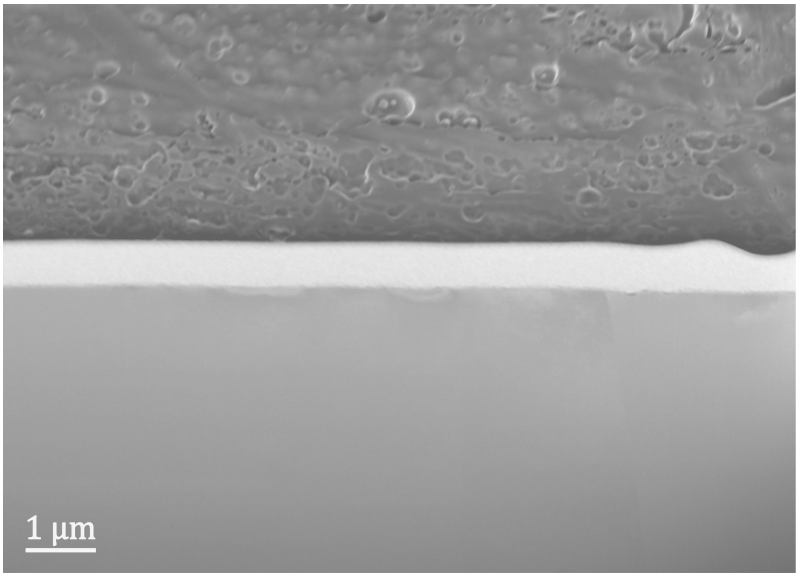

Figure A.19: SEM-FIB cross-section micrograph of the AISI 444 surface.

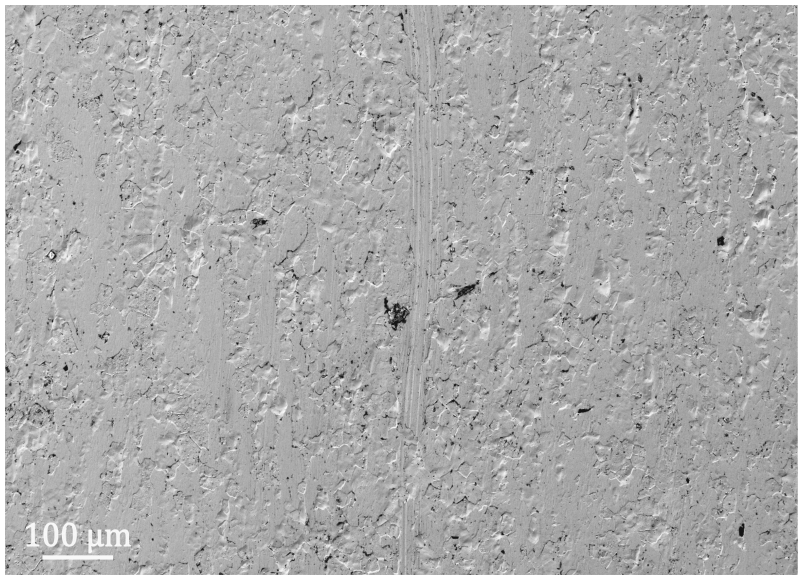

Figure A.20: SEM micrograph of the surface of the AISI 441 sample.

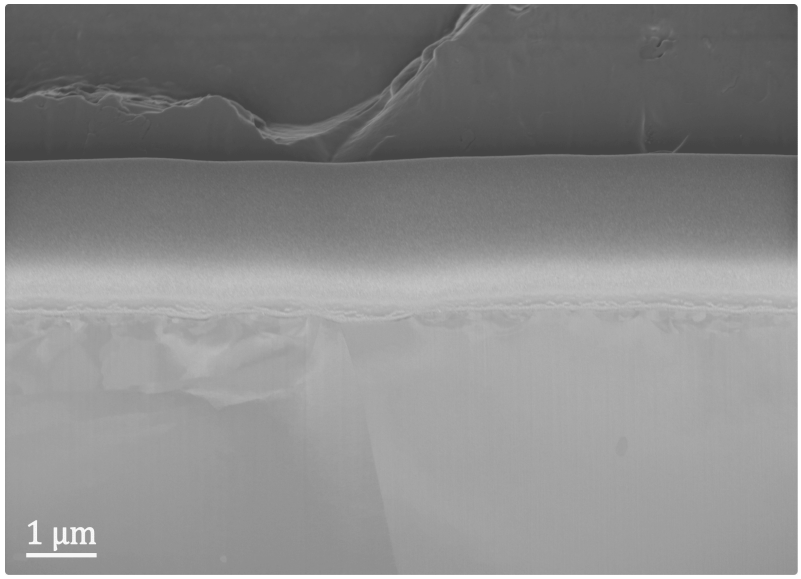

Figure A.21: SEM-FIB cross-section micrograph of the AISI 441 surface.

A.2 Accumulation measurement data

A.2.1 Mild steel samples

Table A.1: Specific outgassing rates for the different mild steels and austenitic stainless steels at 21±2°C after bakeout at 80°C for 48 h. Background signal removed. BSS: Below system sensitivity. The S355J2H outgassing data is taken from previous work from the author using the same accumulation system [150].

Steel grade	Specific outgassing rate [mbar l s^{-1} cm^{-2}]			
	H_2	CH_4	CO	CO_2
S315MC	BSS	7.6×10^{-17}	4.4×10^{-16}	3.2×10^{-16}
FB580	1.1×10^{-15}	1.0×10^{-16}	2.3×10^{-16}	8.5×10^{-16}
ULC-IF	1.5×10^{-15}	6.5×10^{-16}	7.4×10^{-16}	2.3×10^{-16}
ARMCO	1.5×10^{-15}	1.5×10^{-16}	2.8×10^{-15}	6.5×10^{-16}
S355J2+N	1.6×10^{-15}	3.0×10^{-16}	1.8×10^{-15}	9.7×10^{-16}
S355J2+AR	5.9×10^{-15}	2.8×10^{-15}	3.6×10^{-15}	1.1×10^{-15}
P355N	7.0×10^{-14}	2.3×10^{-17}	8.0×10^{-16}	1.0×10^{-16}
S355J2H	1.0×10^{-14}	3.1×10^{-17}	N/A	3.4×10^{-16}
AISI 304L	7.2×10^{-13}	1.1×10^{-15}	2.2×10^{-15}	3.4×10^{-16}

Table A.2: Specific outgassing rates for the different mild steels and austenitic stainless steels at 21±2°C after bakeout at 150°C for 48 h. Background signal removed. BSS: Below system sensitivity.

Steel grade	Specific outgassing rate [mbar l s^{-1} cm^{-2}]			
	H_2	CH_4	CO	CO_2
S315MC	BSS	3.2×10^{-17}	BSS	BSS
FB580	BSS	1.6×10^{-17}	3.4×10^{-17}	BSS
ULC-IF	BSS	4.3×10^{-17}	BSS	BSS
ARMCO	BSS	2.2×10^{-17}	1.5×10^{-16}	BSS
S355J2+N	BSS	1.8×10^{-16}	5.4×10^{-17}	BSS
S355J2+AR	2.2×10^{-15}	2.5×10^{-15}	9.1×10^{-16}	2.9×10^{-16}
P355N	1.7×10^{-14}	BSS	BSS	BSS
S355J2H	1.0×10^{-14}	3.3×10^{-17}	N/A	BSS
AISI 304L	7.5×10^{-12}	3.7×10^{-15}	6.7×10^{-15}	BSS

A.2.2 Ferritic stainless steel

Table A.3: Specific outgassing rates for the different ferritic and austenitic stainless steels at 21±2°C after bakeout at 80°C for 48 h. Background signal removed. BSS: Below system sensitivity.

Steel grade	Specific outgassing rate [mbar l s^{-1} cm^{-2}]			
	H_2	CH_4	CO	CO_2
AISI 304L	7.2×10^{-13}	1.1×10^{-15}	2.2×10^{-15}	3.4×10^{-16}
AISI 444	1.0×10^{-15}	6.1×10^{-16}	4.1×10^{-16}	1.8×10^{-16}
AISI 441	BSS	1.1×10^{-16}	BSS	BSS

Table A.4: Specific outgassing rates for the different ferritic and austenitic stainless steels at 21±2°C after bakeout at 150°C for 48 h. Background signal removed. BSS: Below system sensitivity.

Steel grade	Specific outgassing rate [mbar l s^{-1} cm^{-2}]			
	H_2	CH_4	CO	CO_2
AISI 304L	7.5×10^{-12}	3.7×10^{-15}	6.7×10^{-15}	BSS
AISI 444	BSS	4.3×10^{-16}	9.1×10^{-17}	8.8×10^{-18}
AISI 441	BSS	1.0×10^{-17}	BSS	BSS

A.3 Corrugated prototypes water ultimate pressure

Table A.5: Comparison of the measured and simulated ultimate water partial pressure for the three corrugated chamber baked at 80°C for 7 days. For the definition of AISI run 1 and run, see text.

Chamber	Measured H_2O pressure [$\times 10^{-11}$]	Modelled H_2O pressure [$\times 10^{-11}$]
AISI 304L-VF	4.3	3.2
S315MC	2.2	15.7
AISI 441 (run 1)	1.5	5.3
AISI 441 (run 2)	0.25	2.6

B. Listings

List of Acronyms

2G-GWD	Second Generation of Gravitational Wave Detectors
3G-GWD	Third Generation of Gravitational Wave Detectors
AB	Air-Bakeout
AdVirgo	Advanced Virgo
aLIGO	Advanced Laser Inteferometer Gravitational-wave Observatory
AMU	Atomic Mass Unit
ASD	Amplitude Spectral density
AV	Angle Valve
BA	Bayard-Alpert gauge
BHBH	Black Hole - Black Hole
BSS	Below System Sensitivity

CDR	Conceptual Design Report
CE	Cosmic Explorer
CERN	Conseil Européen pour la Recherche Nucléaire
CF	Con Flat
DLM	Diffusion Limited Model
DN	Diameter Nominal
ET	Einstein Telescope
ET-HF	Einstein Telescope High Frequency
ET-LF	Einstein Telescope Low Frequency
ET-PS	Einstein Telescope Pilot Sector
ETM	End Test Mass
FCC	Face Centered Cubic
FIB	Focused Ion Beam
FPC	Fabry-Perot Cavity
GR	General Relativity
GV	Gate Valve
GW	Gravitational Wave
GWs	Gravitational Waves
HAZ	Heat Affected Zone
HV	High Vacuum
IMG	Inverted Magnetron Gauge
INFN	Istituto Nazionale di Fisica Nucleare
ITM	Input Test Mass
KAGRA	Kamioka Gravitational Wave Detector
KF	*Klein Flansche*
LHC	Large Hadron Collider
LIGO	Laser Inteferometer Gravitational-wave Observatory

MID	Multiple Ion Detection
MME	Mechanical and Materials Engineering
NEG	Non Evaporable Getter
Nikhef	Nationaal Instituut voor Kernfysica en Hoge-EnergieFysica
NSNS	Neutron Star - Neutron Star
PLC	Programmable Logic Controller
PRC	Power Recycling Cavity
RGA	Residual Gas Analyser
RLM	Recombination Limited Model
RoC	Radius of Curvature
SCADA	Supervisory Control And Data Acquisition
SEM	Scanning Electron Microscope
SIP	Sputter Ion Pump
SR	Special Relativity
TDR	Technical Design Report
TMP	Turbo Molecular Pump
TPD	Temperature Programmed Desorption
TSP	Titanium Sublimation Pump
UHV	Ultra High Vacuum
VB	Vacuum Baked
VF	Vacuum Firing/Vacuum Fired
VLV	Variable Leak Valve
VSC	Vacuum, Surfaces and Coatings

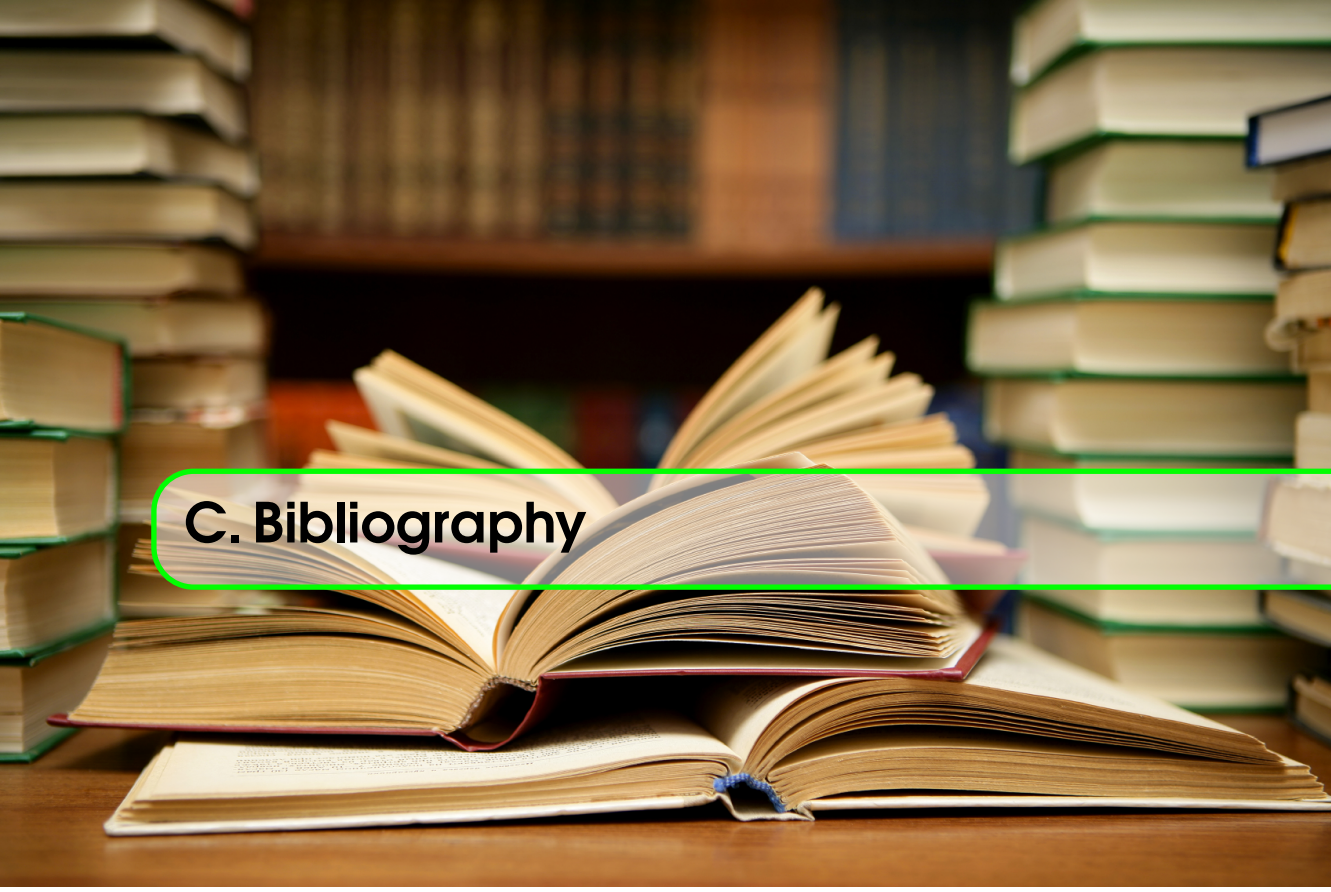

C. Bibliography

Articles

[1] A. Einstein. “Die Grundlage der allgemeinen Relativitätstheorie”. In: *Annalen der Physik* 354.7 (1916), pages 769–822. DOI: https://doi.org/10.1002/andp.19163540702 (cited on page 3).

[2] A. Einstein. “Über Gravitationswellen”. In: *Sitzungsberichte der Königlich Preussischen Akademie der Wissenschaften* (Jan. 1918), pages 154–167 (cited on page 3).

[4] S. Rowan and J. Hough. “The detection of gravitational waves”. In: (1999). DOI: 10.5170/CERN-1999-004.301 (cited on page 4).

[5] B. F. Schutz. “Gravitational wave sources and their detectability”. In: *Classical and Quantum Gravity* 6.12 (Dec. 1989), page 1761. DOI: 10.1088/0264-9381/6/12/006 (cited on page 4).

[6] J. Weber. “Detection and Generation of Gravitational Waves”. In: *Phys. Rev.* 117 (1 Jan. 1960), pages 306–313. DOI: 10.1103/PhysRev.117.306 (cited on page 6).

[7] J. Weber. “Evidence for Discovery of Gravitational Radiation”. In: *Phys. Rev. Lett.* 22 (24 June 1969), pages 1320–1324. DOI: 10.1103/PhysRevLett.22.1320 (cited on page 6).

[8] M. E. Gertsenshtein and V. I. Pustovoit. “On the detection of low frequency gravitational waves”. In: *JETP* 43 (Aug. 1962), pages 605–607 (cited on page 6).

[9] G. E. Moss, L. R. Miller, and R. L. Forward. "Photon-Noise-Limited Laser Transducer for Gravitational Antenna". In: *Appl. Opt.* 10.11 (Nov. 1971), pages 2495–2498. DOI: 10.1364/AO.10.002495 (cited on page 6).

[10] R. Weiss. "Republication of: Electromagnetically coupled broadband gravitational antenna". In: *General Relativity and Gravitation* 54.11 (Nov. 2022), page 153. ISSN: 1572-9532. DOI: 10.1007/s10714-022-03021-3 (cited on page 6).

[11] A. A. Michelson and E. W. Morley. "On the relative motion of the Earth and the luminiferous ether". In: *American Journal of Science* s3-34.203 (Nov. 1887), pages 333–345. DOI: 10.2475/ajs.s3-34.203.333 (cited on page 6).

[12] J. H. Taylor and J. M. Weisberg. "A new test of general relativity - Gravitational radiation and the binary pulsar PSR 1913+16". In: *Astrophysical Journal* 253 (Feb. 1982), pages 908–920. DOI: 10.1086/159690 (cited on page 6).

[13] B. P. Abbott et al. "Observation of Gravitational Waves from a Binary Black Hole Merger". In: *Phys. Rev. Lett.* 116 (6 Feb. 2016), page 061102. DOI: 10.1103/PhysRevLett.116.061102 (cited on page 6).

[14] J. Aasi et al. "Advanced LIGO". In: *Classical and Quantum Gravity* 32.7 (Mar. 2015), page 074001. DOI: 10.1088/0264-9381/32/7/074001 (cited on page 6).

[15] F. Acernese et al. "Advanced Virgo: a second-generation interferometric gravitational wave detector". In: *Classical and Quantum Gravity* 32.2 (Dec. 2014), page 024001. DOI: 10.1088/0264-9381/32/2/024001 (cited on page 6).

[16] K. L. Dooley et al. "GEO 600 and the GEO-HF upgrade program: successes and challenges". In: *Classical and Quantum Gravity* 33.7 (Mar. 2016), page 075009. DOI: 10.1088/0264-9381/33/7/075009 (cited on page 6).

[17] T. Akutsu et al. "Overview of KAGRA: Detector design and construction history". In: *Progress of Theoretical and Experimental Physics* 2021.5 (Aug. 2020), 05A101. ISSN: 2050-3911. DOI: 10.1093/ptep/ptaa125 (cited on page 6).

[18] S. Fairhurst. "Triangulation of gravitational wave sources with a network of detectors". In: *New Journal of Physics* 11.12 (Dec. 2009). DOI: 10.1088/1367-2630/11/12/123006 (cited on page 6).

[19] D. V. Martynov et al. "Sensitivity of the Advanced LIGO detectors at the beginning of gravitational wave astronomy". In: *Physical Review D* 93.11 (July 2016). ISSN: 2470-0029. DOI: 10.1103/physrevd.93.112004 (cited on page 8).

[20] M. Rakhmanov et al. "Characterization of the LIGO 4 km Fabry–Perot cavities via their high-frequency dynamic responses to length and laser frequency variations". In: *Classical and Quantum Gravity* 21.5 (Feb. 2004), S487. DOI: 10.1088/0264-9381/21/5/015 (cited on page 8).

[21] A. A. Muzammil and G. Mueller. “Design of the Advanced LIGO recycling cavities”. In: *Opt. Express* 16.14 (July 2008), pages 10018–10032. DOI: 10.1364/OE.16.010018 (cited on page 8).

[23] D. Ganapathy et al. “Broadband Quantum Enhancement of the LIGO Detectors with Frequency-Dependent Squeezing”. In: *Phys. Rev. X* 13 (4 Oct. 2023), page 041021. DOI: 10.1103/PhysRevX.13.041021 (cited on page 8).

[24] J. Wenxuan et al. “LIGO operates with quantum noise below the Standard Quantum Limit”. In: (2024). arXiv: 2404.14569 [gr-qc] (cited on page 8).

[27] G. González. “Suspensions thermal noise in the LIGO gravitational wave detector”. In: *Classical and Quantum Gravity* 17.21 (Oct. 2000), pages 4409–4435. ISSN: 1361-6382. DOI: 10.1088/0264-9381/17/21/305 (cited on page 9).

[28] T. Ushiba et al. “Cryogenic suspension design for a kilometer-scale gravitational-wave detector”. In: *Classical and Quantum Gravity* 38.8 (Mar. 2021), page 085013. ISSN: 1361-6382. DOI: 10.1088/1361-6382/abe9f3 (cited on page 9).

[29] N. A. Robertson et al. “Quadruple suspension design for Advanced LIGO”. In: *Classical and Quantum Gravity* 19.15 (July 2002), page 4043. DOI: 10.1088/0264-9381/19/15/311 (cited on page 9).

[30] L. Trozzo and F. Badaracco. “Seismic and Newtonian Noise in the GW Detectors”. In: *Galaxies* 10.1 (2022). ISSN: 2075-4434. DOI: 10.3390/galaxies10010020 (cited on page 9).

[33] A. Cavalleri et al. “Gas damping force noise on a macroscopic test body in an infinite gas reservoir”. In: *Physics Letters A* 374.34 (2010), pages 3365–3369. ISSN: 0375-9601. DOI: https://doi.org/10.1016/j.physleta.2010.06.041 (cited on page 10).

[34] B. P. Abbott et al. “GW170817: Observation of Gravitational Waves from a Binary Neutron Star Inspiral”. In: *Phys. Rev. Lett.* 119 (16 Oct. 2017), page 161101. DOI: 10.1103/PhysRevLett.119.161101 (cited on page 10).

[35] G. Stratta and F. Pannarale. “Neutron Star Binary Mergers: The Legacy of GW170817 and Future Prospects”. In: *Universe* 8.9 (2022). ISSN: 2218-1997. DOI: 10.3390/universe8090459 (cited on page 10).

[36] B. P. Abbott et al. “A gravitational-wave standard siren measurement of the Hubble constant”. In: *Nature* 551.7678 (Nov. 2017), pages 85–88. ISSN: 1476-4687. DOI: 10.1038/nature24471 (cited on page 10).

[37] R. Abbott et al. “GW190521: A Binary Black Hole Merger with a Total Mass of 150 $M_{\odot}$”. In: *Phys. Rev. Lett.* 125 (10 Sept. 2020), page 101102. DOI: 10.1103/PhysRevLett.125.101102 (cited on page 10).

[38] The LIGO Scientific Collaboration, the Virgo Collaboration, and the KAGRA Collaboration. “Observation of Gravitational Waves from the Coalescence of a $2.5-4.5\ M_{\odot}$ Compact Object and a Neutron Star”. In: (2024). arXiv: 2404.04248 [astro-ph.HE] (cited on page 10).

[40] B. P. Abbott et al. “Prospects for observing and localizing gravitational-wave transients with Advanced LIGO, Advanced Virgo and KAGRA”. In: *Living Reviews in Relativity* 23 (Dec. 2020). DOI: 10.1007/s41114-020-00026-9 (cited on page 10).

[41] C. J. Moore, R. H. Cole, and C. P. L. Berry. “Gravitational-wave sensitivity curves”. In: *Classical and Quantum Gravity* 32.1 (Dec. 2014), page 015014. DOI: 10.1088/0264-9381/32/1/015014 (cited on page 11).

[43] B. Goncharov, A. H. Nitz, and J. Harms. “Utilizing the null stream of the Einstein Telescope”. In: *Phys. Rev. D* 105 (12 June 2022), page 122007. DOI: 10.1103/PhysRevD.105.122007 (cited on page 11).

[44] E. D. Hall. “Cosmic Explorer: A Next-Generation Ground-Based Gravitational-Wave Observatory”. In: *Galaxies* 10.4 (2022). ISSN: 2075-4434. DOI: 10.3390/galaxies10040090 (cited on page 11).

[45] M. Brachesi et al. “Science with the Einstein Telescope: a comparison of different designs”. In: *Journal of Cosmology and Astroparticle Physics* 2023.07 (July 2023), page 068. DOI: 10.1088/1475-7516/2023/07/068 (cited on page 11).

[49] P. Strubin. “Large high-vacuum systems for CERN accelerators”. In: *J. Phys.: Conf. Ser.* 114 (2008), page 012001. DOI: 10.1088/1742-6596/114/1/012001 (cited on page 16).

[50] M. Arenz et al. “Commissioning of the vacuum system of the KATRIN Main Spectrometer”. In: *Journal of Instrumentation* 11.04 (Apr. 2016). DOI: 10.1088/1748-0221/11/04/P04011 (cited on page 16).

[54] A. N. Itakura et al. “Model of local hydrogen permeability in stainless steel with two coexisting structures”. In: *Scientific Reports* 11.1 (Apr. 2021), page 8553. ISSN: 2045-2322. DOI: 10.1038/s41598-021-87727-5 (cited on pages 24, 90, 118).

[56] J. Frenkel. “Theorie der Adsorption und verwandter Erscheinungen”. In: *Zeitschrift für Physik* 26.1 (Dec. 1924), pages 117–138. ISSN: 0044-3328. DOI: 10.1007/BF01327320 (cited on page 24).

[58] L. Ter Minassian-Saraga. “Thin films including layers: terminology in relation to their preparation and characterization (IUPAC Recommendations 1994)”. In: *Pure and Applied Chemistry* 66.8 (1994), pages 1667–1738. DOI: doi:10.1351/pac199466081667 (cited on page 27).

[59] M. Li and H. F. Dylla. “Model for the outgassing of water from metal surfaces”. In: *Journal of Vacuum Science & Technology A* 11.4 (July 1993), pages 1702–1707. ISSN: 0734-2101. DOI: 10.1116/1.578482 (cited on page 27).

[60] D. Jr. Edwards. “Upper bound to the pressure in an elementary vacuum system”. In: *Journal of Vacuum Science and Technology* 14.1 (Jan. 1977), pages 606–610. ISSN: 0022-5355. DOI: 10.1116/1.569160 (cited on pages 27, 85).

[61] K. Kanazawa. “Analysis of pumping down process”. In: *Journal of Vacuum Science & Technology A* 7.6 (Nov. 1989), pages 3361–3370. ISSN: 0734-2101. DOI: 10.1116/1.576151 (cited on pages 27, 28).

[62] G. Horikoshi. “Physical understanding of gas desorption mechanisms”. In: *Journal of Vacuum Science & Technology A* 5.4 (July 1987), pages 2501–2506. ISSN: 0734-2101. DOI: 10.1116/1.574407 (cited on pages 27, 28).

[63] P. A. Redhead. “Modeling the pump-down of a reversibly adsorbed phase. I. Monolayer and submonolayer initial coverage”. In: *Journal of Vacuum Science & Technology A* 13.2 (1995), pages 467–475. ISSN: 0734-2101. DOI: 10.1116/1.579381 (cited on pages 27–29, 31, 34).

[66] M. I. Temkin and V. Pyzhev. “Kinetics of Ammonia Synthesis on Promoted Iron Catalyst”. In: *Acta. Phys. Chim. USSR* 12 (1940), pages 327–356 (cited on pages 29, 31).

[67] M. M. Dubinin and L. V. Radushkevich. “The equation of the characteristic curve of the activated charcoal”. In: *Proc. Acad. Sci. USSR Phys. Chem. Sect.* 55 (1947), pages 331–333 (cited on page 29).

[68] I. Langmuir. “The adsorption of gases on plane surfaces of glass, mica and platinum”. In: *Journal of the American Chemical Society* 40.9 (1918), pages 1361–1403. DOI: 10.1021/ja02242a004 (cited on page 29).

[70] A. Sieverts. “Die aufnahme von gasen durch metalle”. In: *Zeitschrift für metallkunde* 21 (1929), pages 37–46 (cited on page 35).

[71] H. Wipf. “Solubility and diffusion of hydrogen in pure metals and alloys”. In: *Physica Scripta* 2001.T94 (Jan. 2001), page 43. DOI: 10.1238/Physica.Topical.094a00043 (cited on page 35).

[73] P. C. Novelli et al. “Molecular hydrogen in the troposphere: Global distribution and budget”. In: *Journal of Geophysical Research: Atmospheres* 104.D23 (1999), pages 30427–30444. DOI: https://doi.org/10.1029/1999JD900788 (cited on page 36).

[74] P. Tison. “Influence de l’hydrogène sur le comportement des metaux (Rapport CEA-R-5240(1))”. In: *Commissariat à l’Enérgie Atomique (CEA)* (1994) (cited on page 36).

[75] B. M. Shipilevsky and V. G. Glebovsky. “Competition of bulk and surface processes in the kinetics of hydrogen and nitrogen evolution from metals into vacuum”. In: *Surface Science* 216.3 (1989), pages 509–527. ISSN: 0039-6028 (cited on page 36).

[78] R. Calder and G. Lewin. “Reduction of stainless-steel outgassing in ultra-high vacuum”. In: *British Journal of Applied Physics* 18.10 (Oct. 1967), page 1459. DOI: 10.1088/0508-3443/18/10/313 (cited on pages 39–41, 73, 80).

[81] G. Moraw and R. Dobrozemsky. “Attainment of Outgassing Rates Below 10-13 Torr Liters/Sec Cm2 for Aluminium and Stainless Steel After Bakeout at Moderate Temperatures”. In: *Japanese Journal of Applied Physics* 13.S1 (Jan. 1974), page 261. DOI: 10.7567/JJAPS.2S1.261 (cited on page 41).

[82] J. R. Young. “Outgassing Characteristics of Stainless Steel and Aluminum with Different Surface Treatments”. In: *Journal of Vacuum Science and Technology* 6.3 (May 1969), pages 398–400. ISSN: 0022-5355. DOI: 10.1116/1.1492700 (cited on page 41).

[83] Y. Ishikawa and T. Yoshimura. “Importance of the surface oxide layer in the reduction of outgassing from stainless steels”. In: *Journal of Vacuum Science & Technology A* 13.4 (July 1995), pages 1847–1852. ISSN: 0734-2101. DOI: 10.1116/1.579669 (cited on page 41).

[84] V. Brisson et al. “Ultra-high vacuum qualification of the prototype module for the 2×3km arms of the VIRGO interferometer”. In: *Vacuum* 60.1 (2001). The Sixth European Vacuum Conference, pages 9–14. ISSN: 0042-207X. DOI: https://doi.org/10.1016/S0042-207X(00)00238-4 (cited on page 41).

[85] M. Bernardini et al. “Air bake-out to reduce hydrogen outgassing from stainless steel”. In: *Journal of Vacuum Science & Technology A* 16.1 (Jan. 1998), pages 188–193. ISSN: 0734-2101. DOI: 10.1116/1.580967 (cited on pages 41, 99, 122).

[86] R. A. Oriani. “The diffusion and trapping of hydrogen in steel”. In: *Acta Metallurgica* 18.1 (1970), pages 147–157. ISSN: 0001-6160. DOI: https://doi.org/10.1016/0001-6160(70)90078-7 (cited on pages 43, 93).

[87] A. J. Kumnick and H. H. Johnson. “Hydrogen transport through annealed and deformed armco iron”. In: *Metallurgical transactions* 5.5 (May 1974), pages 1199–1206. ISSN: 2379-0083. DOI: 10.1007/BF02644334 (cited on page 43).

[90] G. M. Pressouyre and I. M. Bernstein. “A kinetic trapping model for hydrogen-induced cracking”. In: *Acta Metallurgica* 27.1 (1979), pages 89–100. ISSN: 0001-6160. DOI: https://doi.org/10.1016/0001-6160(79)90059-2 (cited on page 43).

[91] R. F. Berg. “Hydrogen traps in the outgassing model of a stainless steel vacuum chamber”. In: *Journal of Vacuum Science & Technology A* 32.3 (Mar. 2014), page 031604. ISSN: 0734-2101. DOI: 10.1116/1.4869962 (cited on pages 43, 44).

[92] L. S. Darken and Rodney P. Smith. “Behavior of Hydrogen in Steel During and After Immersion in Acid”. In: *Corrosion* 5 (1949), pages 1–16 (cited on page 43).

[93] A. McNabb and P. K. Foster. “A new analysis of diffusion of hydrogen in iron and ferritic steels”. In: *Transactions of the Metallurgical Society of AIME* 227.3 (1963), page 618 (cited on page 43).

[95] J.-P. Bacher et al. “Thermal desorption study of selected austenitic stainless steels”. In: *Journal of Vacuum Science & Technology A* 21.1 (Dec. 2002), pages 167–174. ISSN: 0734-2101. DOI: 10.1116/1.1527953 (cited on page 44).

[96] W. Y. Choo and J. Y. Lee. “Thermal analysis of trapped hydrogen in pure iron”. In: *Metallurgical Transactions A* 13.1 (Jan. 1982), pages 135–140. ISSN: 2379-0180. DOI: 10.1007/BF02642424 (cited on page 44).

[97] W. Y. Choo and J. Y. Lee. “Hydrogen trapping phenomena in carbon steel”. In: *Journal of Materials Science* 17.7 (July 1982), pages 1930–1938. ISSN: 1573-4803. DOI: 10.1007/BF00540409 (cited on page 44).

[98] H. E. Kissinger. “Reaction Kinetics in Differential Thermal Analysis”. In: *Analytical Chemistry* 29.11 (1957), pages 1702–1706. DOI: 10.1021/ac60131a045 (cited on page 44).

[101] M. I. Baskes. “A calculation of the surface recombination rate constant for hydrogen isotopes on metals”. In: *Journal of Nuclear Materials* 92.2 (1980), pages 318–324. ISSN: 0022-3115. DOI: https://doi.org/10.1016/0022-3115(80)90117-8 (cited on page 46).

[102] V. Nemanič and J. Šetina. “Evolution of hydrogen from AISI 200 stainless steel: A study to determine whether it is a diffusion or recombination limited process and experimental evidence for strongly bound hydrogen”. In: *Vacuum* 109 (2014), pages 102–107. ISSN: 0042-207X. DOI: https://doi.org/10.1016/j.vacuum.2014.06.028 (cited on page 46).

[103] R. Ash and R. M. Barrer. “Permeation of hydrogen through metals”. In: *The Philosophical Magazine: A Journal of Theoretical Experimental and Applied Physics* 4.47 (1959), pages 1197–1206. DOI: 10.1080/14786435908235823 (cited on page 46).

[104] D. E. Beck and E. Miyazaki. “Molecular adsorption: Inclusion of bulk diffusion and its effect on Auger intensities”. In: *Surface Science* 39.1 (1973), pages 37–50. ISSN: 0039-6028. DOI: https://doi.org/10.1016/0039-6028(73)90093-9 (cited on page 46).

[105] V. Nemanič and J. Šetina. “Outgassing in thin wall stainless steel cells”. In: *Journal of Vacuum Science & Technology A* 17.3 (May 1999), pages 1040–1046. ISSN: 0734-2101. DOI: 10.1116/1.581680 (cited on page 46).

[106] R. A. Langley et al. “Data Compendium for Plasma-Surface Interactions”. In: *Nuclear Fusion* 24.S1 (Jan. 1984), S9. DOI: 10.1088/0029-5515/24/S1/001 (cited on page 46).

[107] V. Nemanič and T. Bogataj. “Outgassing of thin wall stainless steel chamber”. In: *Vacuum* 50.3 (1998), pages 431–437. ISSN: 0042-207X. DOI: https://doi.org/10.1016/S0042-207X(98)00087-6 (cited on page 46).

[109] H. Kogelnik and T. Li. “Laser Beams and Resonators”. In: *Appl. Opt.* 5.10 (Oct. 1966), pages 1550–1567. DOI: 10.1364/AO.5.001550 (cited on page 48).

[111] K. S. Thorne. “"Gravitational Radiation," in Three Hundred Years of Gravitation”. In: *Cambridge University Press* (1987), pages 330–458 (cited on page 50).

[121] Y. Saito and R. Takahashi. “Production Process of the Interferometer Beam Tubes in LCGT Project”. In: *Journal of the Vacuum Society of Japan* 54.12 (2011), pages 621–626. DOI: 10.3131/jvsj2.54.621 (cited on page 55).

[125] M. Morcillo et al. “Atmospheric corrosion of mild steel”. In: *Revista de Metalurgia* 5 (Oct. 2011), pages 426–444. DOI: 10.3989/revmetalm.1125 (cited on page 61).

[128] Y. Ishimori et al. “Outgassing Rates of Stainless Steel and Mild Steel after Different Pretreatments”. In: *SHINKU* 14.8 (1971) (cited on page 61).

[129] C. D. Park et al. “Reduction in hydrogen outgassing from stainless steels by a medium-temperature heat treatment”. In: *Journal of Vacuum Science & Technology A* 26.5 (Aug. 2008). ISSN: 0734-2101. DOI: 10.1116/1.2956625 (cited on page 61).

[130] C. Park, T. Ha, and B. Cho. “Thermal outgassing rates of low-carbon steels”. In: *Journal of Vacuum Science & Technology A* 34.2 (Dec. 2015). ISSN: 0734-2101. DOI: 10.1116/1.4936840 (cited on page 61).

[131] C. Park and T. Ha. “Vacuum Characteristic of a Chamber Made of Mild Steel”. In: *Applied Science and Convergence Technology* 24 (July 2015), pages 84–89. DOI: 10.5757/ASCT.2015.24.4.84 (cited on page 61).

[132] J. Kamiya et al. “Vacuum chamber made of soft magnetic material with high permeability”. In: *Vacuum* 98 (2013), pages 12–17. ISSN: 0042-207X. DOI: https://doi.org/10.1016/j.vacuum.2012.10.007 (cited on page 61).

[133] S. Kato et al. “Outgassing Rate Measurement of SUS430 Vacuum Chamber”. In: *Journal of the Vacuum Society of Japan* 55.4 (2012), pages 160–163. DOI: 10.3131/jvsj2.55.160 (cited on page 61).

[135] C. Benvenuti and M. Hauer. “Low pressure limit of the bayard-alpert gauge”. In: *Nuclear Instruments and Methods* 140.3 (1977), pages 453–460. ISSN: 0029-554X. DOI: https://doi.org/10.1016/0029-554X(77)90360-3 (cited on page 66).

[141] H. F. Dylla, D. M. Manos, and P. H. LaMarche. “Correlation of outgassing of stainless steel and aluminum with various surface treatments”. In: *Journal of Vacuum Science & Technology A* 11.5 (Sept. 1993). ISSN: 0734-2101. DOI: 10.1116/1.578617 (cited on page 85).

[142] A. Savitzky and M. J. E. Golay. “Smoothing and Differentiation of Data by Simplified Least Squares Procedures.” In: *Analytical Chemistry* 36.8 (1964). DOI: 10.1021/ac60214a047 (cited on pages 90, 118).

[143] D. M. Grant, Cummings D. L., and D. A. Blackburn. “Hydrogen in 304 steel: Diffusion, permeation and surface reaction”. In: *Journal of Nuclear Materials* 152.2 (1988), pages 139–145. ISSN: 0022-3115. DOI: https://doi.org/10.1016/0022-3115(88)90319-4 (cited on pages 90, 118).

[144] M. R. Louthan and R. G. Derrick. “Hydrogen transport in austenitic stainless steel”. In: *Corrosion Science* 15.6 (1975). ISSN: 0010-938X. DOI: https://doi.org/10.1016/0010-938X(75)90022-0 (cited on pages 90, 118).

[145] K. L. Wilson and M. I. Baskes. “Deuterium trapping in irradiated 316 stainless steel”. In: *Journal of Nuclear Materials* 76-77 (1978), pages 291–297. ISSN: 0022-3115. DOI: https://doi.org/10.1016/0022-3115(78)90160-5 (cited on page 93).

[146] K. L. Wilson and M. I. Baskes. “Deuterium re-emission from 304LN stainless steel”. In: *Journal of Nuclear Materials* 111-112 (1982), pages 622–627. ISSN: 0022-3115. DOI: https://doi.org/10.1016/0022-3115(82)90276-8 (cited on page 93).

[147] C. Scarcia et al. “Study of selected mild steels for application in vacuum systems of future gravitational wave detectors”. In: *Journal of Vacuum Science & Technology B* 42.5 (Sept. 2024) (cited on page 95).

[155] J. A. Fedchak et al. “Vacuum furnace for degassing stainless-steel vacuum components”. In: *Journal of Vacuum Science & Technology A* 36.2 (Jan. 2018), page 023201. ISSN: 0734-2101. DOI: 10.1116/1.5016181 (cited on page 140).

[159] M. Andrés-Carcasona et al. “Study of scattered light in the main arms of the Einstein Telescope gravitational wave detector”. In: *Phys. Rev. D* 108 (10 Nov. 2023), page 102001. DOI: 10.1103/PhysRevD.108.102001 (cited on page 157).

[160] V. Brisson et al. “Large ultra-high-vacuum VAT gate valve with viton gasket for the VIRGO interferometer”. In: *Vacuum* 60.1 (2001). The Sixth European Vacuum Conference, pages 221–227. ISSN: 0042-207X. DOI: https://doi.org/10.1016/S0042-207X(00)00375-4 (cited on page 157).

Books

[55] W.F. Hosford. *Physical Metallurgy*. CRC Press, 2010. ISBN: 9781439882863 (cited on page 24).

[65] H. Freundlich. *Kapillarchemie: eine darstellung der chemie der kolloide und verwandter gebiete*. Akademische verlagsgesellschaft m.b.h., 1909 (cited on page 29).

[69] D. O. Hayward and B. M. W. Trapnell. *Chemisorption*. Butterworths, 1964 (cited on page 31).

[72] E.T. Turkdogan. *Fundamentals of Steelmaking*. Book (Institute of Materials (Great Britain))). Institute of Materials, 1996. ISBN: 9781861250049 (cited on page 35).

[76] J. Crank. *The Mathematics of Diffusion*. Oxford science publications. Clarendon Press, 1979. ISBN: 9780198534112 (cited on pages 37, 38).

[77] A. Pinkus and S. Zafrany. *Fourier Series and Integral Transforms*. Cambridge University Press, 1997 (cited on page 39).

[89] A. R. Troiano, R. Gibala, and R. F. Hehemann. *Hydrogen Embrittlement and Stress Corrosion Cracking: A Troiano Festschrift*. Amer. Soc. for Metals, 1984. ISBN: 9781615031788 (cited on page 43).

[110] A. Yariv. *Optical Electronics*. Saunders College Publishing, 1991. ISBN: 9781600490132. DOI: 10.7907/5r87-m275 (cited on page 49).

[123] M. Wutz, H. Adam, and W. Walcher. *Theory and practice of vacuum technology*. Fried, 1989 (cited on page 61).

[127] M. H. Hablanian. *High-Vacuum Technology: A Practical Guide, Second Edition (2nd ed.)* Routledge, 1997. DOI: https://doi.org/10.1201/9780203751923 (cited on page 61).

[134] P. A. Redhead, J. P. Hobson, and E. V. Kornelsen. *The Physical Basis of Ultrahigh Vacuum*. AVS Classics in Vacuum Science and Technology. American Inst. of Physics, 1997. ISBN: 9781563961229 (cited on page 65).

Dissertations and Theses

[25] A. D. Gillespie. “Thermal Noise in the Initial LIGO Interferometers”. PhD thesis. California Institute of Technology, Jan. 1995 (cited on page 8).

[94] Wolfgang Siegl. “Hydrogen Trapping in Iron and Iron-Based Alloys”. PhD thesis. Montanuniversitaet Leoben, 2021 (cited on pages 44, 45).

[100] P. Massuti Ballester. “Outgassing Analysis of different Copper Materials for Ultra-High Vacuum by Thermal Desorption Spectroscopy”. Presented 16 Aug 2017. Saarland U., 2017 (cited on page 45).

[150] C. Scarcia. “UHV compatibility of mild steel for future gravitational wave detectors”. UNIMORE, 2021 (cited on pages 97, 99, 100, 196).

Proceedings and Reports

[31] S. E. Whitcomb. “Optical Pathlength Fluctuations in an Interferometer Due to Residual Gas”. In: 2023 (cited on pages 10, 47, 48).

[32] M. E. Zucker and S. E. Whitcomb. “Measurement of optical path fluctuations due to residual gas in the LIGO 40-meter interferometer”. In: 1994 (cited on pages 10, 49, 50).

[39] ET steering committee editorial team. “Einstein Telescope Design Report Update 2020 (ET-0007C-20)”. In: Sept. 2020 (cited on pages 10, 11, 13, 16–18, 51, 56, 58, 59, 153, 175).

[42] M. Evans et al. “A Horizon Study for Cosmic Explorer: Science, Observatories, and Community”. In: 2021. arXiv: 2109.09882 [astro-ph.IM] (cited on pages 11, 16, 60).

[46] The Virgo Collaboration. “Advanced Virgo Technical Design Report (VIR-0128A-12)”. In: Apr. 2012 (cited on page 13).

[47] ET science team. “Einstein gravitational wave Telescope: Conceptual Design Study (ET-0106C-10)”. In: 2011 (cited on pages 16, 58, 175).

[48] ET steering committee. “ET cost book (ET-0000A-20)”. In: 2020 (cited on page 16).

[51] H.F. Dylla, R. Weiss, and M. Zucker. “NSF Workshop on Large Ultrahigh-Vacuum Systems for Frontier Scientific Research Instrumentation (P1900072-v1)”. In: LIGO Livingston Observatory. Jan. 2019 (cited on pages 17, 60, 61).

[52] P. Chiggiato. “Outgassing properties of vacuum materials for particle accelerators”. In: 2020. arXiv: 2006.07124 [physics.acc-ph] (cited on pages 23–25, 34–36, 38, 41, 42, 65, 66, 68, 99, 122).

[53] M. Taborelli. “Cleaning and surface properties”. In: CAS - CERN Accelerator School: Vacuum for Particle Accelerators. 2006, pages 321–340 (cited on page 24).

[57] J. P. Hobson. “Desorption of Adsorbed Gas and Re-emission of Gas Previously Pumped by Ionic Pumping”. In: Trans 8th AVS Vac Symp. 1961 (cited on page 26).

[64] R. Weiss. “Notes of Workshop on Control and Measurement of Water in Vacuum systems”. In: NIST, Gaithersburg, MD, 1994. 1994 (cited on page 27).

[79] P. Chiggiato. “Dégazage des solides en ultravide : quelques notions de base pour les techniciens du CERN”. In: 2012 (cited on page 41).

[80] S. Sgobba. “Vacuum for accelerators: introduction to materials and properties”. In: 30 pages. 2020. eprint: 2006.02212 (cited on page 41).

[88] H. J. Grabke and Riecke E. “Absorption and diffusion of hydrogen in steels”. In: 2001 (cited on page 43).

[99] H. E. Kissinger. “Variation of Peak Temperature With Heating Rate in Differential Thermal Analysis”. In: 1956 (cited on page 44).

[108] R. Weiss. “Scattering by Residual Gas (T890025-v1)”. In: 1989 (cited on pages 47–49).

[113] B. Althouse. “LLO Beam Tube Bakeout Readiness Review (LIGO-G990081)”. In: *LIGO DCC*. 1999 (cited on page 53).

[114] W. Carpenter et al. “Data from Beam Tube Pump Down II (LIGO-T970111-00-B)”. In: *LIGO DCC*. 1997 (cited on page 53).

[115] R. Weiss. “Information for the Beam Tube Pumpdown (LIGO-T970110-00-D)”. In: *LIGO DCC*. 1997 (cited on page 53).

[116] R. Weiss. “Residual Gas in the LIGO Beam Tubes (LIGO G030701-00)”. In: *LIGO DCC*. 2003 (cited on page 53).

[117] W. Carpenter et al. “LIGO Beam Tube Component and Module Leak Testing (LIGO P990023-00)”. In: *LIGO DCC*. 1999 (cited on page 53).

[118] VIRGO. “VIRGO Final design report (VIR-TRE-1000-1)”. In: *VIRGO TDS*. 1997 (cited on page 54).

[119] Y. Tanimoto et al. “Impact of the 2024 Noto Peninsula Earthquakeon the Vacuum Equipment of KAGRA, the Large Cryogenic Gravitational Wave Telescope”. In: *6th Workshop on the Operation of Large Vacuum Systems*. 2024 (cited on page 55).

[120] M. Yang et al. “Prototype of Vacuum Monitoring System for KAGRA”. In: *The 9th KAGRA International Workshop*. 2022 (cited on page 55).

[122] H. Lück and the GEO600-Team. “The vacuum system of GEO600”. In: *Second Edoardo Amaldi Conference*. 1998 (cited on page 55).

[126] W. R. Wheeler and M. Carlson. “Transaction of the 8th National Vacuum Symposium, 1961”. In: Pergamon, New York, 1962 (cited on page 61).

[136] Cristoforo Benvenuti, Jean Michel Laurent, and F Scalambrin. “CERN-ISR-VA-77-31”. In: *CERN*. 1977 (cited on page 67).

[138] P. Manini. “Non Evaporable getter (NEG) technology for UHV–XHV systems”. In: *Presentation of the vacuum firm SAES at CERN*. 2011 (cited on page 73).

[139] GS-IS & EN-MME. “Tech. Spec. N°1004 - 1.4306 - Stainless steel sheets/plates for vacuum applications (EDMS N^o: 790767)”. In: *CERN*. 2013 (cited on page 79).

[140] M. Malabaila and L. Ferreira. “Operating procedure for chemical degreasing of parts for highvacuum and ultra-high-vacuum applications (EDMS N^o: 1390437 v.3)”. In: *CERN*. 2022 (cited on page 80).

[148] D. Wagner et al. “A laboratory study of the reduction of iron oxides by hydrogen”. In: *Sohn International Symposium*. 2006 (cited on page 95).

[151] G. Bregliozzi, P. Chiggiato, and J.A. Ferreira Somoza. “Criteria for vacuum acceptance tests (EDMS n° 1752123)”. In: *ACC-V-ES-0001*. 2018 (cited on page 111).

[152] S. Meunier. “Vacuum gauges: Outgassing and sensitivities”. In: *VSC seminars (CERN)*. 2022 (cited on page 125).

[153] Hiden Analytical. “Relative Sensitivity: RS Measurements of Gases ”. In: *(Application Note 282)* (cited on page 128).

[154] A. Grado et. al. “Einstein Telescope beampipe requirements (ET-0385A-24)”. In: *ET collaboration*. 2024 (cited on page 135).

[157] Jr. J. Matolich. “Thermal conductivity and electrical resistivity of type 316 stainless steel from 0 to 1800 F”. In: *(NASA CR-54151 BATT-7096)*. 1965 (cited on page 151).

[158] Agilent Technologies. “Agilent Ion Pump Technical Notes”. In: *(Agilent Ion Pumps Catalog)* (cited on page 156).

Web Addresses

Miscellaneous

[112] *Computational Chemistry Comparison and Benchmark DataBase (CCCBD)*. https://cccbdb.nist.gov/pollistx.asp (cited on pages 52, 164).

[137] Hiden Analytical. *TPD Workstation* (cited on page 68).

Statutory declaration

I, Carlo Scarcia, hereby declare that this dissertation and the contents presented therein are my own and have been generated independently as a result of my original research.

I hereby declare under oath:

1. This work was completed entirely during my doctoral studentship at CERN while affiliated with RWTH.
2. If any part of this dissertation has previously been used for an academic degree or other qualification at this or any other institution, this has been indicated.
3. Whenever other publications from third parties have been used, these have been clearly identified and cited.
4. All essential sources of support have been identified. Parts of this work, specifically some sections of Chapters 3, 4, 5, 6 and 7 have been published previously in:

   (a) *Carlo Scarcia et al.*; Study of selected mild steels for application in vacuum systems of future gravitational wave detectors. *J. Vac. Sci. Technol. B 1 September 2024; 42 (5): 054202*. https://doi.org/10.1116/6.0003820

   (b) *Carlo Scarcia et al.*; Study of the UHV compatibility of selected ferritic stainless steels for application in vacuum systems of future gravitational wave detectors *J. Vac. Sci. Technol. B 11 July 2025; 43 (4): 044203*. https://doi.org/10.1116/6.0004698

Geneva, 30th July 2025

Carlo Scarcia

Acknowledgements

This manuscript reflects a significant and transformative journey made possible by the invaluable contributions of the individuals I had the privilege to work with over the past years. Their insights, guidance, and support have been instrumental in shaping this work.

I extend my deepest gratitude to Prof. Achim Stahl for his generous support of my doctoral studies at CERN through the Gentner Programme. His assistance with administrative tasks and his guidance laid the foundation for this research. I also thank Prof. Ulrich Krupp for kindly accepting the role of engineering reviewer for this work.

During my time at CERN, I had the honor of working under the supervision of Dr. Giuseppe Bregliozzi, whose advice, critical feedback, and unwavering encouragement were invaluable throughout my doctoral journey. His open-door policy, daily engagement, and readiness to support my initiatives greatly fueled my motivation and shaped my approach to tackling operational vacuum challenges.

I am profoundly grateful to Paolo Chiggiato, my group leader, for his trust and support in allowing me to conduct my studies independently and represent the ET vacuum group at CERN across Europe at conferences and symposiums. His mentorship expanded my understanding of vacuum systems and their complexities.

Special thanks to Ivo Wevers, my former supervisor and always a mentor, for teaching me how to critically review vacuum measurements, design systems, and master the art of *fingerspitzengefühl* in experimental work.

I also wish to thank the senior members of the ET vacuum team at CERN—Ana Teresa Fontenla, Dr. Cedric Garion, Dr. Stefano Sgobba, Dr. Jose Ferreira Somoza, Gille Favre, Jan Hansen, Alice Michet, Dr. Mauro Taborelli, and Dr. Leonel Ferreira—for their essential support and expertise, which were crucial to the success of this thesis.

I want to extend my gratitude to all the Cosmic Explorer colleagues: Fred Dylla, Rai Weiss, Mike Zucker, Jon Feicht, Albert Lazzarini, and the entire Cosmic Explorer vacuum studies team for our stimulating discussions on vacuum solutions during our bimonthly meetings and for explaining how these large vacuum systems were designed, commissioned, and operated.

To all my colleagues in TE-VSC, I am deeply appreciative of the fruitful discussions, lessons, and shared knowledge that enriched my doctoral studies far beyond expectations.

A heartfelt thank you goes to my former CERN colleagues Vasco, Patrick, and Joana, for their friendship, support, and countless coffees spent envisioning the future together.

Una menzione special va a coloro che da un decennio oramai ci sono sempre stati: Hassine, Loris, Matteo e Vlad. La vita ci ha sparpagliati, ma l'amicizia non ci separerà mai.

Grazie mamma, grazie papà e grazie Marino pe lu supportu ca miti sempre datu; alla fine su diventatu deveru scienziatu. Senza de vui ca me stimolati e consigliati

sempre no stia a ru sto. Nu grazie va puru alli nonni, a ci nce e non ce chiui ma alla fine ci sarà pe sempre.